frontiers | Research Topics

Multi-scale dynamics modeling of brain physiological functions and pathological mechanisms

Edited by
Ying Wu, Miguel A. F. Sanjuan, Rong Wang, Jiajia Li and Pan Lin

Published in
Frontiers in Neuroscience

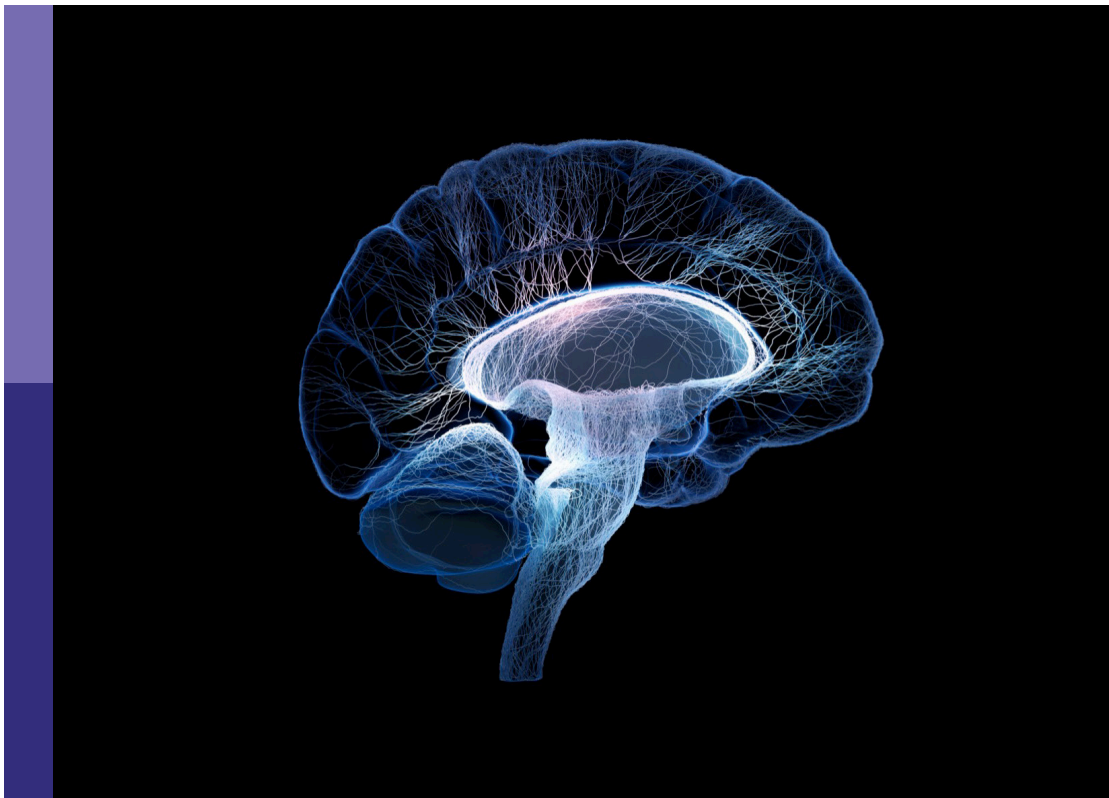

ISSN 1664-8714
ISBN 978-2-8325-3556-1
DOI 10.3389/978-2-8325-3556-1

About Frontiers

Frontiers is more than just an open access publisher of scholarly articles: it is a pioneering approach to the world of academia, radically improving the way scholarly research is managed. The grand vision of Frontiers is a world where all people have an equal opportunity to seek, share and generate knowledge. Frontiers provides immediate and permanent online open access to all its publications, but this alone is not enough to realize our grand goals.

Frontiers journal series

The Frontiers journal series is a multi-tier and interdisciplinary set of open-access, online journals, promising a paradigm shift from the current review, selection and dissemination processes in academic publishing. All Frontiers journals are driven by researchers for researchers; therefore, they constitute a service to the scholarly community. At the same time, the *Frontiers journal series* operates on a revolutionary invention, the tiered publishing system, initially addressing specific communities of scholars, and gradually climbing up to broader public understanding, thus serving the interests of the lay society, too.

Dedication to quality

Each Frontiers article is a landmark of the highest quality, thanks to genuinely collaborative interactions between authors and review editors, who include some of the world's best academicians. Research must be certified by peers before entering a stream of knowledge that may eventually reach the public - and shape society; therefore, Frontiers only applies the most rigorous and unbiased reviews. Frontiers revolutionizes research publishing by freely delivering the most outstanding research, evaluated with no bias from both the academic and social point of view. By applying the most advanced information technologies, Frontiers is catapulting scholarly publishing into a new generation.

What are Frontiers Research Topics?

Frontiers Research Topics are very popular trademarks of the *Frontiers journals series*: they are collections of at least ten articles, all centered on a particular subject. With their unique mix of varied contributions from Original Research to Review Articles, Frontiers Research Topics unify the most influential researchers, the latest key findings and historical advances in a hot research area.

Find out more on how to host your own Frontiers Research Topic or contribute to one as an author by contacting the Frontiers editorial office: frontiersin.org/about/contact

Multi-scale dynamics modeling of brain physiological functions and pathological mechanisms

Topic editors

Ying Wu — Xi'an Jiaotong University, China
Miguel A. F. Sanjuan — Rey Juan Carlos University, Spain
Rong Wang — Xi'an University of Science and Technology, China
Jiajia Li — Xi'an University of Architecture and Technology, China
Pan Lin — Hunan Normal University, China

Citation

Wu, Y., Sanjuan, M. A. F., Wang, R., Li, J., Lin, P., eds. (2023). *Multi-scale dynamics modeling of brain physiological functions and pathological mechanisms*. Lausanne: Frontiers Media SA. doi: 10.3389/978-2-8325-3556-1

Table of contents

frontiers | Frontiers in Neuroscience

TYPE Editorial
PUBLISHED 11 September 2023
DOI 10.3389/fnins.2023.1275481

OPEN ACCESS

EDITED BY
Guo-Yuan Yang,
Shanghai Jiao Tong University, China

REVIEWED BY
Damien Depannemaecker,
Aix Marseille Université, France

*CORRESPONDENCE
Ying Wu
✉ wying36@xjtu.edu.cn

RECEIVED 10 August 2023
ACCEPTED 28 August 2023
PUBLISHED 11 September 2023

CITATION
Li J, Wang R, Lin P, Sanjuan MAF and Wu Y (2023) Editorial: Multi-scale dynamics modeling of brain physiological functions and pathological mechanisms.
Front. Neurosci. 17:1275481.
doi: 10.3389/fnins.2023.1275481

Editorial: Multi-scale dynamics modeling of brain physiological functions and pathological mechanisms

Jiajia Li[1], Rong Wang[2], Pan Lin[3], Miguel A. F. Sanjuan[4] and Ying Wu[5]*

[1]School of Information and Control Engineering, Xi'an University of Architecture and Technology, Xi'an, Shaanxi, China, [2]School of Science, Xi'an University of Science and Technology, Xi'an, China, [3]Center for Mind & Brain Sciences, Hunan Normal University, Hunan, Changsha, China, [4]Nonlinear Dynamics, Chaos and Complex Systems Group, Departamento de Física, Universidad Rey Juan Carlos, Madrid, Spain, [5]State Key Laboratory for Strength and Vibration of Mechanical Structures, School of Aerospace Engineering, Xi'an Jiaotong University, Xi'an, Shaanxi, China

KEYWORDS

dynamics modeling, neuron network, physiological functions, pathological mechanisms, brain function

Editorial on the Research Topic
Multi-scale dynamics modeling of brain physiological functions and pathological mechanisms

1. Introduction

The human brain is an extraordinary organ, sometimes referred to as the most complex system since it is responsible for our thoughts, emotions, and actions. Understanding how the brain works and unraveling the mechanisms underlying neurological disorders are long-outstanding challenges in neuroscience. In this editorial article, we delve into the exciting realm of multi-scale dynamics modeling of brain physiological functions and pathological mechanisms. This Research Topic in Frontiers in Neuroscience brings together a collection of groundbreaking studies that shed light on the complex dynamics of the brain, offering new insights into both normal brain function and the underlying causes of neurological disorders.

2. Exploring the multi-scale dynamics

As is well known, the brain operates across multiple scales, from the interactions between individual neurons to the coordination of large-scale networks. Traditional reductionist approaches have provided valuable insights into specific aspects of the brain function. However, a comprehensive and holistic understanding of the brain dynamics necessitates a multi-scale perspective that integrates information across different levels of organization such as the neuron scale, the neuron network scale, and the brain network scale. Cutting-edge research employing innovative modeling techniques to capture the complexity of brain dynamics across various scales (Xu and Kang; Liu and Sun) is showcased here.

3. Unraveling brain physiological functions

Several articles focus their attention on unraveling the fundamental physiological functions of the brain. By combining experimental data with computational models, researchers have made significant strides in elucidating the mechanisms underlying sensory perception (Xu and Kang), memory formation (Liu and Sun), and attention (Wang et al.). These studies provide valuable insights into the dynamic interplay between different brain regions and shed light on the neural mechanisms that give rise to our cognitive abilities.

4. Unveiling pathological mechanisms

Neurological disorders pose significant challenges to human health and wellbeing. From this perspective, several articles delve into the pathological mechanisms underlying conditions such as epilepsy (Fan et al.; Jiang et al.), Alzheimer's disease (Li et al.), acoustic neuroma (Zhang et al.), pituitary adenoma (Wang et al.), and sleep disorders (Li and Dong). By employing multi-scale modeling approaches, researchers have made remarkable progress in unraveling the complex interactions between genetic, cellular, and network-level abnormalities that contribute to these disorders. Most importantly, this deeper understanding opens new avenues for the development of targeted therapeutic interventions.

5. Bridging the gap between theory and clinical applications

The studies presented here not only advance our theoretical understanding of brain dynamics, but also have important implications for clinical applications (Wang et al.; Xu et al.; Zhang et al.). By elucidating the mechanisms underlying neurological disorders, these findings pave the way for the development of novel diagnostic tools, personalized treatment strategies, and therapeutic interventions. The integration of multi-scale modeling with clinical data holds great promise for improving patient outcomes and transforming the field of neurology.

6. Conclusions

The multi-scale dynamics modeling of brain physiological functions and pathological mechanisms represents a paradigm shift in neuroscience research. This Research Topic in Frontiers in Neuroscience brings together a diverse range of studies that push the boundaries of our understanding of the brain. By integrating knowledge from different scales, these studies provide a comprehensive picture of brain dynamics and offer new avenues for tackling neurological disorders. The insights gained from this research have the potential to transform our approach to brain health and pave the way for more effective treatments in the future.

Author contributions

YW: Writing—review and editing, Supervision. JL: Writing—original draft. RW: Writing—review and editing. PL: Writing—review and editing. MS: Writing—review and editing.

Funding

This work was supported by the National Natural Science Foundation of China (Grant Nos. 12132012, 11972275, 12002251, 12272292, and 62071177). MS acknowledges financial support from the Spanish State Research Agency (AEI) and the European Regional Development Fund (ERDF, EU) under Project No. PID2019-105554GB-I00 (MCIN/AEI/10.13039/501100011033).

Conflict of interest

The authors declare that the research was conducted in the absence of any commercial or financial relationships that could be construed as a potential conflict of interest.

Publisher's note

frontiers | Frontiers in Neuroscience

TYPE Original Research
PUBLISHED 19 January 2023
DOI 10.3389/fnins.2023.1126875

OPEN ACCESS

EDITED BY
Jiajia Li,
Xi'an University of Architecture and Technology, China

REVIEWED BY
Xinlin Song,
Xi'an University of Science and Technology, China
Yongchen Fan,
Xi'an Jiaotong University, China

*CORRESPONDENCE
Guoming Luan
luangm3@163.com

SPECIALTY SECTION
This article was submitted to Translational Neuroscience, a section of the journal Frontiers in Neuroscience

RECEIVED 18 December 2022
ACCEPTED 03 January 2023
PUBLISHED 19 January 2023

CITATION
Fan D, Qi L, Yang Z, Luan G and Wang Q (2023) Putative cause of seizure-induced cognitive alterations: The oscillatory reconfiguration of seizure network.
Front. Neurosci. 17:1126875.
doi: 10.3389/fnins.2023.1126875

Putative cause of seizure-induced cognitive alterations: The oscillatory reconfiguration of seizure network

Denggui Fan[1], Lixue Qi[1], Zecheng Yang[1], Guoming Luan[2]* and Qingyun Wang[3]

[1]School of Mathematics and Physics, University of Science and Technology Beijing, Beijing, China, [2]Epilepsy Center, Sanbo Brain Hospital, Capital Medical University, Beijing, China, [3]Department of Dynamics and Control, Beihang University, Beijing, China

Introduction: The dynamic reconfiguration of network oscillations is connected with cognitive processes. Changes in how neural networks and signaling pathways work are crucial to how epilepsy and related conditions develop. Specifically, there is evidence that prolonged or recurrent seizures may induce or exacerbate cognitive impairment. However, it still needs to be determined how the seizure brain configures its functional structure to shape the battle of strong local oscillations vs. slow global oscillations in the network to impair cognitive function.

Methods: In this paper, we aim to deduce the network mechanisms underlying seizure-induced cognitive impairment by comparing the evolution of strong local oscillations with slow global oscillations and their link to the resting state of healthy controls. Here, we construct a dynamically efficient network of pathological seizures by calculating the synchrony and directionality of information flow between nine patients' SEEG signals. Then, using a pattern-based method, we found hierarchical modules in the brain's functional network and measured the functional balance between the network's local strong and slow global oscillations.

Results and discussion: According to the findings, a tremendous rise in strong local oscillations during seizures and an increase in slow global oscillations after seizures corresponded to the initiation and recovery of cognitive impairment. Specifically, during the interictal period, local strong and slow global oscillations are in metastable balance, which is the same as a normal cognitive process and can be switched easily. During the pre-ictal period, the two show a bimodal pattern of separate peaks that cannot be easily switched, and some flexibility is lost. During the seizure period, a single-peak pattern with negative peaks is showcased, and the network eventually transitions to a very intense strong local oscillation state. These results shed light on the mechanism behind network oscillations in epilepsy-induced cognitive impairment. On the other hand, the differential (similarity) of oscillatory reorganization between the local (non) epileptogenic network and the global network may be an emergency protective mechanism of the brain, preventing the spread of pathological information flow to more healthy brain regions.

KEYWORDS

focal epilepsy, effective brain network, oscillatory reorganization, seizures transitions, cognitive impairment

1. Introduction

Oscillations arise from neuronal interactions that promote communication and information processing between regions of a functional neural network (Engel et al., 2001; Buzsaki and Draguhn, 2004; Wang et al., 2020; Földi et al., 2021). Recent studies have shown that network oscillations temporally link neurons and enhance synaptic plasticity, supporting long-term information consolidation and is a cognitive process necessary for learning and memory (Goltsev et al., 2013; Holmes, 2015; Sadaghiani and Kleinschmidt, 2016). Specifically, tiny timing mistakes in neuronal or oscillatory activity may be magnified in more extensive networks, resulting in cognitive impairment (Buzsáki, 2007). This shows that using network oscillations to investigate cognitive impairment is a viable treatment strategy. Many studies are becoming more interested in the impact of network oscillations on cognitive impairment, focusing on specific frequencies and amplitudes of oscillation (Wilke et al., 2011; Ibrahim et al., 2012; Guo et al., 2018). However, the mechanism through which oscillatory reorganization influences cognitive impairment remains unknown.

In the present study, we surveyed the mechanisms through which network oscillations contribute to seizure-induced cognitive impairment. As a starting point, we investigated the findings of prior studies on the topic. Previous research has shown a causal relationship between the pathophysiological mechanisms that cause seizures and the biology of cognitive impairment, with oscillations acting as one of the essential links (Jensen et al., 2007; Guo et al., 2018). Gamma oscillations are closely associated with sustained learning and memory functions, and oscillation abnormalities may result in cognitive deficits (Ibrahim et al., 2012; Guo et al., 2018). Cognitive memory may be disrupted by seizures caused by intermittent oscillations (Binnie and Marston, 1992; Holmes and Lenck-Santini, 2006; Lévesque et al., 2018). In epileptic patients, abnormalities in brain connection produced by oscillations and impaired temporal coding affect cognition (Holmes, 2015). In patients with temporal lobe epilepsy, seizure-evoked circuits are localized in memory-supporting brain regions, and these regions generate essential physiological high-frequency oscillations required for memory processing (Axmacher et al., 2008; Ewell et al., 2019). However, most research has been limited to specific oscillations or epileptic disorders. Consequently, little is known about the systematic contributions of oscillatory reorganization to cognitive impairment. In addition, several studies have shown that strong local oscillations are more widespread in neuronal networks, with the local connection of neurons limiting their extension (Abela et al., 2014). Slow global oscillations reflect the integration of neuronal activity across regions of the brain throughout sensory or cognitive processes. However, recording technologies have limited investigations of precise mechanisms (Sheybani et al., 2019). There is no evidence that the encoded form of slow global oscillations applies to distributed networks in epileptic diseases. As a result, future research should examine the effects of oscillatory reorganization on seizures and cognitive impairment *via* the joint of strong local oscillations and slow global oscillations.

Moreover, there may be a mutually suppressive relationship between strong local oscillations and slow global oscillations. High-frequency oscillations are connected with local neuronal interactions, whereas slow rhythmic oscillations at lower frequencies are more crucial for the long-distance integration of large-scale networks (Von Stein and Sarnthein, 2000; Donner and Siegel, 2011; Goltsev et al., 2013; Ibrahim et al., 2013). When α oscillation energy rises in a specific brain region, neurogenesis in that region generally decreases. However, oscillatory reorganization's precise effect on cognitive impairment has yet to be investigated, and many fundamental concerns remain unanswered. We have yet to determine, for instance, what change patterns occur in strong local oscillations under the effect of seizures, nor whether strong local oscillations play a role in suppressing slow global oscillations. In this research, we aimed to answer these crucial questions.

Furthermore, brain function does not originate from isolated brain regions but through interactions in large-scale networks (van Diessen et al., 2014), which seem essential for both physiological and pathological conditions. On the one hand, such connections might propagate seizures; or instance, interconnected focal regions may have suffered damage due to peaked wave dissemination, which often results in widespread cognitive impairment (Harkin et al., 2007). Alternatively, other research shows that the brain may have a mechanism to protect healthy brain regions from seizures, which may cause permanent damage. For instance, seizure cessation is characterized by somewhat uniform oscillatory suppression (Truccolo et al., 2014). Intermittent epileptiform discharges have remote inhibitory effects on cognition (Shamshiri et al., 2017; Ung et al., 2017; Guo et al., 2018; Watson, 2018). However, the mechanisms and pathophysiology that control particular functions have yet to be entirely understood. It is uncertain if the resting or task state of the healthy brain exists or has been altered in epileptic patients.

In this research, the pathophysiological mechanisms underlying epilepsy-induced cognitive impairment may be associated with the oscillatory reorganization of functional networks. We focus specifically on the mutually inhibiting effect of strong local oscillations and slow global oscillations. The experiment was based on a quantitative analysis of the synchronization and directionality of information flow between the SEEG signals of nine patients with pathological epilepsy to create a dynamic network. Previous research has only used indicators of complex networks, focusing on particular global or local connection changes. In contrast, we utilize methods based on characteristic mode to identify hierarchical modules and quantify strong local oscillations and slow global oscillations in the network to examine dynamic networks comprehensively. To provide new information, we identify the particular variation rules of strong local oscillations versus slow global oscillations during various seizure phases. These models and findings help characterize an unrecognized dynamic network oscillatory reorganization mechanism in cognitive impairment induced by epilepsy.

2. Materials and methods

2.1. Data preparation

In this research, nearly 100 channels (electrodes) of SEEG data from nine patients hospitalized with refractory focal epilepsy at the Sanbo Brain Hospital of Capital Medical University were visually analyzed and extensively exploited to validate our results independently. The Ethics Committee approved the SMBC of

Capital Medical University's study technique, and a negotiated informed special dispensation was prepared for all participants. This information cannot be shared with the general public due to hospital regulations. Furthermore, the sampling frequency was set at 512 Hz and the average monitoring time was 1 week. Interictal, preictal, seizure, and post-ictal periods were analyzed to determine the network features of people with epilepsy. For each patient, we devised criteria for categorizing the various seizure stages, as indicated in **Table 1**. These criteria were based on the clinical seizures recognized by physicians.

The data for the control group in this study were collected from the EEG Motion/Image Dataset public dataset (Schalk et al., 2004), which includes over 1,500 1- and 2-min EEG recordings from 109 volunteers with 64 electrodes. The volunteers were required to perform a variety of motion and visual tasks. We selected nine data points from healthy individuals from which we extracted segments of resting or task-state EEG to compare with patients.

2.2. Statistic method for epileptic effective brain network

Usually, Pearson correlation coefficients are employed to establish functional networks for analyzing resting-state brain network alterations in healthy individuals. However, compared to FMRI data, the SEEG data employed in this work includes more complex dynamic changes in transients due to its temporal and spatial features. Consequently, this research establishes an effective network based on the statistical method proposed in Quiroga et al. (2002), which may improve the assessment of the information flow in the brain network of patients with epilepsy.

We build a dynamic and efficient network by estimating the synchronization and directionality of developing information flow to represent pathological epilepsy. Therefore, it is essential to define events for time series. Here, the events are defined as the local maximums in the time series, i.e.,

$$\begin{cases} x_{t_k} > x_{t_k+m}, \quad m = -M+1, \ldots, -1, 1, \ldots, M-1 \\ x_{t_k} > x_{t_k \pm M} + h \end{cases} \tag{1}$$

where t_k is the event occurrence time, $M = 10h = 30$ are the two control parameters shaping the event.

Let the event sequences of time series $x^1(n)$ and $x^2(n)$ (total step length L) be $t_r^1 (r = 1, \ldots, m_1)$ and $t_s^2 (s = 1, \ldots, m_2)$, where $m_1 (\ll L)$ and $m_2 (\ll L)$ are the total number of event occurrences in $x^1(n)$ and $x^2(n)$, respectively. The time difference between event occurrences in various time series is then used to determine the causality and synchronization of events. In the time delay scale τ, if an event is recorded in the sequence $x^1(n)$ immediately after an event occurs in the sequence $x^2(n)$, then it is considered that the intensity of the causal effect of $x^1(n)$ on $x^2(n)$ will be enhanced by one step. Conversely, $x^2(n)$ is one step more causality for $x^1(n)$. In addition, regardless of the sequence of events in $x^1(n)$ and $x^2(n)$, as long as two related events are observed to occur close enough, they are considered a simultaneous occurrence, and the amount of synchronization is correspondingly increased by one step.

$$e^{\tau}\left(x^1|x^2\right) = \sum_{r=1}^{m_1}\sum_{s=1}^{m_2} E_{rs}^{\tau}, E_{rs}^{\tau} = \begin{cases} 1, & 0 < t_r^1 - t_s^2 \le \tau \\ \frac{1}{2}, & t_r^1 = t_s^2 \\ 0, & others \end{cases} \tag{2}$$

Remember sequence $x^2(n)$ for $x^1(n)$ event-causal $e^{\tau}(x^1|x^2)$, the size of representative sequence $x^2(n)$ for $x^1(n)$ the causal role of strength. The global time delay,

$$\tau = \min_{r=1,\ldots m_1, s=1,\ldots,m_2} \{\tau_{rs}\} \ ,$$

$$\tau_{rs} = \frac{1}{2}\min\left\{t_{r+1}^1 - t_r^1, t_r^1 - t_{r-1}^1, t_{s+1}^2 - t_s^2, t_s^2 - t_{s-1}^2\right\} \tag{3}$$

is used to limit the smallest time interval between two adjacent events, where τ_{rs} is the local time delay for each pair of adjacent (temporally closest) events (r, s), $E_{rs}^{\tau} = 1/2$ is such set to prevent from double counting for the two simultaneous events. On the contrary, $e^{\tau}(x^2|x^1)$ quantifies the causality from $x^1(n)$ to $x^2(n)$.

Based on $e^{\tau}\left(x^1|x^2\right)$ and $e^{\tau}(x^2|x^1)$, we then define the degree of simultaneity Q^{τ} and causality q^{τ} for $x^1(n)$ and $x^2(n)$ as follows:

$$Q^{\tau} = \frac{e^{\tau}\left(x^2|x^1\right) + e^{\tau}(x^1|x^2)}{\sqrt{m_1 \cdot m_2}}, q^{\tau} = \frac{e^{\tau}\left(x^2|x^1\right) - e^{\tau}(x^1|x^2)}{\sqrt{m_1 \cdot m_2}} \tag{4}$$

Both are normalized to $0 \le Q^{\tau} \le 1$, $-1 \le q^{\tau} \le 1$. $Q^{\tau} = 1$ when and only when all events in both signals occur together. $q^{\tau} = 1$ when and only when all events from $x^1(n)$ act for all events from $x^2(n)$.

Second, to examine the evolution trend of synchronization and causality between the two sequences over time, Q^{τ} and q^{τ} are evaluated for each time step, while their cumulative consequences are investigated over time. We define $q^{\tau}(n)$ as Equation(5),

$$\begin{cases} q^{\tau}(n) = e_n^{\tau}\left(x^2|x^1\right) - e_n^{\tau}\left(x^1|x^2\right) \\ Q^{\tau}(n) = e_n^{\tau}\left(x^2|x^1\right) + e_n^{\tau}\left(x^1|x^2\right) \end{cases}$$

$$e_n^{\tau}\left(x^1|x^2\right) = \sum_{r=1}^{m_1}\sum_{s=1}^{m_2} E_{rs}^{\tau}\Theta\left(\mathrm{n} - \mathrm{t}_{\mathrm{r}}^1\right) \tag{5}$$

where $n = 1, 2, \ldots, L$ is the time point within the series, and Θ is the step function, i.e., $\Theta(\mathrm{x}) = 1$ when $x > 0$ and $\Theta(\mathrm{x}) = 0$ when $x \le 0$. $q^{\tau}(n)$ could be thought of as a random sequence; when the event in x^1 causes the event in x^2 to occur, it increases by one step, and vice versa, it diminishes by one step. The synchronization of progressive events is defined by $Q^{\tau}(n)$ in Equation (5), where $Q^{\tau}(n)$ improves by one step if a pair of events in x^1 and x^2 occur within the period τ and remains nearly constant otherwise.

The rate of change of synchronization at time point n is calculated by averaging the synchronization expansion throughout Δn steps ($\Delta n = 5120$ in the current calculation) using $dQ^{\tau}(n)$ in Equation (6),

$$dQ^{\tau}(n) = \frac{Q(n) - Q(n-\Delta n)}{\sqrt{\Delta n_1 \cdot \Delta n_2}} \ , dq^{\tau}(n) = \frac{q(n) - q(n-\Delta n)}{\sqrt{\Delta n_1 \cdot \Delta n_2}} \tag{6}$$

where Δn_1 and Δn_2 correspond to the number of events in x^1 and x^2 in the band $[n - \Delta n, n]$, respectively. Similarly, we might define the rate of change of the causal level at time point n as choosing to follow $dq^{\tau}(n)$ in Equation (6), where $dQ^{\tau}(n) > 0$ and $dq^{\tau}(n) > 0$ represent a positive increment of synchronization and causality within Δn steps, respectively, and < 0 represents a negative escalation within Δn steps.

Specifically, the synchronization growth rate $dQ^{\tau}(n)$ and the causal level change rate $dq^{\tau}(n)$ at time point n are determined for any two nodes i and j in the network whose relevant time series are x^i and x^j. The magnitude of the weighted directed action of node i

TABLE 1 Clinical patient characteristics.

Patient	Age (years)	Duration (years)	Side	Electrodes/contacts	Recorded seizures	Pathology
1	17	12	R	15/124	4	FCD Ia
2	9	5	L	11/116	6	FCD Ib
3	4	7/12	R	13/122	9	FCD IIa
4	7	1	L	10/120	101	FCD IIb + FCD Ic
5	5	3	R	10/108	2	FCD Ib
6	16	3	L and R	15/119	4	FCD Ib + FCD IIb
7	7	5	L	13/116	1	FCD Ib
8	27	12	L	8/108	5	HS.
9	15	9	R	8/117	17	FCD Ib + GMH

FCD, cortical dysplasia; HS, hippocampal sclerosis; GMH, ectopic gray matter.

on node j at time point n is represented by $a_{ij}(n)$, which also contains data on the synchronization level between the two nodes, as described by Equation (7),

$$a_{ij}(n) = \begin{cases} \gamma \cdot dq_{ij}^{\tau}(n) \cdot dQ_{ij}^{\tau}(n), & dq_{ij}^{\tau}(n) > 0 \\ 0, & dq_{ij}^{\tau}(n) \leq 0 \end{cases} \quad (7)$$

where the amplification factor $\gamma = 1000$ is considered in this research. Furthermore, it is assumed that there are no self-connecting rings in the network, i.e., $a_{ii}(n) = 0, i = 1, 2, \ldots, n_0$, where n_0 is the maximum number of nodes in the network.

2.3. Hierarchical modular division of functional connection matrix

Wang Rong et al. (Wang et al., 2021) proposed that the activation and combination of various structural modal interactions in the eigenmodes lead to generating multiple dynamical modes in the system by nature. Moreover, in this study, to discover the dynamical oscillation reorganization law of the directed weighted network, we propose a new hierarchical eigenmode analysis method that includes examining complex numbers. In particular, the directed weighted network and functional connection matrix in **Figure 1** is an epitome of the causal effects network calculation results. Since the functional connection matrix is asymmetric, the resulting eigenvalues and eigenvectors must include complex conjugate numbers. It is well known that the eigenvalues on the exact number field domain represent the magnitude of the stretching transformation, whereas the eigenvectors represent the direction. In comparison, the complex domain adds a rotational transformation. Under the transformation of polar coordinates, $a + bi$ becomes $r(cos\theta + i * sin\theta)$, where $r = \sqrt{a^2 + b^2}$ represents the stretching quantity, and $\theta = arctan\frac{b}{a}$ represents the rotation. Additionally, the complex eigenvector component $m + ni$ is multiplied with the corresponding eigenvalue $a + bi$, representing the real rotation of the basis vector φ and the stretching transform q (Hitzer, 2002):

$$\begin{aligned} (a + bi)(m + ni) &= r(cos\theta + i{*}sin\theta) {*} q(cos\varphi + i{*}sin\varphi) = \\ & rq[cos\theta cos\varphi - sin\theta sin\varphi + i{*}(sin\theta cos\varphi + cos\theta sin\varphi)] = \\ & rq[cos(\theta + \varphi) + i{*}sin(\theta + \varphi)] \end{aligned} \quad (8)$$

On this foundation, we consider the modal lengths of the eigenvalues and eigenvectors that correspond precisely to the magnitude of the change in a stretch, which makes more physical sense than merely considering the real part.

Immediately following, we provide the specific modal analytical method. First, the eigenvalues are sorted by mode length from largest to smallest $\Lambda_i^2 (i = 1, \ldots, N)$ and the corresponding eigenvectors are rearranged. In order to depict the actual global level of slow oscillations in the brain, the first eigenvector corresponding to the largest eigenvalue modal length was not divided at the first level. The global slow oscillations can be expressed as:

$$H_{in} = \frac{H_1}{N} = \frac{\Lambda_1^2 M_1 (1 - p_1)}{N^2} \quad (9)$$

where the parameters and variations can be explained later.

Level 2 eigenvector separated brain regions into three sub-modules: balance, strong oscillation, and weak oscillation. After the entire module was divided into three parts, the latter oscillatory deformation was much higher than the former. $(AVG + SD, AVG + 2{*}SD)$ represents a balanced oscillatory deformation while cognitive patterns are switched more flexibly, and cognition is at a greater level (complex planes ② and ⑤ in **Figure 1**). $(AVG + 2{*}SD, +\infty)$ represent a strong oscillatory deformation with significant feature differences and shifts. Moreover, the greater the amplitude of the oscillation, the more it may negatively impair cognition (complex planes ③ and ⑥ in **Figure 1**). $(0, AVG + SD)$ denotes a weakening of the oscillation level and a slowing of cognition, tending toward a mode that occurs when the oscillation gets suppressed (complex planes ① and ④ in **Figure 1**). Where *AVG* and *SD*represent the set's mean and standard deviation, respectively, this set is made up of the modal lengths of all components of the whole eigenvector. Nonetheless, it is challenging to quantify the degree of rotation in measures of complex numbers. In this part, we do not distinguish between the effect of the rotation angle on the magnitude of oscillations at each level; further explanation will be given in the Section "4. Discussion."

As the sequence of functional patterns rises, the FC network modularizes until it reaches a state of high modularity. In this process, the case from layer 2 to layer N represents the deformation intensity of the strong local oscillation, expressed as

$$H_{se} = \sum_{i=2}^{N} \frac{H_i}{N} = \sum_{i=2}^{N} \frac{\Lambda_i^2 M_i (1 - p_i)}{N^2} \quad (10)$$

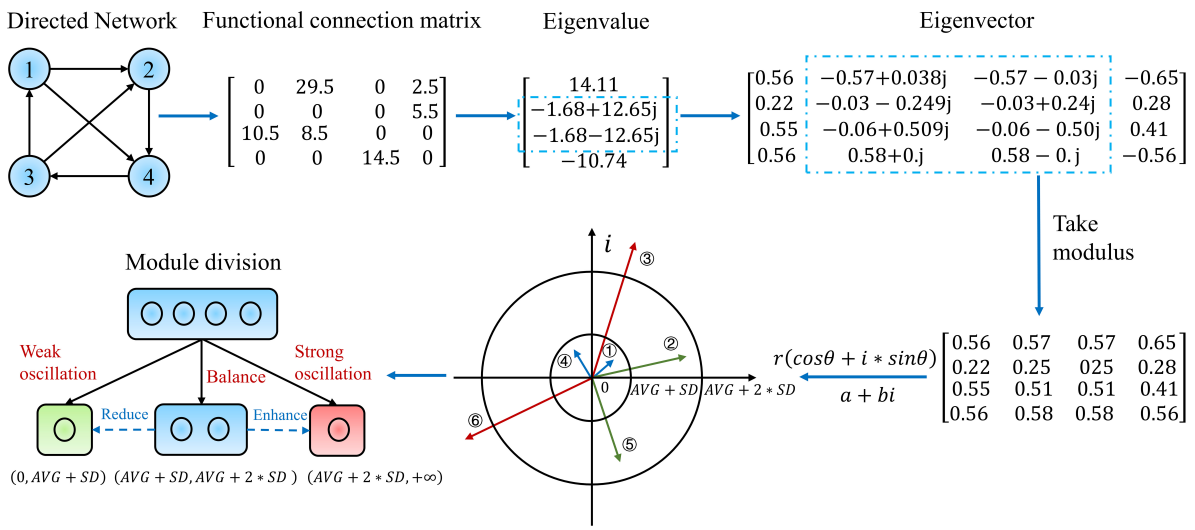

FIGURE 1
Example illustration and detailed description of the eigenmode analysis method. This diagram demonstrates a weighted directed network with four nodes. This network is then assigned a functional connectivity matrix corresponding to the hundred-dimensional matrix acquired from the real epilepsy causal effects network. The eigenvalues and eigenvectors of this matrix are then determined. The eigenvectors are then retrieved in modal length, and their interpretation in the complex plane is provided. The module is subdivided into three submodules based on the modal lengths of the eigenvectors, and the subfigure at the bottom left depicts the precise meaning and classification links of the hierarchical modularity method to oscillatory dynamic reorganization.

where M_i is the number of modules within layer i, which is weighted as $H_i = \frac{\Lambda_i^2 M_i}{N} (i = 1, \ldots, N)$. N is the number of regions in total. Nevertheless, the heterogeneous structure of module sizes causes variations in the evaluation of separation and integration parameters; hence, similar to Wang et al. (2021), we also introduce the correction factor $p_i = \sum_j \left| m_j - \frac{N}{M_i} \right| / N$, where $m_j (j = 1, \ldots, M_i)$ is the module size.

In addition, we set $H_{sb} = H_{in} - H_{se}$: if $H_{sb} < 0$, the brain's functional network is biased toward a state of strong local oscillatory deformation, which has a facilitative effect; if $H_{sb} > 0$, which implies that the network is biased toward a state under which slow global oscillations cooperate, the structure of the entire network is stable; if $H_{sb} = 0$, a sub-stable balance is reached between strong local oscillations and slow global oscillations, and the contribution of the original network to strong local oscillations is roughly equal to the suppression of strong local oscillations by slow global oscillations. Every H_{sb} value is normalized to the range $[-1, 1]$. The closer H_{sb} is to -1, the greater the strong local oscillations and the more excited the proto-network state. The closer H_{sb} is to 1, the higher the degree of slow global oscillation and the greater the suppression of strong local oscillations.

In conclusion, causality and synchronization were used to assess the strength of directional propagation of information flow between two epilepsy network nodes to construct a weighted epilepsy effective network. Meanwhile, we fed SEEG into this network and analyzed the output functional connection matrix. Using a modular hierarchical analysis of the eigenmodes, a dynamic description of the brain network's strong local oscillations versus slow global oscillations in the temporal and spatial dimensions of the patient's seizures were constructed. Ultimately, the dynamic reconfiguration of network oscillations may be the source of cognitive impairment produced by epilepsy. Figure 2 shows the main flowchart of the whole research.

3. Results

3.1. Potential reason for cognitive impairment: Disruption of the balance between strong local and slow global oscillations

We discovered that epileptic seizures damage the metastable balance between local strong and slow global oscillations in large-scale networks. Specifically, we investigated the H_{sb} metrics of healthy individuals, which reflect the metastable balance between strong local oscillations and slow global oscillations. Figure 3 shows the fluctuation of the H_{sb} indication for nine healthy controls over time. We can observe that the H_{sb} fluctuates evenly around 0 and is primarily stable around 0. This indicates that healthy brain networks have balanced oscillatory states and switch between strong local oscillations and slow global oscillations more frequently, hence maintaining regular cognitive functional activity. The brain network's facilitation of strong local oscillations plays off against the suppression of strong local oscillations by slow global oscillations, yet the network is in balance overall. For comparison, we analyzed the variation of brain network states in epileptic patients.

Patient 1 had the exact opposite features compared to healthy controls, as shown in Figure 4. The strong local oscillation index H_{se} and the slow global oscillation index H_{in} exhibited rapid, irregular fluctuations within the range $[-1, 1]$. Similarly, the balance index H_{sb} exhibited the same alterations (Figure 4), which seemed very distinctive from healthy individuals. The primary data implies that the disruptive impact of seizures on the metastable balance of strong local oscillations and slow global oscillations is rather severe. In addition, both strong local oscillations and slow global oscillations in the functional network were enhanced after a period of seizure. In particular, the degree of enhancement is much greater for strong

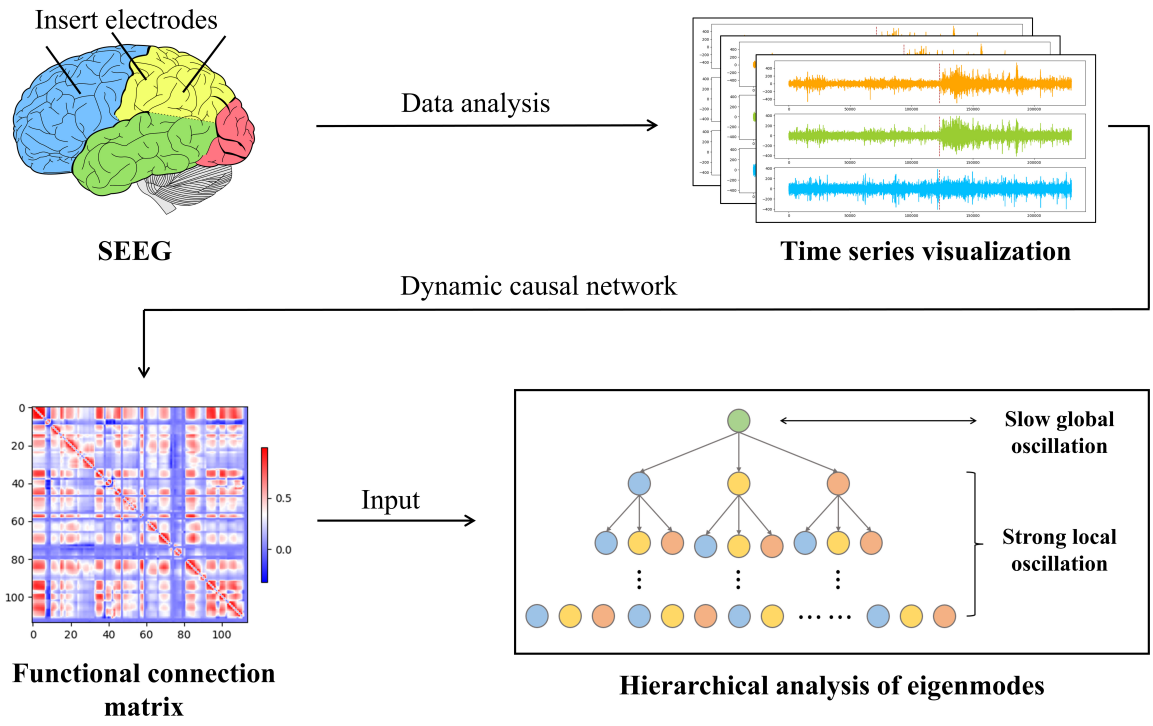

FIGURE 2
The entire workflow of the experimental procedure is in this paper. First, the SEEG data are examined, processed, and computed to establish the network of causal effects. The epilepsy causal impact network then generates a functional connectivity matrix that reflects the synchronization and causality between SEEG data from various locations. Immediately after this, we conducted a statistical analysis of the functional connectivity matrix using eigenmode hierarchical analysis to capture the slow global oscillation index vs. the strong local oscillation index for each patient under each data sample.

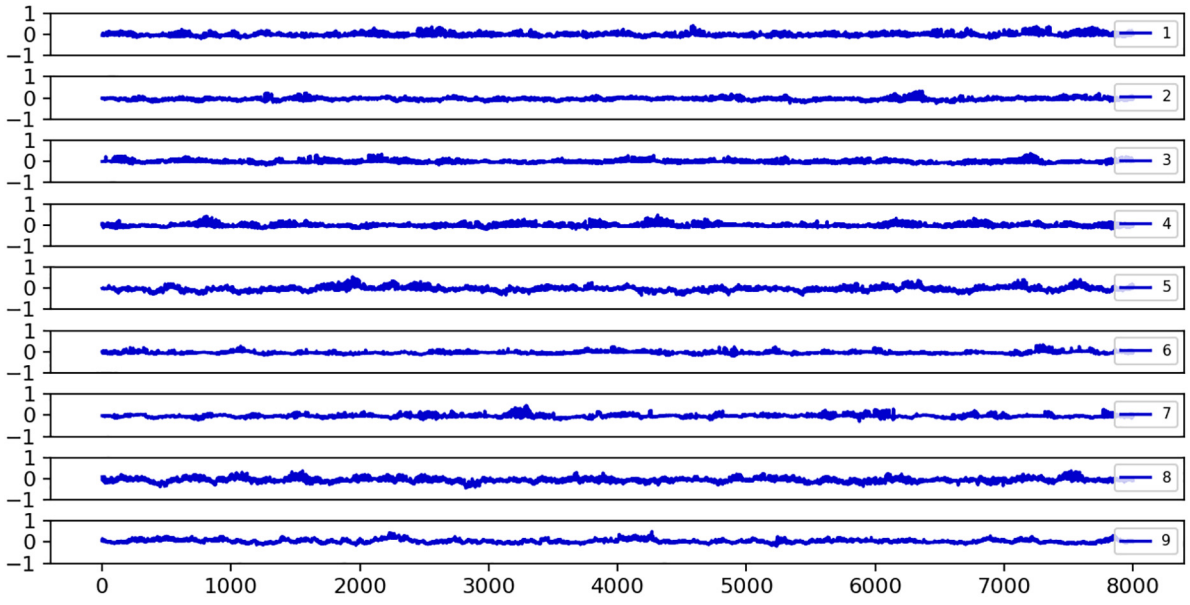

FIGURE 3
The fluctuations of the H_{sb} index over time for nine healthy subjects are plotted. H_{sb} refers to the sub-steady-state equilibrium evaluation index of slow global oscillations relative to strong local oscillations. If $H_{sb} = 0$, the two are in sub-steady state equilibrium; if $H_{sb} < 0$, the network state is more skewed toward strong local oscillations; and if $H_{sb} > 0$, slow global oscillations are more robust in the network. Independent of time, it was noted that the distribution of H_{sb} in healthy participants centered around 0. Each subplot's legend numbers reflect the number of healthy subjects, the horizontal axis is the time series t, and the vertical axis is the H_{sb} size, normalized to the interval $[-1, 1]$.

local oscillations than for slow global oscillations, and it recovers to pre-seizure levels after a seizure. As a result, changing strong local oscillations and slow global oscillations in the functional network may be a pathogenic mechanism that leads to cognitive impairment. In contrast, the interictal phase is associated with a decrease in the flexibility of both strong local oscillations and slow global oscillations.

We assume that not only is there cognitive impairment during seizures but also a general divergence between the configuration of the patient's network's functional structure and the course of cognitive activity in healthy individuals.

3.2. New network oscillation dynamic reconfiguration discoveries may be relevant to cognitive impairment pathophysiology

H_{sb} changes in the form of the distribution of peak nuclear density may be a sign of cognitive impairment caused by seizures. To further validate our conclusion, we investigated the dynamics of strong local oscillations against slow global oscillations throughout various seizure phases for each patient. Figure 5 displays the seizure periods in the H_{sb} kernel density distribution results for each of the three patients. This study demonstrates a high degree of similarity across state transitions, showing that the dynamic hierarchy of oscillatory reorganization of brain networks varies considerably. The states are divided into four groups corresponding to Figure 5's four colors.

During the interictal phase (Figure 5, first column), the peaks were single-peaked or equally distributed, showing normal cognitive function and the ability to transition between local strong and slow global oscillations. During the pre-ictal phase, the distribution of strong local oscillations and slow global oscillations showed a bimodal pattern with independent peaks, suggesting reduced switching flexibility and good cognitive condition by epileptic waves (Figure 5, second column). Immediately after and most notably during the seizure period, the network was significantly biased toward strong local oscillations, exhibiting a single-peaked concentration pattern and accumulating negative values, suggesting almost complete cognitive loss of the brain during seizures (Figure 5, third column). Cognitive activity returned to normal in the late seizure phase, when strong local oscillations reverted to a bimodal pattern or uniform distribution with slow global oscillations, similar to the interictal phase (Figure 5, fourth column).

In contrast, the oscillatory patterns of the functional network are often diffused and distributed in states of strong local oscillations and weak global oscillations. Subsequently, seizures cause them to be concentrated in hyper-intense strong local oscillations states, gradually dispersed following the seizure. The increased concentration of network oscillatory patterns during seizures may be substantially responsible for the start of cognitive impairment associated with epilepsy. However, a fascinating phenomenon was discovered: this decrease in regularity was not absolute. In addition, the peak distribution of network oscillation patterns for a particular patient during a specific seizure period was random. However, seizure variability is not entirely random since the overall trend of attack change remained consistent between patients. Because of differences in seizure intensity, duration, and brain network regions, the impact of these specificities on the results is insignificant.

In order to highlight how changes in the state of strong local oscillation and slow global oscillation vary between patient episodes, we estimated the change in the balance state between local strong and slow global oscillations at the peak for eight patients. The x-axis coordinate value of the H_{sb} distribution's maximum density (blue dashed line in Figure 6) was drastically decreased and restored not only after a seizure but also happened many times. This analysis suggests that seizures cause a significant increase in the number of strong local oscillations in large-scale brain networks and that the inhibitory influence of slow global oscillations on strong local oscillations has almost completely disappeared at this time. However, after a seizure, protective mechanisms in the brain may prevent the loss of cognitive overload. The observed pattern of rapid increases followed by declines in concentration was commonly seen in patients, validating the generalizability of the concentration as mentioned above fluctuations. Again, based on patient-specificity, it is worthwhile to investigate that the indicated characteristics vary in time of commencement and degree of severity and may occur during either phase of the episode.

3.3. Pathological mechanisms that prevent cognitive loss: The oscillatory reconfiguration of networks at various sizes

Given that high levels of strong local oscillations are expected throughout a vast network of distinct patients, we can also anticipate that network features will not limit these measures. To assess this, we also identified smaller, more specialized (non-epileptogenic) local networks for each patient. According to clinical case reports, each local (non)epileptogenic network included 64 loci with (non)epileptiform discharges during the interictal and ictal phases. In addition, H_{sb} plunge intervals and the exact time and number of high-level, locally intense oscillations were evaluated.

Figure 7 demonstrates that despite variations in the size and type of the patient's functional brain networks, the sudden interval of H_{sb} of each patient is the same, and the number of high-level localized strong oscillations is identical or varies by one. Notably, the sudden interval of H_{sb} was more frequent and more prolonged in the localized epileptogenic network. Thus, whereas seizures considerably impact the interplay between strong local oscillations and slow global oscillations within the localized epileptogenic network, high levels of strong local oscillations do not significantly impair cognitive performance within the brain network.

Let us consider the emergence of high levels of locally strong oscillations to represent an extreme cognitive state. It makes sense to consider the relationship between the period during which high levels of locally strong oscillations emerge and when they become clinically apparent. We discovered that the moment of creation of high-level, local, strong oscillations was random among the various patients and network types examined in this research (Figure 7). In principle, the onset of high-level strong local oscillations should correspond with the clinically characterized onset of a seizure or the number six. However, high-level local oscillations are more prevalent during the interictal or pre-ictal phase and less commonly during the late phase. Therefore, can high-level strong local oscillations be utilized as a biomarker to identify seizures, and is this information clinically relevant? Cognitive impairment brought on by high-level strong local oscillations before seizures? This needs additional investigation.

Few research has compared local non-epileptogenic networks with epileptogenic networks, another original and novel aspect of our study. First, we discovered that seizures also impact the local non-epileptogenic brain network. Although seizures are far less common in this network than in the localized epileptogenic network, this

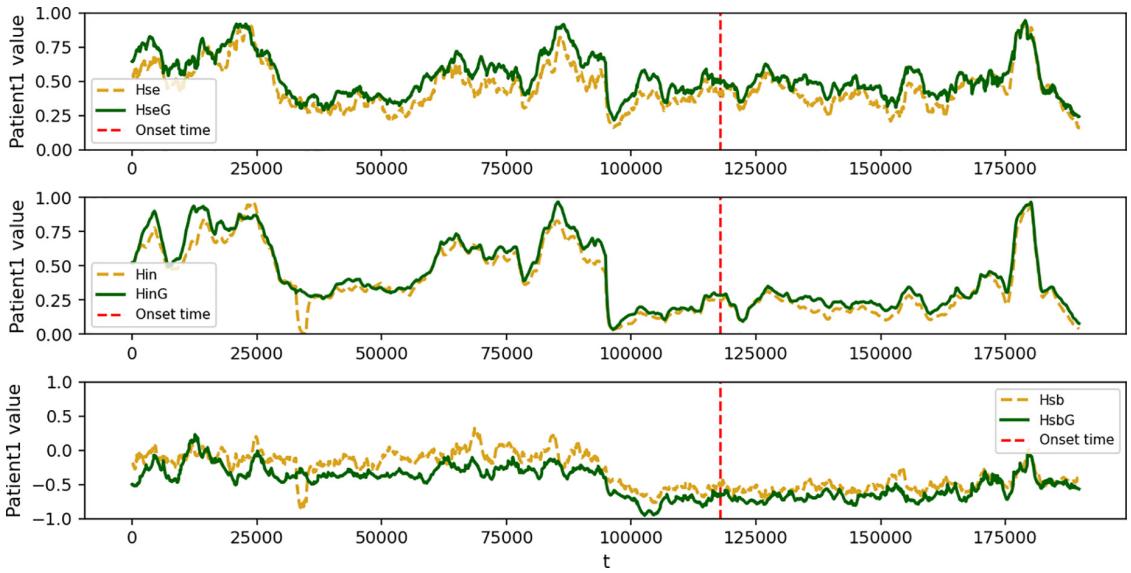

FIGURE 4
Fitted curves of the change in strong local oscillations versus global slow oscillation metrics for patient 1. In each subplot, the green (yellow) curve represents the global (local) epilepsy network, the red dashed line represents the onset time, the horizontal axis represents the time series t, and the vertical axis represents the H_{sb} size, normalized to $[-1, 1]$. Dramatic swings vary from those of healthy people and are modified by time. **(top)** the variation of patient 1's local strong oscillations H_{se} over time; **(middle)** the change of patient 1's global slow oscillation index H_{in} over time; and **(bottom)** the variation of patient 1's sub-stable equilibrium index H_{sb} between strong local and slow global oscillations over time.

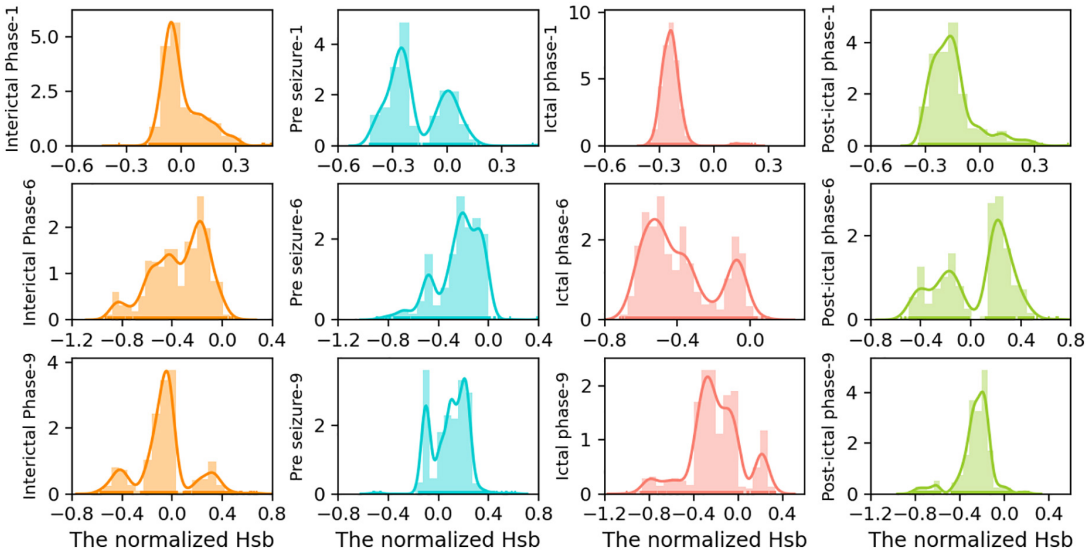

FIGURE 5
Distribution of H_{sb} kernel density of the large-scale network in patients 1, 6, and 9 at different periods of seizures. To further examine the distribution of peak density changes, we intercepted four segments with the same data points from the time series of H_{sb}, indicating interictal, pre-ictal, seizure, and post-ictal phases, corresponding to the four colors from left to right in the figure. kernel density charts for various simultaneous seizure periods for patients 1, patient 6, and patient 9. In each subplot, the x-axis indicates the magnitude of the normalized H_{sb} value, the y-axis represents the density magnitude, and the y-axis labels reflect a time for a particular patient.

network is likely to be more intense. Second, periods with high levels of strong local oscillations in the local non-epileptogenic network were much closer to those in the global network (Figure 7). In conclusion, our findings indicate that networks of varying sizes exhibit significant levels of robust local oscillations during epileptic seizures. In response to the severe oscillatory reconfiguration of large-scale brain networks, the brain often develops pathological protective mechanisms against cognitive impairment.

4. Discussion

Quantitative evaluation of oscillatory reorganization is now restricted to the oscillatory frequency range. Understanding how this research significantly advanced network oscillatory recombination influences and contributed to seizure-induced cognitive impairment. The oscillatory reconfiguration of a network comprises both strong local oscillation and slow global oscillation, as well as the inhibitory

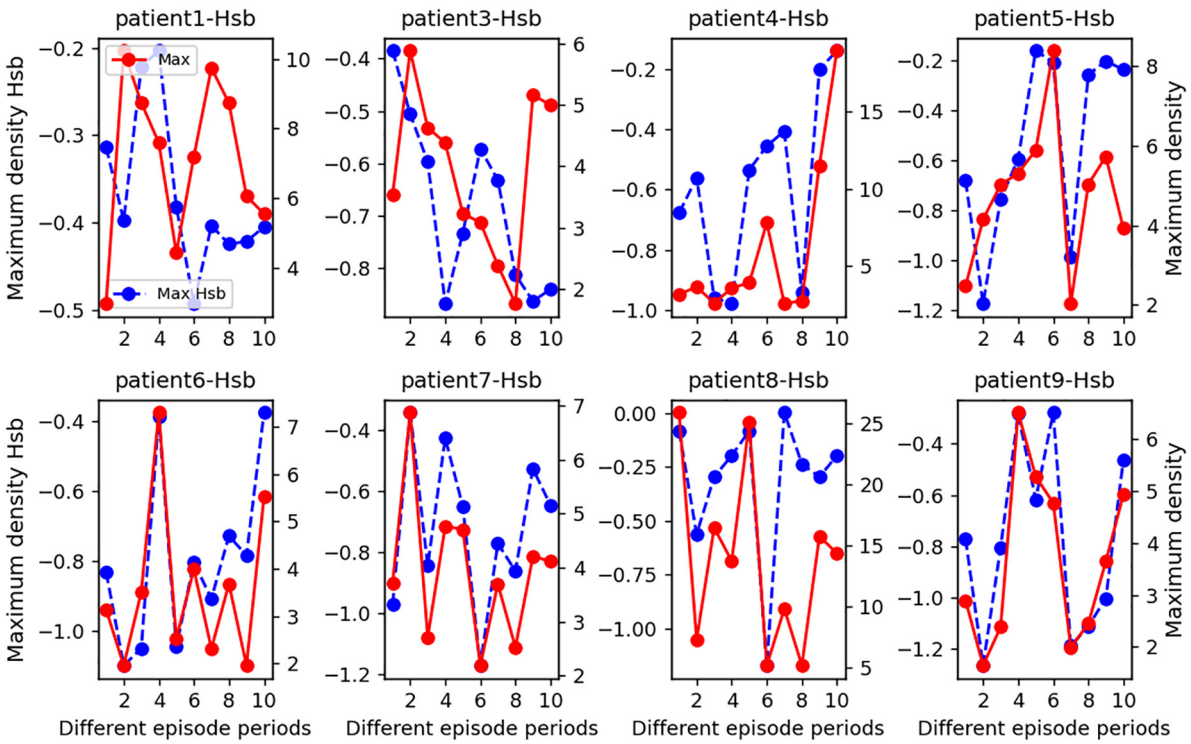

FIGURE 6
A statistical line chart of the maximal H_{sb} nucleus density for seizure durations in eight epileptic individuals. On average, we subdivided each seizure phase into two sections and chose two interictal intervals to examine. Specifically, the x-axis values of each subplot represent several seizure periods: 0–2 for the interictal period 1, 2–4 for the interictal period 2, 4–6 for the pre-ictal period, 6–8 for the seizure period, and 9–10 for the post-ictal period. In addition, we counted the peaks in the H_{sb} nucleus density distribution plot during each phase and recorded the H_{sb} values corresponding to the peaks together with the density values to create this line graph. The patient number is the title of each subplot, the blue dashed line represents the magnitude of the maximum density of H_{sb} values for each time interval, as measured by the left y-axis, and the solid red line represents the maximum density value for each time interval, as measured by the right y-axis.

and facilitative influences between them. In addition, we analyzed particular changes in oscillatory reconfiguration at various seizure periods and network limitation sizes.

Numerous studies have studied the relationship between oscillations and cognitive impairment. However, there are few theoretical investigations on the impact of network oscillations on epilepsy-induced cognitive impairment. Our experimental findings on network oscillations are consistent with earlier research. During wakefulness, the human brain reaches a critical condition and produces many transient α oscillations in global synchronization (Kim and Lee, 2020). Nevertheless, different brain disturbances (such as sleep, anesthesia, and trauma) may lead the brain to depart from the critical state (Hutt et al., 2018). This supports our hypothesis that, during the resting state, the brain is in a metastable balance between local strong and slow global oscillations and that seizures may disturb this balance. Another investigation has shown intermittent discharges contribute to cognitive impairment or epileptogenesis (Staley et al., 2005). Moreover, this investigation revealed that psychopathically elevated band θ connectivity was related to a greater incidence of seizures (Ibrahim et al., 2013). This may indicate that significantly amplified strong local oscillations may be a marker for seizures and a trigger for the onset of cognitive impairment in epileptic patients.

Our findings imply that slow global oscillations aid cognitive recovery after seizures, which is the outcome of a brain-protective mechanism. In addition, the degree of substantial enhancement of strong local oscillations was significantly greater in the local epileptogenic network than in the large-scale network, and the frequency and number of occurrences of substantial enhancement of strong local oscillations were more similar to those in the local non-epileptogenic network, which may be another manifestation of a brain protective mechanism. Slow oscillatory synchronization has been shown to contribute to functional connections across widely dispersed neuronal populations (Llinás et al., 2005). It has been discovered that abnormal slow-wave activity occurs in the brain after seizures marked by impaired consciousness (Yang et al., 2012). These findings are comparable to those we inferred for slow global oscillations.

The specificity of oscillatory recombination in various epileptic patients at different periods is of interest to us. Furthermore, several research might support our findings. For instance, the strength of network connections may be connected to individual variations in cognitive function, and spontaneous oscillatory activity may explain the diversity of task-evoked responses (Boly et al., 2008; Lewis et al., 2009). Additionally, exceptional results on local non-epileptogenic networks have been well supported by previous research. In the kainite mouse model of hippocampal epilepsy, it was shown that the rapid ripples indicative of epileptic symptoms is not localized to the lesion, despite being predominant in the lesion (Sheybani et al., 2018, 2019). Specifically, it has been shown that the time of spike appearance may connect with various cognitive impairment degrees

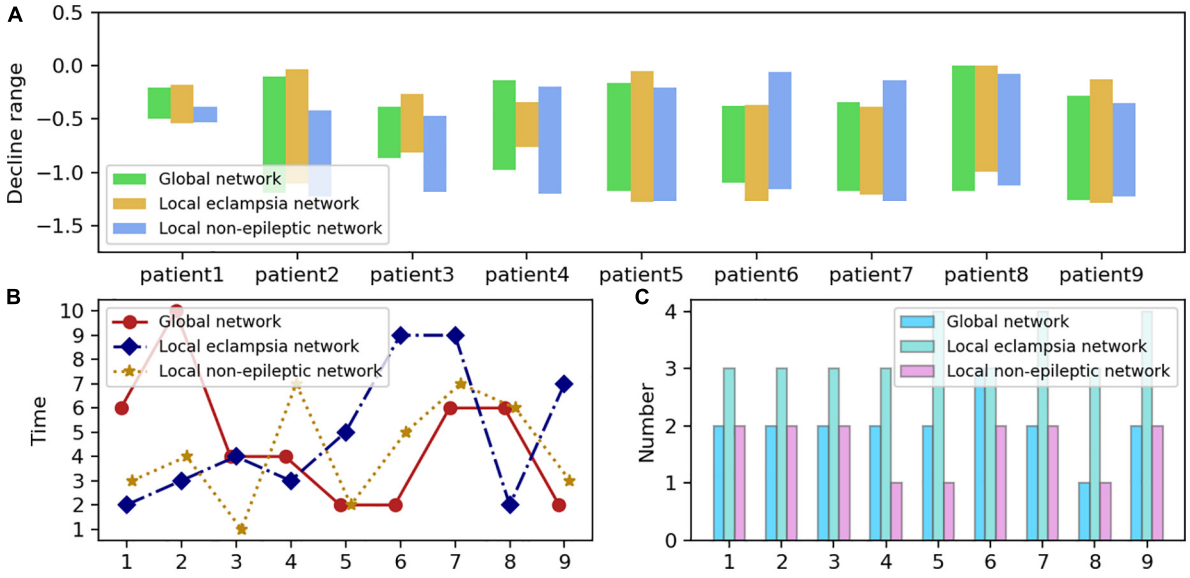

FIGURE 7
Distribution of neural network sizes in nine epilepsy patients. **(A)** The H_{sb} plunge interval for each network size is formed by the highest and lowest values of the blue curve in each subplot of **Figure 6**, which corresponds to the length of each bar. The y-axis value corresponding to the bottom of each bar on the graph is the blue curve, which represents the most negligible value of H_{sb}, while the top represents the highest value of H_{sb}. The x-axis represents the patient number, and the y-axis measures the interval maximums and minimums with the interval lengths. **(B)** Periods during which high-intensity oscillations occur in networks of various sizes, namely, the most significant decrease followed by a rebound in each subplot of **Figure 6**'s blue dashed line. In the graph, the three colors reflect the three network types, the x-axis represents the patient number, and the y-axis denotes the precise time during which the steepest drop occurred, numbered as in **Figure 6** to represent separate seizure episodes. **(C)** The frequency of high-intensity oscillations in the various networks, mainly the frequency of the blue dash's descent and subsequent rebound in each subplot of **Figure 6**. The x-axis represents the number of patients, while the y-axis displays the frequency.

and kinds (Fonseca et al., 2007). This also verifies the variability of the onset of substantial increases in localized slow oscillations.

It has been demonstrated that the physical process of oscillatory steady-state reverberation generates eigenvectors and eigenvalues of a system to quantify the eigenvalues implied in the geometry of external objects and their spectral representations in order to generate metrics and perform more accurate covariant inversion transformations (Jolliffe and Cadima, 2016). Moreover, similarly inside the CNS (Central Nervous System), complex eigenvalues and complex eigenvectors might indicate the contrast between covariant sensory and inverted motion vector representations of external geometry, which compose the system's functional geometry (Pellionisz and Llinas, 1985). Our theoretical analysis then applies more practically to complex eigenvalues and complex eigenvectors. However, few studies provide a precise geometric understanding of complex eigenvalues and complex eigenvectors in high-dimensional spaces. As a result, we need to find an exact expression for the quantization of rotation angles in these spaces, which necessitates additional research.

Neurobiological systems that allow language processing are distinguished by the bidirectional flow of information in directed networks (Schoffelen et al., 2017). Graph-theoretic analysis of directed connection estimates more precisely detects the dynamic connectivity of functional networks in actual epileptic brains than undirected functional connectivity estimates (Dehaene and Changeux, 1997), creating new avenues for human connect omics. Sadly, however, current studies are more based on the role of Markov blankets on in- and out-degree, multivariate non-parametric dynamic Granger causality with directed transfer functions to build directed weighted networks (Lewis et al., 2009; Horvát et al., 2016; Zafeiriou et al., 2020). Next, graph-theoretic analysis techniques, such as typical path length, global efficiency, local efficiency, and clustering coefficients (Rentzeperis and van Leeuwen, 2020; Friston et al., 2021; Qin et al., 2022), were applied to the network. It is pleasant to observe that our analysis of directed networks utilizing the eigenmodal technique is relatively novel. However, we have yet to devote much effort to enhancing the eigenmodal technique to accurately represent the properties and dynamics of directed weighted networks. Our team will likely develop more efficient approaches and novel, generalizable findings in the future.

Nevertheless, there are still some limitations to consider when interpreting our results. For instance, we should have considered the correlation between centrality and node strength. It has been demonstrated that metrics capturing network node correlations can correctly identify motion-related regions in the pre-central and post-central gyri as critical network components and prove the expected hemispheric asymmetry (Frässle et al., 2021). Due to the private nature of the epilepsy patient data, the quantity of data in this research was inadequate to verify the generalizability of the results; hence, future attempts will focus on examining the commonality of network oscillatory reconfiguration using data from more public databases. Second, the current work lacks simulations of kinetic models to understand further the pathophysiological mechanisms behind epileptic seizures' cognitive impairment.

The search for the underlying mechanisms of seizure-induced cognitive impairment has been a focal issue to which our study contributes to some extent. In addition, the game interaction between the network's strong local and slow global oscillations offers a novel method to consider the above difficulties. Their combination is a significant contribution to the study of brain research, which

might aid in detecting and treating brain illnesses. A deeper and more specific study of network oscillatory reorganization might be generalized to studying multiple brain disorders.

5. Conclusion

In conclusion, we investigate the dynamic reorganization of network oscillations, including significant enhancement of strong local oscillations during seizures, disruption of the metastable balance between local strong and slow global oscillations, and changes in the peak oscillation pattern during different periods of seizures. All of these may be potential mechanisms for cognitive impairment caused by seizures. In contrast, enhancing slow global oscillations after seizures may be a significant indicator of cognitive recovery. Significantly less dramatic than in the local epileptogenic network, the substantial enhancement of strong local oscillations in the global network occurred at periods and times more similar to those in the local non-epileptogenic network. This may be a manifestation of a brain protection mechanism. This study provides an excellent opportunity to characterize better seizure-induced cognitive impairment and its possible underlying mechanisms, which may help guide early clinical assessment and treatment aimed at preventing neuropsychological impairment in various dynamic brain function networks in epileptic patients. In addition, it offers a solid foundation for future study on weighted directed functional networks.

Data availability statement

The original contributions presented in this study are included in the article/Supplementary material, further inquiries can be directed to the corresponding author.

Author contributions

DF proposed and supervised the project and contributed to writing the manuscript. LQ analyzed the data, performed the experiments, and wrote the manuscript. LQ and ZY wrote the code. QW supervised the project. GL provided raw data and clinical guidance. All authors contributed to the article and approved the submitted version.

Funding

This research was supported by the National Natural and Science Foundation of China (Grants 12072021 and 11932003) and the Young Teachers International Exchange Growth Program (QNXM20220049).

Conflict of interest

The authors declare that the research was conducted in the absence of any commercial or financial relationships that could be construed as a potential conflict of interest.

Publisher's note

All claims expressed in this article are solely those of the authors and do not necessarily represent those of their affiliated organizations, or those of the publisher, the editors and the reviewers. Any product that may be evaluated in this article, or claim that may be made by its manufacturer, is not guaranteed or endorsed by the publisher.

References

Abela, E., Rummel, C., Hauf, M., Weisstanner, C., Schindler, K., and Wiest, R. (2014). Neuroimaging of epilepsy: Lesions, networks, oscillations. *Clin Neuroradiol.* 24, 5–15.

Axmacher, N., Elger, C. E., and Fell, J. (2008). Ripples in the medial temporal lobe are relevant for human memory consolidation. *Brain* 131, 1806–1817.

Binnie, C. D., and Marston, D. (1992). Cognitive correlates of interictal discharges. *Epilepsia* 33:S11–S17.

Boly, M., Phillips, C., Balteau, E., Schnakers, C., Degueldre, C., Moonen, G., et al. (2008). Consciousness and cerebral baseline activity fluctuations. *Hum. Brain Mapp.* 29, 868–874.

Buzsáki, G. (2007). The structure of consciousness. *Nature* 446, 267–267.

Buzsaki, G., and Draguhn, A. (2004). Neuronal oscillations in cortical networks. *Science* 304, 1926–1929.

Dehaene, S., and Changeux, J. P. (1997). A hierarchical neuronal network for planning behavior. *Proc Natl. Acad Sci. U.S.A.* 94, 13293–13298. doi: 10.1073/pnas.94.24.13293

Donner, T. H., and Siegel, M. (2011). A framework for local cortical oscillation patterns. *Trends Cogn. Sci.* 15, 191–199.

Engel, A. K., Fries, P., and Singer, W. (2001). Dynamic predictions: Oscillations and synchrony in top–down processing. *Nat. Rev. Neurosci.* 2, 704–716.

Ewell, L. A., Fischer, K. B., Leibold, C., Leutgeb, S., and Leutgeb, J. K. (2019). The impact of pathological high-frequency oscillations on hippocampal network activity in rats with chronic epilepsy. *eLife* 8:e42148. doi: 10.7554/eLife.42148

Földi, T., Lőrincz, M. L., and Berényi, A. (2021). Temporally targeted interactions with pathologic oscillations as therapeutical targets in epilepsy and beyond. *Front. Neural Circ.* 15:784085. doi: 10.3389/fncir.2021.784085

Fonseca, A. F. D., Herpin, U., Paula, A. M. D., Victória, R. L., and Melfi, A. J. (2007). Agricultural use of treated sewage effluents: Agronomic and environmental implications and perspectives for Brazil. *Sci. Agric.* 64, 194–209.

Frässle, S., Manjaly, Z. M., Do, C. T., Kasper, L., Pruessmann, K. P., and Stephan, K. E. (2021). Whole-brain estimates of directed connectivity for human connectomics. *NeuroImage.* 225:117491.

Friston, K. J., Fagerholm, E. D., Zarghami, T. S., Parr, T., Hipólito, I., Magrou, L., et al. (2021). Parcels and particles: Markov blankets in the brain. *Netw. Neurosci.* 5, 211–251. doi: 10.1162/netn_a_00175

Goltsev, A. V., Lopes, M. A., Lee, K. E., and Mendes, J. F. F. (2013). "Critical and resonance phenomena in neural networks," in *AIP conference proceedings*, 1510, (College Park, MD: American Institute of Physics), 28–35.

Guo, J., Wu, Q., Zhao, C. W., Xiao, B., and Feng, L. (2018). Dynamic functional disturbances of brain network in seizure-related cognitive outcomes. *Epilepsy Res.* 140, 15–21. doi: 10.1016/j.eplepsyres.2017.12.005

Harkin, L. A., McMahon, J. M., Iona, X., Dibbens, L., Pelekanos, J. T., Zuberi, S. M., et al. (2007). The spectrum of SCN1A-related infantile epileptic encephalopathies. *Brain* 130, 843–852.

Hitzer, E. (2002). *Imaginary eigenvalues and complex eigenvectors explained by real geometry. In applications of geometric algebra in computer science and engineering.* Boston, MA: Birkhäuser, 145–155.

Holmes, G. L. (2015). Cognitive impairment in epilepsy: The role of network abnormalities. *Epileptic Disord.* 17, 101–116.

Holmes, G. L., and Lenck-Santini, P. P. (2006). Role of interictal epileptiform abnormalities in cognitive impairment. *Epilepsy Behav.* 8, 504–515.

Horvát, S., Gămănuț, R., Ercsey-Ravasz, M., Magrou, L., Gămănuț, B., Van Essen, D. C., et al. (2016). Spatial embedding and wiring cost constrain the functional layout of the cortical network of rodents and primates. *PLoS Biol.* 14:e1002512. doi: 10.1371/journal.pbio.1002512

Hutt, A., Lefebvre, J., Hight, D., and Sleigh, J. (2018). Suppression of underlying neuronal fluctuations mediates EEG slowing during general anaesthesia. *Neuroimage* 179, 414–428. doi: 10.1016/j.neuroimage.2018.06.043

Ibrahim, G. M., Akiyama, T., Ochi, A., Otsubo, H., Smith, M. L., Taylor, M. J., et al. (2012). Disruption of rolandic gamma-band functional connectivity by seizures is associated with motor impairments in children with epilepsy. *PloS One.* 7:e39326. doi: 10.1371/journal.pone.0039326

Ibrahim, G. M., Anderson, R., Akiyama, T., Ochi, A., Otsubo, H., Singh-Cadieux, G., et al. (2013). Neocortical pathological high-frequency oscillations are associated with frequency-dependent alterations in functional network topology. *J. Neurophysiol.* 110, 2475–2483.

Jensen, O., Kaiser, J., and Lachaux, J. P. (2007). Human gamma-frequency oscillations associated with attention and memory. *Trends Neurosci.* 30, 317–324.

Jolliffe, I. T., and Cadima, J. (2016). Principal component analysis: A review and recent developments. *Philos. Trans. A Math. Phys. Eng. Sci.* 374:20150202.

Kim, M., and Lee, U. (2020). Alpha oscillation, criticality, and responsiveness in complex brain networks. *Netw. Neurosci.*4, 155–173.

Lévesque, M., Salami, P., Shiri, Z., and Avoli, M. (2018). Interictal oscillations and focal epileptic disorders. *Eur. J. Neurosci.* 48, 2915–2927.

Lewis, C. M., Baldassarre, A., Committeri, G., Romani, G. L., and Corbetta, M. (2009). Learning sculpts the spontaneous activity of the resting human brain. *Proc. Natl. Acad. Sci. U.S.A.* 106, 17558–17563.

Llinás, R., Urbano, F. J., Leznik, E., Ramírez, R. R., and Van Marle, H. J. (2005). Rhythmic and dysrhythmic thalamocortical dynamics: GABA systems and the edge effect. *Trends Neurosci.* 28, 325–333. doi: 10.1016/j.tins.2005.04.006

Pellionisz, A., and Llinas, R. (1985). Tensor network theory of the metaorganization of functional geometries in the central nervous system. *Neuroscience* 16, 245–273. doi: 10.1016/0306-4522(85)90001-6

Qin, Y., Hu, Z., Chen, Y., Liu, J., Jiang, L., Che, Y., et al. (2022). Directed brain network analysis for fatigue driving based on EEG source signals. *Entropy* 24:1093. doi: 10.3390/e24081093

Quiroga, R. Q., Kreuz, T., and Grassberger, P. (2002). Event synchronization: A simple and fast method to measure synchronicity and time delay patterns. *Physical Rev. E* 66:041904.

Rentzeperis, I., and van Leeuwen, C. (2020). Adaptive rewiring evolves brain-like structure in weighted networks. *Sci. Rep.* 10:6075. doi: 10.1038/s41598-020-62204-7

Sadaghiani, S., and Kleinschmidt, A. (2016). Brain networks and α-oscillations: Structural and functional foundations of cognitive control. *Trends Cogn. Sci.* 20, 805–817. doi: 10.1016/j.tics.2016.09.004

Schalk, G., McFarland, D. J., Hinterberger, T., Birbaumer, N., and Wolpaw, J. R. (2004). BCI2000: A general-purpose brain-computer interface (BCI) system. *IEEE Trans. Biomed. Eng.* 51, 1034–1043.

Schoffelen, J. M., Hultén, A., Marquand, A. F., Uddén, J., and Hagoort, P. (2017). Frequency-specific directed interactions in the human brain network for language. *Proc. Natl. Acad. Sci. U.S.A.* 114, 8083–8088. doi: 10.1073/pnas.1703155114

Shamshiri, E. A., Tierney, T. M., Centeno, M., St Pier, K., Pressler, R. M., Sharp, D. J., et al. (2017). Interictal activity is an important contributor to abnormal intrinsic network connectivity in paediatric focal epilepsy. *Hum. Brain Mapp.* 38, 221–236. doi: 10.1002/hbm.23356

Sheybani, L., Birot, G., Contestabile, A., Seeck, M., Kiss, J. Z., Schaller, K., et al. (2018). Electrophysiological evidence for the development of a self-sustained large-scale epileptic network in the kainate mouse model of temporal lobe epilepsy. *J. Neurosci.* 38, 3776–3791. doi: 10.1523/JNEUROSCI.2193-17.2018

Sheybani, L., Van Mierlo, P., Birot, G., Michel, C. M., and Quairiaux, C. (2019). Large-scale 3–5 Hz oscillation constrains the expression of neocortical fast ripples in a mouse model of mesial temporal lobe epilepsy. *Eneuro* 6:ENEURO.494–ENEURO.418. doi: 10.1523/ENEURO.0494-18.2019

Staley, K., Hellier, J. L., and Dudek, F. E. (2005). Do interictal spikes drive epileptogenesis? *Neuroscientist* 11, 272–276.

Truccolo, W., Ahmed, O. J., Harrison, M. T., Eskandar, E. N., Cosgrove, G. R., Madsen, J. R., et al. (2014). Neuronal ensemble synchrony during human focal seizures. *J. Neurosci.* 34, 9927–9944.

Ung, H., Cazares, C., Nanivadekar, A., Kini, L., Wagenaar, J., Becker, D., et al. (2017). Interictal epileptiform activity outside the seizure onset zone impacts cognition. *Brain* 140, 2157–2168.

van Diessen, E., Zweiphenning, W. J., Jansen, F. E., Stam, C. J., Braun, K. P., and Otte, W. M. (2014). Brain network organization in focal epilepsy: A systematic review and meta-analysis. *PloS One.* 9:e114606.

Von Stein, A., and Sarnthein, J. (2000). Different frequencies for different scales of cortical integration: From local gamma to long range alpha/theta synchronization. *Int. J. Psychophysiol.* 38, 301–313. doi: 10.1016/s0167-8760(00)00172-0

Wang, J., Deng, B., Gao, T., Wang, J., Yi, G., and Wang, R. (2020). Frequency-dependent response in cortical network with periodic electrical stimulation. *Chaos* 30:073130.

Wang, R., Liu, M., Cheng, X., Wu, Y., Hildebrandt, A., and Zhou, C. (2021). Segregation, integration, and balance of large-scale resting brain networks configure different cognitive abilities. *Proc. Natl. Acad. Sci. U.S.A.* 118:e2022288118. doi: 10.1073/pnas.2022288118

Watson, B. O. (2018). Cognitive and physiologic impacts of the infraslow oscillation. *Front. Syst. Neurosci.* 12:44. doi: 10.3389/fnsys.2018.00044

Wilke, C., Worrell, G., and He, B. (2011). Graph analysis of epileptogenic networks in human partial epilepsy. *Epilepsia* 52, 84–93.

Yang, Y., Hu, C., and Abu-Omar, M. M. (2012). Conversion of glucose into furans in the presence of AlCl3 in an ethanol–water solvent system. *Bioresou. Technol.* 116, 190–194. doi: 10.1016/j.biortech.2012.03.126

Zafeiriou, M. P., Bao, G., Hudson, J., Halder, R., Blenkle, A., Schreiber, M. K., et al. (2020). Developmental GABA polarity switch and neuronal plasticity in bioengineered neuronal organoids. *Nat. Commun.* 11:3791. doi: 10.1038/s41467-020-17521-w

frontiers | Frontiers in Neuroscience

TYPE Original Research
PUBLISHED 02 March 2023
DOI 10.3389/fnins.2023.1131063

OPEN ACCESS

EDITED BY
Jiajia Li,
Xi'an University of Architecture and Technology, China

REVIEWED BY
Liyuan Zhang,
Beijing University of Technology, China
Xusan Yang,
Northwestern University, United States

*CORRESPONDENCE
Guihua Xiao
✉ xiaoguihua@mail.tsinghua.edu.cn
Xinguang Yu
✉ yuxinguang_301@163.com

†These authors have contributed equally to this work

SPECIALTY SECTION
This article was submitted to Translational Neuroscience, a section of the journal Frontiers in Neuroscience

RECEIVED 24 December 2022
ACCEPTED 13 February 2023
PUBLISHED 02 March 2023

CITATION
Xu H, Jin T, Zhang R, Xie H, Zhuang C, Zhang Y, Kong D, Xiao G and Yu X (2023) Cerebral cortex and hippocampus neural interaction during vagus nerve stimulation under *in vivo* large-scale imaging. *Front. Neurosci.* 17:1131063. doi: 10.3389/fnins.2023.1131063

Cerebral cortex and hippocampus neural interaction during vagus nerve stimulation under *in vivo* large-scale imaging

Hanyun Xu[1,2†], Tingting Jin[3†], Rujin Zhang[4], Hao Xie[5], Chaowei Zhuang[5], Yanyang Zhang[2], Dongsheng Kong[2], Guihua Xiao[5,6*] and Xinguang Yu[2*]

[1]Chinese PLA Medical School, Beijing, China, [2]Department of Neurosurgery, The First Medical Center of Chinese PLA General Hospital, Beijing, China, [3]Pulmonary and Critical Care Department, Wuhu Hospital of East China Normal University, Wuhu, Anhui, China, [4]Department of Anesthesiology, The First Medical Center of Chinese PLA General Hospital, Beijing, China, [5]Department of Automation, Tsinghua University, Beijing, China, [6]BNRist, Tsinghua University, Beijing, China

Objective: The purpose of this study was to study mechanisms of VNS modulation from a single neuron perspective utilizing a practical observation platform with single neuron resolution and widefield, real-time imaging coupled with an animal model simultaneously exposing the cerebral cortex and the hippocampus.

Methods: We utilized the observation platform characterized of widefield of view, real-time imaging, and high spatiotemporal resolution to obtain the neuronal activities in the cerebral cortex and the hippocampus during VNS in awake states and under anesthesia.

Results: Some neurons in the hippocampus were tightly related to VNS modulation, and varied types of neurons showed distinct responses to VNS modulation.

Conclusion: We utilized such an observation platform coupled with a novel animal model to obtain more information on neuron activities in the cerebral cortex and the hippocampus, providing an effective method to further study the mechanisms of therapeutic effects modulated by VNS.

KEYWORDS

vagus nerve stimulation, *in vivo* imaging, hippocampus, cerebral cortex, neuronal activity, fluorescence microscope

1. Introduction

Vagus nerve stimulation (VNS) is widely used as a treatment for various diseases, such as epilepsy, migraine, depression, etc. Although VNS therapy was approved by the US Food and Drug Administration in 1997 as an adjunctive therapy for reducing seizures in patients with refractory epilepsy, the therapeutic mechanisms remain poorly understood (Johnson and Wilson, 2018). The cerebral cortex and the hippocampus have been implicated as pivotal in VNS therapy (Attenello et al., 2016).

Currently, most studies on mechanisms of VNS modulation mainly employ electrophysiological techniques, fluorescence microscope coupled with neurotransmitter

probe, and medical imaging equipment such as MRI, PET, and SPECT (Conway et al., 2006; Vonck et al., 2008; Bartolomei et al., 2016; Mithani et al., 2019; Collins et al., 2021). Electrophysiological techniques are characterized by achieving micro-information (e.g., electrical signaling of neurons). The advantages of medical imaging equipment lie in understanding the functional connectivity among brain regions and the blood flow and metabolism of brain regions. Fluorescence microscope coupled with neurotransmitter probe can analyze neurotransmitters released by neurons. Based on the current studies utilizing these observation technologies, the potential mechanisms of therapeutic effects induced by VNS may be as follows: (1) Anti-inflammatory effects of VNS: Inflammation is a protective response of the body to external stimuli. Nevertheless, excessive inflammation can induce or exacerbate various brain diseases such as epilepsy, depression, etc. (Mehta et al., 2018; Paudel et al., 2018). Many studies have found that VNS could produce therapeutic effects by reducing local and systemic inflammatory response, which has proved to be correlated with the modulation of peripheral release of cytokines from immune cells, blood–brain barrier (BBB) permeability, and status of microglia (Kaya et al., 2013; Kaczmarczyk et al., 2017; Chaudhry et al., 2019). (2) Effects of VNS on central nervous system: (1) Neurotransmitter of norepinephrine (NE) and Gamma-Amino Butyric Acid (GABA)-Some studies have demonstrated that VNS could promote the release of NE in locus coeruleus (LC) and basolateral amygdala (BLA), and notably enhance extracellular NE levels in the prefrontal cortex (PFC) and hippocampus, and VNS-induced antiepileptic effects appeared to be related to the concentrations of NE in the hippocampus (Raedt et al., 2011; Manta et al., 2013). Another animal study showed that VNS took effect through increasing the concentration of NE in limbic, thalamic and cortical brain regions (Landau et al., 2015). Additionally, VNS regulated cortical excitability in brain regions associated with epilepsy, and its therapeutic effects were related to the normalization of cortical GABAA receptor density (Marrosu et al., 2003). In a word, the therapeutic effects of VNS were related to the concentration of NE and GABA in the cerebral cortex and subcortical structures. (2) BDNF-TrkB pathway and neuroplasticity: BDNF, a modulator of hippocampal plasticity and neurogenesis, could play an active role in the prevention of neuronal death (Hofer and Barde, 1988). Long-term VNS induced an increase of BDNF expression in the hippocampus, which was closely related to memory enhancement (Biggio et al., 2009). Similarly, VNS could activate the BDNF signaling pathway through a7nAChR, thus enhancing axonal plasticity and improving long-term neurological rehabilitation (Li et al., 2020). (3) Electrophysiological activity: abnormal hypersynchronous discharge of the cerebral cortex was regarded as a characterized feature of epileptic seizures (Wang et al., 2021). VNS remarkably suppressed epileptiform activity in EEG recordings by enhancing the firing rate of NTS neurons. Epileptiform activities in EEG recordings were obviously inhibited by VNS enhancing the firing rate of nucleus tractus solitarius (NTS) neurons (He et al., 2013). (4) Functional connectivity of brain regions: VNS enhanced the connectivity of thalamus to the anterior cingulate cortex (ACC) and left island and increased the regional homogeneity of the right superior or middle temporal gyrus, therefore resulting in improvement of the clinical manifestations in patients with epilepsy (Ibrahim et al., 2017). (5) Cerebral blood flow: the neuroprotective effects of VNS could be correlated with the modulation of cerebral blood flow (CBF) in brain regions (Conway et al., 2006).

To sum up, the study on mechanisms of VNS modulation from a single neuron perspective is rare, possibly due to the lack of such an effective observation platform with single neuron resolution and widefield of view, real-time imaging, as well as an animal model simultaneously exposing the cerebral cortex and the hippocampus. Here, we established this observation platform as well as a novel mouse model to obtain neuronal activities in the cerebral cortex and hippocampus during VNS and provide a new viewpoint to further explore the mechanisms of therapeutic effects induced by VNS.

2. Materials and methods

2.1. Mouse

All experimental procedures were approved by the Institutional Animal Care and Use Committee at Tsinghua University, Beijing, China. We employed Transgenic mouse Ai148(TIT2L-GC6f-ICL-tTA2)-D × Rasgrf2-2A-dCre (JAX 022864, JAX 030328) expressing Gcamp6f calcium signaling in the specific layer 2/3 of the cerebral cortex for the imaging experiments. All experimental mice were purchased from Animal House of Tsinghua University. All animals were housed in a laboratory environment on a regular 12/12 h light/dark cycle at 20–22°C. Mice had access to *ad libitum* food and water and were individually housed after virus injection, craniotomy, and VNS cuff implantation. All experimental manipulations were conducted during the light phase.

2.2. Chemicals and apparatus

Isoflurane was purchased from the RWD life science company (Shenzhen, China). AAV2/9-hSyn-Flex-GCaMP6f-WPRE-pA (qTiter 1.12e9GC/ml) and AAV2/9-hSyn-Cre-WPRE-pA (qTiter 1.12e9GC/ml) were purchased from Shanghai Taitool Bioscience Company of China. A programmable stimulus isolator was used to stimulate the vagus nerve through connecting electrode cuff. A homemade optical widefield mesoscope was used for Ca^{2+} imaging with a central wavelength at 473 nm.

2.3. Hippocampus virus injection

For hippocampal imaging, the mouse was secured to a stereotaxic frame (the RWD life science company of Shenzhen, China) after anesthesia induction, and the whole injection procedures were performed in an aseptic environment with the mouse under 1–2% isoflurane anesthesia (oxygen flow rate: 1 L/min). An approximately 0.8 cm midline incision was made centered about 0.1 cm behind the bregma. After horizontal calibration adjustment, we placed the micro syringe needle at the bregma point and then reset the coordinates to zero. A 0.5 mm diameter hole was drilled on the right skull region above the hippocampus (coordination, AP: -2.2 mm; ML: 1.5 mm) to reach

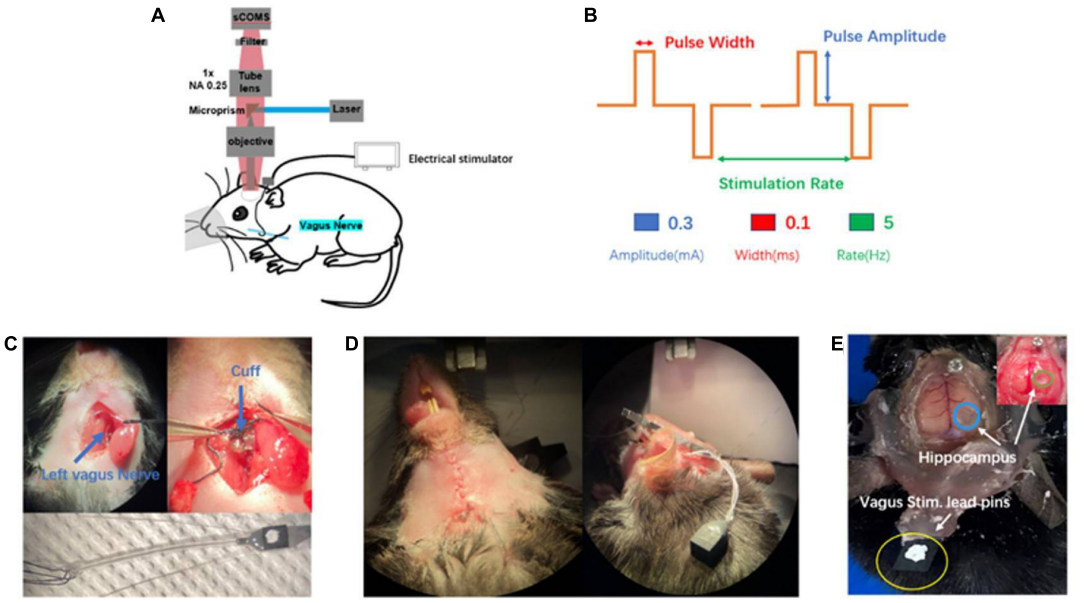

FIGURE 1
Introduction of *in vivo* wild-field imaging and vagus nerve stimulation (VNS). **(A)** Schematic diagram of *in vivo* imaging and vagus nerve stimulation, illustrating that the mouse is under overhead objective for *in vivo* calcium brain imaging and the cuff electrode is positioned around vagus nerve(blue). **(B)** Schematic of VNS pulse waveforms and parameters. Biphasic pulse was delivered in trains lasting 10 s (top). VNS was delivered by the parameter combination of 0.3 mA, 0.1 ms, and 5 Hz (bottom). **(C)** Photograph of vagus nerve cuff position (top) and bipolar VNS cuff design (bottom). **(D)** Photograph of subcutaneous tunnel made in between the ear and eyes from neck incision to the top of the head. **(E)** Photograph of the awake mouse with the fixed head post, showing simultaneous exposure of cerebral cortex and hippocampus (blue and green) as well as vagus stimulation lead pins (yellow) fixed to the rear of the head post using acrylic dental cement.

the dura, then we mixed AAV2/9-hSyn-Flex-GCaMP6f-WPRE-pA at 1:10,000 dilution (qTiter 1.12e9GC/ml, Shanghai Taitool Bioscience company, China) and AAV2/9-hSyn-Cre- WPRE-PA (qTiter 1.9e13 GC/ml, Shanghai Taitool Bioscience company, China) in a ratio of 1:1. A volume of 200 nl was injected into the right hippocampal CA1 (coordination, AP: -2.2 mm; ML: 1.5 mm DV: 1.3 mm) using a thin glass pipette and infusion pump at the rate of 50 nl/min. After injection, wait for 10 min for the virus to fully absorb, then we retracted the pipette and sutured the incision by absorbable suture (8–0). The mouse was returned to their cage for at least 2 weeks before surgical procedures.

2.4. Surgery procedures

The Surgical instruments were sterilized by autoclave for 30 min prior to each surgical procedure. All surgical procedures were performed in an aseptic environment with mice under 1–2% isoflurane anesthesia (oxygen flow rate: 1 L/min). Isoflurane anesthetic gas (1% in oxygen) was used for the entire duration of all surgeries. The temperature of the mouse was maintained between 36.5 and 37.5°C using a homeothermic blanket system. Craniotomy and cylinder implantation above hippocampus CA1. For widefield imaging, we cut the skin between and around the bilateral ears and eyes to expose enough skull space. After horizontal calibration adjustment, we placed the syringe (1 ml volume) needle at the bregma point and then reset the coordinates to zero. After Removing the syringe to a safe location, a trapezoid shape window (8 mm × 10 mm) was made overlying the dorsal cortex using a handheld dental drill. The skull was removed to expose the dura, and the gel foam particles soaked in sterile saline were gently applied on the dura to stop the slight bleeding. Wait until all bleeding was entirely stopped, then Carefully remove the gel foam particles not to disturb the clotting process. Two skull nails were implanted, respectively, in the front and back of the cranial window on the skull in order to secure the glass coverslip. Locating the coordinate of the hippocampus (AP: -2.2 mm; ML: 1.5 mm), the cortex above the hippocampus was aspirated until reaching the CA1 layer of the hippocampus featured of regular stripes was exposed. After the bleeding was completely stopped and the wound was cleaned, a cylinder lens was implanted above CA1 (AP: -2.2 mm; ML: 1.5 mm; DV: –1.3 mm), and then a trapezoid shape glass coverslip was laid over the cranial window and sealed with surgical glue. After 10 min, when the surgical glue around the cranial window was solid, a thin layer of dental acrylic cement was placed around the edges of the glass to solidify it. A semicircular aluminum alloy head post was placed on the edge of the cranial window, ensuring that it was parallel to the glass coverslip. It was then fixed with dental acrylic cement. We applied dental acrylic cement throughout the exposed skull surface and across a small rim of the coverslip to secure it. Cervical vagus nerve cuff electrode implantation. Two platinum-iridium wires were fixed 1 mm apart to biocompatible micro silicone tube. The end of the two lead wires was connected to pins, which were used to connect the cuff to the stimulator. After isoflurane induction, the mouse was placed in a supine position; the surgical site was shaved and cleaned with scrubs of iodophor and alcohol. Under anesthesia, a 1.5–2 cm incision was made from manubrium to jawline along the scalp midline on the ventral aspect of the neck using micro-scissors. With micro scissors and blunt-tipped forceps, the submaxillary gland

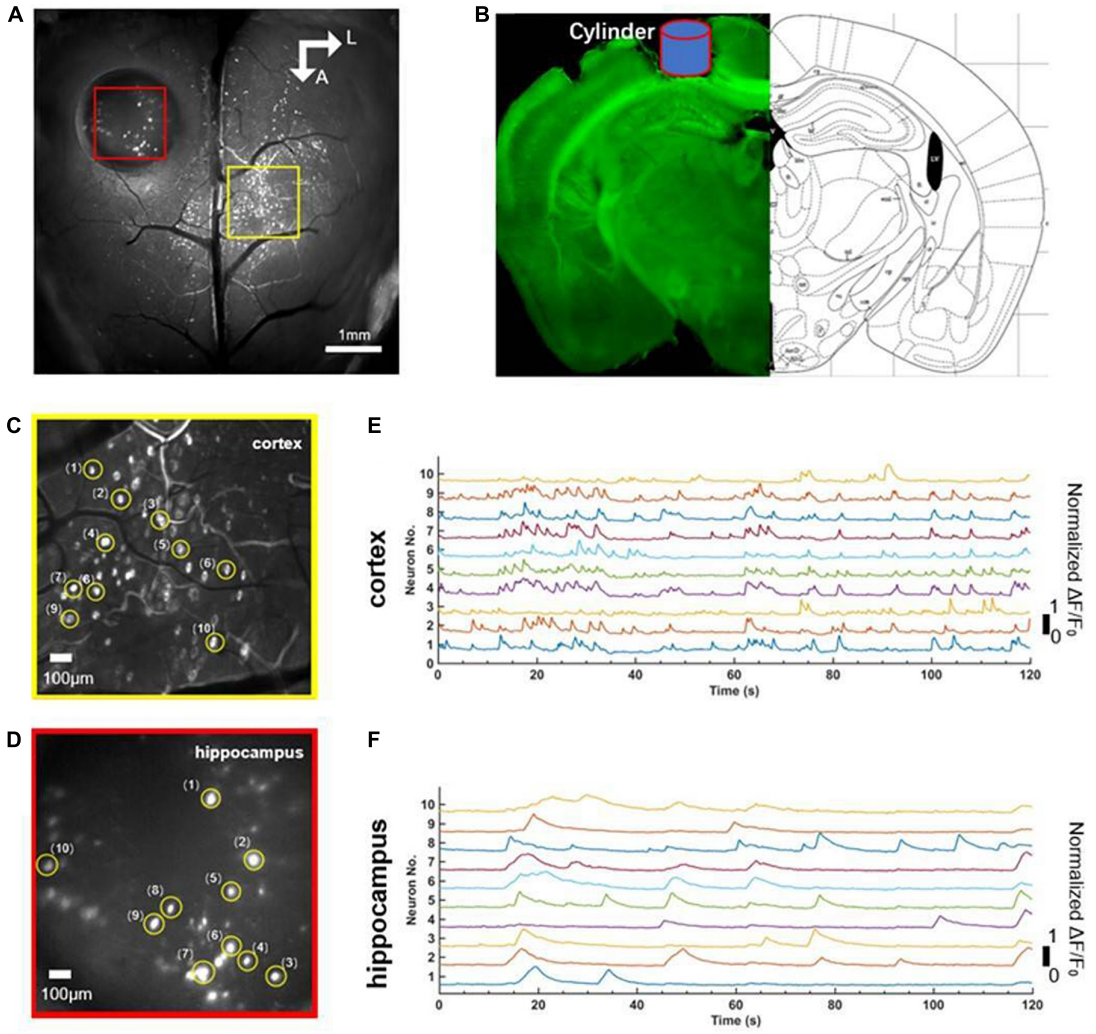

FIGURE 2
Comparison of simultaneous wide-field calcium imaging of cerebral cortex and hippocampus CA1 *in vivo* in awake states. **(A)** Photograph illustrating simultaneous wide-field calcium imaging *in vivo* of the cerebral cortex and the hippocampus CA1. Scale bar, 1 mm. **(B)** Coronal slice of the mouse illustrating the hippocampus CA1 right beneath cylinder (blue) corresponding to the red square in panel **(A)**. **(C)** A field of the enlarged view of neurons (labeled 1–10) in layer 2/3 of cerebral cortex indicated with the yellow square in **(A)**, Scale bar, 100 μm. **(D)** A field of the enlarged view of neurons (labeled 1–10) of hippocampus CA1 indicated with the red square in **(A)**, Scale bar, 100 μm. **(E)** Normalized fluorescence signals fluctuation ($\Delta F/F_0$) for neurons (labeled 1–10) shown in panel **(C)**. **(F)** Normalized fluorescence signals fluctuation ($\Delta F/F_0$) for neurons (labeled 1–10) shown in panel **(E)**.

and connective tissue overlying the left cervical vagus nerve was retracted, and the nerve was separated from the vessels within the carotid sheath. After using a small pair of surgical retractors to hold the muscles apart, a 4–5 mm segment of the left cervical vagus nerve was dissected from the carotid sheath. The cuff electrode was placed around the vagus nerve and secured with suture ensuring that the electrode wires had circumferential or near-circumferential contact with the nerve. The muscles were placed back in their original position, and an absorbable suture (8–0) was used to secure the cuff in position. A subcutaneous tunnel was made in between the ear and eyes from the neck incision to the top of the head, which allowed passing the cuff leads to the skull. Lead pins were fixed to the previously implanted head post using acrylic dental cement. The submaxillary gland was placed back to its original position, and finally the neck incision and the incision of the head's subcutaneous tunnel were sutured closed.

2.5. Vagus nerve stimulation parameters

The animal's head was fixed to the mouse holder. In all experiments, the intertrain interval was set at 50 s, and each pulse train lasted for 10 s. VNS was delivered by the parameter combination of 0.3 mA, 0.1 ms, and 5 Hz. The parameters occurred three times in a session of cerebral cortical and hippocampus axon imaging.

2.6. Data analysis

Widefield images of the cerebral cortex and the hippocampus were aligned to the Allen institute common coordinate framework (CCF) map using structural landmarks and MATLAB code developed by Drs. Matt Kaufman and Shreya Saxena. Widefield

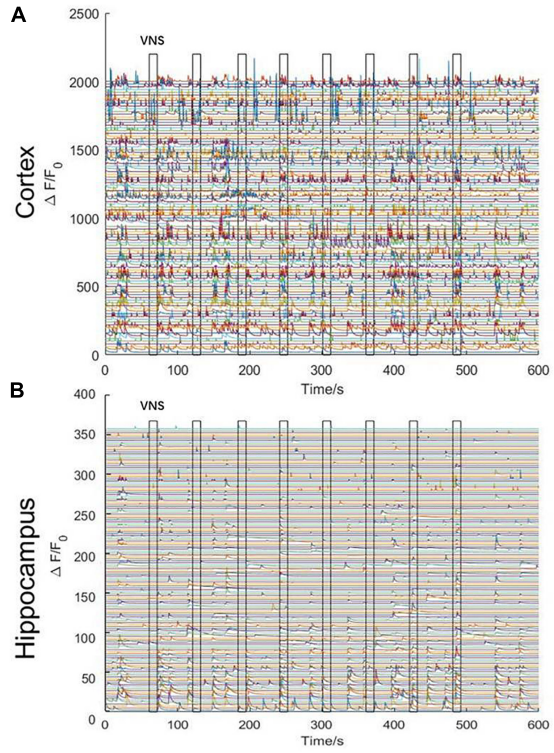

FIGURE 3
Curve diagram of calcium signaling of neurons in the cerebral cortex and hippocampal CA1 in awake states during VNS. **(A)** Curve diagram of calcium signaling of neurons in the cerebral cortex during VNS. **(B)** Curve diagram of calcium signaling of neurons in the hippocampal CA1 during VNS. Narrow gray rectangles indicate time of each VNS application (lasting 10 s). Y-axis indicates neuron numbers.

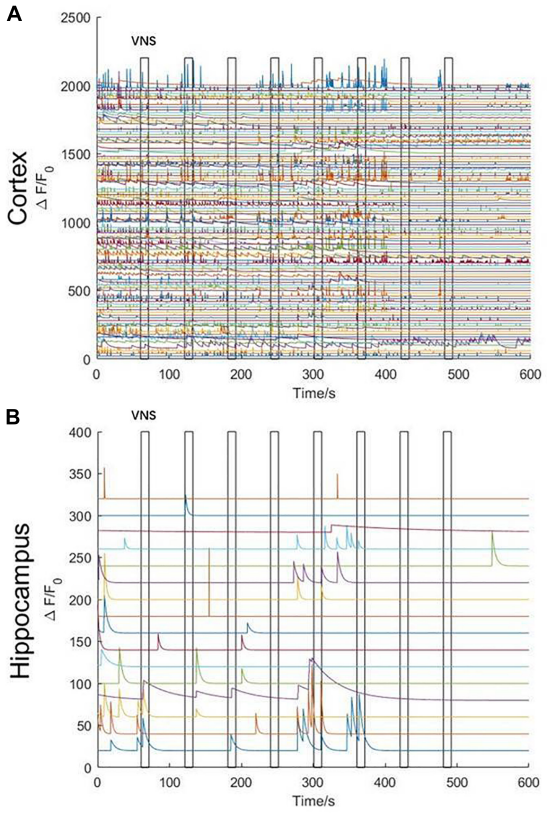

FIGURE 4
Characteristics of calcium signaling of neurons in the cerebral cortex and hippocampal CA1 under isoflurane anesthesia during VNS. **(A)** Curve diagram of calcium signaling of neurons in the cerebral cortex during VNS. **(B)** Curve diagram of calcium signaling of neurons in the hippocampal CA1 during VNS. Narrow gray rectangles indicate time of each VNS application (lasting 10 s). Y-axis indicates neuron numbers.

fluorescence signals were normalized pixel by pixel by the following equation $\Delta F/F_0 = (F_i\text{-}F_0)/F_0$, where Fi is the raw fluorescence of the ith video frame, and F_0 is the mean of the fluorescence baseline. Origin 8.0 was used to analyze the statistical data.

3. Results

3.1. Establishment of experimental observation platform and mouse model

3.1.1. Experimental observation platform

In order to further *in vivo* explore complex neuronal activities of the brain by observation of macroscopic multiple brain regions combined with microscopic neurons, we set up this observation platform (widefield mesoscope) to research the effects of VNS modulation on brain neuronal activities in awake states and under anesthesia. The observation platform's excitation source is a CW laser (MBL-III-473–100 mW, CNI) at a central wavelength of 473 nm. The laser beam is expanded to 12 mm by a beam expander (BE) and a pair of 4f-system lenses. After being focused, then being reflected by a micro prism, the beam passes through an excitation objective and excites neuron fluorescence of the cerebral cortex and hippocampal CA1 region of the mouse. The fluorescence is collected by an epifluorescence setup including the same objective, a tube lens (MVPLAPO 1X, Olympus), a filter and an sCMOS. The FOV of the equipment is 6.6 mm and each pixel in the sCMOS corresponds to 3.25 μm on the image plane with two times magnification and 6.5 μm pixel size (Figure 1A). The equipment is characterized of single-cell resolution, widefield of view, and real-time observation.

3.1.2. Establishment of mouse model for simultaneous *in vivo* imaging of cerebral cortex and hippocampal CA1 region

The experimental mouse model in previous studies was mainly related to small bone window craniotomy, exposing the cerebral cortex with a size of about 3–4 mm in diameter. There was short of an experimental animal model that simultaneously exposed large-scale cerebral cortex and hippocampal CA1 region. In our experiment, we first selected the rasgrf-Cre-Ai148D gene mouse expressing Gcamp6f calcium signaling in the specific layer 2/3 of the cerebral cortex to inject GCamp6f virus into the right hippocampal CA1 region. After 2 weeks, we performed a large-scale craniotomy and cylinder implantation above the hippocampal CA1 region, simultaneously exposing the cerebral cortex (range: 6 mm × 8 mm) and the right hippocampal CA1 region (range:

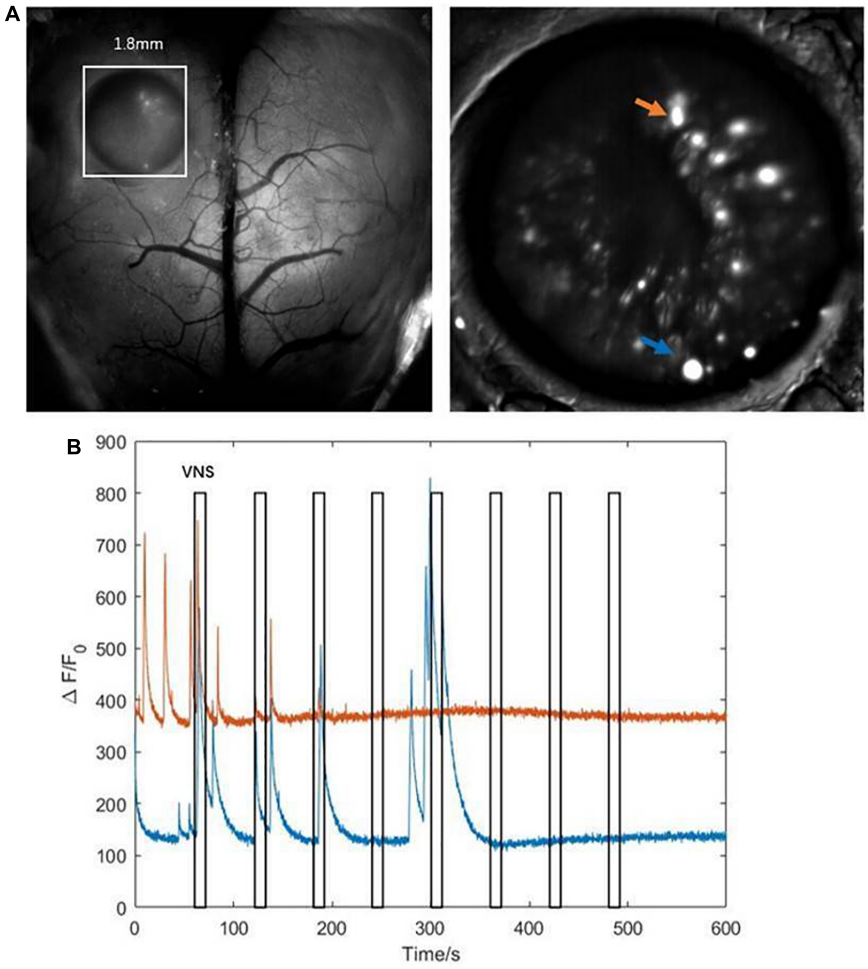

FIGURE 5
Characteristics of calcium signaling of neurons in the hippocampal CA1. (**A** left) The hippocampal CA1 region (white square: 1.8mm × 1.8mm); (right) two typical neurons extracted from hippocampal CA1 (orange arrow and blue arrow). **(B)** The curve diagram of neuronal activities of the two neurons (blue curve and orange curve corresponding to blue arrow and orange arrow shown in **(A)**, respectively). Narrow gray rectangles indicate time of each VNS application (lasting 10 s). Y-axis indicates neuron numbers.

1.8 mm × 1.8 mm) (Figure 1E), which provided observation of the cerebral cortex and the hippocampal CA1 simultaneously. In a word, we established a new and original animal model for further exploring brain activities.

3.1.3. Vagus nerve electrode implantation

In our experiment, we selected the left vagus nerve of the mouse for vagus nerve stimulation electrode implantation (Figure 1C top). We designed and customized the vagus nerve electrode (Figure 1C bottom) according to the size of the mouse vagus nerve. Bipolar VNS cuff can be firmly fixed to cervical vagus nerve and a subcutaneous tunnel was made in between the ear and eyes from the neck incision to the top of the head, which allowed passing the cuff leads to the rear of head post. Lead pins were fixed to the previously implanted head post using acrylic dental cement (Figure 1D). Our mouse model had the following advantages: (1) VNS cuff was firmly fixed to vagus nerve and not easy to fall off, and the electrode wire was buried under the skin, which protected the electrode wire from damage. (2) It avoided the adverse effects caused by exposed electrode wire on the daily behavior of the mouse. (3) Our mouse model could survive for a long time, providing an ideal model for various experimental designs and long-term research on brain activity. In this study, we chose a VNS stimulus parameter within the commonly used range (Figure 1B).

3.2. Characteristics of calcium signaling of neurons in cerebral cortex and hippocampal CA1 region in awake states

Before the experiment, we first positioned the mouse beneath the widefield camera to make it familiar with the surrounding environment. After 10 min, when the mouse was accustomed to the surrounding environment, we used the observation equipment to obtain the characteristics of calcium signaling of neurons located in layer 2/3 of the cerebral cortex and the hippocampus CA1 of the mouse in awake states. We found that neurons of the cerebral cortex and the hippocampus CA1 had spontaneous neuronal activities (Figure 2A). Then, we randomly extracted 10

neurons from near the junction of motor cortex and somatosensory cortex (yellow square, Figure 2C) and the hippocampal CA1 (red square, Figure 2D), respectively. Further analysis showed the single neuron's characteristic curve of Gcamp6f calcium signaling. The calcium signaling curve of neurons of the cerebral cortex and the hippocampal CA1 showed that, compared to neurons of the hippocampal CA1 (Figure 2F), neurons of the cerebral cortex had higher calcium signaling intensity and faster response frequency. The result indicated that the neurons of the cerebral cortex were more active in awake states (Figure 2E). The perfused brain slice showed that the cylinder was right above the hippocampal CA1, and the observation position was appropriate (Figure 2B).

3.3. Characteristics of calcium signaling of neurons in cerebral cortex and hippocampal CA1 in awake states during VNS

We stimulated with trains of biphasic pulses lasting 10 s. Experimental results demonstrated that neuronal activities were not tightly correlated with VNS. In other words, neuronal calcium signaling in the cerebral cortex and the hippocampal CA1 was not significantly changed during VNS, compared to the pre-VNS baseline (Figures 3A, B). Owing to being head-fixed beneath the widefield camera, the limbs and mouth of the mouse had vigorous activities, which could induce neuronal activities. Therefore, we speculated that no significant difference in neuronal activities between during VNS and pre-VNS baseline was associated with relatively small stimulation parameters or intense neuronal activities induced by body movement. That is, the intensity of neuronal activities induced by VNS was significantly lower than the intensity of neuronal activities induced by body movement. Consequently, the neuronal activities induced by VNS were covered by the neuronal activities elicited by body movement, resulting in the finding showing no significant changes in neuronal activities induced by VNS.

3.4. Characteristics of calcium signaling of neurons in cerebral cortex and hippocampal CA1 under isoflurane anesthesia during VNS

In order to remove the disturbance of neuronal activities elicited by noticeable limb movement in awake states, we used isoflurane anesthetics to regulate the mouse into anesthesia. The mouse inhaled oxygen through a mask connected to an anesthesia machine at a flow rate of 1.2 L/min. VNS was delivered when the mouse was under anesthesia without limb movement. In the initial stage of anesthesia, we observed that, neuronal activities in the cerebral cortex were rapidly inhibited (Figure 4A); however, neuronal activities in the hippocampal CA1 were not significantly inhibited. Meanwhile, we also found that the activities of several neurons in the hippocampal CA1 were tightly related to VNS. With the anesthesia deepening, neuronal activities in the hippocampal CA1 vanished and were no longer activated by VNS (Figure 4B). Therefore, we concluded that, at least in the hippocampal CA1 region, some neuronal activities were regulated by VNS.

3.5. Correlation between neuronal activities in the hippocampal CA1 and VNS

The results above showed that the activities of several neurons in the hippocampal CA1 were tightly correlated with VNS (Figure 5A). We further extracted two typical neurons to achieve the curve of neuronal calcium signaling. We analyzed that one neuron (orange curve) showed inhibition characteristics, and the other neuron (blue curve) showed activation characteristics in response to VNS application (Figure 5B). Therefore, we speculated that different types of neurons had varied responses to VNS application.

4. Discussion

vagus nerve stimulation (VNS) is widely used as a treatment for epilepsy, migraine, depression, etc., since VNS therapy was approved by the US Food and Drug Administration in 1997 as an adjunctive therapy for reducing seizures in patients with refractory epilepsy (Johnson and Wilson, 2018). Despite its broad and growing application, the mechanisms by which VNS exerts its clinical benefits are still little known, especially the mechanisms in regulation of neurons. Here, we set up this observation platform, which is characterized of single-cell resolution, widefield of view, and real-time observation, to research the effects of VNS modulation on brain neuronal activities from a combination of macroscope and microscope perspective in awake and anesthetized states. Moreover, we established a new and original mouse model, exposing large-scale cerebral cortex (range: 6 mm × 8 mm) and hippocampal CA1 region (range: 1.8 mm × 1.8 cm), to simultaneously achieve *in vivo*, real-time imaging of cerebral cortex and subcortical region (hippocampal CA1). Utilizing our observation platform and mouse model, we observed that the cerebral cortex and the hippocampal CA1 existed spontaneous neuronal activities, respectively, which showed varied characteristics from each other in awake states. Moreover, we observed that neuronal calcium signaling in the cerebral cortex and the hippocampal CA1 was not significantly changed during VNS in awake states, possibly due to low-intensity stimulations or disturbance of body movement. In order to eliminate the disturbance of body movement, we achieved neuronal activities in the cerebral cortex and the hippocampal CA1 during VNS in anesthetized states. The analysis indicated that at least the activities of several neurons in the hippocampal CA1 were tightly correlated with VNS, and two of these neurons showed distinct characteristics.

4.1. Experimental observation platform and mouse model

Previous studies on the mechanisms underlying VNS modulation centered on either macroscopic multiple brain regions

or microstructures. The macroscopic observation methods mainly utilized devices, including MRI, PET, and SPECT (Conway et al., 2006; Malbert et al., 2019; Borgmann et al., 2021), whose major advantages lay in the power to observe the functional connectivity of multiple brain regions. The microscopic observation methods primarily utilized electrophysiology and optical fiber photometry, which took advantage of observing microstructures such as cells or neurons (Jaseja, 2010; Laricchiuta et al., 2021). However, few studies effectively combined the two observation technology to decipher complex brain neuronal activities *in vivo*. Therefore, we applied this observation platform that combined macro- and microscopic observation, which was characterized of widefield of view (6.6 mm), real-time observation, and single-cell resolution, to further study neuronal activities elicited by VNS. In addition, previous studies have shown that epilepsy and depression were related to the cerebral cortex and subcortical regions (e.g., hippicampus) (Rosso et al., 2020; Wang et al., 2021). Owing to the anatomical location of hippocampus beneath the cerebral cortex, it was challenging to directly observe the hippocampus CA1 for more neuronal activities. Few studies have demonstrated a mouse model simultaneously exposing large-scale cerebral cortex and hippocampus CA1 to study brain activities. However, some studies utilized optical fiber implanted into the corresponding regions to observe synchronous neuronal activities in the motor region of the cerebral cortex and the hippocampus CA1 (Dong et al., 2020). It was challenging to obtain a larger region of neuronal signaling due to the observation scope being confined to a focal point. Our study established an experimental mouse model to simultaneously expose large-scale cerebral cortex (6 mm × 8 mm) and hippocampal CA1 region (1.8 mm × 1.8 mm). Taken together, we set up an experimental observation platform combined with a novel animal model to further explore neuronal activities in the cerebral cortex and hippocampus.

4.2. Characteristics of calcium signaling of neurons in cerebral cortex and hippocampal CA1 in awake states during VNS

Some studies demonstrated that cortical activation was to be dose-dependent. Low-intensity stimulation parameters that evoked little to no arousal change similarly did not elicit detectable changes in cortical excitation, whereas high-intensity stimulation parameters that elicited pupil dilation, whisking, and/or wheel movement also induced large increases in cortical neuronal calcium signaling (Collins et al., 2021; Mridha et al., 2021). In our experiment, neuronal activities in the cerebral cortex and the hippocampal CA1 were not significantly changed during VNS compared to pre-VNS baseline. Therefore, we speculated that neuronal activities in response to VNS application were weak due to relatively small stimulation parameters and the intensity of neuronal activities induced by VNS was much lower than the intensity of neuronal activities elicited by vigorous limb movement. So, there was no significant difference in neuronal activities between during VNS and pre-VNS baseline. Furthermore, the effects of VNS modulation varied among different parameters, and enhancement of performance of behavior tasks and cortical map plasticity was strongest in response to intermediate intensity of stimulation (Ghacibeh et al., 2006; Lai and David, 2021). Therefore, we concluded that there might be an individual difference in the effects of VNS modulation, and the optimal parameters were crucial to VNS application.

4.3. Characteristics of calcium signaling of neurons in cerebral cortex and hippocampal CA1 under anesthesia during VNS

To completely remove any contribution of limb movement-related activities to neuronal calcium signaling, we anesthetized mice with isoflurane. At the onset of anesthesia, neuronal activities in the cerebral cortex were rapidly inhibited; however, neuronal activities in the hippocampal CA1 were not significantly inhibited. Meanwhile, we also found that the activities of several neurons in the hippocampal CA1 were tightly related to VNS. With the anesthesia deepening, neuronal activities in the hippocampal CA1 vanished and were no longer activated by VNS. Therefore, we concluded that, at least in the hippocampal CA1, some neuronal activities were modulated by VNS. In previous studies, Arousal state or sleep disturbances and learning impairment related to hippocampus abnormality occurred across many forms of epilepsy, migraine, and depression, conditions for which VNS has been found to be a useful treatment option (Sedigh-Sarvestani et al., 2014; Gumusyayla et al., 2016; Sun et al., 2017). In an animal study, the finding was that the significant deviations from normal calcium dynamics in CA1 arose before (33 min, on average) the onset of motor convulsions and the intense calcium waves could directly lead to acute cellular damage in live animals (Berdyyeva et al., 2016). Combined with these previous findings, we draw a conclusion that the therapeutic effects of VNS could be partially explained by the modulation of neuronal activities in the hippocampal CA1. Additionally, we further extracted two typical neurons to obtain the curve of neuronal calcium signaling, by which we analyzed that one neuron showed inhibition characteristics and the other neuron showed activation characteristics in response to VNS application. Anatomical and physiological studies have previously demonstrated that VNS may excite cortical neurons through neuromodulatory pathways, including those releasing acetylcholine (Ach) or NE (Dorr and Debonnel, 2006; Roosevelt et al., 2006). Fibers carrying information from the vagus nerve synapse in the nucleus of the solitary tract projected to the noradrenergic LC. Then projections from LC were sent throughout the brain, including to subcortical structures, such as the basal forebrain (BF), thalamus, and cerebral cortex (Kim et al., 2016; Rho et al., 2018). Therefore, we speculated that various neurons existed in the hippocampal CA1, which had varied responses to VNS application.

5. Conclusion

Taken together, we utilized this experimental observation platform coupled with a novel animal model to simultaneously obtain further information from neurons in the cerebral cortex

and the hippocampal CA1, which provided an effective means for further studying mechanisms of VNS modulation. Meanwhile, our experiment shed light on mechanisms of VNS modulation from a single neuron level, providing a new perspective on mechanisms of VNS modulation. Combined with previous studies' findings, we summarized that selection of stimulation parameters was vital to the therapeutic effects of VNS modulation, and different types of neurons in the hippocampal CA1 had varied responses to VNS modulation. Next, future studies may focus on individualized VNS parameters and various types of neurons in the cerebral and the hippocampal, ultimately contributing to improved therapeutic effects of VNS modulation for clinical diseases.

Data availability statement

The raw data supporting the conclusions of this article will be made available by the authors, without undue reservation.

Ethics statement

This animal study was reviewed and approved by the Institutional Animal Care and Use Committee at Tsinghua University, Beijing, China.

Author contributions

HYX, GX, and XY: conceptualization. HX, CZ, and GX: methodology. DK and RZ: validation. YZ and HYX: investigation. HYX, RZ, and GX: data curation. HYX: writing—original draft preparation. HYX, TJ, and GX: writing—review and editing. GX, HX, and XY: supervision and project administration. YZ: funding acquisition. All authors read and agreed to the published version of the manuscript.

Funding

This research was funded by the National Natural Science Foundation of China (62171254) and the Military Young Scholar Medical Research Fund of Chinese PLA 500 General Hospital (No. QNF19071). The funding acquisition: GX and YZ.

Acknowledgments

We thank all staff in the Laboratory Department of Automation of Tsinghua University for assistance with sample preparation and data acquisition.

Conflict of interest

The authors declare that the research was conducted in the absence of any commercial or financial relationships that could be construed as a potential conflict of interest.

Publisher's note

References

Attenello, F., Amar, A., Liu, C., and Apuzzo, M. (2016). Theoretical basis of vagus nerve stimulation. Stimulation of the peripheral nervous system. *Progress Neurol. Surg.* 29, 20–28. doi: 10.1159/000434652

Bartolomei, F., Bonini, F., Vidal, E., Trebuchon, A., Lagarde, S., Lambert, I., et al. (2016). How does vagal nerve stimulation (VNS) change EEG brain functional connectivity? *Epilepsy Res.* 126, 141–146. doi: 10.1016/j.eplepsyres.2016.06.008

Berdyyeva, T., Frady, E., Nassi, J., Aluisio, L., Cherkas, Y., Otte, S., et al. (2016). Direct imaging of hippocampal epileptiform calcium motifs following kainic acid administration in freely behaving mice. *Front. Neurosci.* 10:53. doi: 10.3389/fnins.2016.00053

Biggio, F., Gorini, G., Utzeri, C., Olla, P., Marrosu, F., Mocchetti, I., et al. (2009). Chronic vagus nerve stimulation induces neuronal plasticity in the rat hippocampus. *Int. J. Neuropsychopharmacol.* 12, 1209–1221. doi: 10.1017/S1461145709000200

Borgmann, D., Rigoux, L., Kuzmanovic, B., Edwin Thanarajah, S., Munte, T., Fenselau, H., et al. (2021). Technical note: Modulation of fMRI brainstem responses by transcutaneous vagus nerve stimulation. *Neuroimage* 244:118566. doi: 10.1016/j.neuroimage.2021.118566

Chaudhry, S., Lendvai, I., Muhammad, S., Westhofen, P., Kruppenbacher, J., Scheef, L., et al. (2019). Inter-ictal assay of peripheral circulating inflammatory mediators in migraine patients under adjunctive cervical non-invasive vagus nerve stimulation (nVNS): A proof-of-concept study. *Brain Stimul.* 12, 643–651. doi: 10.1016/j.brs.2019.01.008

Collins, L., Boddington, L., Steffan, P., and McCormick, D. (2021). Vagus nerve stimulation induces widespread cortical and behavioral activation. *Curr. Biol.* 31, 2088–2098.e3. doi: 10.1016/j.cub.2021.02.049

Conway, C., Sheline, Y., Chibnall, J., George, M., Fletcher, J., and Mintun, M. (2006). Cerebral blood flow changes during vagus nerve stimulation for depression. *Psychiatry Res.* 146, 179–184. doi: 10.1016/j.pscychresns.2005.12.007

Dong, X., Zhang, X., Wang, F., Liu, N., Liu, A., Li, Y., et al. (2020). Simultaneous calcium recordings of hippocampal CA1 and primary motor cortex M1 and their relations to behavioral activities in freely moving epileptic mice. *Exp. Brain Res.* 238, 1479–1488. doi: 10.1007/s00221-020-05815-w

Dorr, A., and Debonnel, G. (2006). Effect of vagus nerve stimulation on serotonergic and noradrenergic transmission. *J. Pharmacol. Exp. Ther.* 318, 890–898. doi: 10.1124/jpet.106.104166

Ghacibeh, G., Shenker, J., Shenal, B., Uthman, B., and Heilman, K. (2006). The influence of vagus nerve stimulation on memory. *Cogn. Behav. Neurol.* 19, 119–122. doi: 10.1097/01.wnn.0000213908.34278.7d

Gumusyayla, S., Erdal, A., Tezer, F., and Saygi, S. (2016). The temporal relation between seizure onset and arousal-awakening in temporal lobe seizures. *Seizure* 39, 24–27. doi: 10.1016/j.seizure.2016.05.005

He, W., Jing, X., Zhu, B., Zhu, X., Li, L., Bai, W., et al. (2013). The auriculo-vagal afferent pathway and its role in seizure suppression in rats. *BMC Neurosci.* 14:85. doi: 10.1186/1471-2202-14-85

Hofer, M., and Barde, Y. (1988). Brain-derived neurotrophic factor prevents neuronal death in vivo. *Nature* 331, 261–262. doi: 10.1038/331261a0

Ibrahim, G., Sharma, P., Hyslop, A., Guillen, M., Morgan, B., Wong, S., et al. (2017). Presurgical thalamocortical connectivity is associated with response to vagus nerve stimulation in children with intractable epilepsy. *Neuroimage Clin.* 16, 634–642. doi: 10.1016/j.nicl.2017.09.015

Jaseja, H. (2010). EEG-desynchronization as the major mechanism of anti-epileptic action of vagal nerve stimulation in patients with intractable seizures: Clinical neurophysiological evidence. *Med. Hypotheses.* 74, 855–856. doi: 10.1016/j.mehy.2009.11.031

Johnson, R., and Wilson, C. (2018). A review of vagus nerve stimulation as a therapeutic intervention. *J. Inflamm. Res.* 11, 203–213. doi: 10.2147/JIR.S163248

Kaczmarczyk, R., Tejera, D., Simon, B., and Heneka, M. (2017). Microglia modulation through external vagus nerve stimulation in a murine model of Alzheimer's disease. *J. Neurochem.* [Epub ahead of print] doi: 10.1111/jnc.14284.

Kaya, M., Orhan, N., Karabacak, E., Bahceci, M., Arican, N., Ahishali, B., et al. (2013). Vagus nerve stimulation inhibits seizure activity and protects blood-brain barrier integrity in kindled rats with cortical dysplasia. *Life Sci.* 92, 289–297. doi: 10.1016/j.lfs.2013.01.009

Kim, J., Jung, A., Jeong, D., Choi, I., Kim, K., Shin, S., et al. (2016). Selectivity of neuromodulatory projections from the basal forebrain and locus ceruleus to primary sensory cortices. *J. Neurosci.* 36, 5314–5327. doi: 10.1523/JNEUROSCI.4333-15.2016

Lai, J., and David, S. (2021). Short-term effects of vagus nerve stimulation on learning and evoked activity in auditory cortex. *Eneuro* 8, ENEURO.522–ENEURO.520.

Landau, A., Dyve, S., Jakobsen, S., Alstrup, A., Gjedde, A., and Doudet, D. (2015). Acute vagal nerve stimulation lowers alpha2 adrenoceptor availability: Possible mechanism of therapeutic action. *Brain Stimul.* 8, 702–707. doi: 10.1016/j.brs.2015.02.003

Laricchiuta, D., Sciamanna, G., Gimenez, J., Termine, A., Fabrizio, C., Caioli, S., et al. (2021). Optogenetic stimulation of prelimbic pyramidal neurons maintains fear memories and modulates amygdala pyramidal neuron transcriptome. *Int. J. Mol. Sci.* 22:810. doi: 10.3390/ijms22020810

Li, J., Zhang, Q., Li, S., Niu, L., Ma, J., Wen, L., et al. (2020). alpha7nAchR mediates transcutaneous auricular vagus nerve stimulation-induced neuroprotection in a rat model of ischemic stroke by enhancing axonal plasticity. *Neurosci. Lett.* 730:135031. doi: 10.1016/j.neulet.2020.135031

Malbert, C., Genissel, M., Divoux, J., and Henry, C. (2019). Chronic abdominal vagus stimulation increased brain metabolic connectivity, reduced striatal dopamine transporter and increased mid-brain serotonin transporter in obese miniature pigs. *J. Transl. Med.* 17:78. doi: 10.1186/s12967-019-1831-5

Manta, S., El Mansari, M., Debonnel, G., and Blier, P. (2013). Electrophysiological and neurochemical effects of long-term vagus nerve stimulation on the rat monoaminergic systems. *Int. J. Neuropsychopharmacol.* 16, 459–470.

Marrosu, F., Serra, A., Maleci, A., Puligheddu, M., Biggio, G., and Piga, M. (2003). Correlation between GABAA receptor density and vagus nerve stimulation in individuals with drug-resistant partial epilepsy. *Epilepsy Res.* 55, 59–70.

Mehta, N., Haroon, E., Xu, X., Woolwine, B., Li, Z., and Felger, J. (2018). Inflammation negatively correlates with amygdala-ventromedial prefrontal functional connectivity in association with anxiety in patients with depression: Preliminary results. *Brain Behav. Immun.* 73, 725–730.

Mithani, K., Mikhail, M., Morgan, B., Wong, S., Weil, A., Deschenes, S., et al. (2019). Connectomic profiling identifies responders to vagus nerve stimulation. *Ann. Neurol.* 86, 743–753.

Mridha, Z., de Gee, J., Shi, Y., Alkashgari, R., Williams, J., Suminski, A., et al. (2021). Graded recruitment of pupil-linked neuromodulation by parametric stimulation of the vagus nerve. *Nat. Commun.* 12:1539.

Paudel, Y., Shaikh, M., Shah, S., Kumari, Y., and Othman, I. (2018). Role of inflammation in epilepsy and neurobehavioral comorbidities: Implication for therapy. *Eur. J. Pharmacol.* 837, 145–155.

Raedt, R., Clinckers, R., Mollet, L., Vonck, K., El Tahry, R., Wyckhuys, T., et al. (2011). Increased hippocampal noradrenaline is a biomarker for efficacy of vagus nerve stimulation in a limbic seizure model. *J. Neurochem.* 117, 461–469.

Rho, H., Kim, J., and Lee, S. (2018). Function of selective neuromodulatory projections in the mammalian cerebral cortex: Comparison between cholinergic and noradrenergic systems. *Front. Neural Circuits.* 12:47. doi: 10.3389/fncir.2018.00047

Roosevelt, R., Smith, D., Clough, R., Jensen, R., and Browning, R. (2006). Increased extracellular concentrations of norepinephrine in cortex and hippocampus following vagus nerve stimulation in the rat. *Brain Res.* 1119, 124–132.

Rosso, P., Iannitelli, A., Pacitti, F., Quartini, A., Fico, E., Fiore, M., et al. (2020). Vagus nerve stimulation and Neurotrophins: A biological psychiatric perspective. *Neurosci. Biobehav. Rev.* 113, 338–353.

Sedigh-Sarvestani, M., Thuku, G., Sunderam, S., Parkar, A., Weinstein, S., Schiff, S., et al. (2014). Rapid eye movement sleep and hippocampal theta oscillations precede seizure onset in the tetanus toxin model of temporal lobe epilepsy. *J. Neurosci.* 34, 1105–1114.

Sun, L., Perakyla, J., Holm, K., Haapasalo, J., Lehtimaki, K., Ogawa, K., et al. (2017). Vagus nerve stimulation improves working memory performance. *J. Clin. Exp. Neuropsychol.* 39, 954–964.

Vonck, K., De Herdt, V., Bosman, T., Dedeurwaerdere, S., Van Laere, K., and Boon, P. (2008). Thalamic and limbic involvement in the mechanism of action of vagus nerve stimulation, a SPECT study. *Seizure* 17, 699–706.

Wang, Y., Zhan, G., Cai, Z., Jiao, B., Zhao, Y., Li, S., et al. (2021). Vagus nerve stimulation in brain diseases: Therapeutic applications and biological mechanisms. *Neurosci. Biobehav. Rev.* 127, 37–53.

frontiers | Frontiers in Neuroscience

TYPE Original Research
PUBLISHED 14 March 2023
DOI 10.3389/fnins.2023.1108059

OPEN ACCESS

EDITED BY
Rong Wang,
Xi'an University of Science and Technology, China

REVIEWED BY
Yanbing Jia,
Henan University of Science and Technology, China
Binqiang Chen,
Xiamen University, China
Wessam Al-Salman,
University of Southern Queensland, Australia

*CORRESPONDENCE
Yabing Li
✉ liyabing@xupt.edu.cn

SPECIALTY SECTION
This article was submitted to Translational Neuroscience, a section of the journal Frontiers in Neuroscience

RECEIVED 25 November 2022
ACCEPTED 10 February 2023
PUBLISHED 14 March 2023

CITATION
Li Y and Dong X (2023) A RUSBoosted tree method for k-complex detection using tunable Q-factor wavelet transform and multi-domain feature extraction. *Front. Neurosci.* 17:1108059. doi: 10.3389/fnins.2023.1108059

A RUSBoosted tree method for k-complex detection using tunable Q-factor wavelet transform and multi-domain feature extraction

Yabing Li[1,2,3]* and Xinglong Dong[1]

[1]School of Computer Science and Technology, Xi'an University of Posts and Telecommunications, Xi'an, Shaanxi, China, [2]Shaanxi Key Laboratory of Network Data Analysis and Intelligent Processing, Xi'an University of Posts and Telecommunications, Xi'an, Shaanxi, China, [3]Xi'an Key Laboratory of Big Data and Intelligent Computing, Xi'an University of Posts and Telecommunications, Xi'an, Shaanxi, China

Background: K-complex detection traditionally relied on expert clinicians, which is time-consuming and onerous. Various automatic k-complex detection-based machine learning methods are presented. However, these methods always suffered from imbalanced datasets, which impede the subsequent processing steps.

New method: In this study, an efficient method for k-complex detection using electroencephalogram (EEG)-based multi-domain features extraction and selection method coupled with a RUSBoosted tree model is presented. EEG signals are first decomposed using a tunable Q-factor wavelet transform (TQWT). Then, multi-domain features based on TQWT are pulled out from TQWT sub-bands, and a self-adaptive feature set is obtained from a feature selection based on the consistency-based filter for the detection of k-complexes. Finally, the RUSBoosted tree model is used to perform k-complex detection.

Results: Experimental outcomes manifest the efficacy of our proposed scheme in terms of the average performance of recall measure, AUC, and F_{10}-score. The proposed method yields 92.41 ± 7.47%, 95.4 ± 4.32%, and 83.13 ± 8.59% for k-complex detection in Scenario 1 and also achieves similar results in Scenario 2.

Comparison to state-of-the-art methods: The RUSBoosted tree model was compared with three other machine learning classifiers [i.e., linear discriminant analysis (LDA), logistic regression, and linear support vector machine (SVM)]. The performance based on the kappa coefficient, recall measure, and F_{10}-score provided evidence that the proposed model surpassed other algorithms in the detection of the k-complexes, especially for the recall measure.

Conclusion: In summary, the RUSBoosted tree model presents a promising performance in dealing with highly imbalanced data. It can be an effective tool for doctors and neurologists to diagnose and treat sleep disorders.

KEYWORDS

k-complexes detection, electroencephalogram (EEG), multi-domain features extraction, tunable-Q factor wavelet transform, RUSBoosted tree model

1. Introduction

In addition to monitoring sleep disorder disease, sleep analysis hinged on an electroencephalogram (EEG) can also play a critical role in people's mental and physical health (Al-Salman et al., 2021, 2022b). K-complex, as one of the most prominent transient waveforms in sleep stage 2, is usually utilized for sleep research and clinical diagnosis (Al-Salman et al., 2019b; Latreille et al., 2020). Due to this significance, the determination of the k-complex in an epoch is extremely important for sleep experts. K-complex, which was first discovered in Loomis et al. (1938), is a transient waveform of more than ±75 mV for a first negative sharp wave immediately followed by a slower positive component, and it was also reported that the frequency scales focus on 12–14 Hz waves (Richard and Lengellé, 1998). The duration of k-complexes was between 1 and 2 s, and other studies reported that the maximum duration is between 1 and 3 s (Al-salman et al., 2018; Al-Salman et al., 2019b). In general, k-complex detection based on sleep specialist visually scored is regarded as the gold standard. However, it is time-consuming, subjective, and onerous (Lajnef et al., 2015). Thus, more and more researchers focus on developing an automatic k-complex detection method to speed up diagnosis and alleviate the burden of neurologists.

A large number of studies on the automated detection of the k-complexes have been developed, which focus on feature extraction, feature selection, and pattern recognition stages. Some studies presented the literature concerning feature extraction, such as temporal information (Hassan and Bhuiyan, 2016a, 2017a; Al-Salman et al., 2022a), spectral estimation (Herman et al., 2008; Hassan and Subasi, 2016), and chaotic information estimation (Peker, 2016; Al-salman et al., 2018; Al-Salman et al., 2019a; Nawaz et al., 2020). Aykut et al. employed features based on amplitude and duration properties of the k-complex waveform, and the results were evaluated with the ROC analysis which proved up to 91% success in detecting the k-complex (Erdamar et al., 2012). Hassan et al. presented a method of analyzing EEG waveforms based on the spectral features computed from tunable Q-factor wavelet transform (TQWT) sub-bands, and the reported results were significantly better than the existing results (Hassan and Bhuiyan, 2016b). The scheme based on TQWT and bootstrap aggregating for EEG signals was developed, and the results showed that the proposed method is superior in terms of sensitivity, specificity, and accuracy (Hassan et al., 2016). Tokhmpash et al. used the TQWT method to transform EEG signals, and then various features were extracted from the TQWT sub-bands. The empirical results showed the high efficiency of the proposed method in the analyzing of EEG signals (Tokhmpash et al., 2021). The TQWT is also applied to decompose an EEG signal into various sub-bands at different levels; the findings showed that the proposed scheme with estimating the Hjorth parameters preserves efficiency and is appropriate for the automated identification of EEG signals (Geetika et al., 2022). Some time and frequency analysis methods based on variational mode decomposition were utilized to determine the k-complex, and the highest average accuracy was obtained at 92.29% (Yücelbaş et al., 2017). Wessam proposed an efficient method based on fractal dimension to detect k-complexes from EEG signals, and the findings revealed that the proposed method yields better classification results than other existing methods (Al-Salman et al., 2019b).

However, to the best of our knowledge, one of the state-of-the-art linear or non-linear features in the detection of k-complex has not been undertaken yet. Hence, selecting optimal feature sets plays an essential role in the k-complex detection system. In recent years, various methods have been applied successfully in many fields to realize the optimal feature subset selection (Xu et al., 2020; Jainendra et al., 2021). Moreover, pattern recognition techniques also offer a great potential to analyze EEG signals more effectively, which is typically based on supervised or unsupervised approaches (Hassan and Bhuiyan, 2017b; Zhang et al., 2022). Rakesh et al. put forward a fuzzy neural network for k-complex and achieved better results with an accuracy of 87.65% and a sensitivity of 94.04% (Ranjan et al., 2018). Ankit et al. presented a sparse optimization method, and the authors concluded that the proposed method is promising for the practical detection of k-complex (Parekh et al., 2015). Huy et al. proposed a hybrid-synergic machine learning method to detect k-complex, and the results indicate that the performance of the proposed model was at least as good as a human expert (Vu et al., 2012). The ensemble model combining a least square support vector machine, k-means, and naive Bayes is used to identify the detection of the k-complex. The results demonstrate that the proposed approach is efficient in EEG signals (Al-Salman et al., 2019b).

To build a reliable detection model, adequate volumes of k-complexes and non-k-complex datasets are necessary. Unfortunately, the number of epochs obtained from EEG signals with non–k-complexes is greater to a larger degree than that of those with k-complexes. Considering that most classifiers have a strong ability to predict instances with majority volumes while having a weak ability to predict instances belonging to the minority volumes. Hence, the problem to classify imbalanced data effectively is becoming the biggest challenge in k-complex detection.

In this study, to develop and present a procedure of k-complex detection in an epoch, a robust method for the imbalance dataset was proposed based on TQWT coupled with the RUSBoosted tree classifier. The block diagram of the proposed methodology is depicted in Figure 1. Each EEG signal of 30 min was filtered with a fourth-order pass-band Butterworth filter at 0.5–30 Hz to smooth the EEG signal and remove the environment noise caused by muscle activity and eye movement. Then, the EEG signal was segmented into epochs of 0.5 s with an overlapping of 0.4 s, each epoch corresponding to a signal state for k-complex or non–k-complex. The multi-domain features (time, spectral, and chaotic theory) were extracted from each sub-bands of epoch based on TQWT decomposing. To minimize the complexity and reduce the dimensionality of features, the feature selection method based on search-based feature selection consistency (SFS consistency) is employed before classification. For further analysis, the RUSBoosted tree algorithm was implemented to improve the performance in recall for the imbalanced dataset.

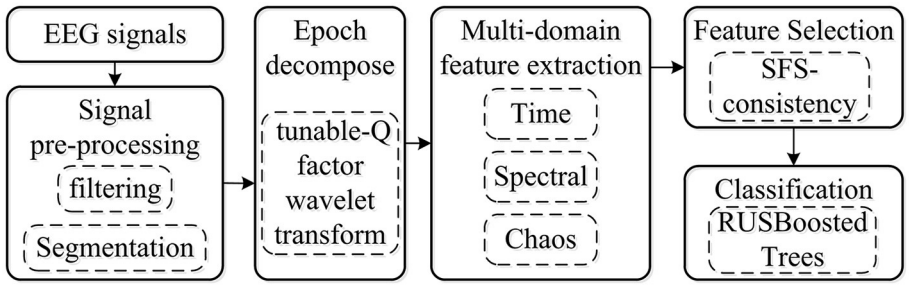

FIGURE 1
Schematic outline of the proposed computer-assisted k-complex detection scheme.

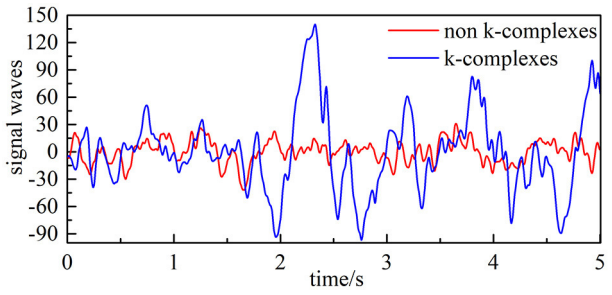

FIGURE 2
Filtered EEG signal (the blue line is EEG signals with k-complex, and the red line represents EEG signals with non–k-complex).

2. Materials and methods

2.1. The EEG recordings

The EEG dataset analyzed in this study was acquired from 10 subjects (aged 28.1 ± 9.95 years, which consists of four men and six women). All were recorded at a sleep laboratory of a Belgium hospital (Brussels, Belgium) at a sampling frequency of 200 Hz, and can be found online at https://zenodo.org/record/2650142. The waveform of k-complex and non–k-complex is presented in Figure 2. The EEG recordings were visually scored by two experts with the specified recommendation (Devuyst et al., 2010). As the duration time of the k-complex is about 0.5–2 s, the EEG signals were divided into segments for k-complex detection using the sliding window technique (Siuly et al., 2011; Al-Salman et al., 2021). Based on previous empirically-based studies, the window size was selected as 0.5 s with an overlap of 0.4 s in this study (Al-Salman et al., 2019c). The multi-domain features based on the analysis of the EEG signals were employed to represent k-complex and non–k-complex from each 0.5 s EEG segment. All the analyses were carried out based on the Cz-A1 channel.

For the DREAMS database, only five of the 10 subjects are annotated by two experts, and the rest are annotated by expert 1. In this study, two different evaluation scenarios were used. The first scenario considers the annotations marked by expert 1 for all subjects, and the second scenario consists of the annotations marked by expert 2 for the five subjects. Table 1 presents the number of k-complex by the experts for Scenarios 1 and 2 in the DREAMS database. It is found that the number of k-complex by the first expert is dramatically greater than the number by the second expert. Therefore, the choice of different scenarios has a direct influence on the results and can be used to verify the performance of the proposed method.

2.2. Tunable Q-factor wavelet transform (TQWT)

The tunable Q-factor wavelet transform, which is proposed by Selesnick (2011), is a flexible discrete wavelet transform (DWT). Similar to the DWT, TQWT employs a two-channel filter bank, which consists of a low-pass filter with parameter α and a high-pass filter with parameter β, to decompose EEG signal into transient components and sustained components using adjustable Q-factors. It can be expressed mathematically as Equations 1, 2. For further analysis, the sustained component's output of the low-pass filter is regarded as the input signal for the next two-channel filter bank. The transient components' output of the high-pass filter for each layer is deemed as the output signal. One simple example of wavelet transform with J level is illustrated in Figure 3.

$$H_L^J = \begin{cases} \prod_{j=0}^{J-1} H_L\left(\omega/\alpha^j\right) & |\omega| \le \alpha^J \pi \\ 0 & \alpha^J \pi \le |\omega| \le \pi \end{cases} \tag{1}$$

$$H_H^J = \begin{cases} H_H\left(\omega/\alpha^{J-1}\right) \prod_{j=0}^{J-2} H_L\left(\omega/\alpha^j\right) & (1-\beta)\,\alpha^{J-1}\pi \le |\omega| \le \alpha^{J-1}\pi \\ 0 & others \end{cases} \tag{2}$$

Here,

$$\begin{gathered} H_L = \theta\left(\frac{\omega+(\beta-1)\pi}{\alpha+\beta-1}\right) \\ H_H = \theta\left(\frac{\alpha\pi-\omega}{\alpha+\beta-1}\right) \\ \theta(t) = 0.5\,(1+\cos(t))\,\sqrt{2-\cos(t)} \end{gathered} \tag{3}$$

Q-factor: This parameter determines the width of the band-pass filter. TQWT decomposition achieves flexibility by tuning and adapting this parameter of the wavelet transform. The higher the Q-factor is, the more effective the extraction of the sustained

TABLE 1 Number of k-complex in each EEG recording.

Subject	Scenario 1		Scenario 2	
	Number of segments with k-complex	Number of segments without k-complex	Number of segments with k-complex	Number of segments without k-complex
ID1	263	17,733	95	17,901
ID2	299	17,697	41	17,955
ID3	104	17,892	14	17,982
ID4	661	17,335	60	17,936
ID5	285	17,711	98	17,898
ID6	204	17,792	/	/
ID7	87	17,909	/	/
ID8	36	17,960	/	/
ID9	26	17,970	/	/
ID10	117	17,879	/	/

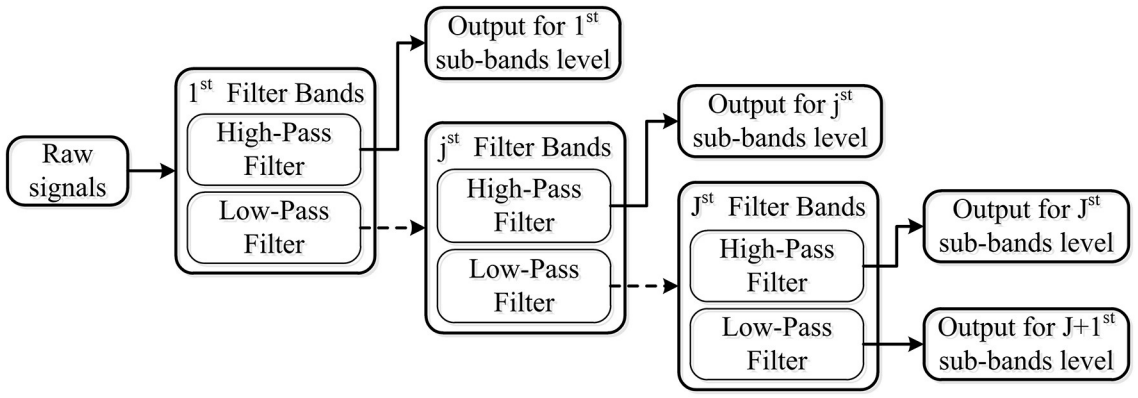

FIGURE 3
Wavelet transform with J level using a two-channel filter bank, which consists of the low-pass filter and high-pass filter.

components. Meanwhile, the decomposing waveform based on a lower Q-factor is suitable for extracting the features of the transient component.

Number of decomposition levels (J): If the number of filter bands is denoted by J, an input signal will be decomposed into J+1 sub-bands. Among these bands, J sub-bands were obtained from the high-pass filter of each level filter band, and one came from the low-pass filter of the final level filter band. With the increase of the decomposition level, the time domain waveform becomes wider, and the features increase dramatically.

Taking into consideration various ranges of motivation, the TQWT is used in the proposed scheme (Hassan and Bhuiyan, 2016b). First of all, considering that k-complex waves are characterized by the appearance of multifarious rhythms, TQWT can improve localization in the frequency domain by varying the Q-factor. Hence, this decomposition method is suitable for spectral analysis. Second, the filters employed in TQWT are more computationally efficient in the frequency domain (Selesnick, 2011). Third, EEG is a non-stationary signal and its chaos properties alter between k-complex and non–k-complex. TQWT decomposition can also give the wave in the time domain; hence, it has emerged as a powerful technique in both time features and chaos features for EEG analysis (Fraiwan et al., 2010). These superiorities verified that the TQWT decomposition is an effective tool for the analysis of EEG and hence it is employed in the proposed scheme.

2.3. Multi-domain feature extraction from TQWT sub-bands

To derive salient features from the raw EEG data that can effectively reflect the epochs to the respective k-complex is the main objective of the feature extraction stage of the EEG-based k-complex detection system. Hence, a multi-domain method, based on time domain estimation, spectral estimation, and chaotic analysis, was employed to extract the representative features from each 5 s EEG epoch. A total of 25 hybrid features were extracted from each sub-band.

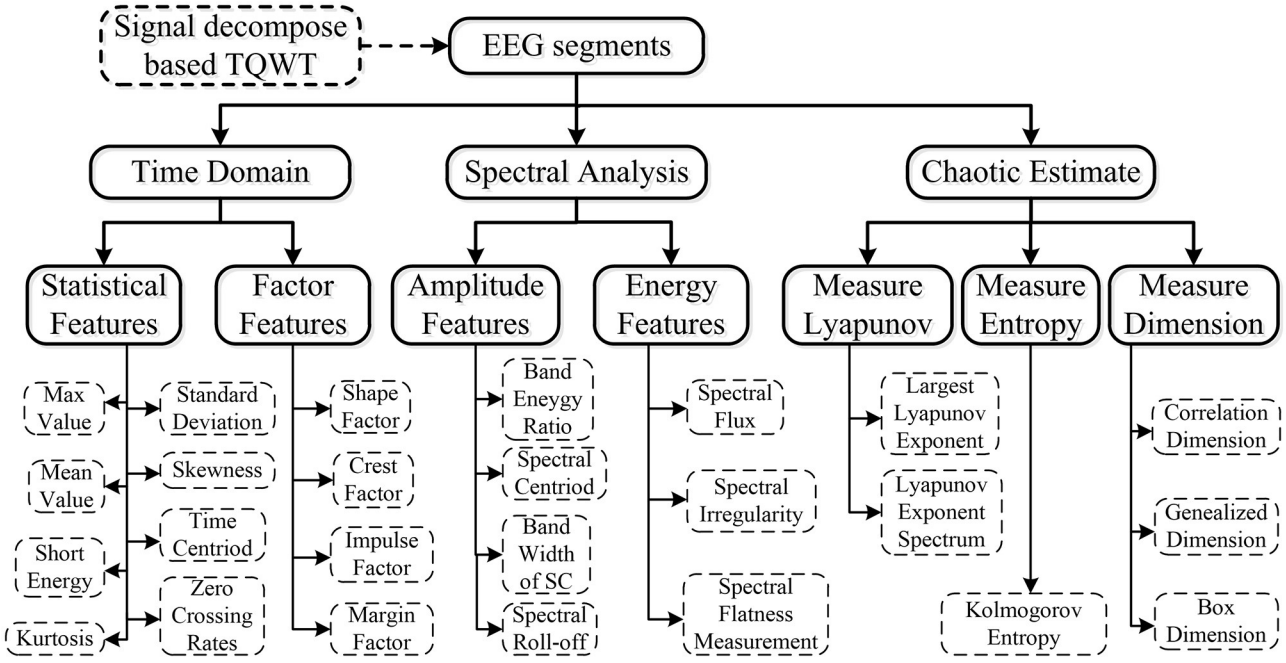

FIGURE 4
Multi-domain features extraction framework.

The extraction feature methods based on the time domain have been proven to be an efficient method for analyzing the characteristics of EEG signals (Vidaurre et al., 2009). Though it is widely used in speech and audio signal classification (Chu et al., 2009), spectral features have been used for EEG signals (Hassan and Bhuiyan, 2016b). These features are typically calculated by applying a fast Fourier transform (FFT) to short-time window segments of EEG signals followed by further processing. Considering that the property of EEG signals is somewhat chaotic, in addition to the traditional features of the EEG signal, the chaotic features based on non-linear dynamical analysis are also highly recommended to investigate the dynamic characteristics of EEG (Li et al., 2017; Nawaz et al., 2020). In the current study, 12 time domain features, seven spectral features, and six chaotic features are extracted for further analysis, as shown in Figure 4.

We have computed the feature vector for each EEG sub-bands based on TQWT decomposition. As the decomposed EEG signals with J+1 sub-bands, the feature vector of J+1 sub-bands on each epoch is computed to construct a 25*(J+1)-dimensional feature vector.

2.4. Search-based feature selection using consistency measures

Considering that reducing the dimensionality of feature sets may be improving the performance in reducing costs and enhancing the ability of comprehensibility, another effective step in the detection system for k-complex is to find optimal feature subsets. Selection features based on search-based feature selection (SFS) analyses were used in this study to research and select the important features. The following context briefly illustrates the selection features (Dash and Liu, 2003; Hernández-Pereira et al., 2016).

The SFS method based on the consistency filter, as one of the most effective methods, traverses all the candidate subsets to find the best one using the evaluation measures based on the independence of an inductive algorithm (shown in Figure 5). The evaluation measure evaluates the attributes of selected features according to the inconsistency rate (IR). If the IR for current selection features is smaller than the pre-selection features, current selection features are deemed as the selected features. Although SFS has the disadvantage in time-consuming, it does not need the stopping criterion or a pre-specified threshold.

2.5. RUSBoosted tree model for the k-complex detection

The distribution across k-complex or not is highly skewed: non–k-complexes have more epochs than those k-complexes. Therefore, the detection problem for the imbalanced dataset is a major challenge for k-complex detection. The RUSBoosted tree model, as an efficient way to overcome this problem, can improve the prediction performance by reducing bias between positive and negative samples at the expense of a slight decrease in the large group sets (Khoshnevis and Sankar, 2020; Jain and Ganesan, 2021; Noor et al., 2022).

The present research fused a random under-sampling (RUS) technique and adaptive boosting (AdaBoost) algorithm with a decision tree as the RUSBoosted tree model, as shown in Figure 6. First of all, to obtain the balanced distribution, the under-sampling

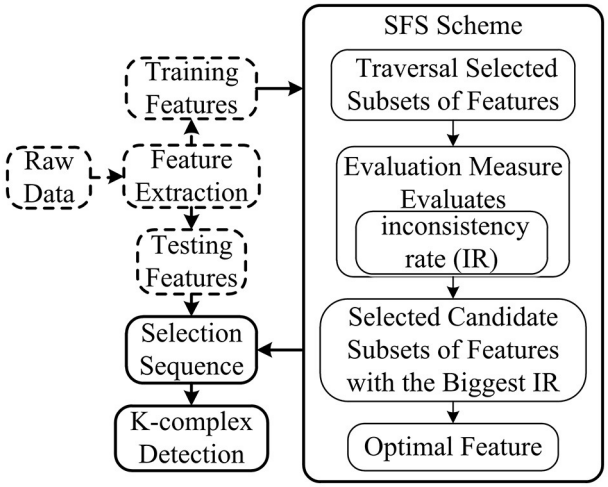

FIGURE 5
Scheme of SFS. The dimension of feature subsets is reduced based on features selected by SFS, and the selected features are used for further analysis.

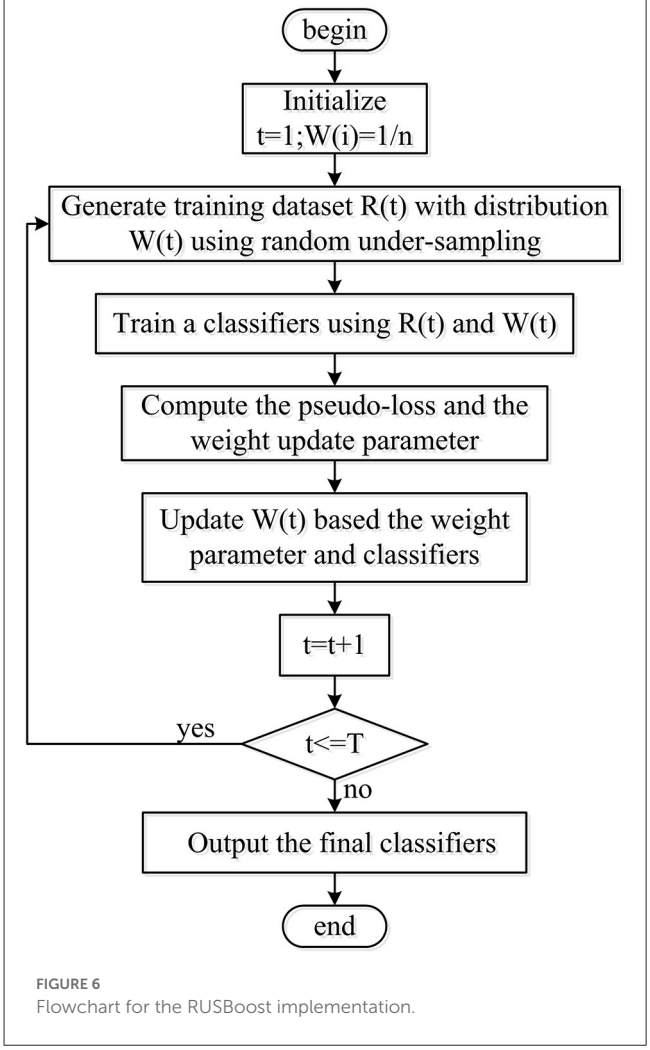

FIGURE 6
Flowchart for the RUSBoost implementation.

method was implemented to deal with the minority and majority class size for the imbalanced training dataset. Second, considering the AdaBoost algorithm's ability to reduce bias and variance mistakes, it is employed to tackle problems involving imbalanced datasets. Hence, the RUS technique along with AdaBoost is utilized by combining an ensemble of decision trees as a classifier for further analysis.

In this study, the parameters (i.e., the number of classifiers was selected as 30 for the model, with a maximum number of splits of 20 and a learning rate of 0.1) were melded into the RUSBoosted tree for the detection of k-complex.

2.6. Performance evaluation

First, statistical hypothesis testing is performed to validate the relevance and suitability of features according to discriminatory capability are statistically significant or not. If the features are not statistically significant, they have to be ignored for negative influence on performance. To estimate the significant level of k-complexes and non–k-complexes, we perform a one-way analysis of variance (ANOVA). The difference is considered to be statistically significant if the p-value is <0.05 at a 95% confidence level.

Second, to evaluate the detection ability of the proposed method, some metrics based on the confusion matrix (shown in Table 2) were used. In Table 2, TP describes the situation that both the actual k-complexes and predicted states are yes. FN represent the situation that predicted k-complexes as no while actual k-complexes as yes. FP means the actual state is not k-complexes, which is adverse to the predicted label based on an algorithm. TN means the situation that both the actual k-complexes and predicted states are no.

To evaluate the performance of the detection algorithm, Cohen's kappa coefficient, recall, and F-measure are computed. In addition to these metrics, the area under the ROC curve (AUC) was also used to estimate the performance of a classifier. Further details about the metrics are provided in the following paragraphs.

TABLE 2 Confusion matrix of the k-complex detection problem.

		Predicted k-complexes	
		Yes	No
Actual k-complexes	Yes	True positive (TP)	False negative (FN)
	No	False positive (FP)	True negative (TN)

The kappa coefficient, calculated based confusion matrix, as a measurement for consistency tests, can also be used to measure classification accuracy. It is defined as Equation 4 as follows:

$$kappa = \frac{\frac{TP+TN}{TP+FN+FP+TN} - P_e}{1 - P_e} \quad (4)$$

Here, P_e is obtained as follows:

$$P_e = \frac{\sum_i sum(M(i,:)) \times sum(M(:,i))}{(\sum M)^2}; M \text{ is confusion matrix} \quad (5)$$

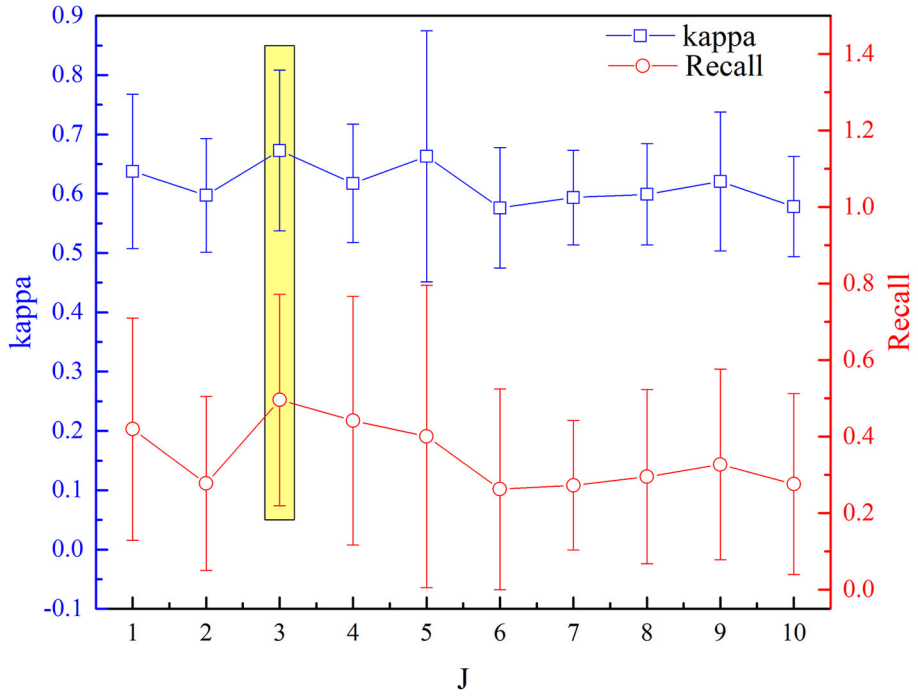

FIGURE 7
Variation of kappa and recall value with J for the detection of k-complexes.

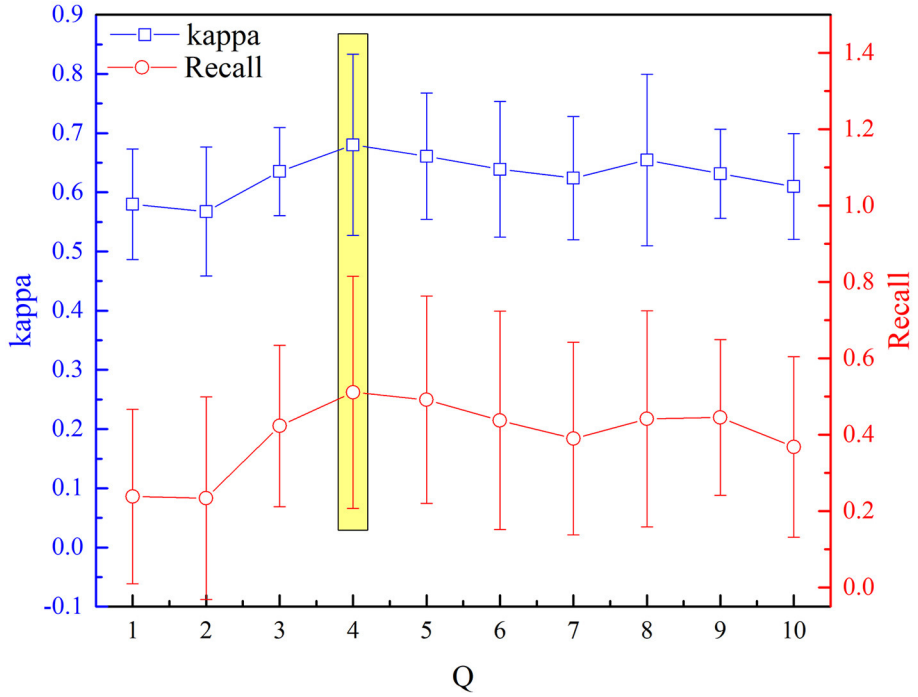

FIGURE 8
Variation of kappa and recall value with Q for the detection of k-complexes.

Recall measure, which is also called sensitivity measurement, reflects the proportion of the actual positive prediction. It can be expressed mathematically from Equation 6 as follows:

$$\text{Recall} = \frac{TP}{TP + FN} \tag{6}$$

TABLE 3 The *P*-value of the proposed features computed from various TQWT sub-bands indicates the difference in features between k-complex and non–k-complex.

Features		Sub-band 1	Sub-band 2	Sub-band 3	Sub-band 4
Time features	Maximum	0.023802	0.000803	**NaN**	**0.87868**
	Mean	**0.291217**	**0.702964**	**0.308926**	**0.458965**
	Standard deviation	0.010885	0.007884	**0.546545**	**0.861432**
	Skewness	0.008726	0.000836	**NaN**	**0.881254**
	Kurtosis	**0.05654**	**0.72175**	0.048551	**0.731241**
	Shape factor	0.001473	0.008128	**0.548529**	**0.816636**
	Crest factor	0.00672	0.000878	**NaN**	**0.916789**
	Impulse factor	0.037651	**0.092862**	0.01697	**0.206266**
	Margin factor	0.000359	0.008451	0.031723	**0.683969**
	Short energy	9.47E-17	2.54E-16	**0.279627**	0.01927
	Zero-crossing rate	1.68E-13	4.13E-27	2.52E-10	9.76E-19
	Time centroid	6.49E-22	1.36E-08	5.27E-05	**0.951018**
Spectral features	Band energy ratio	**0.956247**	0.007944	**0.889128**	**0.289102**
	Spectral flux	0.004931	**0.733733**	**0.797405**	**0.780187**
	Spectral centroid	0.008618	**6.77E-01**	**0.793363**	0.002373
	Band width of SC	**0.709624**	**0.946816**	**0.363672**	0.023152
	Spectral flatness measurement	**0.561545**	**0.701588**	**0.077005**	**0.263733**
	Spectral roll-off	**0.594201**	8.66E-05	7.65E-05	2.65E-11
	Spectral irregularity	0.01874	**0.127941**	0.000109	5.51E-07
Chaotic features	Correlation dimension	**0.087149**	**6.52E-01**	**0.395171**	0.000795
	Kolmogorov entropy	**0.346332**	**0.309228**	**0.309228**	**0.865964**
	Largest Lyapunov exponent	**7.69E-01**	0.007019	0.031744	**0.890812**
	Lyapunov exponent spectrum	**0.318448**	**0.318448**	**0.813963**	**0.988225**
	Box dimension	**0.803216**	1.88E-09	0.00112	2.02E-17
	Generalized dimension	1.51E-09	2.39E-13	7.73E-24	7.73E-24

It is noted that the features with not statistically significant are highlighted in bold.

F-measure is the top priority measurement in analyzing the overlapping between the two sets. It can be defined by weighted recall and precision, and β reflects the relative importance.

$$F_\beta = \frac{(1+\beta^2) \times Precision \times Recall}{(\beta^2 \times Precision) + Recall} \quad (7)$$

If the parameter of $\beta > 1$, it means that recall has more influence on F-measure. $0 < \beta < 1$ reflects that precision has a broader effect on F-measure, compared with recall. $\beta = 1$ represents the measurement degenerates into standard F-measure. It is noted that $\beta = 10$ is selected.

To further illustrate the effectiveness of features selected using a feature selection-based consistency-based filter, the separability analysis using Fisher criteria was applied, which is obtained from Equation 9 as follows:

$$J_F = \mathrm{tr}(S_w^{-1} S_m) \quad (8)$$

Here, S_w and S_m represent the within-class and between-class scatter matrix, respectively. tr(S) means the trace of square matrix S.

To evaluate the performance of the proposed method, the 5-fold cross-validation method is utilized. The k-complex segments and non–k-complex segments are divided into five groups, respectively. For each time, the training dataset consists of four k-complex groups and four non–k-complex, while the resting groups are deemed as testing groups. All groups are tested in turn. In this study, the overall performance is computed over the five iterations.

3. Results and discussion

3.1. Parameter selection for TQWT

The selected optimal parameters to decompose the EEG epoch are J and Q. The detection performance (kappa measures and recall value) based on the aforementioned procedure of feature extraction

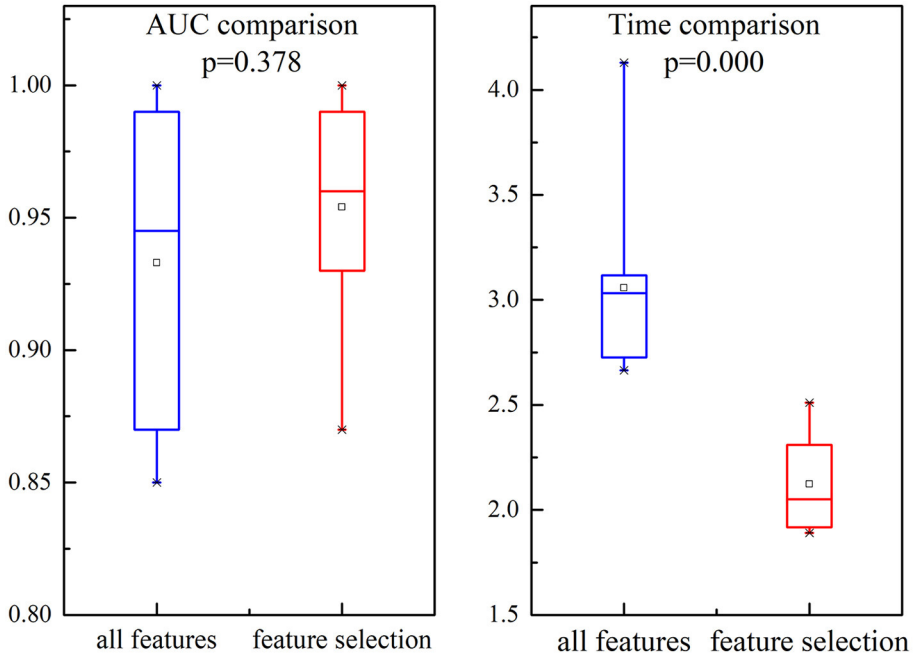

FIGURE 9
Illustration of the comparison for AUC and time in all features and selected features. Each box represents the 25–75th percentiles, the central line is the median value, and the tiny vertical lines extend to the most extreme data not considered outliers, which are plotted individually.

and selection has been analyzed sequentially for incremental values of Q range from 1 to 10 with an increment of one. Figures 7, 8 depict the influence of parameters on detection performance for the k-complex. It is observed from Figure 7 that the optimal parameter of J is 3, in which the best kappa measures and recall value are achieved. The optimal value for J is determined in the same way. From our experimental analyses, as shown in Figure 8, it has been observed that the best matrices are achieved for Q = 4.

3.2. Quality evaluation for feature extraction and selection

In this section, the results of all the features computed from various TQWT sub-bands were present in terms of significance, as shown in Table 3. The test is performed at a 95% confidence level. It can be observed from Table 3 that the features highlighted in bold are not significant ($p > 0.05$), and a difference is statistically significant if $p \leq 0.05$. The results show that the performance of time domain features to classify k-complex was significantly better than other features for sub-bands 1 and 2. In sub-band 3, spectral features significantly outperformed time and chaotic features. However, the statistical performance of time features in sub-band 4 was the worst in all three kinds of features. Based on these results, we can conclude that not all of the sub-bands features achieved good discriminatory capability for k-complex detection. Hence, it is necessary to select some of these features to improve the k-complex detection performance and decrease time consumption.

We investigate the AUC and time performance for two different feature sets, namely all features and selected features. The comparisons of the performance are shown in Figure 9. It is evident that the AUC based on selection features is slightly incremented than all feature sets. Compared with the performance of all feature sets, there is a dramatic decrement in time comparison for selected feature sets.

In this study, we also investigate the separability of the two different feature sets using J_F. The larger the value of J_F is, the more separable the features are. Figure 10 presents the value of J_F and compares different feature sets (all features or selected features are used). It is evident that the J_F based on selected features is higher, which confirmed that the selected features can characterize the k-complex effectively. It can be confirmed by the inferences drawn from Figure 9. According to these results, the feature selection method was more effective, particularly in AUC, time comparison, and separability estimation. Furthermore, the experimental outcomes presented in Figures 9, 10 confirm that the feature selection method is more effective.

3.3. Performance for various classification models

For this research, we have verified several classification methods such as linear discriminant analysis (LDA), logistic regression, linear support vector machine (linear SVM), and RUSBoosted tree. Figure 11A indicates the receiver operating characteristic (ROC) curve for different classification methods. According to the results, the line in the upper left represents better performance in the detection of k-complexes. The area under the curve (AUC) of 1 indicates a perfect classification performance. Although this

comparison is for the data set of subject 1, it has to be noticed that the k-complex classification can be improved using RUSBoosted tree methods. Figure 11B demonstrates a box plot of the area under the curve (AUC) for different pattern recognition methods. The AUC was obtained as 0.931 ± 0.085, 0.814 ± 0.166, 0.925 ± 0.127, and 0.954 ± 0.043 for LDA, logistic regression, linear SVM, and RUSBoosted tree, respectively. According to these results, we conclude that the AUC of the RUSBoosted tree is significantly better than others.

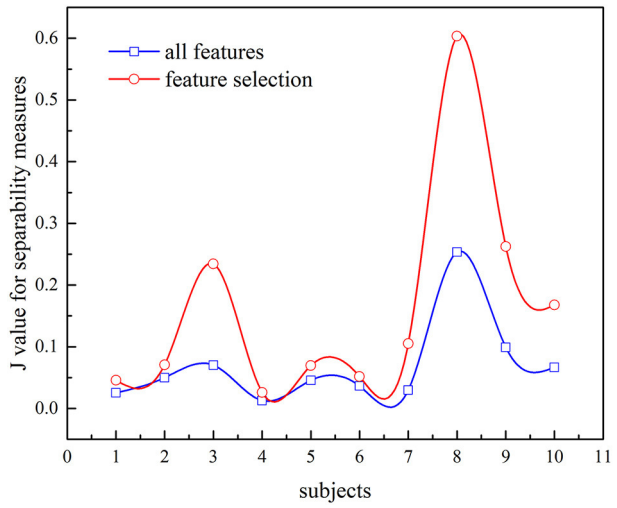

FIGURE 10
Comparison of J_F values between all features and feature selection for k-complex detection.

The purpose of this investigation is to establish the suitability of the RUSBoosted tree algorithm for imbalanced dataset problems. The performance of the RUSBoosted tree algorithm is investigated for several traditionally state-of-the-art classifiers including LDA, logistic regression, and linear SVM. For further evaluation, Figure 12 reports the performance of some of these classifiers for the proposed scheme. The kappa coefficient, recall measure, AUC, and F_{10}-score were used to evaluate the effectiveness of the proposed scheme. The proposed method achieved an average performance of recall measure, AUC, and F_{10}-score of 92.34 ± 7.06%, 95.4 ± 4.32%, and 83.59 ± 8.23%, respectively. Depending on the results, the performance based on the kappa coefficient, recall measure, and F_{10}-score provided evidence that the RUSBoosted tree surpassed other algorithms in the detection of the k-complexes. However, the performances based on the kappa coefficient using the RUSBoosted tree (54.22 ± 4.04%) are slightly worse than linear discriminant analysis (59.26 ± 14.67%). In summary, the prediction results confirmed a superiority value for different metrics and a balanced classification performance. It also indicated that the prediction algorithm based on the RUSBoosted tree model was tending to outperform than the traditional classifiers, especially for the minority classes.

3.4. Performance comparison of the proposed method based on the ratio of segment number

To verify the performance of the proposed methods, the execution time, recall, and F_{10} scores are used. Figure 13 presents the execution time of the RUSBoosted tree model and the others classifiers. For further analysis, we assume that the number of the

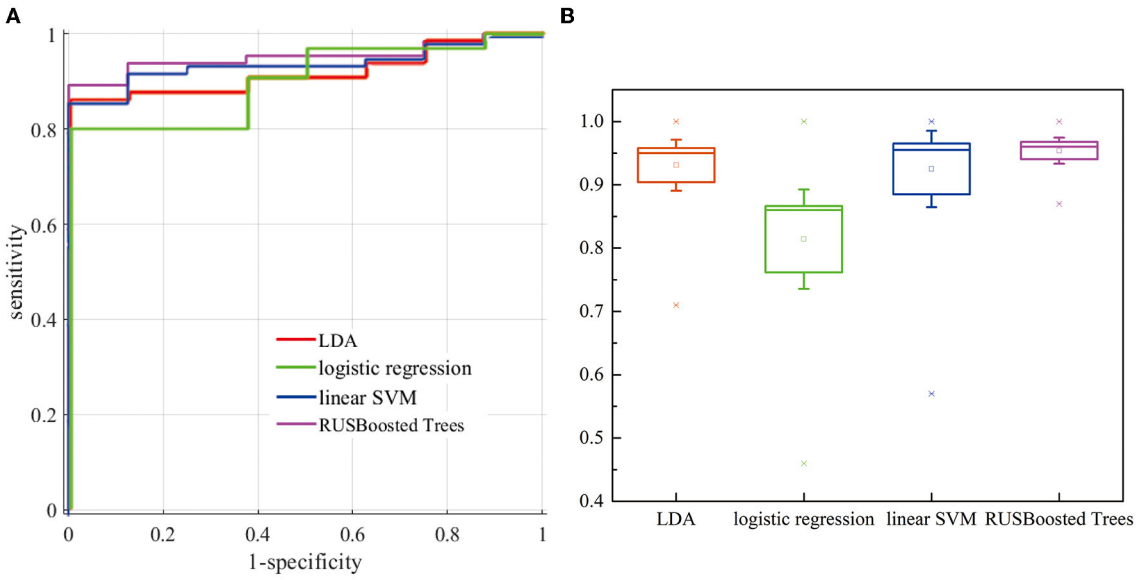

FIGURE 11
(A) Evaluation of the ROC curves (the plot of sensitivity vs. (1-specificity) for distinguishing k-complexes) for subjects 1. **(B)** Comparison of AUC for different methods.

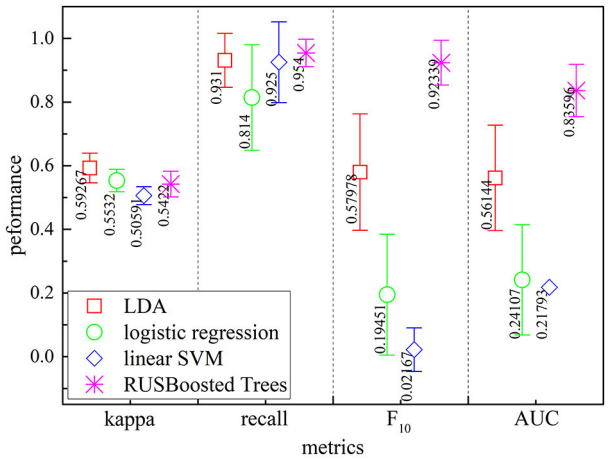

FIGURE 12
Performance comparison of the proposed method with different machine learning algorithms for the detection of k-complexes [LDA (red diamond), logistic regression (green circle), linear SVM (blue diamond), and RUSBoosted tree (pink star)]. Error bars correspond to the standard error of the mean.

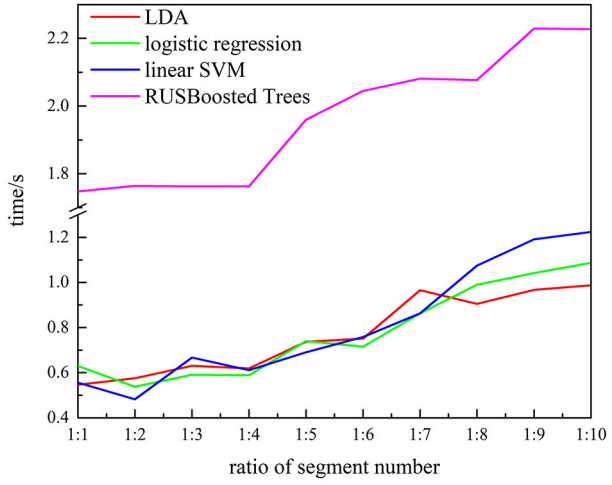

FIGURE 13
Relationship between the execution time and ratio of segment numbers for subject 1 (the number of k-complex is fixed as 263, and the segment number of non–k-complex is multiple of the number of k-complex from 1 to 10).

segments of the k-complex is fixed at 263, and the number of the segments of the non–k-complex is outnumbering k-complex (the number of segments of the non–k-complex increased from 1 to 10 times compared to the number of the segments of k-complex, and the number of segments was selected randomly from the database). The time to train the classification model was deemed as execution time. According to Figure 13, the slowest execution time was recorded with the RUSBoosted tree model compared with other classifiers. Along with the increasing number of segments, the execution time is also increased dramatically. In addition, the performance was also compared with the other three classifiers based on recall and F_{10} scores. Figure 14 achieves the results that the proposed method is slightly increased along with the increase in the ratio of the number of the segments between non–k-complex and k-complex. While the other classifiers' performance significantly decreased. High F_{10} values mean that the proposed method is inclined to small samples. From these results, we can get the conclusion that the proposed method was suitable to deal with the imbalanced dataset.

3.5. Comparison with existing methods based on Scenario 1

According to previously reported methods, some of the automatic k-complex detection methods have been estimated using the same database as discussed in Section 2.1. In Table 4, the proposed method is compared with existing methods. Krohne et al. (2014) detected k-complexes using wavelet transformation combined with feature thresholds with the same database. In this study, pseudo-k-complexes were identified from each EEG segment and then the feature threshold method was used to reject false positives. A mean recall of 74% was achieved. Parekh et al. (2015) reported their results of the k-complex detection using a fast non-linear optimization algorithm, an average recall and kappa of 61% and 0.54 were achieved, respectively. Another study was made by Ranjan et al. (2018), in which a fuzzy algorithm combined with an artificial neural network was used to detect k-complex, they reported an average accuracy and specificity of 87.65 and 76.2%, respectively. A fractal dimension coupled with an undirected graph features technique was utilized by Al-Salman et al. (2019b) to detect k-complexes. The accuracy and specificity of 97 and 94.7% were reported, and the performance was highest than others. Oliveira et al. (2020) focused on designing a multitaper-based k-complex detection method in EEG signals and achieved a recall of 85.1%. The proposed method outperforms the other methods in almost all performance metrics (accuracy and specificity), except the method of fractal dimension coupled with undirected graph features (Al-Salman et al., 2019b). In terms of recall and kappa, the proposed method achieves the highest performance. These results demonstrated that the proposed method achieved a better performance in terms of detection performance.

3.6. Comparison based on different scenarios

As already mentioned, some of the automatic k-complex detection methods have been proposed and compared with the proposed method with the regard to the scenarios previously discussed, as shown in Table 5. In Scenario 1, the proposed methods achieved a mean accuracy of 92.19 $\pm$ 3.9% and a mean recall of 92.41 $\pm$ 7.47%. The proposed method achieved a dramatically better recall than others (Devuyst et al., 2010; Yazdani et al., 2018; Oliveira et al., 2020), but slightly worse accuracy. A higher recall value indicates that the proposed method is able to detect the most of small samples (true k-complex marked by an expert).

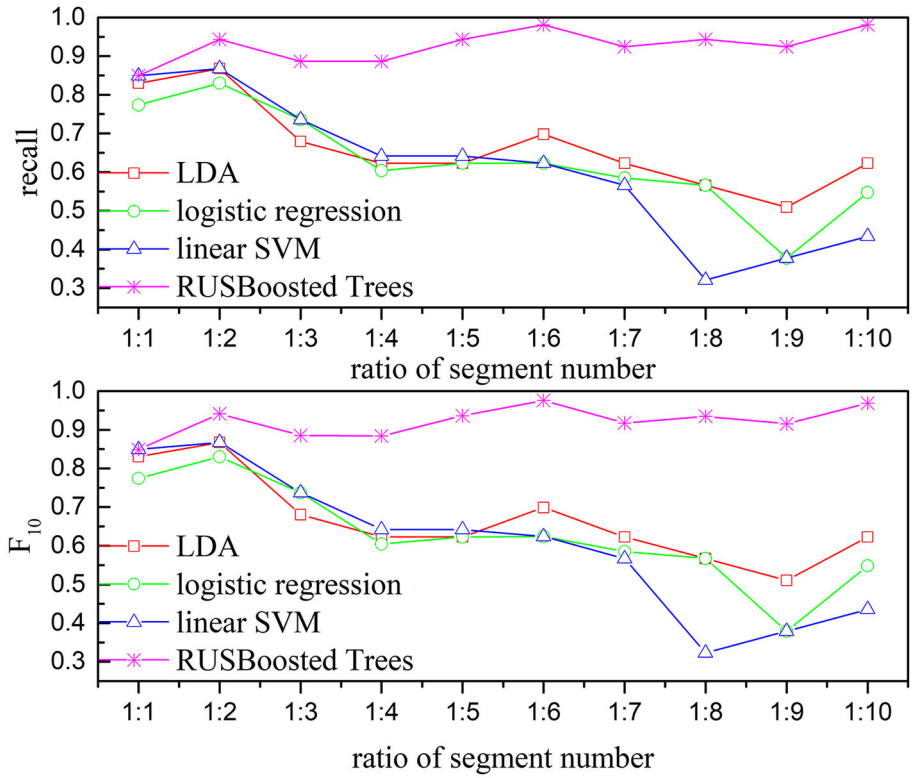

FIGURE 14
Relationship between the performance-based kappa and F_{10} and the ratio of segments number for subject 1 (the number of k-complex is fixed as 263, and the segment number of non–k-complex is multiple of the number of k-complex from 1 to 10).

TABLE 4 Performance comparisons between the proposed method and other different detection methods with the same datasets based on Scenario 1.

Methods	Accuracy (%)	Recall (%)	Specificity (%)	Kappa (%)
Wavelet transformation (Krohne et al., 2014)	/	74	/	/
Spare optimization (Parekh et al., 2015)	/	61	/	54
Fuzzy neural network (Ranjan et al., 2018)	87.65	/	76.2	/
Short-term event extraction algorithm (Yazdani et al., 2018)	/	67.79	/	/
Fractal dimension coupled with undirected graph features (Al-Salman et al., 2019b)	**97**	/	**94.7**	/
Multitaper-based method (Oliveira et al., 2020)	/	85.1	/	/
Proposed methods	92.18	**92.41**	92.41	**54.54**

The bold value indicates the best performances are highlighted compared with other methods.

TABLE 5 Performance comparisons between the proposed method and other existing methods for Scenarios 1 and 2.

Methods	Scenario 1		Scenario 2	
	Accuracy (%)	Recall (%)	Accuracy (%)	Recall (%)
Devuyst et al. (2010)	98.59	61.72	99.29	60.94
Yazdani et al. (2018)	**98.78**	67.79	**99.3**	73.02
Oliveira et al. (2020)	/	85.1 ± 5.05	/	77.2 ± 15.5
Proposed methods	92.19 ± 3.9	**92.41 ± 7.47**	87.95 ± 6.16	**80.85 ± 11.33**

The bold value indicates the best performances are highlighted compared with other methods.

In Scenario 2, compared to previous studies, the trade-off accuracy and recall obtained from the proposed method are similar to those obtained in Scenario 1. Compared to Scenario 1, the mean accuracy and recall are smaller, i.e., 87.95 ± 6.16% and 80.85

± 11.33%, respectively. The reason why the recall and accuracy decrease for the scenario may be that the second expert marked few labels as k-complex compared to expert 1. It is consistent with Table 1. It is denoted that the proposed method was effective to detect the k-complex.

4. Conclusion

This study developed a k-complex detection scheme, consisting of TQWT, multi-domain features, feature selection, and RUSBoosted tree algorithm to overcome the shortages of the existing classification–misclassification of classifier training from the imbalanced data. According to the results, the highest recall value was achieved for the proposed scheme. The results denoted that the methods could be worth utilizing in the automatic identify the k-complex for sleep specialists. It has been evidenced that the proposed scheme is comparable to or better than the state-of-the-art classifiers. The results also show that the ability of the RUSBoosted tree model to deal with the imbalanced classification problems compared with the state-of-art methods is quite well. In general, according to the experimental outcomes, we can conclude that the proposed scheme can relieve physicians of the burden of visually inspecting a large volume of EEG data.

However, the study suffers from several drawbacks. First, it is necessary for researchers to locate the locations of the k-complex in the related epochs. Second, the proposed scheme relied on a single channel to detect k-complex. While as one of the important features of brain activity, the interaction between brain regions is not fully utilized.

Data availability statement

Publicly available datasets were analyzed in this study. This data can be found at: https://zenodo.org/record/2650142.

Ethics statement

Ethical review and approval was not required for the study on human participants in accordance with the local legislation and institutional requirements. Written informed consent for participation was not required for this study in accordance with the national legislation and the institutional requirements. Written informed consent was not obtained from the individual(s) for the publication of any potentially identifiable images or data included in this article.

Author contributions

YL contributed to the conception and design of the study. YL and XD performed the statistical analysis and wrote the first draft of the manuscript. Both authors contributed to the manuscript revision and read and approved the submitted version.

Funding

Funding was provided by the Natural Science Basic Research Program of Shaanxi Program (2022JQ-598), the Scientific Research Plan Projects of Shaanxi Education Department (20JK0917), and the Doctoral Scientific Research Starting Foundation of Xi'an University of Posts and Telecommunications (315020018). This study also obtained support from Shaanxi's Key Disciplines of Special Funds to Finance Projects.

Acknowledgments

The authors would like to express our gratitude to the reviewers and the editor for their valuable and insightful suggestions.

Conflict of interest

The authors declare that the research was conducted in the absence of any commercial or financial relationships that could be construed as a potential conflict of interest.

Publisher's note

References

Al-Salman, W., Li, Y., Oudah, A. Y., and Almaged, S. (2022a). Sleep stage classification in EEG signals using the clustering approach based probability distribution features coupled with classification algorithms. *Neurosci. Res.* 2022, S0168–0102. doi: 10.1016/j.neures.2022.09.009

Al-Salman, W., Li, Y., and Wen, P. (2019a). Detecting sleep spindles in EEGs using wavelet fourier analysis and statistical features. *Biomed. Sign. Process. Contr.* 48, 80–92. doi: 10.1016/j.bspc.2018.10.004

Al-Salman, W., Li, Y., and Wen, P. (2019b). Detection of EEG K-complexes using fractal dimension of time frequency images technique coupled with undirected graph features. *Front. Neuroinformat.* 13, 1–19. doi: 10.3389/fninf.2019.00045

Al-Salman, W., Li, Y., and Wen, P. (2019c). K-complexes detection in EEG signals using fractal and frequency features coupled with an ensemble classification model. *Neuroscience* 422, 119–133. doi: 10.1016/j.neuroscience.2019.10.034

Al-Salman, W., Li, Y., and Wen, P. (2021). Detection of k-complexes in EEG signals using a multi-domain feature extraction coupled with a least square support vector machine classifier. *Neurosci. Res.* 172, 26–40. doi: 10.1016/j.neures.2021.03.012

Al-salman, W., Li, Y., Wen, P., and Diykh, M. (2018). An efficient approach for EEG sleep spindles detection based on fractal dimension coupled with time frequency image. *Biomed. Sign. Process. Contr.* 41, 210–221. doi: 10.1016/j.bspc.2017.11.019

Al-Salman, W., Li, Y., Wen, P., Miften, F. S., Oudah, A. Y., and AlGhayab, H. R. (2022b). Extracting epileptic features in EEGs using a dual-tree complex wavelet transform coupled with a classification algorithm. *Brain Res.* 1779, 147777. doi: 10.1016/j.brainres.2022.147777

Chu, S., Narayanan, S., and Kuo, C.-C. J. (2009). Environmental sound recognition with time–frequency audio features. *IEEE Trans. Audio Speech Lang. Process.* 17, 1142–1158. doi: 10.1109/TASL.2009.2017438

Dash, M., and Liu, H. (2003). Consistency-based search in feature selection. *Artif. Intell.* 151, 155–176. doi: 10.1016/S0004-3702(03)00079-1

Devuyst, S., Dutoit, T., Stenuit, P., and Kerkhofs, M. (2010). "Automatic K-complexes detection in sleep EEG recordings using likelihood thresholds," in *Annual International Conference of the IEEE Engineering in Medicine and Biology* (Buenos Aires: IEEE), 2626447.

Erdamar, A., Duman, F., and Yetkin, S. (2012). A wavelet and teager energy operator based method for automatic detection of K-complex in sleep EEG. *Expert Syst. Appl.* 39, 1284–1290. doi: 10.1016/j.eswa.2011.07.138

Fraiwan, L., Lweesy, K., Khasawneh, N., Fraiwan, M., Wenz, H., and Dickhaus, H. (2010). Classification of sleep stages using multi-wavelet time frequency entropy and LDA. *Methods Inform. Med.* 49, 230–237. doi: 10.3414/ME09-01-0054

Geetika, K., Pramod, G., Raj, S. R., and Bilas, P. R. (2022). EEG signal based seizure detection focused on Hjorth parameters from tunable-Q wavelet sub-bands. *Biomed. Sign. Process. Contr.* 76, 103645. doi: 10.1016/j.bspc.2022.103645

Hassan, A. R., and Bhuiyan, M. I. H. (2016a). Automatic sleep scoring using statistical features in the EMD domain and ensemble methods. *Biocybernet. Biomed. Eng.* 36, 248–255. doi: 10.1016/j.bbe.2015.11.001

Hassan, A. R., and Bhuiyan, M. I. H. (2016b). A decision support system for automatic sleep staging from EEG signals using tunable Q-factor wavelet transform and spectral features. *J. Neurosci. Methods* 271, 107–118. doi: 10.1016/j.jneumeth.2016.07.012

Hassan, A. R., and Bhuiyan, M. I. H. (2017a). Automated identification of sleep states from EEG signals by means of ensemble empirical mode decomposition and random under sampling boosting. *Comput. Methods Progr. Biomed.* 140, 201–210. doi: 10.1016/j.cmpb.2016.12.015

Hassan, A. R., and Bhuiyan, M. I. H. (2017b). An automated method for sleep staging from EEG signals using normal inverse gaussian parameters and adaptive boosting. *Neurocomputing* 219, 76–87. doi: 10.1016/j.neucom.2016.09.011

Hassan, A. R., Siuly, S., and Zhang, Y. (2016). Epileptic seizure detection in EEG signals using tunable-Q factor wavelet transform and bootstrap aggregating. *Comput. Methods Progr. Biomed.* 137, 247–259. doi: 10.1016/j.cmpb.2016.09.008

Hassan, A. R., and Subasi, A. (2016). Automatic identification of epileptic seizures from EEG signals using linear programming boosting. *Comput. Methods Progr. Biomed.* 136, 65–77. doi: 10.1016/j.cmpb.2016.08.013

Herman, P., Prasad, G., McGinnity, T. M., and Coyle, D. (2008). Comparative analysis of spectral approaches to feature extraction for EEG-based motor imagery classification. *IEEE Trans. Neural Syst. Rehabil. Eng.* 16, 317–326. doi: 10.1109/TNSRE.2008.926694

Hernández-Pereira, E., Bolón-Canedo, V., Sánchez-Maroño, N., Álvarez-Estévez, D., Moret-Bonillo, V., and Alonso-Betanzos, A. (2016). A comparison of performance of K-complex classification methods using feature selection. *Informat. Sci.* 328, 1–14. doi: 10.1016/j.ins.2015.08.022

Jain, R., and Ganesan, R. A. (2021). Reliable sleep staging of unseen subjects with fusion of multiple EEG features and RUSBoost. *Biomed. Sign. Process. Contr.* 70, 103061. doi: 10.1016/j.bspc.2021.103061

Jainendra, S., Miguel, B.-A., Joan, O., Nandi, G. C., and Domenec, P. (2021). Feature extraction and selection for emotion recognition from electrodermal activity. *IEEE Trans. Affect. Comput.* 12, 1949–3045. doi: 10.1109/TAFFC.2019.2901673

Khoshnevis, S. A., and Sankar, R. (2020). Classification of the stages of Parkinson's disease using novel higherorder statistical features of EEG signals. *Neural Comput. Appl.* 33, 7615–7627. doi: 10.1007/s00521-020-05505-2

Krohne, L. K., Hansen, R. B., Christensen, J. A. E., Sorensen, H. B. D., and Jennum, P. (2014). "Detection of K-complexes based on the Wavelet Transform," in *2014 36th Annual International Conference of the IEEE Engineering in Medicine and Biology Society* (Chicago, IL: IEEE), 6944859.

Lajnef, T., Chaibi, S., Eichenlaub, J.-B., Ruby, P. M., Aguera, P.-E., Samet, M., et al. (2015). Sleep spindle and K-complex detection using tunable Q-factor wavelet transform and morphological component analysis. *Front. Hum. Neurosci.* 9, 414. doi: 10.3389/fnhum.2015.00414

Latreille, V., Ellenrieder, N., Peter-Derex, L., François Dubeau Gotman, J., and Frauscher, B. (2020). The human K-complex: Insights from combined scalp-intracranial EEG recordings. *NeuroImage* 213, 116748. doi: 10.1016/j.neuroimage.2020.116748

Li, Y., Xie, S., Zhao, J., Liu, C., and Xie, X. (2017). Improved GP algorithm for the analysis of sleep stages based on grey model. *ScienceAsia* 43, 312–318. doi: 10.2306/scienceasia1513-1874.2017.43.312

Loomis, A. L., Harvey, E. N., and Hobart, G. A. (1938). Distribution of disturbance patterns in the human electroencephalogram, with special reference to sleep. *J. Neurophysiol.* 1, 413–430. doi: 10.1152/jn.1938.1.5.413

Nawaz, R., Cheah, K. H., Nisar, H., and Yap, V. V. (2020). Comparison of different feature extraction methods for EEG-based emotion recognition. *Biocybernet. Biomed. Eng.* 40, 910–926. doi: 10.1016/j.bbe.2020.04.005

Noor, N. S. E. M., Ibrahim, H., Lah, M. H. C., and Abdullah, J. M. (2022). Prediction of recovery from traumatic brain injury with EEG power spectrum in combination of independent component analysis and RUSBoost model. *BioMedInformatics* 2, 10007. doi: 10.3390/biomedinformatics2010007

Oliveira, G. H. B. S., Coutinho, L. R., Silva, J. C. d., Pinto, I. J. P., Ferreira, J. M. S., Silva, F. J. S., et al. (2020). Multitaper-based method for automatic k-complex detection in human sleep EEG. *Expert Syst. Appl.* 151, 1–16. doi: 10.1016/j.eswa.2020.113331

Parekh, A., Selesnick, I. W., Rapoport, D. M., and Ayappa, I. (2015). Detection of K-complexes and sleep spindles (DETOKS) using sparse optimization. *J. Neurosci. Methods* 251, 37–46. doi: 10.1016/j.jneumeth.2015.04.006

Peker, M. (2016). An efficient sleep scoring system based on EEG signal using complex-valued machine learning algorithms. *Neurocomputing* 207, 165–177. doi: 10.1016/j.neucom.2016.04.049

Ranjan, R., Arya, R., Fernandes, S. L., Sravya, E., and Jain, V. (2018). A fuzzy neural network approach for automatic K-complex detection in sleep EEG signal. *Patt. Recogn. Lett.* 115, 74–83. doi: 10.1016/j.patrec.2018.01.001

Richard, C., and Lengellé, R. (1998). Joint time and time-frequency optimal detection of K-complexes in sleep EEG. *Comput. Biomed. Res.* 31, 209–229. doi: 10.1006/cbmr.1998.1476

Selesnick, I. W. (2011). Wavelet transform with tunable Q-factor. *IEEE Trans. Sign. Process.* 59, 3560–3575. doi: 10.1109/TSP.2011.2143711

Siuly, A., Li, Y., and Wen, P. (2011). Clustering technique-based least square support vector machine for EEG signal classification. *Comput. Methods Progr. Biomed.* 104, 358–372. doi: 10.1016/j.cmpb.2010.11.014

Tokhmpash, A., Hadipour, S., and Shafai, B. (2021). Epileptic seizure detection using tunable Q-factor wavelet transform and machine learning. *Adv. Neuroergon. Cogn. Eng.* 259, 78–85. doi: 10.1007/978-3-030-80285-1_10

Vidaurre, C., Krämer, N., Blankertz, B., and Schlögl, A. (2009). Time domain parameters as a feature for EEG-based brain-computer interfaces. *Neural Netw.* 22, 1313–1319. doi: 10.1016/j.neunet.2009.07.020

Vu, H. Q., Li, G., Sukhorukova, N. S., Beliakov, G., Shaowu, L., Philippe, C., et al. (2012). K-complex detection using a hybrid-synergic machine learning method. *IEEE Trans. Syst. Man Cybernet.* 42, 1478–1490. doi: 10.1109/TSMCC.2012.2191775

Xu, X., Wei, F., Zhu, Z., Liu, J., and Wu, X. (2020). "EEG feature selection using orthogonal regression: Application to emotion recognition," in *IEEE International Conference on Acoustics, Speech and Signal Processing* (Barcelona: IEEE), 9054457.

Yazdani, S., Fallet, S., and Vesin, J.-M. (2018). A novel short-term event extraction algorithm for biomedical signals. *IEEE Trans. Biomed. Eng.* 65, 754–762. doi: 10.1109/TBME.2017.2718179

Yücelbaş, C., Yücelbaş, S., Özşen, S., Tezel, G., Küççüktürk, S., and Yosunkaya, S. (2017). A novel system for automatic detection of K-complexes in sleep EEG. *Neural Comput. Appl.* 29, 137–157. doi: 10.1007/s00521-017-2865-3

Zhang, X., Landsness, E. C., Chen, W., Miao, H., Tang, M., Brier, L. M., et al. (2022). Automated sleep state classification of wide-field calcium imaging data *via* multiplex visibility graphs and deep learning. *J. Neurosci. Methods* 366, 109421. doi: 10.1016/j.jneumeth.2021.109421

frontiers | Frontiers in Neuroscience

TYPE Original Research
PUBLISHED 04 April 2023
DOI 10.3389/fnins.2023.1132980

OPEN ACCESS

EDITED BY
Ying Wu,
Xi'an Jiaotong University, China

REVIEWED BY
Qingyun Wang,
Beihang University, China
Yangyang Yu,
Xi'an Jiaotong University, China

*CORRESPONDENCE
Xiaojuan Sun
✉ sunxiaojuan@bupt.edu.cn

SPECIALTY SECTION
This article was submitted to Translational Neuroscience, a section of the journal Frontiers in Neuroscience

RECEIVED 28 December 2022
ACCEPTED 20 March 2023
PUBLISHED 04 April 2023

CITATION
Liu M and Sun X (2023) Spatial integration of dendrites in fast-spiking basket cells. *Front. Neurosci.* 17:1132980. doi: 10.3389/fnins.2023.1132980

Spatial integration of dendrites in fast-spiking basket cells

Ming Liu and Xiaojuan Sun*

School of Science, Beijing University of Posts and Telecommunications, Beijing, China

Dendrites of fast-spiking basket cells (FS BCs) impact neural circuit functions in brain with both supralinear and sublinear integration strategies. Diverse spatial synaptic inputs and active properties of dendrites lead to distinct neuronal firing patterns. How the FS BCs with this bi-modal dendritic integration respond to different spatial dispersion of synaptic inputs remains unclear. In this study, we construct a multi-compartmental model of FS BC and analyze neuronal firings following simulated synaptic protocols from fully clustered to fully dispersed. Under these stimulation protocols, we find that supralinear dendrites dominate somatic firing of FS BC, while the preference for dispersing is due to sublinear dendrites. Moreover, we find that dendritic diameter and Ca^{2+}-permeable AMPA conductance play an important role in it, while A-type K^{+} channel and NMDA conductance have little effect. The obtained results may give some implications for understanding dendritic computation.

KEYWORDS

fast-spiking basket cells, compartmental model, dendritic non-linearity, spatial integration, hippocampus

1. Introduction

Across all cortical circuits, GABAergic interneurons represent a minority yet serve a critical impact on modulating circuit functions (Hu et al., 2014). They set a limited time window for synaptic integration and plasticity in principal neurons and coordinate synchronous activity during neuronal oscillations (Buzsaki and Draguhn, 2004; Hu et al., 2010; Chiovini et al., 2014). As one particular type of GABAergic interneuron, fast-spiking basket cells (FS BCs) can be distinguished by their morphological properties, expression of molecular markers, and functional characteristics (Hu et al., 2014). For fast-spiking basket cells, their action potentials present short duration and fast-spiking phenotype (Jonas et al., 2004), and synapses located on their dendrites contain GluR2-lacking Ca^{2+}-permeable AMPA (cp-AMPA) receptors and low levels of NMDA receptors (Geiger et al., 1997; Adesnik and Nicoll, 2007; Freund and Katona, 2007; Povysheva et al., 2013). Among them, cp-AMPARs possess faster deactivation kinetics (Geiger et al., 1995; Isaac et al., 2007), and FS BCs with cp-AMPA conductances in rat prefrontal cortex are reported to exhibit prominent synaptic facilitation (Wang and Gao, 2010). These features above make FS BCs essential regulators of network oscillations (Jiang et al., 2016) and memory consolidation (Xia et al., 2017). Due to these essential roles that FS BCs played in the brain, investigating the information processing mechanisms in them is vital for understanding the correlated brain functions.

Dendritic integration, a fundamental part of neuronal information processing, is classified into linear, sublinear, and supralinear integration. Previous studies have revealed that dendrites of interneurons exhibit mostly linear or sublinear integration (Tzilivaki et al., 2022), and dendrites of some CA1 interneurons could show supralinear integration (Katona et al., 2011). Except for these neurons, dendritic integration has also been discussed in

other neurons, such as granule cells (Krueppel et al., 2011), etc. Neuronal response to spatiotemporal synaptic inputs depends heavily on the type of dendritic integration. In CA1 pyramidal neurons with supralinear integration, stimulations on synapses clustered within a branch can cause more robust responses than on dispersed allocated synapses (Poirazi et al., 2003). While for other neuron types with sublinear dendrites, their response is usually sensitive to scattered synaptic inputs (Cazé et al., 2013). Meanwhile, the dendritic integration mode can affect the output precision (Gasparini and Magee, 2006) and further neural oscillation (Wang, 2010).

Dendritic integration has been found to be related to neuronal physiological properties (Araya et al., 2006; Vervaeke et al., 2012; Kamijo et al., 2014; Mueller and Egger, 2020; Di Maio, 2021). For example, narrow dendritic diameters produce more significant local input impedance, thus inducing prominent sublinear integration in stellate cells (Abrahamsson et al., 2012). Sodium ion channels and NMDA receptors are the main amplification mechanism for supralinear integration of pyramidal neurons (Nevian et al., 2007). Alike, dendritic properties such as fast inactivating K^+ current (Shibata et al., 2000) and dendritic morphology (Hartveit et al., 2022), or synaptic conductances can affect spatial integration and the first spike latency, which together provide precise mediation of the postsynaptic neurons.

Previous studies on spatial integration mainly focused on fully clustered (Carter et al., 2007; Gökçe et al., 2016; Dembrow and Spain, 2022) or fully dispersed (Farinella et al., 2014) synaptic inputs, without paying attention to the intermediate state, which is difficult to realize in the experiment, thus hindering understanding of the specific connection mode in the brain. Recently, supralinear and sublinear integration coexisting(bi-modal integration) on the same dendrite of FS BCs has been reported (Tzilivaki et al., 2019). They reveal that FS BCs present dispersed preference due to the specific morphological features, A-type potassium channels, and the existence of sublinear dendrites. Nevertheless, the underlying mechanisms in FS BCs to transform discriminate spatial synaptic inputs and the role of the two non-linear dendrites in it remain elusive.

In this paper, we aim to investigate how supralinear and sublinear dendrites of FS BCs influence their responses to synaptic inputs with different spatial dispersion. Using a biophysically-detailed compartmental model of a CA3 fast-spiking basket cell, under the knowledge of sublinear dendrites making FS BCs prefer dispersed spatial synaptic inputs as reported by Tzilivaki et al. (2019), we further find that supralinear dendrites play a dominant role in FS BCs' firing response. Responses of FS BCs to spatial synaptic inputs stimulus of the whole dendritic tree are consistent with that to the supralinear dendrites stimulus only. And this result is independent of the proportion of sublinear dendrites to supralinear dendrites. To understand the mechanisms of this spatial integration, we alter several biophysical properties in dendrites. We find that dendritic diameter varies somatic response in a nonmonotonic way and is the determining factor in regulating the precise firing of FS BCs. Then, we apply the same spatial simulation protocols after blocking cp-AMPA and NMDA synapses separately. The results demonstrate that cp-AMPA receptors improve the integration capacity immensely, while the presence of NMDA currents is insufficient for active dendritic spikes. Our findings may provide insights into the role of spatial integration in interneurons, leading to the speed and temporal precision operation of GABA release and the regulation of interneurons in memory updating further.

2. Materials and methods

2.1. Compartmental modeling

Compartmental model of the CA3 fast-spiking basket cell is implemented and run within the NEURON simulation environment (Hines and Carnevale, 1997). The detailed dendritic morphology model J31a.CNG.swc is obtained from the NeuroMorpho.org database uploaded by Tukker et al. (2013), consisting of 217 compartments. Dendrites distance from soma less than 100 μm is defined as proximal dendrites, otherwise as distal dendrites (Hu et al., 2014). Axonal compartments of B13a.CNG.swc in the same brain area is adopted since the lack of axons in the J31a model. And segment number of all compartments is set the same as the number of synaptic inputs.

Passive cable properties and active conductance of ionic channels in the model are all based on experimental data (Supplementary Tables 1, 2) (Goldberg et al., 2003; Hu et al., 2010; Konstantoudaki et al., 2014). Fast Na^+ ion channels (Hu et al., 2014) and delayed rectifier K^+ current are inserted into all compartments. Slow inactivation K^+, two Ca^{2+}-dependent potassium, and h currents are inserted only in soma. Other channels such as A-type K^+ are for proximal and distal dendrites, while L-, N-, and T-type Ca^{2+} currents are added to each dendritic and somatic compartment. Meanwhile, all compartments include a calcium buffering mechanism except axon (Konstantoudaki et al., 2014). For synaptic inputs, synapses with Ca^{2+} permeable AMPA (cp-AMPA) and NMDA receptors are considered, and inhibitory synapses are not considered in our simulation due to the very low ratio of them in all incoming inputs (Freund and Katona, 2007; Hu et al., 2014). Values of all synaptic weights are consistent with Tzilivaki et al. (2019).

2.2. Spatial simulation protocols

In all simulation protocols, 20 pairs of cp-AMPA and NMDA synapses are randomly located on the dendrites with an average diameter being less than 1.2 μm are activated by a 50 Hz Poisson spike train (Emri et al., 2001). In the following, if not specialized, all the dendrites refer to those with diameters less than 1.2 μm. In order to study the different roles of supralinear and sublinear dendrites on the response of FS BCs, synaptic stimulations are put into the whole dendrites, only supralinear dendrites or sublinear dendrites, respectively. And the locations of the activated synapses change from fully clustered on a single dendritic branch to fully dispersed on the whole dendritic tree, among which the selected compartment for dispersing is random. The results obtained in this paper are the average over N since simulation protocols repeat N times. Here, N is the number of non-linear dendrites when

the activated synapses are located on the whole dendrites, and is the number of supralinear/sublinear dendrites when the activated synapses are located only on supralinear/sublinear dendrites.

3. Results

3.1. Preference of FS BCs to dispersed spatial synaptic inputs

Unlike the former opinion that dendrites integrate signals linearly, fast-spiking basket cells have been authenticated to perform both supralinear and sublinear computations. To investigate the different roles of supralinear and sublinear dendrites on the response of FS BCs, we need to identify each dendrite of FS BCs to be supralinear or sublinear. Toward this goal, we stimulate gradually increasing cp-AMPA and NMDA synaptic inputs(from 1 to 20 pairs) to each dendrite and block sodium channels in soma and axon to avoid backpropagation effects. By comparing the actual EPSP (measured EPSP) recorded in soma with linearly summed EPSP (expected EPSP), dendritic compartments are labeled as supralinear/sublinear if measured EPSP is larger/less than the expected EPSP, as shown in Figure 1. And we find that the studied FS BC has 151 supralinear dendrites and 17 sublinear ones.

Dendritic integration plays important role in neuronal responses to different spatial synaptic inputs (Tran-Van-Minh et al., 2015). We implement diverse spatial synaptic input patterns on selected dendrites to investigate the roles of different non-linear dendrites in FS BCs' responses (see "Methods"). As shown in Figure 2A, synaptic inputs are placed randomly on dendrites from fully clustered to fully dispersed. Responses of FS BC to synaptic inputs subjected to the whole dendrites, to only supralinear or sublinear dendrites are exhibited by blue, red, and orange lines in Figures 2B, C, respectively. The firing rate of the whole dendritic tree increased from an average of 0.79 ± 3.2Hz to a maximum of 35.6 ± 4.3Hz. In Figures 2B, C, both somatic firing rate and peak amplitude of FS BC's spike train increase with synaptic inputs' dispersity when active synapses are located at the whole dendrites or only on supralinear dendrites. For active synapses located at only sublinear dendrites, the somatic firing rate doesn't change too much, and peak amplitude increases while can't reach the peak value as supralinear dendrites. It indicates that supralinear dendrites prefer dispersed synaptic inputs with the existence of sublinear ones, and they play a dominant role since the trajectories are similar for synaptic inputs putting only on supralinear dendrites and the whole dendrites. With the variation of peak amplitude, it can be seen that dendritic spikes occurring on supralinear dendrites make the membrane potential of soma come to the peak (Goldberg et al., 2003), not sublinear ones.

The ratio of supralinear dendrites over the number of sublinear dendrites of our model is about 8.88. To test whether this cluster-disperse response is related to the ratio of the non-linear dendrites, we repeat the same simulation protocols on another FS basket cell with more sublinear dendrites than supralinear dendrites (ratio = 0.25). Results show that although the ratio is diametrically changed, this cell also prefers dispersed synaptic inputs (Figure 2D), and supralinear dendrites play a dominant role in this preference too. It indicates that FS BCs' preference for dispersed synaptic inputs with the existence of sublinear ones is independent of the nonlinear dendrites' ratio. This independence property may provide a way for us to deduce the spatial dispersion of synaptic inputs from the firing rate of FS BCs.

In summary, under simulated synaptic protocols from fully clustered to fully dispersed, we find that supralinear dendrites play a dominant role in the somatic firings of FS BCs. They can trigger and transmit enough dendritic spikes to the soma. Meanwhile, the preference of FS BCs for dispersed synaptic inputs is due to the existence of sublinear dendrites.

3.2. Dendritic diameters play a crucial role in the spatial responses of FS BCs

Dendritic morphology and A-type potassium channels have been reported to contribute to the dispersed preference in FS BCs (Hu et al., 2014). To explore their impact on responses of FS BCs under spatial synaptic inputs, we repeat the above simulation protocols after increasing the dendritic diameter to 2 μm. As shown in Figure 3A, compared with the data on the right side that dendritic diameters are unchanged, the somatic firing rate with spatial synaptic inputs located on the whole dendrites tends to concentrate to lower values, ranging from 3.4 Hz to 17.54 Hz. And its nonmonotonic variation tendency is still consistent with the one under stimulations only on the supralinear dendrites, even though somatic firing rate increases with a dispersion of spatial synaptic inputs put only on sublinear dendrites (Figure 3B). This diversity is also reflected in peak amplitude. As shown in Figure 3C, whether synapses are activated in the whole dendrites or supralinear/sublinear dendrites, the membrane potential of soma can always reach the peak and the difference becomes smaller than the results shown in Figure 2C. It also reveals that the narrow diameter of dendrites may hamper the response produced by clustered inputs, while a large diameter may reduce the response produced by dispersed inputs.

To more intuitively reflect the changing response in different non-linear dendrites, we use Student's t-test for statistically compared. Variations between the two non-linear dendrites are significant(p = 0.00011), where the median in the sublinear dendrites is larger than 10 (Figure 3D). Together these results further confirm that supralinear dendrites dominate the firing in FS BCs, and dendritic diameter plays a vital role in the spatial response of FS BCs which is also an essential factor in determining the firing properties of sublinear dendrites.

To further test the impacts of dendritic morphology on EPSP-spike coupling, we analyze the first spike latency for synaptic inputs located on the whole, the supralinear dendrites, and sublinear dendrites respectively. First spike latency is defined as the interval between the onset of the simulation and the peak of the first spike. Under control conditions (diameter of dendrites doesn't change), the dependence of first spike latency on dispersion for spatial synaptic inputs on the whole dendrites is still consistent with the ones on the supralinear dendrites. And the nonmonotonic dependence of first spike latency on dispersion (Figure 4A, blue and red dotted line) is different from the increasing one for inputs on only sublinear dendrites (Figure 4A, yellow dotted line). When the

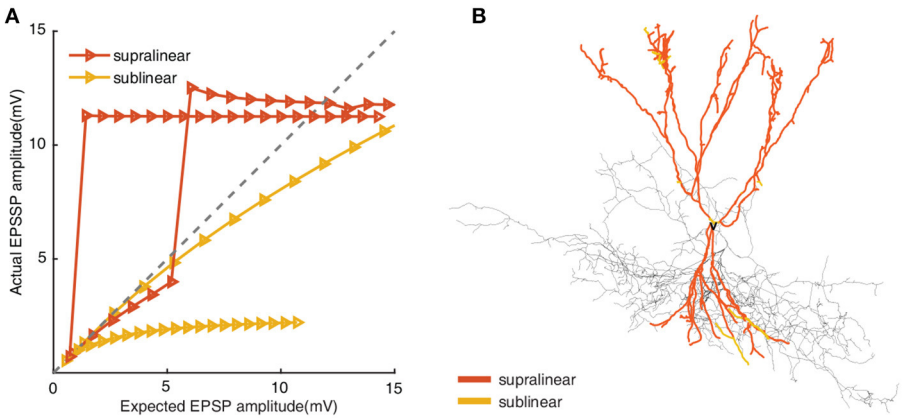

FIGURE 1
(A) Input-output relationships from supralinear and sublinear dendrites in FS BC model. Increasing numbers of synapses(from 1 to 20 pairs) activate on each compartment. The *x*-axis presents the linear summed EPSP, while the *y*-axis shows the actual EPSP amplitude recorded in the soma. The gray line indicates linear summation. **(B)** Morphological reconstructions of the modeled FS BC with supralinear (red) and sublinear (yellow) dendrites. The removed dendritic branches are also colored according to the actual integrated properties in each compartment, but the removed dendritic branches are not considered in subsequent simulations.

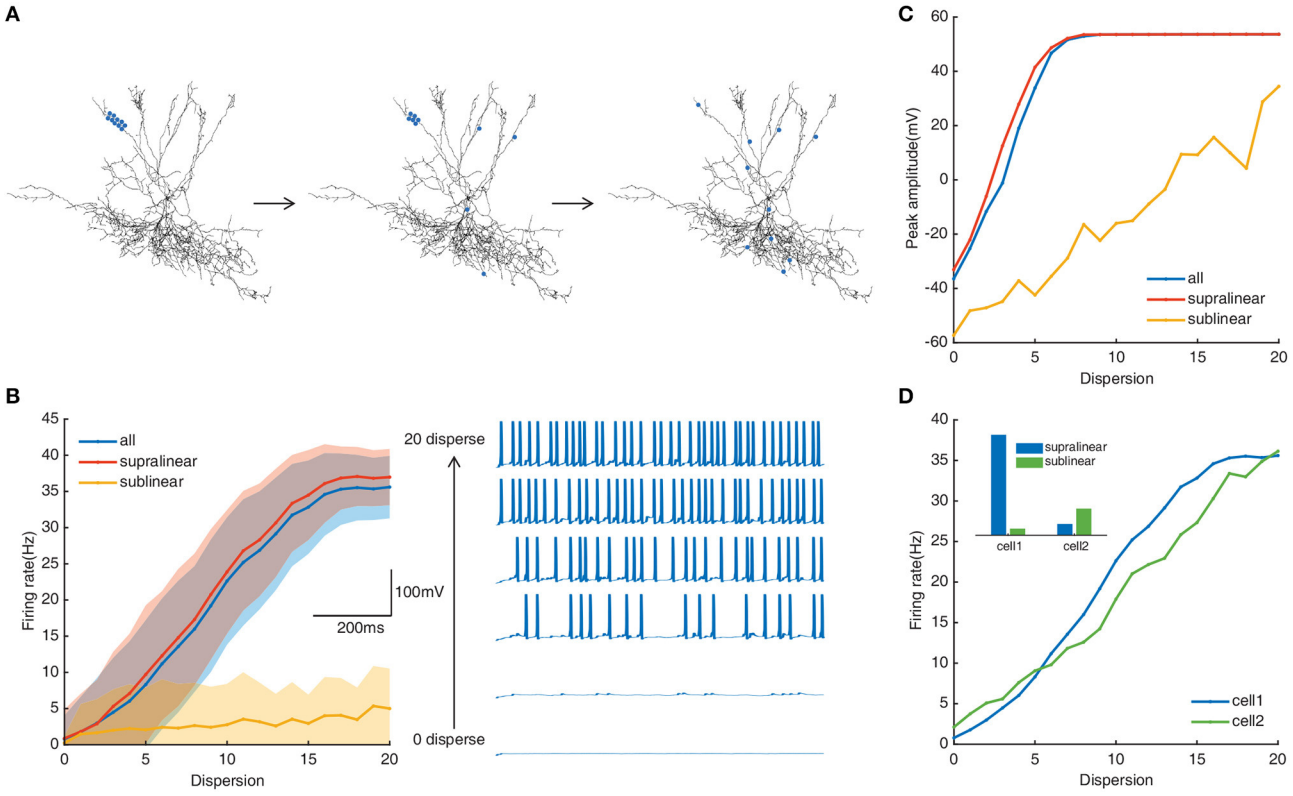

FIGURE 2
(A) Schematic diagram of spatial simulation protocols. Twenty pairs of synapses randomly located on selected dendrites from fully clustered to fully dispersed (blue dots represent the stimulation site). All processes cycle for *N* times (*N* is the number of stimulated branches). Output is recorded in the soma. **(B)** Left: Traces of the somatic firing rate in the whole dendrites (blue line), supralinear dendrites (red line), and sublinear dendrites (yellow line) under the spatial simulation protocol. Every shaded area denotes the corresponding standard deviation. Right: Example of somatic membrane potentials on a selected dendrite (every three dispersion degrees). **(C)** Peak membrane potential record in the whole dendritic tree, supralinear dendrites, and sublinear dendrites. **(D)** Somatic firing rate of two neuron models. Cell1 represents the neuron with a ratio of supralinear dendrites to sublinear dendrites of 8.88 (blue); cell2 represents the neuron with a ratio of 0.25 (green). Inset denotes the histogram of the number of non-linear dendrites in two neurons (blue: supralinear, green: sublinear).

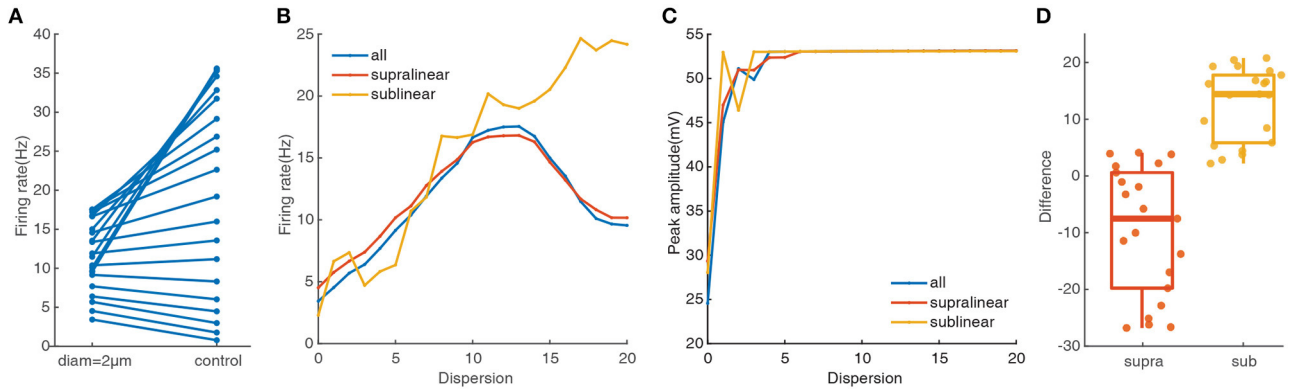

FIGURE 3
Dendritic morphology affect notably on the cluster-disperse spatial responses. **(A)** Firing rate evoked in the neuron after and before changing the diameter. The points located at the right side of the figure are the somatic firing rate under the normal condition when the dendritic diameters have not changed. All the following parts are the same. **(B)** Traces of firing rate in the whole dendrites and different non-linear dendrites after changing the diameter. **(C)** Peak membrane potential record in the whole dendrites and other non-linear dendrites under 2 μm diameter. **(D)** Box plot and scatter plot of the differences in firing rate between the normal condition and changing the diameter in two non-linear dendrites. Red: supralinear dendrites, yellow: sublinear dendrites.

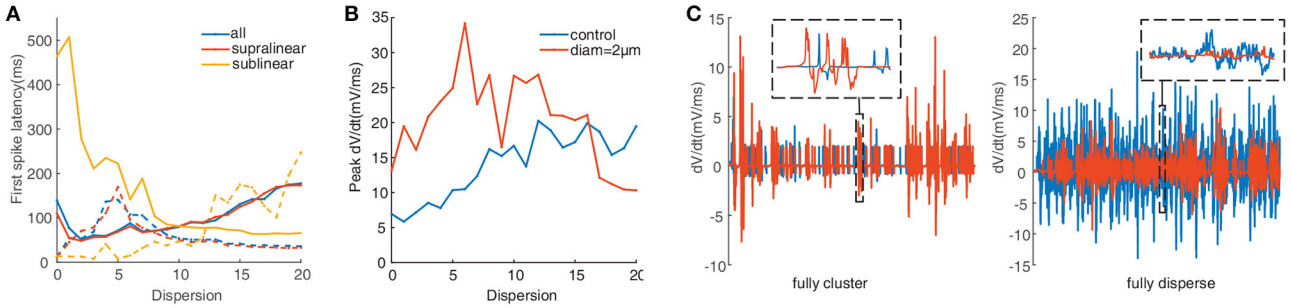

FIGURE 4
(A) First spike latency before (dotted lines) and after (solid lines) changing the diameter. **(B)** Peak dV/dt against dispersion of synaptic inputs calculated before (blue) and after (red) changing the diameter. **(C)** Detailed differentiated membrane potential (dV/dt) traces under fully clustered and fully dispersed, insets are the enlarged image. The line color is consistent with the legend color in **(B)**.

dendritic diameter changes to 2 μm, the dependence of first spike latency has changed conversely. For example, first spike latency decreases with dispersion (Figure 4A, yellow solid line), which is contrary to the one under control condition. And for the other two cases, first spike latency decreases first and then increases with dispersion (Figure 4A, blue and red solid line), which is also different from the ones increasing first and then decreasing for the control condition (Figure 4A, blue and red dotted line). These obtained results indicate that dendritic diameter could alter signal transfer efficiency in FS BCs.

Peak of the derivation membrane potential(dV/dt) versus degree of dispersion can provide another perspective of investigation (Losonczy and Magee, 2006). The blue line in Figure 4B shows that the peak dV/dt rises gradually under control conditions. After increasing the dendritic diameter to 2 μm, the peak dV/dt is more eminent at lower dispersion, and then it clips to a lower value (Figure 4B, red line). Figure 4C presents the variation of dV/dt for fully clustered or dispersed stimulations. For fully clustered synaptic stimulation, dV/dt with the diameter being 2 μm fluctuates much more greatly than the one under control condition (Figure 4C, left), while vice versa for fully dispersed synaptic stimulation (Figure 4C, right). These results indicate that dendritic diameter is associated with the peak dV/dt, notably for higher dispersion stimulation.

A-type K^+ channels are reported to be an important factor for controlling neuronal response. To investigate their contribution to the response of the studied FS BC to spatial synaptic inputs with different dispersions, we repeat the simulation protocols after setting the conductance of A-type K^+ channels to zero. As shown in Figure 5A, the somatic firing rate for inputs on the whole dendrites increases slightly after blocking the A-type K^+ channels. The difference in Figure 5B reflects somatic firing rises more in the supralinear dendrites than sublinear dendrites. Therefore A-type K^+ channels contribute little effect on the cluster-disperse response.

In summary, these simulations demonstrate that the specific morphology features of FS BCs conduct the discrepancy in the cluster-disperse integration of different non-linear dendrites and play a key element in controlling the release timing precisely, while A-type K^+ channels present minor effects.

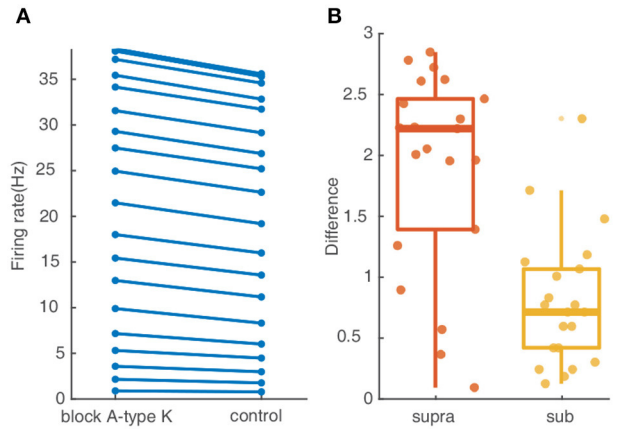

FIGURE 5
A-type K^+ channel affect little on the cluster-disperse spatial responses. **(A)** Firing rate evoked in the neuron after and before blocking A-type K^+ channels. **(B)** Box plot and scatter plot of the differences in firing rate between the normal condition and blocking the A-type K^+ channel in two non-linear dendrites. Red: supralinear dendrites, yellow: sublinear dendrites.

3.3. Synaptic conductances determine responses and output precision of FS BCs to spatial synaptic inputs

Since the type of excitatory synapses influences synaptic integration, we reason that they may also act to the cluster-disperse spatial responses of FS BC (Schiller et al., 2000). To test this, we apply synapses consisting of only cp-AMPA or NMDA under the same stimulation protocols. For simulations involving NMDA-only, the neuron barely generates action potentials and the somatic firing rate range from 0.26 ± 1.2 Hz to 4.15 ± 5.6 Hz, which decreases from beta wave to alpha wave (Figure 6A). Same as Figure 3B, the disperse-sensitive response disappears. While the tendency is still increased first and then decreased, the difference between the two ends becomes smaller (Figure 6B). Noticed when synapses are added to the sublinear dendrites only, the somatic firing rate does not increase with the dispersion, this suggests that synaptic conductance does not affect the characteristics of sublinear dendrites. For peak amplitude, its maximum decreases to nearly zero (Figure 6C) as compared to the one under the control condition as exhibited in Figure 2C. Variation of dependence of peak amplitude on stimulation dispersion could explain why the somatic firing rate drops to alpha bands. The difference shown in Figure 6D reveals when synapses contain NMDA only, dendritic spikes on the supralinear dendrites reduce a lot, which indicates the necessity of cp-AMPA conductances for dendritic spikes.

When synapses contain cp-AMPA only, somatic firing in the whole dendrites increases significantly, from 1.65 Hz of minimum to 55.7 Hz, which is consistent with the supralinear and sublinear dendrites (Figures 7A, B). Meanwhile, the variation of peak amplitude with dispersion reveals the dispersion needed for reaching the maximum value of peak amplitude is lower (Figure 7C). In addition to several outliers at low dispersion, Figure 7D further presents a strong and uniform influence of cp-AMPA on the supralinear dendrites rather than the sublinear dendrites. These results demonstrate that cp-AMPA conductance is required for the dispersion-sensitive properties of FS BCs, which point out that it becomes another crucial element in spatial integration by inducing dendritic spikes.

Synaptic conductances also affect the temporal input-output relationship of neurons (Wang and Liu, 2010; Di Maio et al., 2021). As illustrated in Figure 8, compared with the dotted lines in Figure 4A, the change of nonmonotonic trajectory in both cases is the same as that under normal conditions, which increases first and then decreases. When NMDA conductance is added only, the latency of the first spike is longer, and the existence of 0 in sublinear dendrites is due to the absence of firing (Figure 8A, solid yellow line). However, no matter how the first spike latency changes under different conditions, sublinear dendrites still react contrastively to others.

The calculation of peak dV/dt increases following the blockade of NMDA receptors, corresponding with the change of somatic outputs (Figure 8B, green line). In contrast, for NMDA-only conductance, the peak dV/dt decreases with the degree of dispersion (Figure 8B, blue line). Altogether these data indicate that cp-AMPA synapses can further reduce the transmission threshold of the dendritic spike, while the threshold increases sharply with NMDA inputs only.

In summary, we find that the faster kinetics of cp-AMPA synapses influences the response of spatial dispersion inputs in FS BCs. They can regulate both the summation and timing of dendritic spikes and further affect neuronal firing. On the other hand, NMDA conductance has a minor effect on this cluster-disperse response, and more effects may have to be studied on a longer time scale.

4. Discussion

Dendritic integration is one of the critical components of neuronal computation, and different type of integration leads to diverse spatial response (Kastellakis et al., 2015; Li and Gulledge, 2021). Exciting new findings show that the dendrites of fast-spiking basket cells in the hippocampus present both supralinear and sublinear integration (Tzilivaki et al., 2019) (Figure 1). How this bi-modal dendritic integration responds to synaptic inputs from fully clustered to fully dispersed of have not been previously examined. Here, using a compartmental model, we investigate how the supralinear and sublinear dendrites in FS BCs participate in the process of transforming the cluster-disperse patterns of synaptic inputs into outputs.

Our results demonstrate that supralinear dendrites play a dominant role in FS BCs' response to the cluster-disperse synaptic inputs, they dominate the somatic firing by generating dendritic spikes, and sublinear branches compute the disperse preference (Figure 2). Neurons employ a variety of mechanisms to combat spatial variability in synaptic inputs, and dendritic properties can significantly affect the ability of synaptic input to generate, propagate, and time action potentials (Psarrou et al., 2014). Similar to previous studies in other neurons, we find that dendritic morphology is the main cause of this diversity of spatial integration in non-linear dendrites (Single and Borst, 1998; Ran et al., 2020). Larger diameters diminish the disperse-sensitive responses in a nonmonotonic way of the whole and supralinear

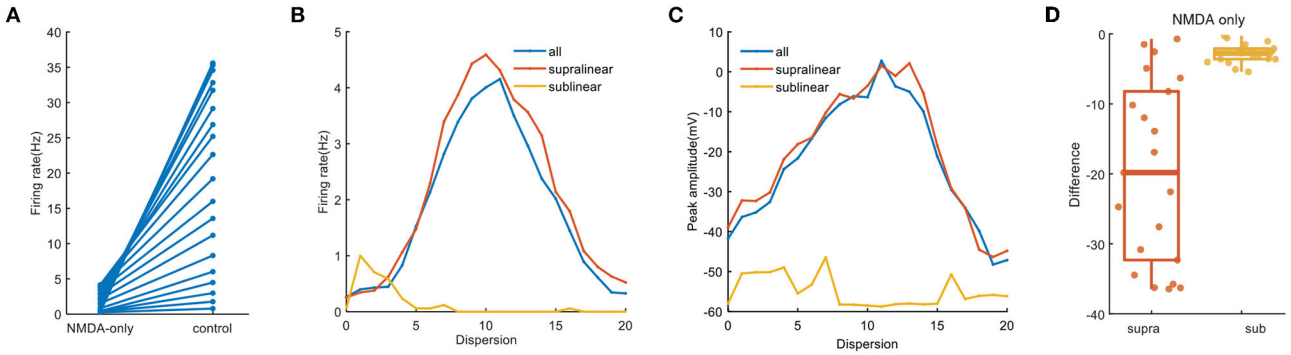

FIGURE 6
NMDA-only synapses on spatial responses. **(A)** Plot of firing rate in the whole dendrites for synaptic inputs having NMDA-only (same as the blue line in **B**) and normal condition. **(B)** Traces of firing rate with dispersion in the whole dendrites and two non-linear dendrites with NMDA synapses only. **(C)** Peak membrane potential with NMDA synapses only. **(D)** Box plot with scatter plot of the differences in firing rate between the normal condition and blocking cp-AMPA synapses in two non-linear dendrites.

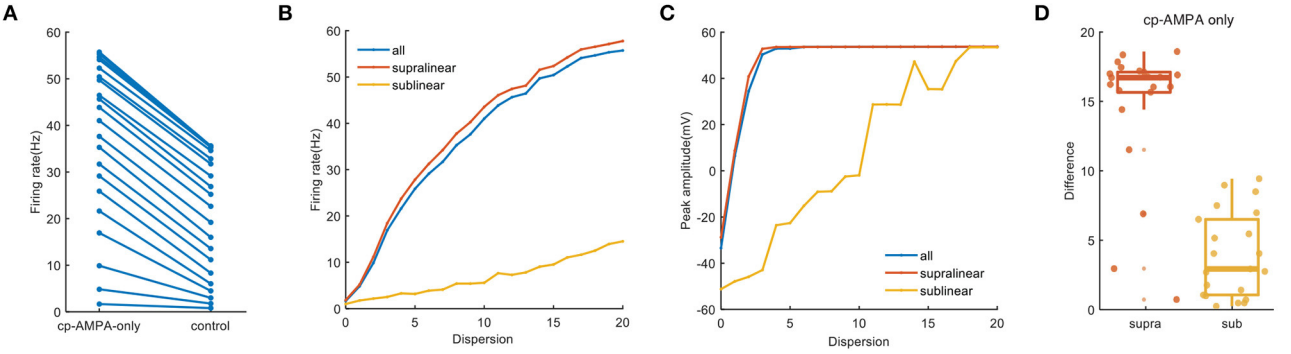

FIGURE 7
Cp-AMPA-only synapses on spatial responses. **(A)** Plot of firing rate in the whole dendrites for synaptic inputs having cp-AMPA only and normal condition. **(B)** Traces of firing rate with dispersion in the whole dendrites and two non-linear dendrites with cp-AMPA synapses only. **(C)** Peak membrane potential record in the whole dendrites and different non-linear dendrites with cp-AMPA synapses only. **(D)** Box plot with scatter plot of the differences in firing rate between the normal condition and blocking NMDA synapses in two non-linear dendrites. There are several outliers in the difference of supralinear dendrites.

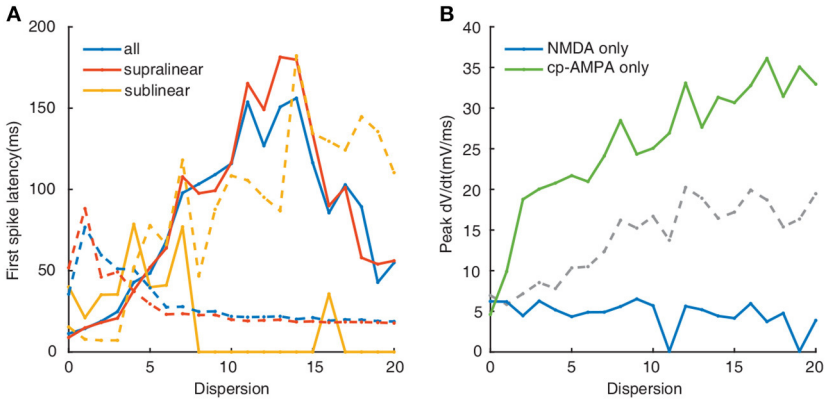

FIGURE 8
(A) First spike latency when applied NMDA synapses only (solid lines) and cp-AMPA synapses only(dotted line). Colors indicate as in legend. **(B)** Plot of peak dV/dt against dispersion of synaptic inputs. Colors (blue, green, and gray) indicate NMDA, cp-AMPA, and both cp-AMPA and NMDA synaptic synapses, respectively.

dendrites, while intensely increasing the firing in the sublinear dendrites (Figure 3). As the dendritic diameter is a morphological parameter of the neuron itself, the firing properties in sublinear dendrites completely change when the dendritic diameter alters to an abnormal value. Besides the firing rate, precise temporal propagation is essential in signal transfer, time course of synapses defines the time window for the firing of basket cells and their influence on the pyramidal neurons (London et al., 2002; Molineux et al., 2005; Wlodarczyk et al., 2013). The relationship between the first-spike latency and morphology shows an intriguing result on non-linear dendrites, supporting that this particular morphology of FS BCs determines its accurate timing transmission of information (Figure 4). Unlike previous studies, although K^+ channels influence neuronal responses (Misonou et al., 2005; Tzilivaki et al., 2019), blocking the A-type K^+ channels in the model has a minor influence on the cluster-disperse responses (Figure 5). Still, specificity in this model can not be ruled out.

The gating properties of cp-AMPA or NMDA receptors can also affect the participation of different non-linear dendrites in spatial integration (Mcbain and Dingledine, 1993; Isaac et al., 2007). Among them, cp-AMPARs mediate excitatory postsynaptic current raises and decays rapidly (Carter and Regehr, 2002; Walker et al., 2002), the EPSP arriving at the soma has a relatively short half-duration (Angulo et al., 1999; Jonas et al., 2004). Separately blocking the synaptic conductance in the model, we observe that activating NMDA synapses only causes minor somatic firing and peak amplitude (Figure 6). Meanwhile, cp-AMPA current can effectively enhance somatic response and involve the sensitivity for dispersed synaptic input (Figure 7). The results on non-linear dendrites show that supralinear dendrites are more easily affected by synaptic conductance, and unlike changing the diameter, the firing property of the sublinear dendrites doesn't change. As dendritic spike initiation is associated with the rising rate of the somatic voltage response (Gasparini et al., 2004), and the local dendritic spike threshold becomes more depolarized as dV/dt decreases, we find that the specific morphology and cp-AMPA conductance will provide the required level of rapid dendritic depolarization (Figures 4B, 8B) (Golding and Spruston, 1998; Gasparini and Magee, 2006). These findings may support the essential role of increased cp-AMPAR transition induced by plasticity-related events in memory consolidation, retrieval, and updating (Torquatto et al., 2019).

Once action potential in GABAergic interneurons occurs will trigger GABA release (Martina et al., 2000). This process needs temporal and spatial integration precision. As for basket cells, they densely target the perisomatic region and will thus control the firing possibility of the pyramidal cell (Piskorowski and Chevaleyre, 2012). Therefore, how FS BCs spatially filter synaptic inputs is critical to their function in the operation of neuronal networks. Our work provides insight into the responses of FS BCs to spatial dispersion inputs, demonstrating the superiority of their specific morphology and cp-AMPA current on neuronal outputs. These results are likely necessary to generate precise signals for the temporal coding of information and control spike-timing-dependent plasticity at glutamatergic synapses.

Data availability statement

The raw data supporting the conclusions of this article will be made available by the authors, without undue reservation.

Author contributions

ML and XS designed the study, performed the research, analyzed data, and wrote the paper. All authors agree to accountable for the content of the work. All authors contributed to the article and approved the submitted version.

Funding

This study was financially supported by the National Natural Science Foundation of China (Grant No. 12072046).

Conflict of interest

The authors declare that the research was conducted in the absence of any commercial or financial relationships that could be construed as a potential conflict of interest.

Publisher's note

Supplementary material

The Supplementary Material for this article can be found online at: https://www.frontiersin.org/articles/10.3389/fnins.2023.1132980/full#supplementary-material

References

Abrahamsson, T., Cathala, L., Matsui, K., Shigemoto, R., and DiGregorio, D. A. (2012). Thin dendrites of cerebellar interneurons confer sublinear synaptic integration and a gradient of short-term plasticity. *Neuron* 73, 1159–1172. doi: 10.1016/j.neuron.2012.01.027

Adesnik, H., and Nicoll, R. A. (2007). Conservation of glutamate receptor 2-containing AMPA receptors during long-term potentiation. *J. Neurosci.* 27, 4598–4602. doi: 10.1523/JNEUROSCI.0325-07.2007

Angulo, M., Rossier, J., and Audinat, E. (1999). Postsynaptic glutamate receptors and integrative properties of fast-spiking interneurons in the rat neocortex. *J. Neurophysiol.* 82, 1295–1302. doi: 10.1152/jn.1999.82.3.1295

Araya, R., Eisenthal, K. B., and Yuste, R. (2006). Dendritic spines linearize the summation of excitatory potentials. *Proc. Natl. Acad. Sci. U. S. A.* 103, 18799–18804. doi: 10.1073/pnas.0609225103

Buzsaki, G., and Draguhn, A. (2004). Neuronal oscillations in cortical networks. *Science* 304, 1926–1929. doi: 10.1126/science.1099745

Carter, A., and Regehr, W. (2002). Quantal events shape cerebellar interneuron firing. *Nat. Neurosci.* 5, 1309–1318. doi: 10.1038/nn970

Carter, A. G., Soler-Llavina, G. J., and Sabatini, B. L. (2007). Timing and location of synaptic inputs determine modes of subthreshold integration in striatal medium spiny neurons. *J. Neurosci.* 27, 8967–8977. doi: 10.1523/JNEUROSCI.2798-07.2007

Cazé, R. D., Humphries, M., and Gutkin, B. (2013). Passive dendrites enable single neurons to compute linearly non-separable functions. *PLoS Comput. Biol.* 9, e1002867. doi: 10.1371/journal.pcbi.1002867

Chiovini, B., Turi, G. F., Katona, G., Kaszas, A., Palfi, D., Maak, P., et al. (2014). Dendritic spikes induce ripples in parvalbumin interneurons during hippocampal sharp waves. *Neuron* 82, 908–924. doi: 10.1016/j.neuron.2014.04.004

Dembrow, N. C., and Spain, W. J. (2022). Input rate encoding and gain control in dendrites of neocortical pyramidal neurons. *Cell Rep.* 38, 110382. doi: 10.1016/j.celrep.2022.110382

Di Maio, V. (2021). The glutamatergic synapse: a complex machinery for information processing. *Cogn. Neurodyn.* 15, 757–781. doi: 10.1007/s11571-021-09679-w

Di Maio, V., Santillo, S., and Ventriglia, F. (2021). Synaptic dendritic activity modulates the single synaptic event. *Cogn. Neurodyn.* 15, 279–297. doi: 10.1007/s11571-020-09607-4

Emri, Z., Antal, K., Gulyas, A., Megias, M., and Freund, T. (2001). Electrotonic profile and passive propagation of synaptic potentials in three subpopulations of hippocampal CA1 interneurons. *Neuroscience* 104, 1013–1026. doi: 10.1016/S0306-4522(01)00136-1

Farinella, M., Ruedt, D. T., Gleeson, P., Lanore, F., and Silver, R. A. (2014). Glutamate-bound NMDARs arising from *in vivo*-like network activity extend spatio-temporal integration in a L5 cortical pyramidal cell model. *PLoS Comput. Biol.* 10, e1003590. doi: 10.1371/journal.pcbi.1003590

Freund, T. F., and Katona, I. (2007). Perisomatic inhibition. *Neuron* 56, 33–42. doi: 10.1016/j.neuron.2007.09.012

Gasparini, S., and Magee, J. (2006). State-dependent dendritic computation in hippocampal CA1 pyramidal neurons. *J. Neurosci.* 26, 2088–2100. doi: 10.1523/JNEUROSCI.4428-05.2006

Gasparini, S., Migliore, M., and Magee, J. (2004). On the initiation and propagation of dendritic spikes in CA1 pyramidal neurons. *J. Neurosci.* 24, 11046–11056. doi: 10.1523/JNEUROSCI.2520-04.2004

Geiger, J. R., Lübke, J., Roth, A., Frotscher, M., and Jonas, P. (1997). Submillisecond AMPA receptor-mediated signaling at a principal neuron-interneuron synapse. *Neuron* 18, 1009–1023. doi: 10.1016/S0896-6273(00)80339-6

Geiger, J. R. P., Melcher, T., Koh, D. S., Sakmann, B., Seeburg, P. H., Jonas, P., et al. (1995). Relative abundance of subunit mRNAs determines gating and Ca^{2}+ permeability of AMPA receptors in principal neurons and interneurons in rat CNS. *Neuron* 15, 193–204. doi: 10.1016/0896-6273(95)90076-4

Gökçe, O., Bonhoeffer, T., and Scheuss, V. (2016). Clusters of synaptic inputs on dendrites of layer 5 pyramidal cells in mouse visual cortex. *Elife* 5, e09222. doi: 10.7554/eLife.09222

Goldberg, J., Yuste, R., and Tamas, G. (2003). Ca^{2+} imaging of mouse neocortical interneuron dendrites: contribution of Ca^{2+}-permeable AMPA and NMDA receptors to subthreshold Ca^{2+} dynamics. *J. Physiol.* 551, 67–78. doi: 10.1113/jphysiol.2003.042598

Golding, N. L., and Spruston, N. (1998). Dendritic sodium spikes are variable triggers of axonal action potentials in hippocampal CA1 pyramidal neurons. *Neuron* 21, 1189–1200. doi: 10.1016/S0896-6273(00)80635-2

Hartveit, E., Veruki, M. L., and Zandt, B.-J. (2022). Dendritic morphology of an inhibitory retinal interneuron enables simultaneous local and global synaptic integration. *J. Neurosci.* 42, 1630–1647. doi: 10.1523/JNEUROSCI.0695-21.2021

Hines, M. L., and Carnevale, N. T. (1997). The neuron simulation environment. *Neural Comput.* 9, 1179–1209. doi: 10.1162/neco.1997.9.6.1179

Hu, H., Gan, J., and Jonas, P. (2014). Fast-spiking, parvalbumin^{+} GABAergic interneurons: From cellular design to microcircuit function. *Science* 345, 1255263. doi: 10.1126/science.1255263

Hu, H., Martina, M., and Jonas, P. (2010). Dendritic mechanisms underlying rapid synaptic activation of fast-spiking hippocampal interneurons. *Science* 327, 52–58. doi: 10.1126/science.1177876

Isaac, J. T. R., Ashby, M., and McBain, C. J. (2007). The role of the GluR2 subunit in AMPA receptor function and synaptic plasticity. *Neuron* 54, 859–871. doi: 10.1016/j.neuron.2007.06.001

Jiang, X., Lachance, M., and Rossignol, E. (2016). "Involvement of cortical fast-spiking parvalbumin-positive basket cells in epilepsy", in *Neurobiology of Epilepsy, Volume 226 of Progress in Brain Research*, eds E. Rossignol, L. Carmant, and J.-C. Lacaille (Elsevier), 81–126.

Jonas, P., Bischofberger, J., Fricker, D., and Miles, R. (2004). Interneuron diversity series: fast in, fast out–temporal and spatial signal processing in hippocampal interneurons. *Trends Neurosci.* 27, 30–40. doi: 10.1016/j.tins.2003.10.010

Kamijo, T. C., Hayakawa, H., Fukushima, Y., Kubota, Y., Isomura, Y., Tsukada, M., et al. (2014). Input integration around the dendritic branches in hippocampal dentate granule cells. *Cogn. Neurodyn.* 8, 267–276. doi: 10.1007/s11571-014-9280-6

Kastellakis, G., Cai, D. J., Mednick, S. C., Silva, A. J., and Poirazi, P. (2015). Synaptic clustering within dendrites: an emerging theory of memory formation. *Prog. Neurobiol.* 126, 19–35. doi: 10.1016/j.pneurobio.2014.12.002

Katona, G., Kaszas, A., Turi, G. F., Hajos, N., Tamas, G., Vizi, S., et al. (2011). Roller coaster scanning reveals spontaneous triggering of dendritic spikes in CA1 interneurons. *Proc. Nat. Acad. Sci. U. S. A.* 108, 2148–2153. doi: 10.1073/pnas.1009270108

Konstantoudaki, X., Papoutsi, A., Chalkiadaki, K., Poirazi, P., and Sidiropoulou, K. (2014). Modulatory effects of inhibition on persistent activity in a cortical microcircuit model. *Front. Neural Circ.* 8, 7. doi: 10.3389/fncir.2014.00007

Krueppel, R., Remy, S., and Beck, H. (2011). Dendritic integration in hippocampal dentate granule cells. *Neuron* 71, 512–528. doi: 10.1016/j.neuron.2011.05.043

Li, C., and Gulledge, A. T. (2021). NMDA receptors enhance the fidelity of synaptic integration. *Eneuro* 8, 2. doi: 10.1523/ENEURO.0396-20.2020

London, M., Schreibman, A., Häusser, M., Larkum, M. E., and Segev, I. (2002). The information efficacy of a synapse. *Nat. Neurosci.* 5, 332–340. doi: 10.1038/nn826

Losonczy, A., and Magee, J. (2006). Integrative properties of radial oblique dendrites in hippocampal CA1 pyramidal neurons. *Neuron* 50, 291–307. doi: 10.1016/j.neuron.2006.03.016

Martina, M., Vida, I., and Jonas, P. (2000). Distal initiation and active propagation of action potentials in interneuron dendrites. *Science* 287, 295–300. doi: 10.1126/science.287.5451.295

Mcbain, C. J., and Dingledine, R. (1993). Heterogeneity of synaptic glutamate receptors on CA3 stratum radiatum interneurones of rat hippocampus. *J. Physiol.* 462, 373–392. doi: 10.1113/jphysiol.1993.sp019560

Misonou, H., Mohapatra, D. P., Menegola, M., and Trimmer, J. S. (2005). Calcium- and metabolic state-dependent modulation of the voltage-dependent Kv2.1 channel regulates neuronal excitability in response to ischemia. *J. Neurosci.* 25, 11184–11193. doi: 10.1523/JNEUROSCI.3370-05.2005

Molineux, M. L., Fernandez, F. R., Mehaffey, W. H., and Turner, R. W. (2005). A-type and T-type currents interact to produce a novel spike latency-voltage relationship in cerebellar stellate cells. *J. Neurosci.* 25, 10863–10873. doi: 10.1523/JNEUROSCI.3436-05.2005

Mueller, M., and Egger, V. (2020). Dendritic integration in olfactory bulb granule cells upon simultaneous multispine activation: low thresholds for nonlocal spiking activity. *PLoS Biol.* 18, e3000873. doi: 10.1371/journal.pbio.3000873

Nevian, T., Larkum, M. E., Polsky, A., and Schiller, J. (2007). Properties of basal dendrites of layer 5 pyramidal neurons: a direct patch-clamp recording study. *Nat. Neurosci.* 10, 206–214. doi: 10.1038/nn1826

Piskorowski, R. A., and Chevaleyre, V. (2012). Synaptic integration by different dendritic compartments of hippocampal CA1 and CA2 pyramidal neurons. *Cell. Mol. Life Sci.* 69, 75–88. doi: 10.1007/s00018-011-0769-4

Poirazi, P., Brannon, T., and Mel, B. (2003). Pyramidal neuron as two-layer neural network. *Neuron* 37, 989–999. doi: 10.1016/S0896-6273(03)00149-1

Povysheva, N. V., Zaitsev, A. V., Gonzalez-Burgos, G., and Lewis, D. A. (2013). Electrophysiological heterogeneity of fast-spiking interneurons: chandelier versus basket cells. *PLoS ONE* 8, e70553. doi: 10.1371/journal.pone.0070553

Psarrou, M., Stefanou, S. S., Papoutsi, A., Tzilivaki, A., Cutsuridis, V., and Poirazi, P. (2014). A simulation study on the effects of dendritic morphology on layer V prefrontal pyramidal cell firing behavior. *Front. Cell. Neurosci.* 8, 287. doi: 10.3389/fncel.2014.00287

Ran, Y., Huang, Z., Baden, T., Schubert, T., Baayen, H., Berens, P., et al. (2020). Type-specific dendritic integration in mouse retinal ganglion cells. *Nat. Commun.* 11, 2101. doi: 10.1038/s41467-020-15867-9

Schiller, J., Major, G., Koester, H., and Schiller, Y. (2000). NMDA spikes in basal dendrites of cortical pyramidal neurons. *Nature* 404, 285–289. doi: 10.1038/35005094

Shibata, R., Nakahira, K., Shibasaki, K., Wakazono, Y., Imoto, K., and Ikenaka, K. (2000). A-type K^{+} current mediated by the Kv4 channel regulates the generation of action potential in developing cerebellar granule cells. *J. Neurosci.* 20, 4145–4155. doi: 10.1523/JNEUROSCI.20-11-04145.2000

Single, S., and Borst, A. (1998). Dendritic integration and its role in computing image velocity. *Science* 281, 1848–1850. doi: 10.1126/science.281.5384.1848

Torquatto, K. I., Menegolla, A. P., Popik, B., Casagrande, M. A., and de Oliveira Alvares, L. (2019). Role of calcium-permeable AMPA receptors in memory consolidation, retrieval and updating. *Neuropharmacology* 144:312–318. doi: 10.1016/j.neuropharm.2018.10.030

Tran-Van-Minh, A., Cazé, R. D., Abrahamsson, T., Cathala, L., Gutkin, B. S., and DiGregorio, D. A. (2015). Contribution of sublinear and supralinear dendritic integration to neuronal computations. *Front. Cell. Neurosci.* 9, 67. doi: 10.3389/fncel.2015.00067

Tukker, J. J., Lasztoczi, B., Katona, L., Roberts, J. D. B., Pissadaki, E. K., Dalezios, Y., et al. (2013). Distinct dendritic arborization and in vivo firing patterns of parvalbumin-expressing basket cells in the hippocampal area CA3. *J. Neurosci.* 33, 6809–6825. doi: 10.1523/JNEUROSCI.5052-12.2013

Tzilivaki, A., Kastellakis, G., and Poirazi, P. (2019). Challenging the point neuron dogma: FS basket cells as 2-stage nonlinear integrators. *Nat. Commun.* 10, 1–14. doi: 10.1038/s41467-019-11537-7

Tzilivaki, A., Kastellakis, G., Schmitz, D., and Poirazi, P. (2022). GABAergic interneurons with nonlinear dendrites: from neuronal computations to memory engrams. *Neuroscience* 489, 34–43. doi: 10.1016/j.neuroscience.2021.11.033

Vervaeke, K., Lrincz, A., Nusser, Z., and Silver, R. A. (2012). Gap junctions compensate for sublinear dendritic integration in an inhibitory network. *Science* 335, 1624–1628. doi: 10.1126/science.1215101

Walker, H., Lawrence, J., and McBain, C. (2002). Activation of kinetically distinct synaptic conductances on inhibitory interneurons by electrotonically overlapping afferents. *Neuron* 35, 161–171. doi: 10.1016/S0896-6273(02)00734-1

Wang, H.-X., and Gao, W.-J. (2010). Development of calcium-permeable AMPA receptors and their correlation with NMDA receptors in fast-spiking interneurons of rat prefrontal cortex. *J. Physiol.* 588, 2823–2838. doi: 10.1113/jphysiol.2010.187591

Wang, X.-J. (2010). Neurophysiological and computational principles of cortical rhythms in cognition. *Physiol. Rev.* 90, 1195–1268. doi: 10.1152/physrev.00035.2008

Wang, Y., and Liu, S.-C. (2010). Multilayer processing of spatiotemporal spike patterns in a neuron with active dendrites. *Neural Comput.* 22, 2086–2112. doi: 10.1162/neco.2010.06-09-1030

Wlodarczyk, A. I., Xu, C., Song, I., Doronin, M., Wu, Y.-W., Walker, M. C., et al. (2013). Tonic GABAA conductance decreases membrane time constant and increases EPSP-spike precision in hippocampal pyramidal neurons. *Front. Neural Circuits* 7, 205. doi: 10.3389/fncir.2013.00205

Xia, F., Richards, B. A., Tran, M. M., Josselyn, S. A., Takehara-Nishiuchi, K., and Frankland, P. W. (2017). Parvalbumin-positive interneurons mediate neocortical-hippocampal interactions that are necessary for memory consolidation. *Elife* 6, e27868. doi: 10.7554/eLife.27868

frontiers | Frontiers in Neuroscience

TYPE Original Research
PUBLISHED 11 May 2023
DOI 10.3389/fnins.2023.1198409

OPEN ACCESS

EDITED BY
Rong Wang,
Xi'an University of Science and Technology, China

REVIEWED BY
Denggui Fan,
University of Science and Technology Beijing, China
Xiang Liao,
Chongqing University, China

*CORRESPONDENCE
Jian Song
✉ songjian0505@smu.edu.cn

RECEIVED 01 April 2023
ACCEPTED 24 April 2023
PUBLISHED 11 May 2023

CITATION
Wang S, Fu Z, Sun Y, Zhang M, Chen A, Cao C and Song J (2023) Altered hemispheric asymmetry of attentional networks in patients with pituitary adenoma: an event-related potential study.
Front. Neurosci. 17:1198409.
doi: 10.3389/fnins.2023.1198409

Altered hemispheric asymmetry of attentional networks in patients with pituitary adenoma: an event-related potential study

Shuochen Wang[1,2], Zhenghao Fu[1,2], Yuanyi Sun[1,2], Meng Zhang[2], Aobo Chen[3], Chenglong Cao[3] and Jian Song[1,2]*

[1]The First School of Clinical Medicine, Southern Medical University, Guangzhou, Guangdong, China, [2]Department of Neurosurgery, The General Hospital of Central Theater Command, Wuhan, Hubei, China, [3]Department of Neurosurgery, The First Affiliated Hospital of University of Science and Technology of China, Hefei, Anhui, China

Background: Emerging evidence has been reported of attentional dysfunction in pituitary adenoma patients. However, the effect of pituitary adenomas on lateralized attention network efficiency remained to be clear. Thus, the present study aimed to investigate the impairment of lateralized attention networks in patients with pituitary adenoma.

Methods: Eighteen pituitary adenoma patients (PA group) and 20 healthy controls (HCs) were included in this study. Both behavioral results and event-related potentials (ERPs) were acquired while subjects performed the Lateralized Attention Network Test (LANT).

Results: Behavioral performances indicated the PA group had a slower reaction time and a similar error rate relative to the HCs group. Meanwhile, significantly increased executive control network efficiency suggested the dysfunction of inhibition control in PA patients. Regarding ERP results, there were no group differences in the alerting and orienting networks. The target-related P3 was significantly reduced in the PA group, suggesting an impairment of executive control function and attentional resources allocation. Moreover, the mean amplitude of P3 was significantly lateralized to the right hemisphere, and interacted with the visual field, exhibiting that the right hemisphere dominated the bilateral visual field, whereas the left hemisphere dominated the left visual field. In the specific high-conflict condition, the pattern of hemispheric asymmetry in the PA group was altered due to a mixed effect resulting from the compensatory recruitment of attentional resources in the left central parietal area and the destructive effects of hyperprolactinemia.

Conclusion: These findings suggested that, in the lateralized condition, the decreased P3 in the right central parietal area and the diminished hemispheric asymmetry under high conflict load, may serve as the potential biomarkers of attentional dysfunction in patients with pituitary adenoma.

KEYWORDS

event-related potentials, lateralized attention network test, hemispheric asymmetry, alerting, orienting, executive control, pituitary adenoma

1. Introduction

Pituitary adenoma (PA) is one of the common benign intracranial tumors of the central nervous system, accounting for almost 15% of all cases (Hauser et al., 2019; Melmed, 2020). Emerging studies have established cognitive impairments in executive control, attention, and working memory both before and after surgery in patients with pituitary adenoma (Psaras et al., 2011; Butterbrod et al., 2019; Pertichetti et al., 2020), but the underlying neurophysiological mechanisms remain unclear. The physical compression, treatment strategy, surgical approach, and especially abnormal hormone levels may be responsible for the impairment of cognitive function (Peace et al., 1997, 1998; de Oliveira et al., 2008; Tooze et al., 2009; Tooze and Sheehan, 2018). In Yao's opinion (Yao et al., 2017), prolactinoma patients exhibited decreased gray matter volume (GMV) in the left hippocampus, left orbitofrontal cortex, right middle frontal cortex, and right inferior frontal cortex, providing seminal evidence for deficits in verbal memory and executive control in patients with prolactinoma. The dysfunction of attention and inhibition control has been extensively examined in patients with pituitary adenomas based on neuropsychological scales and behavioral outcomes (Müssig et al., 2011; Pertichetti et al., 2020). To our knowledge, however, there have been few studies investigating the lateralized attentional networks in PA patients systematically.

According to the classical attention network theory, proposed by Posner and colleagues (Posner and Petersen, 1990; Petersen and Posner, 2012; Posner et al., 2019), the attention network has been divided into alerting, orienting, and executive control networks: Alerting refers to the state of obtaining and maintaining vigilance to upcoming information. This network may be associated with the right hemisphere (RH), frontal, parietal, and thalamic regions, and influenced by the norepinephrinergic system. Orienting network is for selecting specific information from the environment by focusing on one modality or location. Orienting is related to the cholinergic system and is associated with the frontal eye field (FEF), intraparietal sulcus (IPS), and other areas. Executive control network plays a major role in monitoring and resolving task-related conflicts, including error decision-making, and planning. This network primarily involved the dorsal anterior cingulate cortex and the lateral prefrontal cortex and corresponded to the dopaminergic system.

Despite their bilateral distribution, studies have shown that attentional functions might be dominated in the right hemisphere, particularly in the right parietal area (Mesulam, 1999; Brooks et al., 2014). Furthermore, for visuospatial attention, attending to one side of the visual stimuli typically corresponds to the activation of contralateral parietal areas. Based on the above findings and the ANT paradigm, Greene and colleagues proposed the LANT paradigm to assess the hemispheric asymmetry in each attention network as well as the attentional volume of each hemisphere (Greene et al., 2008). The LANT paradigm revealed the hemispheric lateralization of each attention network by rotating the original up and down target stimuli by 90° and presenting to the left and right visual fields (LVF, RVF). Previous studies of attentional networks indicated that multiple disorders, including mild traumatic brain injury (Chen et al., 2021) and attention deficit hyperactivity disorder (ADHD) (Adólfsdóttir et al., 2008; Lundervold et al., 2011), have the potential to impair attentional networks. Apart from a few studies related to stroke (Russell-Giller et al., 2021) and cerebral small vessel disease (Cao et al., 2020), to the best of our knowledge, systematic and comprehensive investigations based on the theory of the lateralized attention network in patients with pituitary adenoma were limited.

Referring to the comparable Attention Network Test (ANT) studies (Fan et al., 2002, 2005; Neuhaus et al., 2010; Williams et al., 2016), the cue-N1 component was associated with alerting and orienting networks. N1 was defined as an early visual attention component that appeared 150–250 ms after the cue stimulus and was distributed in the parietal and occipital regions. N1 was considered an early visual processing of stimulus properties, and the amplitude increased when the visual stimulus appeared in the attended spatial location. Furthermore, N1 also reflected the facilitation of early preattentive processing (Kaufman et al., 2016). Target-P3 components were associated with the executive control network and typically appeared around 250-500 ms after target presentation. P3 originated in the anterior cingulate gyrus and was located in the central parietal region, which mirrored the response inhibition process and attentional resource allocation (Polich, 2004, 2007).

In summary, in the present study, the LANT paradigm and ERPs were combined to investigate the hemispheric lateralization of attention networks in patients with pituitary adenoma. We hypothesized that (1) PA patients have significantly decreased behavioral and ERP results in attention networks; (2) Attention networks might be exhibited hemispheric asymmetry in two groups; (3) The pattern of hemispheric asymmetry in PA patients might be different from that in HCs; and (4) The serum prolactin (PRL) level may impair attention networks in patients with pituitary adenoma.

2. Materials and methods

2.1. Participants

Twenty patients with pituitary adenoma and 25 healthy adults matched for gender, age, and education were recruited from the General Hospital of Central Theater Command. Inclusion criteria for the PA group were: (1) Age: 16–55 years old; (2) Right-handedness; (3) Education: more than 6 years; (4) Tumor size: less than 30 mm; (5) Vision: normal or corrected visual acuity and visual field (VF); and (6) Pathological diagnosed with pituitary adenoma. Exclusion criteria for the PA group were: (1) Recurrent pituitary adenoma or pituitary apoplexy and (2) Had taken dopaminergic inhibitors such as bromocriptine or radiation therapy such as gamma knife before surgery. Common exclusion criteria for both groups were as follows: (1) Had taken neurological and psychotropic drugs such as dipipanone; (2) History of drug or alcohol abuse in the past 3 months before surgery; (5) Female subjects who were menstruating. Informed consent was obtained from all subjects, and the study was approved by the ethics committee of the General Hospital of Central Theater Command ([2018] 003–1).

2.2. Procedure and stimulus

The revised lateralized attention network test which was originally designed by Green et al. was conducted to measure the efficiency of attention networks within each hemisphere. Each trial, as shown in Figure 1, was first presented with a 400-1,600 ms random fixation on a white background and was followed by a 100 ms cue stimulus presented randomly. A cue-to-target interval of 400 ms was then

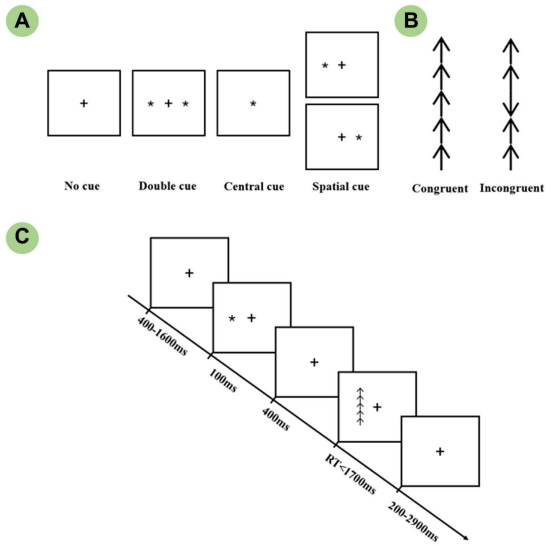

FIGURE 1
The schematic of the Lateralized Attention Network Test (LANT). **(A)** Four cue conditions: No cue, Double cue, Central cue, and Spatial cue. **(B)** Two target conditions: Congruent and Incongruent targets. **(C)** The procedure of a single trial.

presented to avoid the overlap between two adjacent ERP components. The target was presented up to 1700 ms until the subject made a response. A blank screen with fixation was presented at the end of the trial. Each trial lasted for 4,000 ms, and the subject was instructed to respond to the target as quickly as possible. The cue stimuli comprised five conditions: No cue, Central cue, Double cue, and Left and Right spatial cue. All spatial cues used in this study were validated, i.e., the target always appeared in the cued visual field. Each target stimulus was composed of a matrix of five arrows, the arrow array was displayed at 1.62° to the left or right of fixation, as well as 1.72° of each vertical side. The central arrow was flanked by arrows in the same direction as the target (Congruent condition), or in the opposite direction from the target (Incongruent). In comparison to the congruent conditions, the incongruent target induced stronger conflict interference, which, in turn, required more attentional resources. There was one practice block and four experimental blocks, with a 2 min break between each section. The experimental block consisted of 32 conditions: 4 warning cues (No cue, Central cue, Double cue, Spatial cue) × 2 target locations (Left or Right) × 2 flanker types (Congruent, Incongruent) × 2 target directions (Up or Down). The presentation was randomly selected, and each block contained 3 circles, for a total of $32 \times 3 = 96$ trials. Briefly, the whole experiment contained $4 \times 96 = 384$ valid recorded trials, which were divided into 16 condition combinations (4 cue × 2 flanker × 2 visual field), each combination consisted of 24 trials for the averaging of EEG epochs. Twenty-four trials covering each condition were randomly presented for practice until the accuracy reached over 90. The whole experiment took approximately 35 min in total.

The cue and target stimuli were presented using E-prime 2.0 software (Psychology Software Tools, Inc., Sharpsburg, PA, United States) on a 17-inch Dell monitor which was placed 60 cm away from the eyes. In a semi-dark, quiet room, all participants were instructed to quickly respond using the same hand's middle or index finger. The mouse was rotated 90° and the target direction corresponded to the upward and downward buttons. Response hand was counterbalanced with a fixed order of "right–left–right–left" across four experimental blocks, which minimized the impact of motor reaction on the hemispheric attentional functions.

2.3. Behavioral measures

Efficiencies of hemispheric attention networks were measured by comparing reaction time (RT) and error rate (ER) across conditions. Noted that responses longer than 1700 ms or shorter than 200 ms were considered delayed responses or expectancy effects and should be excluded. Therefore, lateralized network effects were calculated using the following equations, and the error rates were calculated by the same RT formula.

(1) Right alerting effect = $RT_{no\ cue} - RT_{double\ cue}$ (right target)
(2) Left alerting effect = $RT_{no\ cue} - RT_{double\ cue}$ (left target)
(3) Right orienting effect = $RT_{central\ cue} - RT_{right\ spatial\ cue}$ (right target)
(4) Left orienting effect = $RT_{central\ cue} - RT_{left\ spatial\ cue}$ (left target)
(5) Right executive control effect = $RT_{incongruent\ flanker} - RT_{congruent\ flanker}$ (right target)
(6) Left executive control effect = $RT_{incongruent\ flanker} - RT_{congruent\ flanker}$ (left target)

2.4. EEG recording and analysis

A 64-channel EEG data was recorded by ANT Neuro's eegoTM mylab EEG system and the electrode distribution was matched to the international 10–20 system. Online EEG acquisition was performed with eegoTM acquisition software, with a sampling rate of 1,000 Hz and an online bandpass of 0.3–100 Hz. The impedance was reduced below 10 KΩ, and all electrodes were referenced to the CPz electrode. Offline EEG data was analyzed with MATLAB 2020b platform and was performed with a bandpass of 1–40 Hz, as well as a notch filter at 50 Hz to remove alternative interferences. All EEG data were segmented from 200 ms pre-stimulus to 1,000 ms post-stimulus, and the baseline was corrected by the mean amplitude of the 200 ms pre-stimulus. Artifacts were removed by independent component analysis (Chaumon et al., 2015). EEG data were re-referenced to average reference, and EEG epochs were then separately extracted and averaged across conditions for each subject. Finally, the mean amplitude of ERP component was extracted for visualization of the topographic map and further statistical analysis.

2.5. Serum hormone levels assessment

In patients with pituitary adenoma, rapid peripheral venous blood samples were taken at 8:00–9:30 am to minimize the effect of hormonal circadian rhythms. Chemiluminescent immunoassays (Roche, Cobas 8,000, Switzerland) were used to determine the serum prolactin level (ng/ml). Serum was also diluted 1:100 if necessary to rule out hook effects.

2.6. Statistical analysis

Behavioral and EEG data were analyzed using the statistical software SPSS 27.0. The demographic characteristics of the two groups were compared by independent samples *t*-test (e.g., age, education) and Chi-square test (gender). Behavioral data were extracted and summarized for each condition, and the mean reaction time and the mean error rate of the subjects were computed. Condition-level analysis: All data were included in a 4-way repeated-measures ANOVA for further analysis. 4 Cue (No cue, Central cue, Double cue, Spatial cue) × 2 Target (Congruent, Incongruent) × 2 Visual field (Left and Right) × 2 Group (PA and HCs). Network-level analysis: A 2-way repeated-measures ANOVA (2 Visual field × 2 Group) was conducted for each network based on the network effect results.

The EEG segments were averaged separately for 4 cues and 2 target stimuli. Alerting network: The mean amplitude of N1 in the averaged left (P7) and right (P8) parietal regions was extracted and included in a 2-way repeated-measures ANOVA (2 Cue type × 2 Group). Orienting network: The same N1 component was used to measure the orienting effect. Given the cue stimuli were presented in both visual fields, the factors of visual field (LVF, RVF) and hemisphere (Left hemisphere (LH), Right hemisphere (RH)) were included in a 3-way repeated-measures ANOVA (3 Cue type × 2 hemisphere × 2 group). Executive control network: Resembling the orienting network, the visual field, and the hemisphere factors were added in a 4-way repeated-measures ANOVA (2 Target type × 2 visual field × 2 hemisphere × 2 group). Multivariate test results were examined if violations of sphericity. *Post-hoc* simple effect results were corrected by the Bonferroni approach. At the same time, a Spearman correlation analysis was performed to investigate the relationship between serum PRL levels and attentional function. $\alpha = 0.05$.

3. Results

3.1. Demographic characteristics

Twenty patients with pituitary adenomas were recruited in this study, and 2 were excluded because of excessive artifacts in the EEG data. Twenty-five healthy controls were recruited, 1 was excluded due to high error rates, and 4 were excluded due to poor data quality. Ultimately, 18 patients and 20 healthy controls matched for age, sex, and education were included in this study. Detailed characteristics are shown in Table 1.

3.2. Behavioral results

3.2.1. Condition-level analysis

RT: A 2 group × 4 cue × 2 flanker ×2 visual field 4-way repeated-measures ANOVA was conducted to investigate the group differences across conditions. A main group effect was found [F (1,36) = 13.815, $p = 0.001$], Post-hoc analysis revealed that the reaction time in the PA group was longer than HCs. [**PA:** (713.840 ± 21.851) ms; **HCs:** (601.888 ± 20.730) ms]. Meanwhile, there was a significant main effect of cue and flanker condition [**Cue:** F (3,34) = 247.788, $p < 0.001$; **Flanker:** F (1,36) = 299.561, $p < 0.001$]. Further analysis indicated a significant group interaction effect with cue and flanker. [**Cue*Group:** F (3,34) = 2.966, $p = 0.046$; **Flanker*Group:** F (1,36) = 18.533, $p < 0.001$]. Simple analysis suggested that RTs were significantly longer in the PA group for all types of cues and flankers ($p < 0.01$).

ER: Resembling ANOVA was conducted, and the results revealed a significant main cue effect [F (3,108) = 6.264, $p < 0.001$] and main flanker effect [F (1,36) = 12.615, $p = 0.001$]. For both groups, the ANOVAs revealed a flanker × cue interaction effect. [F (3,108) = 2.736, $p = 0.047$]. In contrast, there was no significant difference between two groups [F (1,36) = 0.625, $p = 0.434$].

3.2.2. Network-level analysis

RT: The ANOVA of alerting network exhibited a significant main group effect. [F (1,36) = 8.460, $p = 0.006$], with the HCs group showing greater network efficiency than the PA group [**PA:** (33.041 ± 4.884) ms; **HCs:** (52.624 ± 4.634) ms]. The main visual field effect was significant [F (1,36) = 7.003, $p = 0.012$], showing a left visual field bias in alerting network efficiency [**R:** (35.157 ± 4.528) ms; **L:** (50.507 ± 4.357) ms]. For the orienting network, both main group effect and group interaction effects were not reached significant differences. [F (1,36) = 0.434, $p = 0.514$]. Concerning the executive control network, a significant difference was found between the two groups [F (1,36) = 17.251, $p < 0.001$], with the PA group having a significantly greater efficiency. [**PA:** (104.924 ± 7.872) ms; **HCs:** (59.858 ± 7.468) ms].

ER: For each attentional subnetwork, no significant main effects or interaction effects were found in the ER analysis. [**Alert:** F (1,36) = 0.045, $p = 0.832$; **Orient:** F (1,36) = 0.037, $p = 0.849$; **Executive:** F (1,36) = 0.339, $p = 0.564$].

3.3. Electrophysiological results

3.3.1. Alerting (no cue vs. double cue)

The waveforms of ERPs evoked by no cue and double cue are depicted in Figure 2. The mean amplitudes of cue-locked N1 in the time window of 180–230 ms were averaged and extracted for both temporoparietal regions (P7, P8). Data were calculated for a 2 group (PA vs. HCs) × 2 cue (No cue vs. Double cue) repeated-measures ANOVA. Although the results indicated that both groups showed the main cue effect [F (1,36) = 85.585, $p < 0.001$], no group differences were found in the alerting network [F (1,36) = 0.115, $p = 0.736$].

3.3.2. Orienting (central cue vs. spatial cue)

Figure 3 shows ERPs evoked by central and spatial cues in two groups. Given the lateralization of the orienting network, bilateral temporoparietal regions (Left-P7, Right-P8) were considered for extracting the mean amplitude of N1 within the defined time window of 180–230 ms. The ANOVA results showed a significant cue effect

TABLE 1 Comparison of the demographic characteristics in both groups.

	HCs	Patients	*p*
N	20	18	/
Females/Males	8/12	12/6	0.100
Age (years) (M ± SD)	34.55 ± 11.048	38.78 ± 10.619	0.238
Education (years) (M ± SD)	14.45 ± 3.332	12.67 ± 3.531	0.118

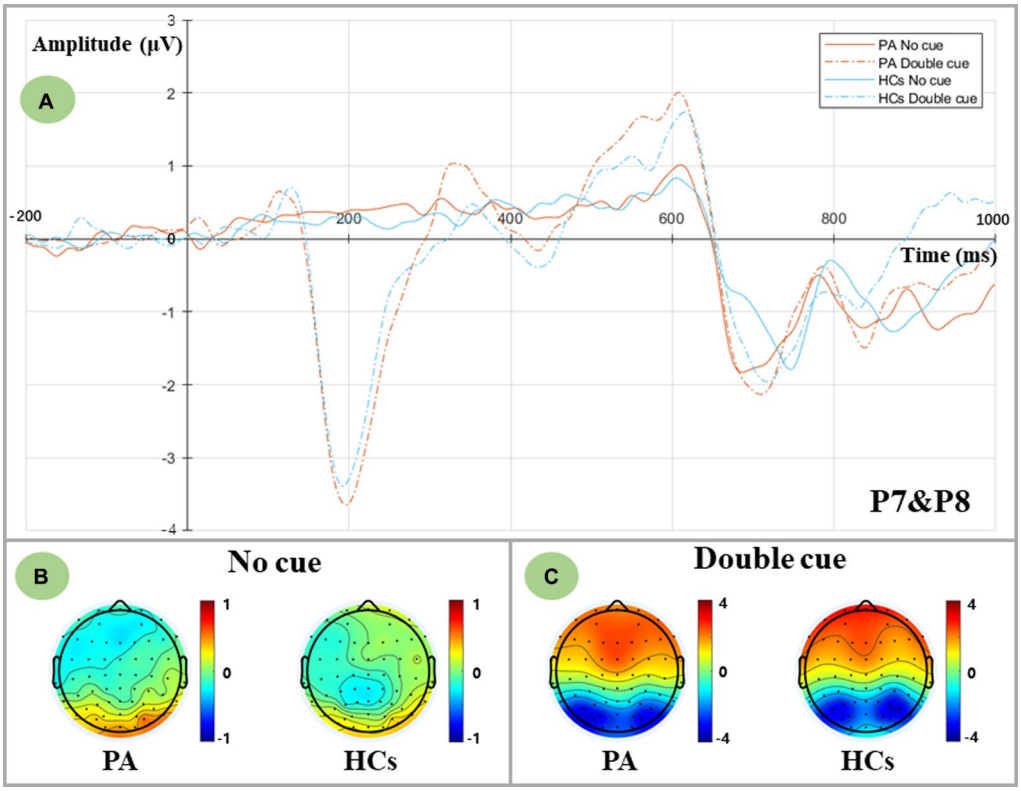

FIGURE 2
Alerting-related N1 components as measured at averaged P7 and P8 electrodes and topographic voltage maps for two groups. **(A)** Grand-averaged N1 components at averaged P7 and P8 electrodes. PA group: red lines; HCs group: blue lines; No cue condition: solid lines; Double cue condition: dashed lines. **(B)** Topographic voltage maps in the no cue condition for both groups. **(C)** Topographic voltage maps in the double cue condition for both groups.

and a Cue×Hemisphere interaction [**Cue:** F (2,35) = 13.493, $p < 0.001$; **Cue*Hemisphere:** F (2,35) = 70.476, $p < 0.001$]. Post-hoc simple effect analysis revealed a larger N1 amplitude in the central cue compared to the two spatial cues [Central cue: (−2.122 ± 0.311) μV; Right cue: (−1.643 ± 0.243) μV; Left cue: (−1.442 ± 0.245) μV]. Regarding the interaction effects, in the central cue condition, a similar distribution of N1 was found in both left and right hemispheres [F (1,36) = 0.693, $p = 0.411$], whereas the unilateral visual field orienting response (spatial cue) elicited contralateral parietal activation [**Right cue:** F (1,36) = 42.566, $p < 0.001$; **Left cue:** F (1,36) = 42.565, $p < 0.001$]. In contrast, no group effect was found in the orienting network [F (1,36) = 0.017, $p = 0.898$], suggesting that comparable orienting functions were elicited in both groups.

3.3.3. Executive control (incongruent vs. congruent)

The incongruent and congruent conditions are shown in Figure 4. We defined the time window of P3 as 290–400 ms based on the peak latency. To further examine the distribution of P3 in both hemispheres, P1 and P3 were categorized as the left central parietal area (LCP), and P2 and P4 were categorized as the right central parietal area (RCP). The ANOVA results indicated that there was a significant main group effect and a flanker×group interaction [**Group:** F (1,36) = 6.854, $p = 0.013$; **Flanker*Group:** F (1,36) = 5.283, $p = 0.027$]. Post-hoc analysis revealed that the P3 amplitude of the HCs was larger than that of the PA [HCs: (1.179 ± 0.284) μV; PA: (0.098 ± 0.300) μV], and both flanker conditions exhibited an increase in the amplitude of P3 in the HCs compared to the PA group [**Incon:** F (1,36) = 4.796, $p = 0.035$; **Con:** F (1,36) = 9.065, $p = 0.005$]. Notably, a significant main effect of the hemisphere has been observed in the ANOVA results and interacted with the visual field [**Hemisphere:** F (1,36) = 7.162, $p = 0.011$; **VF*Hemisphere:** F (1,36) = 11.254, $p = 0.002$]. Simple effect analysis showed significant lateralization of the right hemispheric which indicated a larger P3 amplitude in the RCP compared with the LCP [**LH:** (0.426 ± 0.229) μV; **RH:** (0.851 ± 0.213) μV]. Moreover, no difference in P3 distribution was observed when the target presented in the LVF [F (1,36) = 0.091, $p = 0.764$], while significant RCP-biased P3 distribution was observed when the target presented in the RVF [F (1,36) = 18.479, $p < 0.001$], showing an asymmetric distribution of P3.

Furthermore, a significant main group effect was found in the flanker×VF×hemisphere interaction [F (1,36) = 7.544, $p = 0.009$], and a further simple effect analysis indicated that regardless of the flanker conditions and the different visual fields, HCs elicited a larger mean P3 amplitude in the RCP compared to the PA group ($p < 0.05$). Considering the incongruent right visual field, a consistent RCP dominance of the P3 was found in the HCs [F (1,36) = 16.431, $p < 0.001$], whereas a uniform distribution of P3 was found in the PA group [F (1,36) = 3.669, $p = 0.063$].

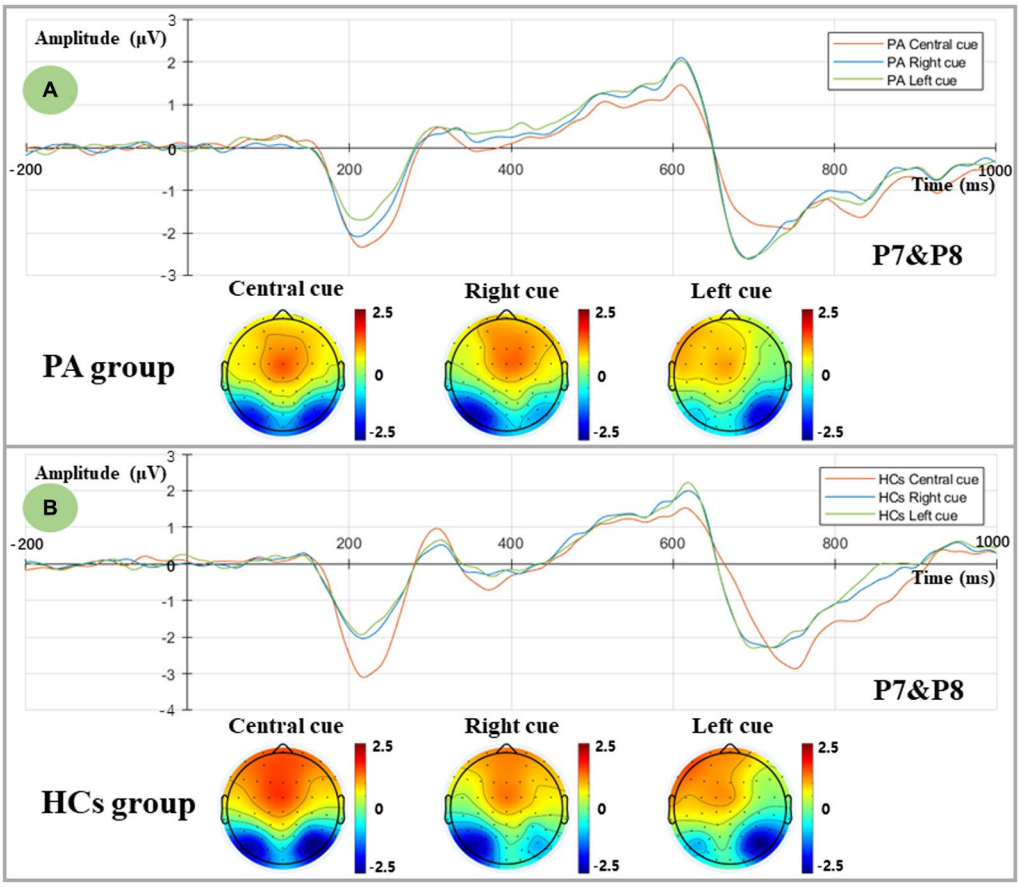

FIGURE 3
Orienting-related N1 components as measured at averaged P7 and P8 electrodes and topographic voltage maps for two groups. **(A)** Grand-averaged N1 components and topographic voltage maps in the central, right, and left spatial cue conditions for the PA group. Central cue: red line; Right spatial cue: blue line; Left spatial cue: green line. **(B)** Grand-averaged N1 components and topographic voltage maps in the central, right, and left spatial cue conditions for the HCs group. Central cue: red line; Right spatial cue: blue line; Left spatial cue: green line.

3.4. Correlation analysis results

In the PA group, a bivariate Spearman correlation analysis was performed between the serum PRL level and mean amplitude of P3 across conditions. The results revealed that a positive correlation was observed between the serum PRL level and the P3 amplitude of the LCP in the incongruent RVF conditions ($r = 0.498$, $p = 0.035$; Figure 5).

3.5. Exploration results

Behavioral findings depicted increased efficiency of the executive control network in the PA group. Reversed P3 results were demonstrated, suggesting executive dysfunction in the PA group. Thus, to resolve the conflict results, we conducted another 2 visual field × 2 flanker × 2 group, 3-way repeated-measures ANOVA. The results revealed a main group effect and a significant flanker×group interaction [**Group:** $F(1,36) = 14.671$, $p < 0.001$; **Flanker*Group:** $F(1,36) = 17.251$, $p < 0.001$]. Simple effect analysis results exhibited a prolonged RT in the PA group [**PA:** (716.488 ± 21.729) ms; **HCs:** (601.762 ± 20.614) ms]. Furthermore, PA patients responded more slowly than HCs in both flanker conditions [**Incon:** $F(1,36) = 18.902$, $p < 0.001$; **Con:** $F(1,36) = 9.925$, $p = 0.003$]. In contrast, the target effect size (RT_{incon} - RT_{con}) was significantly larger in the PA group relative to the HCs group [**PA:** (104.924 ± 7.872) ms; **HCs:** (59.858 ± 7.468) ms].

4. Discussion

We combined a lateralized attention network paradigm with event-related potential techniques to examine the impairment and lateralization of each attention subnetwork in pituitary adenoma patients. In terms of behavioral performance, the temporal and spatial cue effects, as well as the flanker effect, could be evoked significantly by the LANT task. In line with previous findings based on ANT and LANT paradigms (Greene et al., 2008; Neuhaus et al., 2010; Thiebaut de Schotten et al., 2011), the decreased reaction time reflected the facilitatory effect of temporal and spatial cues on target responses. Both groups exhibited similar error rates in each subnetwork, but the PA group showed prolonged RTs in all conditions relative to HCs. To maintain relatively high accuracy for the same cue and target stimuli, excessed attentional resources have to pay for conflict resolution. Thus, we believed that the pituitary adenoma was more likely to impair global attentional processing, which has been demonstrated in previous studies (Chen et al., 2022).

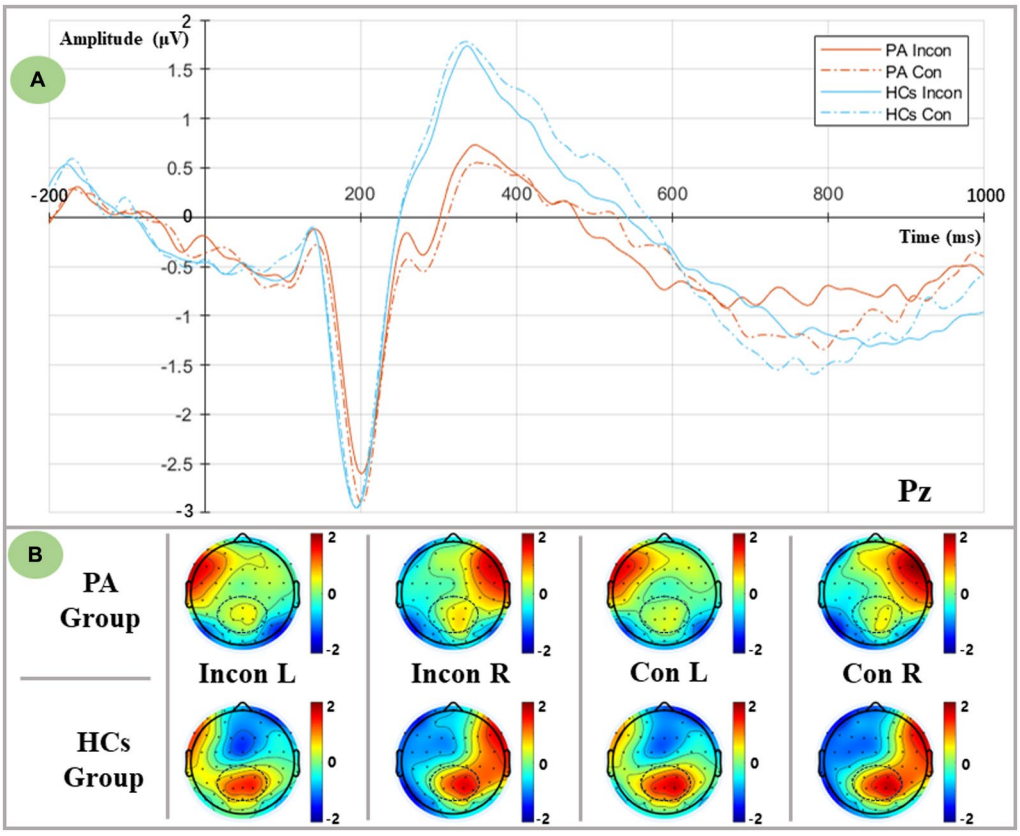

FIGURE 4
Executive-related P3 components as measured at the Pz electrode, and lateralized topographic voltage maps between groups and conditions. **(A)** Grand averaged P3 components from the Pz electrode in both flanker conditions. PA group: red lines; HCs group: blue lines; Incongruent condition: solid lines; Congruent condition: dashed lines. **(B)** Lateralized topographic voltage maps between two groups in (1) Incongruent left spatial condition, (2) Incongruent right spatial condition, (3) Congruent left spatial condition, and (4) Congruent right spatial condition.

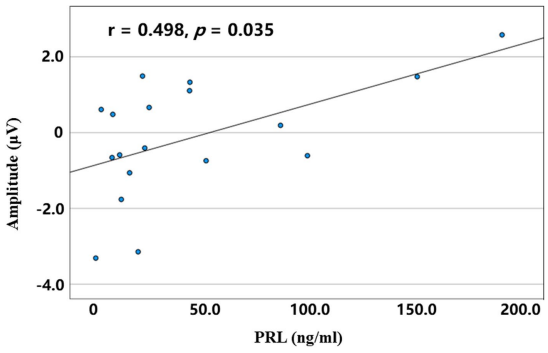

FIGURE 5
The correlation between serum PRL level and mean amplitudes of the left central parietal P3 in the incongruent right spatial condition for the PA group.

Network efficiency results revealed that the PA group had lower alerting network efficiency but higher executive control network efficiency relative to the HCs. Given the differences in the visual field, a significant LVF alerting effect was found in the PA group. Although some studies have shown a significant LVF-RH dominance for alerting (Heilman and Van Den Abell, 1979; Funnell et al., 2003), these warning cues were only presented on the unilateral visual field instead of bilateral visual fields. In line with the present study, the results of Asanowicz (Asanowicz et al., 2012) indicated no visual field differences in the alerting network efficiency, which was induced by a revised LANT paradigm. Therefore, the visual field differences in alerting network in the PA group could be explained by the small sample size and the heterogeneity of tumor types. Regarding the inconsistent alerting network results in the N1, we hypothesized that RT was an indicator that measured alerting indirectly, Because RT reflected the full stages of cognition from receiving warning signals, arousing the alerting state to making a response ultimately. ERPs, on the other hand, can capture and quantify the alerting state specifically, and may not be predicted accurately by the behavioral results.

Although greater executive control efficiency was found in the PA group compared to HCs, further results from the ANOVA revealed that the PA group had prolonged RTs in both flanker conditions, and the difference was still greater than the HCs. Whereas the PA group responded slower in both target conditions, and significantly longer RTs were observed in the PA group when an incongruent condition was presented. Thus, we believed that the smaller efficiency of the executive control network indicated greater executive functions, which was consistent with previous evidence explained by the right hemisphere specialization in executive functions (Milham et al., 2001; Asanowicz et al., 2012). Overall, we hypothesized that greater

efficiency of the executive control network corresponded to worse executive functions, indicating dysfunction of inhibition control in the PA group.

P3 modulated the inhibition control processes to the target stimuli, as well as the allocation of attentional resources (Polich, 2007; Kratz et al., 2011). In the HCs, the direction of P3 evoked by the target was opposite to RT, with larger P3 amplitudes corresponding to shorter RTs, which may be interpreted as task difficulty (Polich, 1987). More difficult tasks required greater attentional demands and evoked smaller P3 components, in other words, decreased P3 components mirrored the limitation of attentional capacity. Therefore, reduced P3 amplitudes across conditions in the PA group were indicative of executive control dysfunction and decreased attention allocation, which was supported by previous findings in PA patients (Tooze et al., 2009). The LANT task provided a notable advantage for investigating the lateralization of attention networks. The stimuli in the ANT task were presented on the midline, thus no visual field differences were induced, whereas the stimuli in the LANT task were presented in both visual fields and might be induced by the hemispheric differences in the P3 component. Studies have found a right hemisphere dominance in executive functions, whereas the left hemisphere has been shown to play an important role in semantic information processing (MacLeod, 1991; Russell-Giller et al., 2021). Therefore, the RCP distribution of the P3 component in the present study supported the RH dominance theory of executive function. Furthermore, the ANOVA results also exhibited a significant VF × hemisphere interaction, which indicated that the RH dominated the bilateral visual field information, while the LH only predominantly processed the left visual field information. The interaction results partially supported the theory of hemispheric lateralization (Nobre et al., 1997). Indeed, studies with a rapid serial visual presentation (RSVP) task have demonstrated that larger RH P3 was evoked in the RVF, whereas the LVF predominantly evoked the P3 in the LH, indicating a significant ipsilateral activation (Zhang et al., 2022). Further efforts at lateralization were needed to interpret the potential VF asymmetry of the executive control network.

Surprisingly, the 4-way (Flanker×VF × Hemisphere×Group) ANOVA ERPs results showed a main group effect in the pattern of hemispheric asymmetry when the flanker factor was included. Unlike the HCs group with a right hemispheric dominance when an incongruent target presented on the RVF, the PA group manifested a bilateral distribution of the P3. One reasonable interpretation was that reduced RCP capacity to RVF stimuli led to a compensatory activation in the LCP, highlighting the recruitment of resources from the non-task-dominant hemisphere. This view was consistent with Paitel's findings for age-related alteration in inhibitory control, whereas compensatory recruitment occurred at low-moderate task demands, which was indicative of depleted neural reserves (Paitel and Nielson, 2021). However, different from the stop-signal task (SST), the P3 component evoked by LANT was correlated with the allocation of attentional resources and conflict resolution. Therefore, under high attentional demand, additional contralateral hemispheric resources of attention were recruited for task response, leading to enhanced activation in the LCP and the absence of RH dominance. In Weissman and Welcome's view (Weissman and Banich, 2000; Welcome and Chiarello, 2008), increasing task difficulty required the recruitment of both hemispheres, resulting in an attenuated hemispheric asymmetry. Overall, to overcome the decreased attentional function in the RCP under high conflict conditions, attentional resources in the LCP were required in patients with pituitary adenomas, which led to the elimination of the RH-dominated pattern.

This pattern of contralateral activation in the orienting network was consistent with previous evidence (Hill-Jarrett et al., 2015). Unfortunately, however, the pattern of N1 activation was similar in both groups, suggesting that PA patients may preserve adequate orienting function. Retinal eccentricity modulated attentional demands (Beaton and Blakemore, 1981; Asanowicz et al., 2012), and larger eccentricities may make targets difficult to discriminate and require additional attentional resources. Therefore, in the present study, cues and target stimuli may not be presented peripherally enough for allocating resources in orienting. The greater horizontal distance of stimuli presentation and increased differentiation of orienting networks between groups may be beneficial for the further investigation in functional status of orienting networks in PA patients.

Lastly, a significant negative correlation between serum PRL levels and executive functions was found in prolactinoma patients, suggesting the toxic effect of hyperprolactinemia on cognitive functions (Yao et al., 2017; Chen et al., 2022). Meanwhile, the absence of lateralization in the PA group may result from compound factors that mainly contained the compensatory effect of LH and the destructive effect of hyperprolactinemia. The former enhanced the recruitment of attentional resources, and the latter may attenuate the standard lateralized activation pattern and reduce the efficiency of the executive control network.

5. Conclusion

The present study provided behavioral and electrophysiological evidence of alteration in lateralized attention networks evoked by the LANT paradigm in patients with pituitary adenoma. No ERP differences were found in alerting and orienting network, except for a specialized pattern of contralateral activation in orienting N1 component. More importantly, the executive network P3 exhibited lateralization to RH, and decreased P3 amplitude in the PA group revealed impairment of inhibition control and reduced attentional resource allocation. Moreover, attenuated hemispheric asymmetry of P3 was observed in PA patients, which may be attributed to the mixed effect including the compensatory recruitment of attentional resources in LCP and the destructive effects of hyperprolactinemia. These findings suggested that, in the lateralized condition, the decreased P3 in the RCP and the diminished hemispheric asymmetry under high conflict load, may serve as the potential biomarkers of attentional dysfunction in patients with pituitary adenoma. In addition, the findings above provide further evidence for functional recovery in post-surgery pituitary adenoma patients.

Data availability statement

The original contributions presented in the study are included in the article/supplementary material, further inquiries can be directed to the corresponding authors.

Ethics statement

The studies involving human participants were reviewed and approved by the Ethics Committee of the General Hospital of Central Theater Command. Written informed consent to participate in this study was provided by the participants' legal guardian/next of kin.

Author contributions

SW proposed and performed the present study, and contributed to collecting and analyzing the experimental data, as well as writing the manuscript. ZF reviewed the manuscript and suggested article revisions. YS contributed to collecting data and writing code. MZ provided clinical guidance. AC and CC contributed to designing the experiment. JS supervised and funded the present study. All authors contributed to the article and approved the submitted version.

Funding

The funding of the present study was provided by the National Natural Science Foundation of China (81870863).

Conflict of interest

The authors declare that the research was conducted in the absence of any commercial or financial relationships that could be construed as a potential conflict of interest.

Publisher's note

References

Adólfsdóttir, S., Sørensen, L., and Lundervold, A. J. (2008). The attention network test: a characteristic pattern of deficits in children with ADHD. *Behav. Brain Funct.* 4:9. doi: 10.1186/1744-9081-4-9

Asanowicz, D., Marzecová, A., Jaśkowski, P., and Wolski, P. (2012). Hemispheric asymmetry in the efficiency of attentional networks. *Brain Cogn.* 79, 117–128. doi: 10.1016/j.bandc.2012.02.014

Beaton, A., and Blakemore, C. (1981). Orientation selectivity of the human visual system as a function of retinal eccentricity and visual hemifield. *Perception* 10, 273–282. doi: 10.1068/p100273

Brooks, J. L., Della Sala, S., and Darling, S. (2014). Representational pseudoneglect: a review. *Neuropsychol. Rev.* 24, 148–165. doi: 10.1007/s11065-013-9245-2

Butterbrod, E., Gehring, K., Voormolen, E. H., Depauw, P., Nieuwlaat, W. A., Rutten, G. M., et al. (2019). Cognitive functioning in patients with nonfunctioning pituitary adenoma before and after endoscopic endonasal transsphenoidal surgery. *J. Neurosurg.* 133, 709–716. doi: 10.3171/2019.5.Jns19595

Cao, S., Zhang, J., Wang, Z., Pan, W., Tian, Y., Hu, P., et al. (2020). Laterality of Attentional networks in patients with cerebral small vessel disease. *Front. Aging Neurosci.* 12:21. doi: 10.3389/fnagi.2020.00021

Chaumon, M., Bishop, D. V., and Busch, N. A. (2015). A practical guide to the selection of independent components of the electroencephalogram for artifact correction. *J. Neurosci. Methods* 250, 47–63. doi: 10.1016/j.jneumeth.2015.02.025

Chen, A., Cao, C., Liu, B., Wang, S., Wu, S., Xu, G., et al. (2022). Hyperprolactinemia associated with Attentional processing and interference control impairments in patients with Prolactinomas. *Brain Sci.* 12:1091. doi: 10.3390/brainsci12081091

Chen, A., Zhang, Z., Cao, C., Lu, J., Wu, S., Ma, S., et al. (2021). Altered attention network in paratroopers exposed to repetitive subconcussion: evidence based on behavioral and event-related potential results. *J. Neurotrauma* 38, 3306–3314. doi: 10.1089/neu.2021.0253

de Oliveira, C., Naliato, E., Dutra Violante, A. H., Caldas, D., Lamounier Filho, A., Rezende Loureiro, C., et al. (2008). Quality of life in women with microprolactinoma treated with dopamine agonists. *Pituitary* 11, 247–254. doi: 10.1007/s11102-008-0091-9

Fan, J., McCandliss, B. D., Fossella, J., Flombaum, J. I., and Posner, M. I. (2005). The activation of attentional networks. *NeuroImage* 26, 471–479. doi: 10.1016/j.neuroimage.2005.02.004

Fan, J., McCandliss, B. D., Sommer, T., Raz, A., and Posner, M. I. (2002). Testing the efficiency and independence of attentional networks. *J. Cogn. Neurosci.* 14, 340–347. doi: 10.1162/089892902317361886

Funnell, M. G., Corballis, P. M., and Gazzaniga, M. S. (2003). Temporal discrimination in the split brain. *Brain Cogn.* 53, 218–222. doi: 10.1016/s0278-2626(03)00113-1

Greene, D. J., Barnea, A., Herzberg, K., Rassis, A., Neta, M., Raz, A., et al. (2008). Measuring attention in the hemispheres: the lateralized attention network test (LANT). *Brain Cogn.* 66, 21–31. doi: 10.1016/j.bandc.2007.05.003

Hauser, B. M., Lau, A., Gupta, S., Bi, W. L., and Dunn, I. F. (2019). The Epigenomics of pituitary adenoma. *Front Endocrinol (Lausanne)* 10:290. doi: 10.3389/fendo.2019.00290

Heilman, K. M., and Van Den Abell, T. (1979). Right hemispheric dominance for mediating cerebral activation. *Neuropsychologia* 17, 315–321. doi: 10.1016/0028-3932(79)90077-0

Hill-Jarrett, T. G., Gravano, J. T., Sozda, C. N., and Perlstein, W. M. (2015). Visuospatial attention after traumatic brain injury: the role of hemispheric specialization. *Brain Inj.* 29, 1617–1629. doi: 10.3109/02699052.2015.1075155

Kaufman, D. A., Sozda, C. N., Dotson, V. M., and Perlstein, W. M. (2016). An event-related potential investigation of the effects of age on alerting, orienting, and executive function. *Front. Aging Neurosci.* 8:99. doi: 10.3389/fnagi.2016.00099

Kratz, O., Studer, P., Malcherek, S., Erbe, K., Moll, G. H., and Heinrich, H. (2011). Attentional processes in children with ADHD: an event-related potential study using the attention network test. *Int. J. Psychophysiol.* 81, 82–90. doi: 10.1016/j.ijpsycho.2011.05.008

Lundervold, A. J., Adolfsdottir, S., Halleland, H., Halmøy, A., Plessen, K., and Haavik, J. (2011). Attention network test in adults with ADHD--the impact of affective fluctuations. *Behav. Brain Funct.* 7:27. doi: 10.1186/1744-9081-7-27

MacLeod, C. M. (1991). Half a century of research on the Stroop effect: an integrative review. *Psychol. Bull.* 109, 163–203. doi: 10.1037/0033-2909.109.2.163

Melmed, S. (2020). Pituitary-tumor Endocrinopathies. *N. Engl. J. Med.* 382, 937–950. doi: 10.1056/NEJMra1810772

Mesulam, M. M. (1999). Spatial attention and neglect: parietal, frontal and cingulate contributions to the mental representation and attentional targeting of salient extrapersonal events. *Philos. Trans. R. Soc. Lond. Ser. B Biol. Sci.* 354, 1325–1346. doi: 10.1098/rstb.1999.0482

Milham, M. P., Banich, M. T., Webb, A., Barad, V., Cohen, N. J., Wszalek, T., et al. (2001). The relative involvement of anterior cingulate and prefrontal cortex in attentional control depends on nature of conflict. *Brain Res. Cogn. Brain Res.* 12, 467–473. doi: 10.1016/s0926-6410(01)00076-3

Müssig, K., Besemer, B., Saur, R., Klingberg, S., Häring, H. U., Gallwitz, B., et al. (2011). Deteriorated executive functions in patients with successful surgery for pituitary adenomas compared with other chronically ill patients. *J. Int. Neuropsychol. Soc.* 17, 369–375. doi: 10.1017/s1355617710001645

Neuhaus, A. H., Urbanek, C., Opgen-Rhein, C., Hahn, E., Ta, T. M., Koehler, S., et al. (2010). Event-related potentials associated with attention network test. *Int. J. Psychophysiol.* 76, 72–79. doi: 10.1016/j.ijpsycho.2010.02.005

Nobre, A. C., Sebestyen, G. N., Gitelman, D. R., Mesulam, M. M., Frackowiak, R. S., and Frith, C. D. (1997). Functional localization of the system for visuospatial attention using positron emission tomography. *Brain* 120, 515–533. doi: 10.1093/brain/120.3.515

Paitel, E. R., and Nielson, K. A. (2021). Temporal dynamics of event-related potentials during inhibitory control characterize age-related neural compensation. *Symmetry (Basel)* 13:2323. doi: 10.3390/sym13122323

Peace, K. A., Orme, S. M., Padayatty, S. J., Godfrey, H. P., and Belchetz, P. E. (1998). Cognitive dysfunction in patients with pituitary tumour who have been treated with transfrontal or transsphenoidal surgery or medication. *Clin. Endocrinol.* 49, 391–396. doi: 10.1046/j.1365-2265.1998.00543.x

Peace, K. A., Orme, S. M., Thompson, A. R., Padayatty, S., Ellis, A. W., and Belchetz, P. E. (1997). Cognitive dysfunction in patients treated for pituitary tumours. *J. Clin. Exp. Neuropsychol.* 19, 1–6. doi: 10.1080/01688639708403831

Pertichetti, M., Serioli, S., Belotti, F., Mattavelli, D., Schreiber, A., Cappelli, C., et al. (2020). Pituitary adenomas and neuropsychological status: a systematic literature review. *Neurosurg. Rev.* 43, 1065–1078. doi: 10.1007/s10143-019-01134-z

Petersen, S. E., and Posner, M. I. (2012). The attention system of the human brain: 20 years after. *Annu. Rev. Neurosci.* 35, 73–89. doi: 10.1146/annurev-neuro-062111-150525

Polich, J. (1987). Task difficulty, probability, and inter-stimulus interval as determinants of P300 from auditory stimuli. *Electroencephalogr. Clin. Neurophysiol.* 68, 311–320. doi: 10.1016/0168-5597(87)90052-9

Polich, J. (2004). Clinical application of the P300 event-related brain potential. *Phys. Med. Rehabil. Clin. N. Am.* 15, 133–161. doi: 10.1016/s1047-9651(03)00109-8

Polich, J. (2007). Updating P300: an integrative theory of P3a and P3b. *Clin. Neurophysiol.* 118, 2128–2148. doi: 10.1016/j.clinph.2007.04.019

Posner, M. I., and Petersen, S. E. (1990). The attention system of the human brain. *Annu. Rev. Neurosci.* 13, 25–42. doi: 10.1146/annurev.ne.13.030190.000325

Posner, M. I., Rothbart, M. K., and Ghassemzadeh, H. (2019). Restoring attention networks. *Yale J. Biol. Med.* 92, 139–143.

Psaras, T., Milian, M., Hattermann, V., Gerlach, C., and Honegger, J. (2011). Executive functions recover earlier than episodic memory after microsurgical transsphenoidal resection of pituitary tumors in adult patients – a longitudinal study. *J. Clin. Neurosci.* 18, 1340–1345. doi: 10.1016/j.jocn.2011.01.027

Russell-Giller, S., Wu, T., Spagna, A., Dhamoon, M., Hao, Q., and Fan, J. (2021). Impact of unilateral stroke on right hemisphere superiority in executive control. *Neuropsychologia* 150:107693. doi: 10.1016/j.neuropsychologia.2020.107693

Thiebaut de Schotten, M., Dell'Acqua, F., Forkel, S. J., Simmons, A., Vergani, F., Murphy, D. G., et al. (2011). A lateralized brain network for visuospatial attention. *Nat. Neurosci.* 14, 1245–1246. doi: 10.1038/nn.2905

Tooze, A., Gittoes, N. J., Jones, C. A., and Toogood, A. A. (2009). Neurocognitive consequences of surgery and radiotherapy for tumours of the pituitary. *Clin. Endocrinol.* 70, 503–511. doi: 10.1111/j.1365-2265.2008.03464.x

Tooze, A., and Sheehan, J. P. (2018). Neurocognitive changes in pituitary adenoma patients after gamma knife radiosurgery. *J. Neurosurg.* 129, 55–62. doi: 10.3171/2018.7.Gks181595

Weissman, D. H., and Banich, M. T. (2000). The cerebral hemispheres cooperate to perform complex but not simple tasks. *Neuropsychology* 14, 41–59. doi: 10.1037//0894-4105.14.1.41

Welcome, S. E., and Chiarello, C. (2008). How dynamic is interhemispheric interaction? Effects of task switching on the across-hemisphere advantage. *Brain Cogn.* 67, 69–75. doi: 10.1016/j.bandc.2007.11.005

Williams, R. S., Biel, A. L., Wegier, P., Lapp, L. K., Dyson, B. J., and Spaniol, J. (2016). Age differences in the attention network test: evidence from behavior and event-related potentials. *Brain Cogn.* 102, 65–79. doi: 10.1016/j.bandc.2015.12.007

Yao, S., Song, J., Gao, J., Lin, P., Yang, M., Zahid, K. R., et al. (2017). Cognitive function and serum hormone levels are associated with gray matter volume decline in female patients with Prolactinomas. *Front. Neurol.* 8:742. doi: 10.3389/fneur.2017.00742

Zhang, S., Chen, X., Wang, Y., Liu, B., and Gao, X. (2022). Visual field inhomogeneous in brain-computer interfaces based on rapid serial visual presentation. *J. Neural Eng.* 19:016015. doi: 10.1088/1741-2552/ac4a3e

frontiers | Frontiers in Neuroscience

TYPE Original Research
PUBLISHED 16 May 2023
DOI 10.3389/fnins.2023.1191683

OPEN ACCESS

EDITED BY
Jiajia Li,
Xi'an University of Architecture and Technology, China

REVIEWED BY
Haitao Yu,
Tianjin University, China
Jia Zhao,
Southwest University, China

*CORRESPONDENCE
Liyuan Zhang
✉ LiyuanZhang@bjut.edu.cn

†These authors have contributed equally to this work

RECEIVED 22 March 2023
ACCEPTED 14 April 2023
PUBLISHED 16 May 2023

CITATION
Jiang X, Liu X, Liu Y, Wang Q, Li B and Zhang L (2023) Epileptic seizures detection and the analysis of optimal seizure prediction horizon based on frequency and phase analysis. *Front. Neurosci.* 17:1191683. doi: 10.3389/fnins.2023.1191683

Epileptic seizures detection and the analysis of optimal seizure prediction horizon based on frequency and phase analysis

Ximiao Jiang[1†], Xiaotong Liu[2†], Youjun Liu[1], Qingyun Wang[2], Bao Li[1] and Liyuan Zhang[1*]

[1]Department of Biomedical Engineering, Faculty of Environment and Life, Beijing University of Technology, Beijing, China, [2]Department of Dynamics and Control, Beihang University, Beijing, China

Changes in the frequency composition of the human electroencephalogram are associated with the transitions to epileptic seizures. Cross-frequency coupling (CFC) is a measure of neural oscillations in different frequency bands and brain areas, and specifically phase–amplitude coupling (PAC), a form of CFC, can be used to characterize these dynamic transitions. In this study, we propose a method for seizure detection and prediction based on frequency domain analysis and PAC combined with machine learning. We analyzed two databases, the Siena Scalp EEG database and the CHB-MIT database, and used the frequency features and modulation index (MI) for time-dependent quantification. The extracted features were fed to a random forest classifier for classification and prediction. The seizure prediction horizon (SPH) was also analyzed based on the highest-performing band to maximize the time for intervention and treatment while ensuring the accuracy of the prediction. Under comprehensive consideration, the results demonstrate that better performance could be achieved at an interval length of 5 min with an average accuracy of 85.71% and 95.87% for the Siena Scalp EEG database and the CHB-MIT database, respectively. As for the adult database, the combination of PAC analysis and classification can be of significant help for seizure detection and prediction. It suggests that the rarely used SPH also has a major impact on seizure detection and prediction and further explorations for the application of PAC are needed.

KEYWORDS

electroencephalogram (EEG), phase-amplitude coupling (PAC), frequency-domain analysis, seizure prediction horizon (SPH), machine learning

1. Introduction

Epilepsy is a chronic brain disorder, characterized by recurrent seizures. The reason for the pathological dynamics is the abnormally synchronous discharge of groups of, in particular, cortical neurons (Tsipouras, 2019). Seizure onset can lead to loss of consciousness, disorders of mood, and, in extreme cases, even death of the patients (Yang et al., 2021). It affects nearly 50 million people worldwide (Acharya et al., 2017; World Health Organization Epilepsy, 2023). Seizures can be treated through drug treatment, surgical intervention, and neuromodulation (He et al., 2021; Mueller et al., 2022). However, in the process of treatment, inconsistent availability of clinical data, the complexity of epilepsy etiology, and the lack of standard diagnostic procedures often make diagnosis and follow-up treatment difficult. Thus, exploring effective methods to detect and predict seizure onset is an important Research Topic.

The electroencephalogram (EEG) measures the electrical activity of the brain and is thus an important examination tool for the clinical diagnosis of neurological disorders including epilepsy and Alzheimer's disease (Cho et al., 2017; Yu et al., 2020). According to the collection method, there are two common types of EEG recordings, namely, scalp electroencephalography (scalp EEG) and intracranial electroencephalography (iEEG) (Jayakar et al., 2016). In humans, oscillatory brain activity occurs in a variety of frequency bands reflecting electrophysiological signals generated by large ensembles of synchronized neuronal firing (Jensen and Colgin, 2007). Specifically, the amplitude of high-frequency oscillation has been suggested as a biomarker of the seizure onset area (Charupanit et al., 2020). In clinical practice, the diagnosis is typically based on a patient's clinical representation and available multimodal data. However, this has some disadvantages, particularly being time-consuming (Vidyaratne and Iftekharuddin, 2017; Duan et al., 2022). Concerning the EEG, in addition to contributions from neural activity, the signals contain interfering signals from other sources, which may make the diagnosis difficult. There is a need for reliable algorithms, specifically for automatic seizure onset detection as recorded in the EEG.

In recent years, researchers have designed various methods to extract various features from EEG recordings. There are three main analysis methods, namely time domain analysis, frequency domain analysis, and time–frequency domain analysis. In terms of frequency domain analysis, researchers have extracted various features, including mean frequency and root mean square, and achieved an excellent result on seizure detection. Cross-frequency coupling (CFC) is a method to dynamically measure interactions of neural oscillations in different frequency bands and between brain areas. CFC also appears to detect neural correlates of various cognitive states (Liu et al., 2018). Three types of algorithms, namely phase–amplitude coupling (PAC), phase–phase coupling (PPC), and amplitude–amplitude coupling (AAC), are common methods for CFC analysis (Munia and Aviyente, 2021). Among them, PAC, which quantifies the interplay between the amplitude of high-frequency oscillations and the phase of low-frequency oscillations, has recently become a topic of interest (Munia and Aviyente, 2019). In the context of epilepsy, it was shown that interictal PAC is helpful for the localization of the epileptogenic zone (Motoi et al., 2018; Ma et al., 2021). Although most studies emphasized PAC analysis for seizure onset zone (SOZ) detection, few studies have also applied it to the (temporal) detection and prediction of seizure onset (Edakawa et al., 2016; Grigorovsky et al., 2020; Yamamoto et al., 2021). Due to the non-linearity and non-stationarity of EEG signals, the synchronization process of epilepsy is also discussed to analyze the mechanism as well as the complex underlying dynamics of seizure (Fan and Chou, 2019). For quantitative analysis, functional brain networks and graph theory have provided opportunities to understand the complex mechanism changes (Yu et al., 2018; Akbarian and Erfanian, 2020; Fallahi et al., 2021; Liu et al., 2021). The network metrics including the efficiency, clustering, small worlds, and modular organizations are the meaningful information to extract the topological properties of the brain network.

Recently, machine learning with powerful computing ability has made available algorithms to potentially improve classical data analysis. A variety of machine learning models have been proposed for classification. Common classification algorithms include the support vector machine (Hussain, 2018), decision trees, K-nearest neighbor (Jukic et al., 2020), and random forest (Sun Q. et al., 2021). In Sun Q. et al. (2021), the authors combined the random forest algorithm with time domain and non-linear characteristics for seizure detection and were able to obtain a high accuracy of state classification. Similar methods based on the random forest algorithm have been applied to differentiate between types of seizures and achieved a good performance (Basri and Arif, 2021). A method combining machine learning and functional brain networks has been adopted by researchers in more and more fields. Yu et al. (2019) applied it to automatically identify acupuncture manipulations and with the support vector machine algorithm, the highest accuracy can be obtained. With the improvement and optimization of algorithms and models, deep learning has also gradually been applied to the study of epilepsy. Convolutional Neural Network (CNN) has stood out and was applied in many research in terms of image recognition (Ryu et al., 2021; Wang et al., 2022). Compared with the conventional CNN, Graph Convolutional Network (GCN) can preserve rich marginal features having the advantage of explaining the connective relationships between features (Chen et al., 2021; Jia et al., 2022; Li et al., 2022). The deep learning method acquires abundant EEG data. However, rare public datasets can provide such an amount of EEG data which is a wicked problem.

In the context of seizure detection and prediction, the main goal is to classify the interictal stage and the preictal stage (Snyder et al., 2008; Yang et al., 2021). To achieve that, the seizure prediction horizon (SPH) and the seizure occurrence period (SOP) were suggested (Maiwald et al., 2004). The SOP is a time period when a seizure is predicted to occur and the SPH is the interval from the alarm to the beginning of the SOP. A correct prediction is achieved when a seizure onset occurs after the SPH and within the SOP. Recently, studies have addressed the problem of the length of SPH and SOP. Wang et al. compared the prediction effect of SOP between 30 and 60 min with the SPH of 5 min achieving an excellent performance (Wang et al., 2022). Moreover, Aarabi et al. conducted prediction experiments on iEEG data with an SOP of 30 and 50 min and an SPH of 10 s (Aarabi and He, 2017). Additionally, Zhang et al. acquired a high sensitivity by setting SPH to zero. In contrast, few studies emphasized the length of SPH which was also called the intervention time (Wang et al., 2022). In clinical practice, it was still important to find an appropriate SPH to leave enough time for providing effective intervention.

In this study, we propose a method for epileptic seizure onset detection and for the classification of preictal and interictal states. Frequency domain analysis is performed on two databases, the Siena Scalp EEG database and the CHB-MIT database. Based on the single-channel analysis, the length of SPH is adjusted to find the optimal SPH for potential treatment.

2. Material and methods

This section describes the database used for the experiment and the method, which can be categorized into three

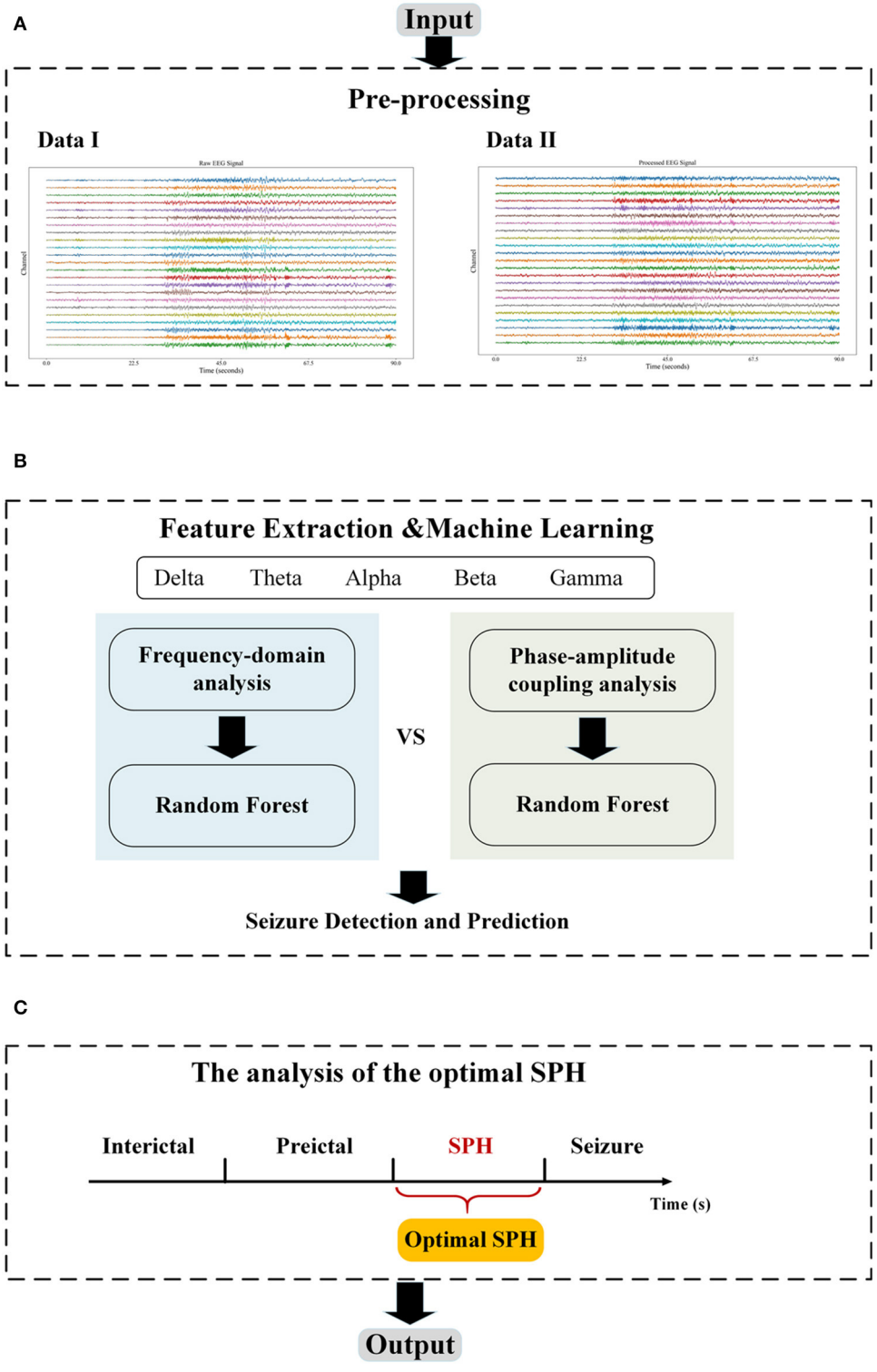

FIGURE 1
The flowchart. **(A)** The pre-processing module includes filtering and Independent Components Analysis (ICA); **(B)** The feature extraction module includes frequency domain and PAC, and the machine learning module performs the classification; and **(C)** The optimization module adjusts the length of SPH to find the optimal SPH. The data I in **(A)** are the raw EEG data from chb01 in the CHB-MIT database and the Data II are the output of the pre-processing module.

major parts: first, the EEG signal is preprocessed; second, features including single-channel PAC, peak frequency, and median frequency are extracted; and third, the random forest classifier is applied for classification. The flowchart of the proposed method in this study is illustrated in Figure 1.

TABLE 1 Data of the patients in the Siena Scalp EEG database.

Patient	Gender	Age (years)	EEG Chan.	Seiz.
1	M	46	29	2
3	M	54	29	2
5	F	51	29	3
6	M	36	29	5
7	F	20	29	1
9	F	27	29	3
11	F	58	29	1
12	M	71	29	4
13	F	34	29	3
14	M	49	29	4
16	F	41	29	2
17	M	42	29	2

EEG Chan., the number of EEG channels; Seiz., the number of seizures; F, Female; M, Male. For comparison, the patient numbers here are marked in the original database without modification.

TABLE 2 Data of the patients in the CHB-MIT database.

Patient	Gender	Age (years)	EEG Chan.	Seiz.
1	F	11	23	7
2	M	11	23	3
3	F	14	23	7
4	M	22	23	4
5	F	7	23	5
6	F	1.5	23	10
7	F	14.5	23	3
8	M	3.5	23	5
9	F	10	23	4
10	M	3	23	7
11	F	12	23	3
12	F	2	23	40
13	F	3	23	12
14	F	9	23	8
15	M	16	31	20
16	F	7	28	10
17	F	12	28	3
18	F	18	22	6
19	F	19	28	3
20	F	6	28	8
21	F	13	28	4
22	F	9	28	3
23	F	6	23	7
24	-	-	23	16

EEG Chan., the number of EEG channels; Seiz., the number of seizures; F, Female; M, Male.

2.1. Database

Two databases were used in this study: the Siena Scalp EEG database and the CHB-MIT database.

The Siena Scalp EEG database (https://www.physionet.org/content/siena-scalp-eeg/1.0.0/) collected by the Unit of Neurology and Neurophysiology at the University of Siena (Detti et al., 2020). It consists of scalp EEG recordings from 14 patients including nine men (ages 36–71) and five women (ages 20–58). The recordings were captured with a sampling rate of 512 Hz, with electrodes arranged on the international 10–20 system. In total, this database has a component of 47 seizures on about 128 recording hours. In the study, we used 29 channels ("Fp1", "F3", "C3", "P3", "O1", "F7", "T3", "T5", "Fc1", "Fc5", "Cp1", "Cp5", "F9", "Fz", "Cz", "Pz", "F4", "C4", "P4", "O2", "F8", "T4", "T6", "Fc2", "Fc6", "Cp2", "Cp6", "F10", and "Fp2"). Table 1 reports the details of the data.

The second database is the CHB-MIT database (https://www.physionet.org/content/chbmit/1.0.0/) which contains the widely used scalp EEG recordings from 23 patients at Children's Hospital Boston (Shoeb, 2009; Truong et al., 2018; Yang et al., 2021). Among them, chb21 was obtained 1.5 years after case chb01, from the same female subject, and chb24 with incomplete information was added to the database later. The records were captured at a rate of 256 samples per second sampling by 16-bit resolution using the International 10–20 Electrode Position System. A total of 983 h of consecutive EEG recordings and 198 seizures are available in the database. In most cases, files contain only 1 h of digitized EEG signal, although files belonging to case chb10 are 2 h, and files belonging to cases chb04, chb06, chb07, chb09, and chb23 are 4 h. In this study, we used 22 channels ("FP1-F7", "F7-T7", "T7-P7", "P7-O1", "FP1-F3", "F3-C3", "C3-P3", "P3-O1", "FP2-F4", "F4-C4", "C4-P4", "P4-O2", "FP2-F8", "F8-T8", "T8-P8", "P8-O2", "FZ-CZ", "CZ-PZ", "P7-T7", "T7-FT9", "FT9-FT10", and "FT10-T8") contained in most records. Table 2 reports the details of the data.

2.2. Pre-processing

To obtain valid features of the signal, pre-processing including filtering and ICA is essential. By appropriate filtering, the noise in EEG data can be effectively reduced. In other words, in a given frequency band, EEG signals can be filtered to improve the corresponding signal-to-noise ratio. The raw EEG signals were contaminated by power line contributions at 60 Hz and 50 Hz for the CHB-MIT and the Siena, respectively. Therefore, a notch filter was utilized to remove this power-line interference. The filtered data were processed by ICA to remove physiological artifacts, e.g., eye movements and other muscular noise. For further analysis, the preprocessed EEG data were decomposed into the classical EEG frequency bands using a fifth-order Butterworth bandpass filter.

We followed the definition of SPH and the SOP mentioned in Maiwald et al. (2004), Zhang and Parhi (2016), and Shokouh Alaei et al. (2019) as illustrated in Figure 2 for state division. The seizure onset may not occur immediately and exactly after the SPH, which indicates the uncertainty of the prediction. To better achieve the prediction, we assumed that the seizure onset was followed by the SPH in our experiments. For an effective and practical prediction,

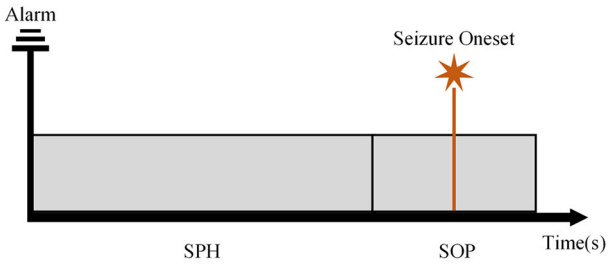

FIGURE 2
The schematic diagram of the seizure prediction horizon (SPH) and the seizure occurrence period (SOP).

the SPH should not be too long. At the same time, from a clinical perspective, the SPH ought not to be too close to the seizure onset to allow for an intervention of patients. In the case of seizure clusters, we focus on the leading seizure. Thus, when a second seizure starts soon after the previous seizure, we considered them as only one seizure.

According to Truong et al. (2018) and Sun B. et al. (2021), the preictal length was set to 30 min. Referring to Ryu et al. (2021), the SPH existed before the ictal state, and the time after the preictal state was assumed to be 5 min. At the same time, the rest of the recording was defined as an interictal state. The final partition of each state is shown in Figure 3. PN00 and PN10 in the Siena Scalp EEG database have insufficient preictal and interictal data. After removal, 12 subjects from this database were used.

For a specified EEG sequence, an EEG window length of 30-s with a slide step of 15-s was used to obtain 30-s segments of EEG signals (Truong et al., 2018).

2.3. Feature extraction

The single-channel PAC was calculated. For comparison, two common frequency domain features, namely, peak frequency and median frequency, were also extracted (Sánchez-Hernández et al., 2022).

Traditionally, PAC can be calculated as follows (Dupré la Tour et al., 2017). First, a bandpass filter is performed to decompose the EEG signal $x(t)$ on each channel into low frequency f_x and high frequency f_y, and the range is divided into delta (0.5–4 Hz), theta (4–8 Hz), alpha (8–13 Hz), beta (13–30 Hz), and gamma (30–80 Hz), which are the commonly used frequency bands for human EEG (Liu et al., 2021). Second, the Hilbert transform is applied to obtain the phase sequence Φ_x of a low-frequency band and the amplitude sequence a_y of a high-frequency band. Third, a metric is used to quantify the correlation between Φ_x and a_y. In this study, the modulation index (MI) is chosen, which is robust against noise and short data epochs and overall the commonly used measurement method (Hulsemann et al., 2019; Munia and Aviyente, 2019; Liu et al., 2021; Ma et al., 2021).

To calculate the value of MI, we refer to Tort et al. (2008), in which 18 bins of 20° each are used (−180°-180°). The average amplitude of the high-frequency component is computed and normalized as follows:

$$P(j) = \frac{\bar{f}_y(j)}{\sum_{i=1}^{N} \bar{f}_{y(i)}} \tag{1}$$

where $\bar{f}_y(j)$ is the average of a_y within each bin, N is the total number of bins, and the range of j is $[1, N]$ (Fujita et al., 2022). Subsequently, the Shannon entropy is calculated by the following formula:

$$H(P) = -\sum_{j=1}^{N} P(j)\, logP(j) \tag{2}$$

Here, P is the vector of the normalized averaged amplitude in each bin and N is the total number of bins. The Shannon entropy depends on the number of bins and so does the MI. According to Tort et al. (2008) and Hulsemann et al. (2019), 18 bins were employed.

PAC is significantly associated with the deviation from the uniform distribution. The Kullback–Leibler distance, a measure for the disparity of the distributions, is calculated by the following formula:

$$KL(U,X) = \log N - H(P) \tag{3}$$

where U is the uniform distribution, X is the distribution of the data, N is the total number of bins, and $\log N$ is the maximum entropy value. The final MI is computed as follows:

$$MI = \frac{KL(U,\ X)}{\log N} \tag{4}$$

where $KL(U, X)$ is the Kullback–Leibler distance according to Eq. 3 and N is the total number of bins.

We used the Welch function to obtain the signal power spectrum for each band, and the peak frequency and median frequency were calculated to characterize the highest peak in the power spectral density (Sánchez-Hernández et al., 2022).

2.4. Classification

A classical machine learning algorithm was employed for the classification based on the extracted features. As an ensemble learning algorithm, the random forest classifier stands out among traditional classifiers (Basri and Arif, 2021). It is based on ensemble decision trees trained by the bagging method. For an input sample, M trees will have M classification results. The algorithm then integrates all the classification voting results and designates the category with the most votes as the final output.

For the input data D, max–min normalization was used according to the given formula:

$$\mathrm{D}_{\mathrm{scaled}} = \frac{D - D.\min(axis{=}0)}{D.\max(axis{=}0) - D.\min(axis{=}0)} * (max - min) + \min \tag{5}$$

Where max and min are the maximum and minimum values of the given mapping range. In our experiments, the mapping range was set to be (−1, 1).

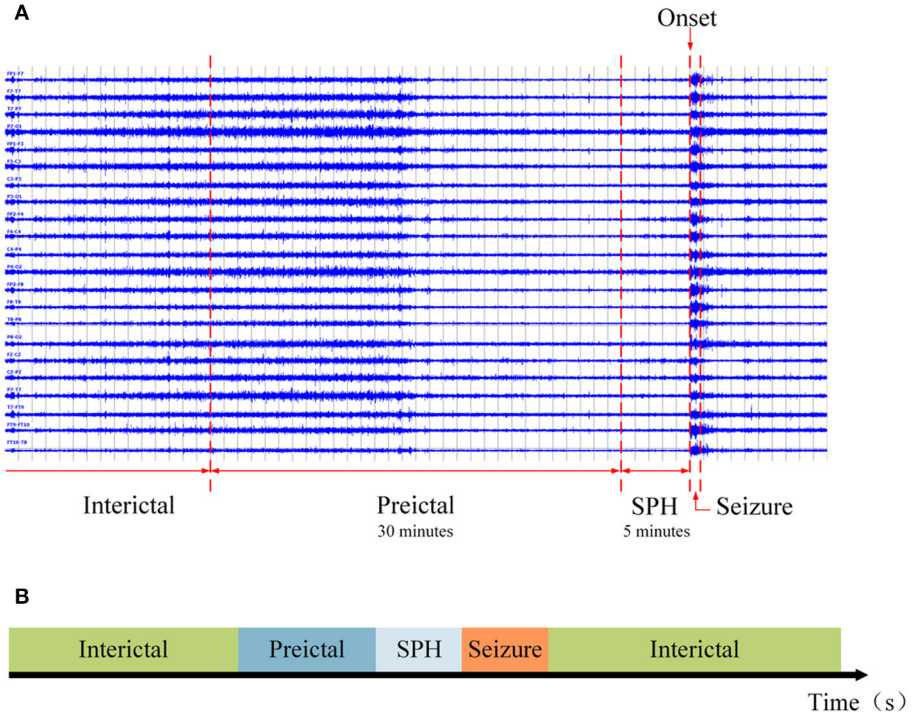

FIGURE 3
The ictal, SPH, preictal, and interictal states. **(A)** An example of a segmented EEG signal. The rightmost line is a landmark of the epileptic seizure onset. The SPH is set 5 min before seizure onset, the preictal state is 30 min earlier than SPH, and the interictal state follows the preictal state. **(B)** A schematic diagram of the segmentation.

TABLE 3 Workstation configuration.

Library	Version
Numpy	1.18.5
Scipy	1.4.1
Scikit-learn	0.24.1
MNE	0.23.0

As for the parameters adjustment, three parameters, namely, estimator, min-sample-split, and max-depth, were selected, and the grid search method was applied to find the best parameter value.

For the division of the data into the training and testing sets, the k-fold cross-validation method was employed for k=10 (Sameer and Gupta, 2020). Based on the seizures, the extracted features were randomly divided into 10 equal parts, nine of which were used for training and one for testing.

2.5. Statistical analysis

In this study, the analysis was conducted on a workstation with the Python 3.8.8 configuration as shown in Table 3. The overall goal was to classify the interictal and preictal states and to predict the ictal state. To evaluate the performance of the model, four evaluation metrics were calculated, namely, accuracy, precision, recall, and F-1 score, given as follows:

$$\text{Accuracy} = \frac{TP+TN}{TP+TN+FP+FN} \quad (6)$$

$$\text{Precision} = \frac{TP}{TP+FP} \quad (7)$$

$$\text{Recall} = \frac{TP}{TP+FN} \quad (8)$$

$$\text{F-1 score} = \frac{2^{*}Precision^{*}Recall}{Precision+Recall} \quad (9)$$

The true positive (TP) is the number of segments that are correctly classified as preictal. The true negative (TN) is the number of segments that are correctly identified as interictal. The false positive (FP) represents the number of segments that are incorrectly classified as preictal, and the false negative (FN) represents the segments that are incorrectly recognized as interictal.

3. Results

3.1. The performance of seizure detection and prediction based on frequency domain analysis

The average results of a single-channel frequency domain analysis based on the different sub-bands are provided in Figure 4. From the results of both databases, it can be seen that a better performance occurs at high frequencies, i.e., either the beta or

10.3389/fnins.2023.1191683

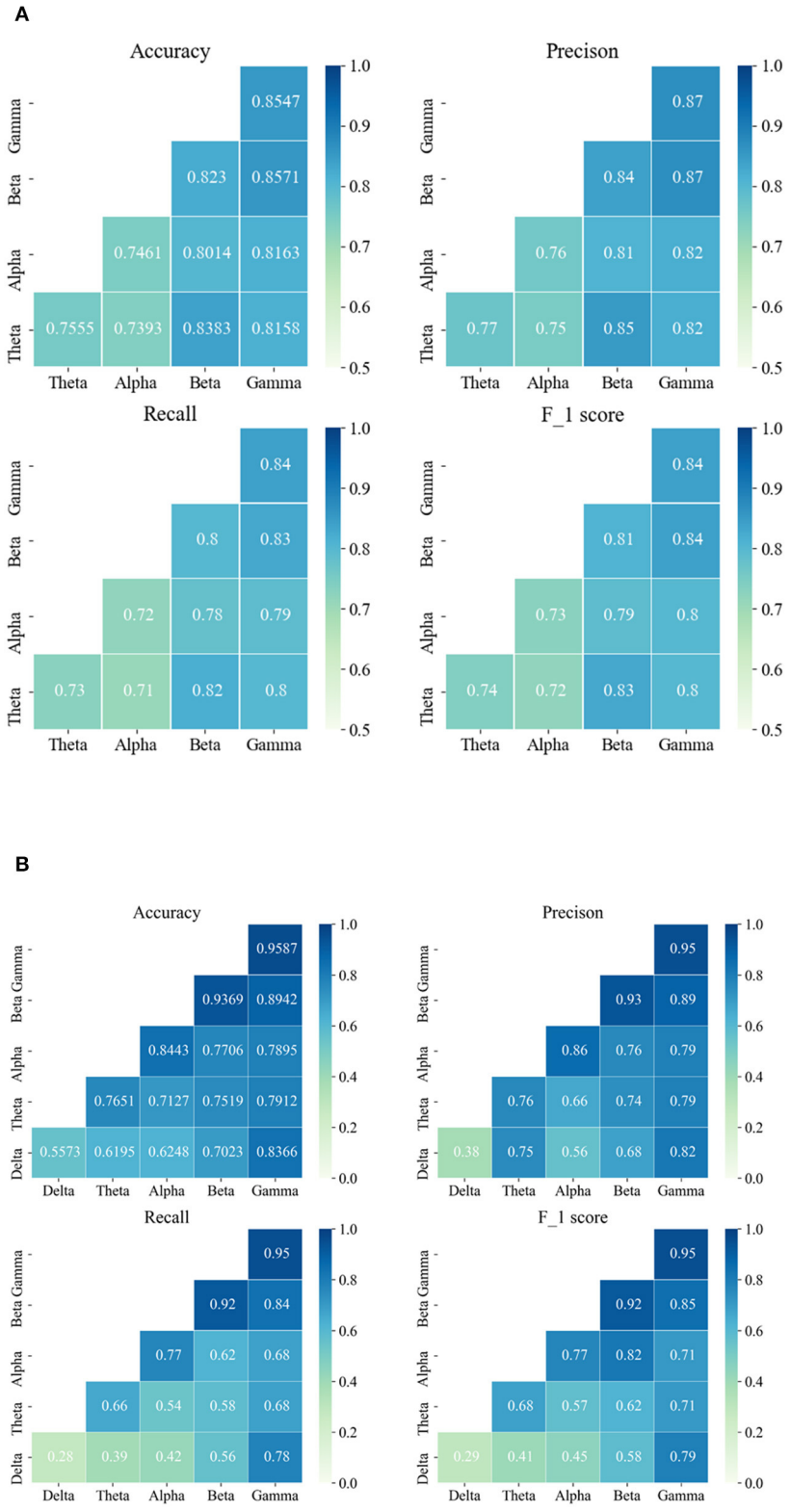

FIGURE 4
The seizure detection and prediction average results are based on the single-channel frequency domain analysis and PAC analysis, respectively. **(A)** The average results of the Siena Scalp EEG database are based on a single channel. **(B)** The average results of the CHB-MIT database are based on the single channel. The data on the diagonal represent the results of frequency domain analysis and the data on the lower triangle represent the results of PAC analysis.

gamma frequency band. For the Siena Scalp EEG database, the best performance was obtained in the gamma band, followed by the beta band. For the CHB-MIT database, an accuracy of 95.87% was achieved with the gamma band. Similarly, a high accuracy also can be obtained with the beta band. By comparing the results of different frequency bands, the performance weakens from the high- to low-frequency band, which suggests that the high-frequency band has more valid information for classification. Particularly in the CHB-MIT database, we observe that all evaluation metrics have improved a lot. For patients in the Siena Scalp EEG database, the EEG data came pre-processed by high-pass filtering at either 1.6 Hz or 5.3 Hz. We, therefore, excluded the delta band and evaluated the other four bands.

3.2. The effect of seizure detection and prediction based on phase–amplitude coupling analysis

For further exploration, the MI was computed and the average PAC results are shown in Figure 4. Based on the results, the beta-gamma leading AC has the best performance on both databases. To be specific, the highest average accuracy of 85.71% was obtained on the Siena EEG database, while an average accuracy of 89.42% was achieved on the CHB-MIT database. Apart from that, it can be found that beta-theta leading PAC also had a good performance on the Siena EEG database. For the Siena Scalp EEG database, the average accuracy was enhanced by 4.13% from 81.58% to 85.71%; for the CHB-MIT database, the average accuracy improved by 5.76% from 83.66% to 89.42%.

Figure 5 illustrates the MI pseudo-color graph of interictal and preictal for all electrode channels with the 30-s slide windows moved. PAC presented a different characteristic in the interictal and preictal state. As shown in Figure 5, the interictal PAC was rare and weak, while the preictal PAC bursts rhythmically during some periods of time, which were indicated by red rectangle boxes. Also, PAC can occur on different channels at different times, indicating that the PAC varied with time.

Comparing the results of the single-channel frequency domain analysis with the PAC, we can find some nuances in both databases. For the Siena EEG database, the adult database, the best result was obtained by applying the PAC method; for the CHB-MIT database, the child database, the single gamma frequency band achieved the best performance. More interestingly, for the CHB-MIT database, the delta band with other high-frequency bands and PAC can improve the results compared with the single delta band.

3.3. The results of seizure detection and prediction based on the analysis of optimal SPH

The above results are based on the SPH of 5 min (Truong et al., 2018; Ryu et al., 2021; Wang et al., 2022). In this section, we adjust the length of SPH to between 10 and 15 min, respectively, to analyze the influence on seizure detection and prediction caused by the length of SPH. Based on the above results, the following analysis is conducted on the gamma band (frequency domain analysis) and the beta-gamma PAC, the optimal frequency band, for the CHB-MIT database and the Siena EEG database, respectively.

Supplementary Tables 1, 2 show the accuracy, precision, recall, and F-1 score for each patient from two databases according to the length of SPH. For each patient, there are three major outcomes. First, for most patients, a higher accuracy can be achieved when the SPH of 5 min was used. Second, some patients had better accuracy with the SPH of 10 or 15 min. Third, there was no difference for different lengths of SPH. For the first two cases, we selected patient 01 and patient 05 from the Siena EEG database, for example. The former obtained an accuracy of 87.12% and 79.53% at an SPH of 5 and 15 min, respectively. The latter obtained an accuracy of 81.47% and 88.73% at an SPH of 5 and 10 min, respectively. In the third case, for some patients from the CHB-MIT database, high accuracy can be obtained at these three interval lengths. What needed to be noticed was that some patients (e.g., 11 from the CHB-MIT database) have very few valid seizures considering the definition of the SOP and SPH displayed in Figure 2 and results do not vary with the interval length. There was no result with an SPH of 15 min due to the lack of a preictal state in the data.

An average accuracy, precision, recall, and F-1 score are illustrated in Figure 6. Combining the results of the two databases, comprehensively, we find that the best performance was obtained with an SPH of 5 min. Although, the accuracy at the SPH of 5 min does not have a predominant advantage on both databases. There was, in terms of numerical results, a slight difference among the SPH of 5, 10, and 15 min. Supplementary Figures 1, 2 plot the results of the Kruskal–Wallis test between 5 min, 10 min, and 15 min SPH from the two databases. The p-values of the two databases are all more than 0.05. It suggests that at a certain range, the change of SPH has no significant effect on the accuracy of detection. Therefore, it is necessary to take the time expense to cure the patients and the feeling of the patients into consideration. If the length of the SPH is extended, it can increase the psychological stresses of patients. With a similar accuracy, thus, the SPH of 5 min can detect and predict the seizure faster and more efficiently.

4. Discussion and conclusion

In this study, frequency domain and PAC analysis are used to classify the interictal and the preictal states for seizure detection and prediction in EEG recordings from two cohorts of patients with epilepsy. The PAC classification analysis with the random forest classifier achieved better overall performance on the Siena Scalp EEG database for adults compared to the pediatric CHB-MIT database. In particular, the beta-gamma PAC stands out. The frequency domain analysis had the best performance on the pediatric CHB-MIT database. With both methods of feature extraction, the results improved from low- to high-frequency bands. In terms of the length of SPH, comprehensively, we found that the best overall performance was obtained with an SPH of 5 min, although some patients also had a good performance when the SPH was 10 or 15 min. Clinically, the highest accuracy does not necessarily mean practicality, that is the length of the warning time and the accuracy of the analysis need to be weighed against each other. Overall, it is found in this study that applying the SPH of

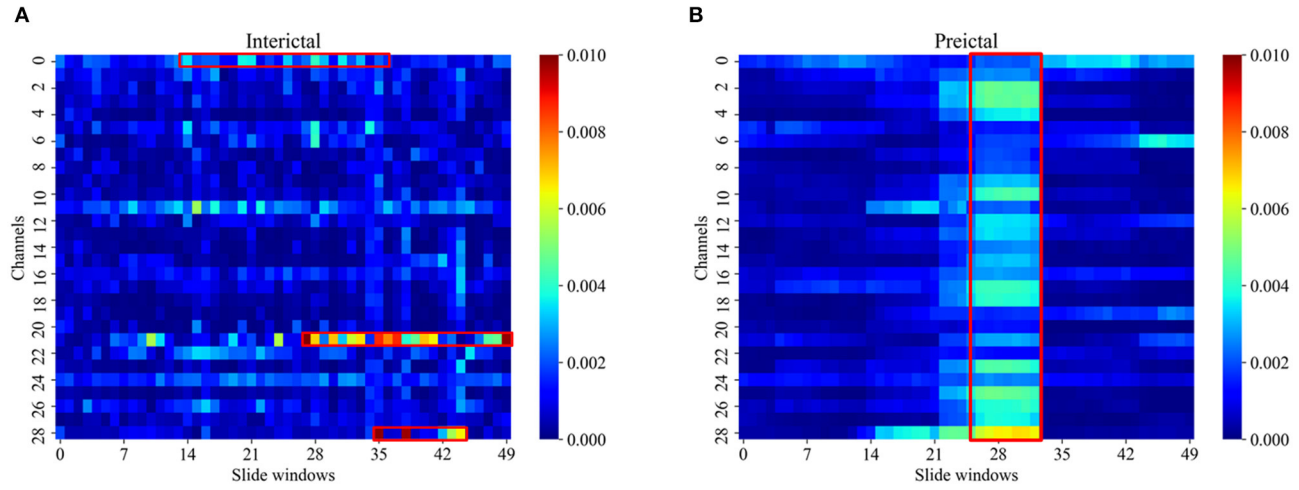

FIGURE 5
The MI pseudo-color graph of interictal **(A)** and preictal **(B)**. The MI was computed in 30 s windows shifted by 15 s for all electrode channels of patient 07 in the Siena EEG database. The usually significant channels and time points of change were labeled by red rectangle boxed.

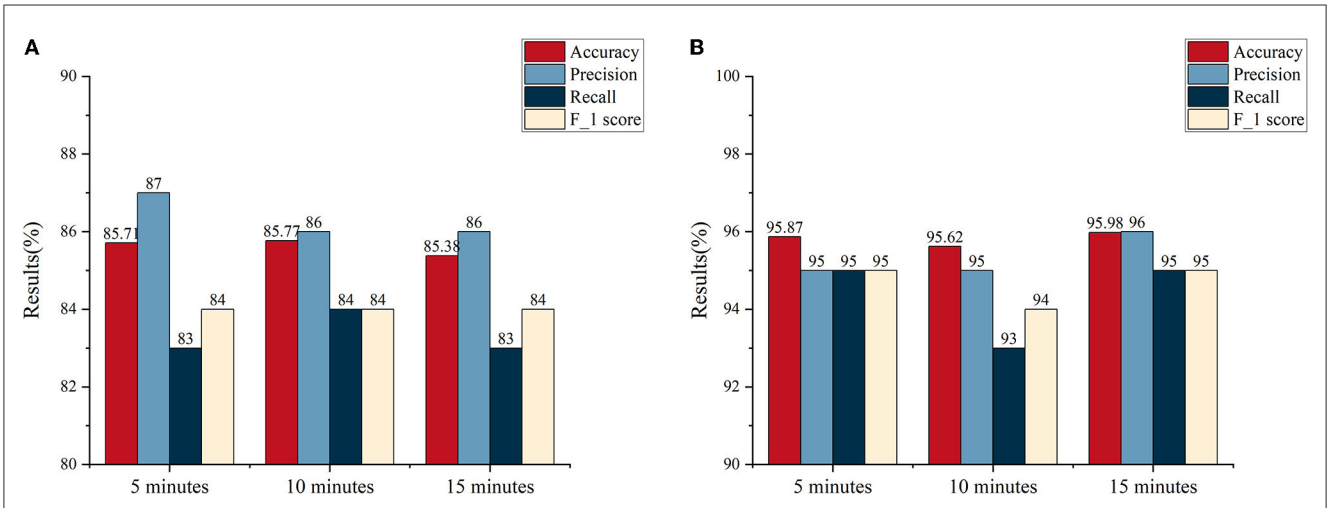

FIGURE 6
The average results of interval lengths of 5, 10, and 15 min, respectively. **(A)** The average results of the Siena Scalp EEG database. **(B)** The average results of the CHB-MIT database.

TABLE 4 The comparison of seizure detection and prediction with other algorithms based on the CHB-MIT database.

Authors	Subjects	Features	Classifier	SPH (minutes)	Acc	Pre	Recall	F-1
Ryu et al. (2021)	24	DWT	DenseNet-LSTM	5	0.9328	-	-	0.923
Hu et al. (2019)	24	MAS	CNN	20	0.8625	-	-	-
This work	24	Peak frequency and median frequency	Random forest	5	0.9587	0.95	0.95	0.95

Acc, Accuracy; Pre, Precision; F-1, F-1 score; DWT, discrete wavelet transform; MAS, mean amplitude spectrum; CNN, convolutional neural network.

5 min can contribute to a better performance for seizure prediction, which has greater value for clinical prevention.

There is growing evidence that oscillatory activity in the brain plays a role in cognitive activities including sensory processing, feedback processing, and working memory (Jensen and Colgin, 2007). Scalp EEG recording of epilepsy was used in this study, which provides a general reflection of the activity of neurons on the scalp surface, important for clinical diagnosis, focal potentials, and postoperative review (Kobayashi et al., 2012; Tatum et al., 2018). High-frequency oscillation is considered to be a distinctive feature of the epileptogenic zone (Melani et al., 2013; Nariai et al., 2017). The acquisition of scalp EEG is more uncertain than that of iEEG. Artifacts from data preprocessing, muscle signals, and other factors can interfere with the analysis. Despite the

above-described interference occurring during processing, there is a difference between the high-frequency activity caused by it and the pathological high-frequency rhythm produced by seizures (Kobayashi et al., 2004; Otsubo et al., 2007). Also, studies have highlighted that ictal slow waves are associated with ictal gamma rhythms. In spasms showing beta activity, the gamma rhythm is superimposed with it (Melani et al., 2013). This is a characteristic that is not present in non-pathological high-frequency rhythms. Consequently, we added cross-frequency coupling features to the frequency domain features to help predict seizures.

With unique coupling properties, CFC has been widely investigated in this context. Due to the distinctive and persistent PAC, researchers put much attention to its analysis during the seizure. However, the PAC of the interictal period and the preictal period are also of importance. Fujita et al. (2022) indicated that compared with healthy controls, epilepsy patients have abnormal PAC characteristics that can promote the discrimination between epileptic and normal. Amiri et al. (2016) found that the increased PAC is likely to be a sign of some fundamental abnormality in the interictal state. Ma et al. (2021) came to the conclusion that being paroxysmal, PAC of the interictal state and the preictal state can be used for accurate location of the epileptogenic zone. Also, the coupling of PAC can vary during the seizure. According to our results, there are distinct differences between the PAC of the interictal and the preictal state which is observed in Figure 5. It suggests that the PAC can help to classify them, particularly in the beta-gamma coupling band. Moreover, the proposed approach yields better results in the higher frequency bands. This is consistent with prior findings where the high-frequency range has a crucial role in cognitive function (Cho et al., 2017).

The incidence rate of epilepsy is particularly high in infancy and childhood. The characteristics of early infant EEG are various spatially distributed activities, rather than the more typical posterior rhythm in the mature EEG (Rosch et al., 2018). In addition, the electrographic symptoms of seizures in children are not as typical as those in adults. Lee and Lee (2013) indicated that, in terms of clinical features and interictal EEG, there were significant differences between patients who had temporal lobectomy in childhood and those having the operation during adulthood. Because the brain function of children is immature, it can easily be affected by adverse factors inside and outside the skull, potentially resulting in seizures. Most of the current studies have used data from the CHB-MIT database, which contains data from pediatric patients. Therefore, the Siena Scalp EEG database which is made up of adult data was added to our investigation to give a more comprehensive picture.

There are some limitations. First, our approach for seizure prediction is suitable only for EEG signals recorded continuously over a long period of time. The length of the data has a great influence on the final performance. Another limitation is that there are significant differences among different patients whose characteristics and dynamics of the peri-ictal states vary greatly (Yang et al., 2021). The proposed approach may thus not be suitable for all types of epileptic seizures. As displayed in Supplementary Tables 1, 2, it can be seen that, in terms of the length of SPH, the variation of the results is not uniform for each patient. A possible explanation for this is that they contain different types of seizures. Consequently, further work could consider the influence caused by the specific seizure type. Moreover, in the process of research, we found that the PAC has temporal and spatial differences. Since the two databases were public, however, the experiments were lack of patients' specific clinical information.

We compared the results of our work with previous studies in terms of SPH. To the best of our knowledge, there are only a few studies of SPH based on the CHB-MIT database. Table 4 gives the details including subjects, feature extraction method, classifier, SPH, and the four evaluation metrics based on the CHB-MIT database. As shown in Table 4, the method combining DWT and DenseNet-LSTM in Ryu et al. (2021) achieved an accuracy of 0.9328 and an F-1 score of 0.923. Hu et al. (2019) obtained an accuracy of 0.8625 with an SPH of 20 min. Compared to this, our method with an SPH of 5 min has a better performance.

Currently, several studies have applied many frequency domain features for seizure detection and prediction and obtained valuable results. While PAC is more widely used for seizure onset detection and dynamic network connections in epilepsy, few studies have applied it to seizure prediction. Based on the experiments, the integration of PAC and machine learning may be a significant help to achieve an early warning of an imminent seizure for the adult database. Although the signal-channel PAC in our experiments is not absolutely predominant, our results show that the proposed method has the potential to become a reliable seizure detection and prediction tool for auxiliary clinical diagnosis and prediction. Moreover, the length of SPH is analyzed, and the results show that at a certain range, an SPH of 5 min has an overall performance on the seizure prediction. In clinical, it can be helpful to give timely aid before a seizure occurs. The next step will be to further explore the application of PAC in EEG data of children with epilepsy and to incorporate the algorithm into a practical EEG setting to support early intervention and hopefully improve the quality of life of patients.

Data availability statement

The original contributions presented in the study are included in the article/Supplementary material, further inquiries can be directed to the corresponding author.

Author contributions

XJ and XL contributed equally to this study. XJ, XL, YL, QW, BL, and LZ collected, processed, and analyzed epilepsy datasets to do seizure detection and prediction. All authors wrote and revised the study. All authors contributed to the article and approved the submitted version.

Funding

This study was supported by the National Key Research and Development Program of China (Grant No. 2021YFA1000202) and the National Natural Science Foundation of China (Grant Nos. 12102014, 11932003, 11832003, 32271361, and 12202022).

Conflict of interest

The authors declare that the research was conducted in the absence of any commercial or financial relationships that could be construed as a potential conflict of interest.

Publisher's note

All claims expressed in this article are solely those of the authors and do not necessarily represent those of their affiliated organizations, or those of the publisher, the editors and the reviewers. Any product that may be evaluated in this article, or claim that may be made by its manufacturer, is not guaranteed or endorsed by the publisher.

Supplementary material

The Supplementary Material for this article can be found online at: https://www.frontiersin.org/articles/10.3389/fnins.2023.1191683/full#supplementary-material

References

Aarabi, A., and He, B. (2017). Seizure prediction in patients with focal hippocampal epilepsy. *Clini. Neurophysiol.* 128, 1299–1307. doi: 10.1016/j.clinph.2017.04.026

Acharya, U. R., Oh, S. L., Hagiwara, Y., Tan, J. H., and Adeli, H. (2017). Deep Convolutional Neural Network for the Automated Detection and Diagnosis of Seizure Using EEG Signals. *Comput Biol Med.* 100, 270–278. doi: 10.1016/j.compbiomed.2017.09.017

Akbarian, B., Erfanian, A, A. (2020). Framework for seizure detection using effective connectivity, graph theory, and multi-level modular network. *Biomed Signal Process Control.* 59, 101878. doi: 10.1016/j.bspc.2020.101878

Amiri, M., Frauscher, B., and Gotman, J. (2016). Phase-amplitude coupling is elevated in deep sleep and in the onset zone of focal epileptic seizures. *Front Hum Neurosci.* 10, 387. doi: 10.3389/fnhum.2016.00387

Basri, A., and Arif, M. (2021). Classification of seizure types using random forest classifier. *Adv SciTechnol Res J.* 15, 167–178. doi: 10.12913/22998624/140542

Charupanit, K., Sen-Gupta, I., Lin, J. J., and Lopour, B. A. (2020). Amplitude of high frequency oscillations as a biomarker of the seizure onset zone. *Clini Neurophysiol.* 131, 2542–2550. doi: 10.1016/j.clinph.2020.07.021

Chen, X., Zheng, Y., Dong, C., and Song, S. (2021). Multi-dimensional enhanced seizure prediction framework based on graph convolutional network. *Front Neuroinform.* 15, 605729. doi: 10.3389/fninf.2021.605729

Cho, D., Min, B., Kim, J., and Lee, B. (2017). EEG-based prediction of epileptic seizures using phase synchronization elicited from noise-assisted multivariate empirical mode decomposition. *IEEE Trans. Neural Syst. Rehabilitation Eng.* 25, 1309–1318. doi: 10.1109/TNSRE.2016.2618937

Detti, P., Vatti, G., and Lara, G. Z. M. (2020). EEG synchronization analysis for seizure prediction: a study on data of noninvasive recordings. *Processes.* 8, 846. doi: 10.3390/pr8070846

Duan, L., Wang, Z., Qiao, Y., Wang, Y., Huang, Z., Zhang, B., et al. (2022). An automatic method for epileptic seizure detection based on deep metric learning. *IEEE J Biomed Health Informat.* 26, 2147–2157. doi: 10.1109/JBHI.2021.3138852

Dupré la Tour, T., Tallot, L., Grabot, L., Doyère, V., van Wassenhove, V., Grenier, Y., et al. (2017). Non-linear auto-regressive models for cross-frequency coupling in neural time series. *PLoS Comp. Biol.* 13, e1005893. doi: 10.1371/journal.pcbi.1005893

Edakawa, K., Yanagisawa, T., Kishima, H., Fukuma, R., Oshino, S., Khoo, H. M., et al. (2016). Detection of epileptic seizures using phase-amplitude coupling in intracranial electroencephalography. *Scient. Reports.* 2016, 25422. doi: 10.1038/srep25422

Fallahi, A., Pooyan, M., Lotfi, N., Baniasad, F., Tapak, L., Mohammadi-Mobarakeh, N., et al. (2021). Dynamic functional connectivity in temporal lobe epilepsy: a graph theoretical and machine learning approach. *neurological Sci.* 42, 2379–2390. doi: 10.1007/s10072-020-04759-x

Fan, M., and Chou, C. A. (2019). Detecting abnormal pattern of epileptic seizures via temporal synchronization of EEG signals. *IEEE Trans Biomed Eng.* 66, 601–608. doi: 10.1109/TBME.2018.2850959

Fujita, Y., Yanagisawa, T., Fukuma, R., Ura, N., Oshino, S., Kishima, H., et al. (2022). Abnormal Phase-amplitude coupling characterizes the interictal state in epilepsy. *J Neural Eng.* 19, 026056. doi: 10.1088/1741-2552/ac64c4

Grigorovsky, V., Jacobs, D., Breton, V. L., Tufa, U., Lucasius, C., Del Campo, J. M., et al. (2020). Delta-gamma phase-amplitude coupling as a biomarker of postictal generalized EEG suppression, *Brain Commun*. (2020) 2022, fcaa182. doi: 10.1093/braincomms/fcaa182

He, L. Y., Hu, M. B. Li, R. L., Zhao, R., Fan, L. H., He, L., et al. (2021). Natural medicines for the treatment of epilepsy: bioactive components, pharmacology and mechanism. *Front Pharmacol.* 12, 604040. doi: 10.3389/fphar.2021.604040

Hu, W., Cao, J., Lai, X., and Liu, J. (2019). Mean amplitude spectrum based epileptic state classification for seizure prediction using convolutional neural networks. *J Ambient Intell. Humanized Comp*. 1–11. doi: 10.1007/s12652-019-01220-6

Hulsemann, M. J., Naumann, E., and Rasch, B. (2019). Quantification of phase-amplitude coupling in neuronal oscillations: comparison of phase-locking value, mean vector length, modulation index, and generalized-linear-modeling-cross-frequency-coupling. *Front Neurosci.* 13, 573. doi: 10.3389/fnins.2019.00573

Hussain, L. (2018). Detecting epileptic seizure with different feature extracting strategies using robust machine learning classification techniques by applying advance parameter optimization approach. *Cogn Neurodyn.* 12, 271–294. doi: 10.1007/s11571-018-9477-1

Jayakar, P., Gotman, J., Harvey, A. S., Palmini, A., Tassi, L., Schomer, D., et al. (2016). Diagnostic utility of invasive eeg for epilepsy surgery: indications, modalities, and techniques. *Epilepsia.* 57, 1735–1747. doi: 10.1111/epi.13515

Jensen, O., and Colgin, L. L. (2007). Cross-frequency coupling between neuronal oscillations. *Trends Cogn Sci.* 11, 267–269. doi: 10.1016/j.tics.2007.05.003

Jia, M., Liu, W., Duan, J., Chen, L., Chen, C. L. P., Wang, Q., et al. (2022). Efficient graph convolutional networks for seizure prediction using scalp EEG. *Front Neurosci.* 16, 967116. doi: 10.3389/fnins.2022.967116

Jukic, S., Saracevic, M., Subasi, A., and Kevric, J. (2020). Comparison of ensemble machine learning methods for automated classification of focal and non-focal epileptic EEG signals. *Mathematics.* 2020, 8. doi: 10.3390/math8091481

Kobayashi, K., Miya, K., Akiyama, T., Endoh, F., Oka, M., Yoshinaga, H., et al. (2012). Cortical contribution to scalp EEG gamma rhythms associated with epileptic spasms. *Brain Dev. (2013)* 35:762–770. doi: 10.1016/j.braindev.2012.12.012

Kobayashi, K., Oka, M., Akiyama, T., Inoue, T., Abiru, K., Ogino, T., et al. (2004). Very fast rhythmic activity on scalp EEG associated with epileptic spasms. *Epilepsia.* 45, 488–496. doi: 10.1111/j.0013-9580.2004.45703.x

Lee, Y. J., and Lee, J. S. (2013). Temporal lobe epilepsy surgery in children versus adults: from etiologies to outcomes. *Korean J Pediatr.* 56, 275–281. doi: 10.3345/kjp.2013.56.7.275

Li, Y., Liu, Y., Guo, Y. Z., Liao, X. F., Hu, B., Yu, T., et al. (2022). Spatio-temporal-spectral hierarchical graph convolutional network with semisupervised active learning for patient-specific seizure prediction. *IEEE Trans Cybern.* 52, 12189–12204. doi: 10.1109/TCYB.2021.3071860

Liu, X., Han, F., Fu, R., Wang, Q., and Luan, G. (2021). Epileptogenic zone location of temporal lobe epilepsy by cross-frequency coupling analysis. *Front Neurol.* 12, 764821. doi: 10.3389/fneur.2021.764821

Liu, Y., Wang, J., Cai, L., Chen, Y., and Qin, Y. (2018). Epileptic seizure detection from EEG signals with phase–amplitude cross-frequency coupling and support vector machine. *Int. J. Modern Phys. B.* 32. doi: 10.1142/S0217979218500868

Ma, H., Wang, Z., Li, C., Chen, J., and Wang, Y. (2021). Phase-amplitude coupling and epileptogenic zone localization of frontal epilepsy based on intracranial EEG. *Front Neurol.* 12, 718683. doi: 10.3389/fneur.2021.718683

Maiwald, T., Winterhalder, M., Aschenbrenner-Scheibe, R., Voss, H. U., Schulze-Bonhage, A., Timmer, J., et al. (2004). Comparison of three nonlinear seizure prediction methods by means of the seizure prediction characteristic. *Physica D: Nonlinear Phenomena.* 194, 357–368. doi: 10.1016/j.physd.2004.02.013

Melani, F., Zelmann, R., Dubeau, F., and Gotman, J. (2013). Occurrence of scalp-fast oscillations among patients with different spiking rate and their role as epileptogenicity marker. *Epilepsy Res.* 106, 345–356. doi: 10.1016/j.eplepsyres.2013.06.003

Motoi, H., Miyakoshi, M., Abel, T. J., Jeong, J. W., Nakai, Y., Sugiura, A., et al. (2018). Phase-amplitude coupling between interictal high-frequency activity and slow waves in epilepsy surgery. *Epilepsia.* 59, 1954–1965. doi: 10.1111/epi.14544

Mueller, J. S., Tescarollo, F. C., and Sun, H. (2022). DREADDs in epilepsy research: network-based review. *Front Mol Neurosci.* 15, 863003. doi: 10.3389/fnmol.2022.863003

Munia, T. T. K., and Aviyente, S. (2019). Time-frequency based phase-amplitude coupling measure for neuronal oscillations. *Sci Rep.* 9, 12441. doi: 10.1038/s41598-019-48870-2

Munia, T. T. K., and Aviyente, S. (2021). multivariate analysis of bivariate phase-amplitude coupling in EEG data using tensor robust PCA. *IEEE Trans. Neural Syst. Rehabilitation Eng.* 29, 1268–1279. doi: 10.1109/TNSRE.2021.3092890

Nariai, H., Beal, J., Galanopoulou, A. S., Mowrey, W. B., Bickel, S., Sogawa, Y., et al. (2017). Scalp EEG Ictal gamma and beta activity during infantile spasms: evidence of focality. *Epilepsia*. 58, 882–892. doi: 10.1111/epi.13735

Otsubo, H., Ochi, A., Imai, K., Akiyama, T., Fujimoto, A., Go, C., et al. (2007). High-frequency oscillations of ictal muscle activity and epileptogenic discharges on intracranial EEG in a temporal lobe epilepsy patient. *Clini Neurophysiol.* 119:862–868. doi: 10.1016/j.clinph.2007.12.014

Rosch, R., Baldeweg, T., Moeller, F., and Baier, G. (2018). Network dynamics in the healthy and epileptic developing brain. *Network Neurosci.* 2, 41–59. doi: 10.1162/NETN_a_00026

Ryu, S., Joe, I., and Hybrid, A. (2021). DenseNet-LSTM model for epileptic seizure prediction. *Applied Sciences.* 11, 7661. doi: 10.3390/app11167661

Sameer, M., and Gupta, B. (2020). Detection of epileptical seizures based on alpha band statistical features. *Wireless Pers Commun.* 115, 909–925. doi: 10.1007/s11277-020-07542-5

Sánchez-Hernández, S. E., Salido-Ruiz, R. A., Torres-Ramos, S., and Román-Godínez, I. (2022). Evaluation of feature selection methods for classification of epileptic seizure EEG signals. *Sensors.* 22, 3066. doi: 10.3390/s22083066

Shoeb, A. H. (2009). *Application of Machine Learning to Epileptic Seizure Onset Detection and Treatment*. Massachusetts: Massachusetts Institute of Technology.

Shokouh Alaei, H., Khalilzadeh, M. A., and Gorji, A. (2019). Optimal selection of SOP and SPH using fuzzy inference system for on-line epileptic seizure prediction based on eeg phase synchronization. *Aust. Phys. Eng. Sci. Med.* 42, 1049–1068. doi: 10.1007/s13246-019-00806-w

Snyder, D. E., Echauz, J., Grimes, D. B., and Litt, B. (2008). The statistics of a practical seizure warning system. *J Neural Eng.* 5, 392–401. doi: 10.1088/1741-2560/5/4/004

Sun, B., Lv, J. J., Rui, L. G., Yang, Y. X., Chen, Y. G., Ma, C., et al. (2021). Seizure prediction in scalp EEG based channel attention dual-input convolutional neural network. *Physica A: Stat Mech. Appl.* 584, 126376. doi: 10.1016/j.physa.2021.126376

Sun, Q., Liu, Y., and Li, S. (2021). "Patient-specific automatic seizure detection method from EEG signals based on random forest," in *2021 14th International Congress on Image and Signal Processing, Biomedical Engineering and Informatics* (Shanghai: IEEE), 1–5. doi: 10.1109/CISP-BMEI53629.2021.9624400

Tatum, W. O., Rubboli, G., Kaplan, P. W., Mirsatari, S. M., Radhakrishnan, K., Gloss, D., et al. (2018). Clinical utility of EEG in diagnosing and monitoring epilepsy in adults. *Clini Neurophysiol.* 129, 1056–1082. doi: 10.1016/j.clinph.2018.01.019

Tort, A. B. L., Kramer, M. A., Thorn, C., Gibson, D. J., Kubota, Y., Graybiel, A. M., et al. (2008). Dynamic cross-frequency couplings of local field potential oscillations in rat striatum and hippocampus during performance of a T-maze task. *Proc Nat Acad Sci.* 105, 20517–20522. doi: 10.1073/pnas.0810524105

Truong, N. D., Nguyen, A. D., Kuhlmann, L., Bonyadi, M. R., Yang, J., Ippolito, S., et al. (2018). Convolutional neural networks for seizure prediction using intracranial and scalp electroencephalogram. *Neural Networks.* 105, 104–111. doi: 10.1016/j.neunet.2018.04.018

Tsipouras, M. G. (2019). Spectral information of EEG signals with respect to epilepsy classification. *EURASIP J Adv Signal Process.* 2019, 1–17. doi: 10.1186/s13634-019-0606-8

Vidyaratne, L. S., and Iftekharuddin, K. M. (2017). Real-time epileptic seizure detection using EEG. *IEEE Trans. Neural Syst. Rehabilitation Eng.* 25, 2146–2156. doi: 10.1109/TNSRE.2017.2697920

Wang, X., Zhang, G., Wang, Y., Yang, L., Liang, Z., Cong, F., et al. (2022). One-dimensional convolutional neural networks combined with channel selection strategy for seizure prediction using long-term intracranial EEG. *Int J Neural Syst.* 32, 2150048. doi: 10.1142/S0129065721500489

World Health Organization Epilepsy (2023). Available online at: https://www.who.int/news-room/fact-sheets/detail/epilepsy/ (accessed February 9, 2023).

Yamamoto, S., Yanagisawa, T., Fukuma, R., Oshino, S., Tani, N., Khoo, H. M., et al. (2021). Data-driven electrophysiological feature based on deep learning to detect epileptic seizures. *J Neural Eng.* 18, 056040. doi: 10.1088/1741-2552/ac23bf

Yang, X., Zhao, J., Sun, Q., Lu, J., and Ma, X. (2021). An effective dual self-attention residual network for seizure prediction. *IEEE Trans. Neural Syst. Rehabilitation Eng.* 29, 1604–1613. doi: 10.1109/TNSRE.2021.3103210

Yu, H., Lei, X., Song, Z., Liu, C., and Wang, J. (2020). Supervised network-based fuzzy learning of EEG signals for alzheimer's disease identification. *IEEE Transact. Fuzzy Syst* 28, 60–71. doi: 10.1109/TFUZZ.2019.2903753

Yu, H., Li, X., Lei, X., and Wang, J. (2019). Modulation effect of acupuncture on functiona.l networks and classification of its manipulation with EEG signals. *IEEE Trans. Neural Syst. Rehabilitation Eng.* 27, 1973–1984. doi: 10.1109/TNSRE.2019.2939655

Yu, H., Wu, X., Cai, L., Deng, B., and Wang, J. (2018). Modulation OF spectral power and functional connectivity in human brain by acupuncture stimulation. *IEEE Trans. Neural Syst. Rehabilitation Eng.* 26, 977–986. doi: 10.1109/TNSRE.2018.2828143

Zhang, Z., and Parhi, K. K. (2016). Low-complexity seizure prediction from ieeg/seeg using spectral power and ratios of spectral power. *IEEE Trans Biomed Circuits Syst.* 10, 693–706. doi: 10.1109/TBCAS.2015.2477264

frontiers | Frontiers in Neuroscience

TYPE Original Research
PUBLISHED 23 May 2023
DOI 10.3389/fnins.2023.1171549

OPEN ACCESS

EDITED BY
Pan Lin,
Hunan Normal University, China

REVIEWED BY
Delaram Sadeghi,
Islamic Azad University of Mashhad, Iran
Wen-Xu Wang,
Beijing Normal University, China

*CORRESPONDENCE
Zi-Gang Huang
✉ huangzg@xjtu.edu.cn
Nan Yao
✉ yaonan@xaut.edu.cn

†These authors have contributed equally to this work

‡Data used in preparation of this article were obtained from the Alzheimer's Disease Neuroimaging Initiative (ADNI) data base (https://adni.loni.usc.edu). As such, the investigators within the ADNI contributed to the design and implementation of ADNI and/or provided data but did not participate in analysis or writing of this report. A complete listing of ADNI investigators can be found at: https://adni.loni.usc.edu/wpcontent/uploads/how to apply/ADNI Acknowledgement List.pdf

RECEIVED 22 February 2023
ACCEPTED 13 April 2023
PUBLISHED 23 May 2023

CITATION
Li Y, An S, Zhou T, Su C, Zhang S, Li C, Jiang J, Mu Y, Yao N, Huang Z-G and Alzheimer's Disease Neuroimaging Initiative (2023) Triple-network analysis of Alzheimer's disease based on the energy landscape.
Front. Neurosci. 17:1171549.
doi: 10.3389/fnins.2023.1171549

Triple-network analysis of Alzheimer's disease based on the energy landscape

Youjun Li[1,2†], Simeng An[1,2†], Tianlin Zhou[1,2], Chunwang Su[1,2], Siping Zhang[1,2], Chenxi Li[3], Junjie Jiang[1,2], Yunfeng Mu[4], Nan Yao[2,5*], Zi-Gang Huang[1,2,6*] and Alzheimer's Disease Neuroimaging Initiative[‡]

[1]The Key Laboratory of Biomedical Information Engineering of Ministry of Education, Institute of Health and Rehabilitation Science, School of Life Science and Technology, Xi'an Jiaotong University, The Key Laboratory of Neuro-informatics and Rehabilitation Engineering of Ministry of Civil Affairs, Xi'an, Shaanxi, China, [2]Research Center for Brain-inspired Intelligence, Xi'an Jiaotong University, Xi'an, Shaanxi, China, [3]Department of Military Medical Psychology, Air Force Medical University, Xi'an, Shaanxi, China, [4]Department of Gynecological Oncology, Shaanxi Provincial Cancer Hospital, Xi'an, China, [5]Department of Applied Physics, Xi'an University of Technology, Xi'an, China, [6]The State Key Laboratory of Congnitive Neuroscience and Learning, Beijing Normal University, Beijing, China

Introduction: Research on the brain activity during resting state has found that brain activation is centered around three networks, including the default mode network (DMN), the salient network (SN), and the central executive network (CEN), and switches between multiple modes. As a common disease in the elderly, Alzheimer's disease (AD) affects the state transitions of functional networks in the resting state.

Methods: Energy landscape, as a new method, can intuitively and quickly grasp the statistical distribution of system states and information related to state transition mechanisms. Therefore, this study mainly uses the energy landscape method to study the changes of the triple-network brain dynamics in AD patients in the resting state.

Results: AD brain activity patterns are in an abnormal state, and the dynamics of patients with AD tend to be unstable, with an unusually high flexibility in switching between states. Also , the subjects' dynamic features are correlated with clinical index.

Discussion: The atypical balance of large-scale brain systems in patients with AD is associated with abnormally active brain dynamics. Our study are helpful for further understanding the intrinsic dynamic characteristics and pathological mechanism of the resting-state brain in AD patients.

KEYWORDS

triple-network, energy landscape, Alzheimer's disease, resting-state fMRI, dynamics analysis

1. Introduction

Alzheimer's disease (AD) is a common degenerative neurological disease that typically begins with memory loss and progresses to impairments in a series of higher cognitive functions, followed by a loss of ability to live independently and eventual death. The onset of AD is obscure and seriously affects the normal life of patients. The etiology and specific pathogenesis of the

disease have not been fully elucidated (Delbeuck et al., 2003; Cummings et al., 2019; Lei et al., 2021). Therefore, methods designed to better understand the pathogenesis of AD and identify specific brain abnormalities in the early stages of AD are crucial.

Resting-state fMRI reflects the spontaneous activity of neurons when the brain is not performing a task. It has been widely employed in studies of a variety of neurological and psychiatric disorders. Because it does not require subjects to perform any task, resting-state fMRI is ideal for AD patients with cognitive decline (Vemuri et al., 2012; Yang et al., 2020). Different functional connectivity networks have been described based on the synchronization of low-frequency BOLD signals in the resting state (Damoiseaux et al., 2006). Vinod Menon proposed that among the inherent functional networks in the human brain, the default mode network (DMN), the salient network (SN), and the central executive network (CEN) are particularly crucial (Menon, 2011). The DMN is more active in the resting state, while the DMN is inhibited instead during the execution of tasks. In contrast, the CEN is less activated in the resting state and more activated when subjects are performing tasks or receiving external stimuli. The SN is generally considered to coordinate the DMN and CEN (Buckner et al., 2008; Lerman et al., 2014; Liao et al., 2021). Therefore, some studies have proposed the three networks as a "triple-network" model, which suggests that these three networks play an important role in the functions related to cognitive tasks performed by the brain, and they are considered the core networks related to the cognitive functions of the brain (Menon, 2011). The "triple-network" model is widely used to study various diseases. Previous studies have found that these three networks are closely associated with cognitive impairment in AD patients, and all three networks are damaged to varying degrees by the disease (Balthazar et al., 2014).

In a conventional resting-state fMRI analysis, functional connectivity is the most commonly investigated metric, which assumes that the BOLD signal is temporally stationary within the scan duration (Greicius et al., 2003). Actually, the brain is a complex and dynamic system with important features such as self-adaptation, self-organization, and multi-stability. A previous study indicated that the activity patterns of the resting brain are presumably in a nonequilibrium process of continuous switching between multiple states and show considerable variability on different time scales (Yao et al., 2020). Revealing the dynamic mechanism of spontaneous neural activity in the resting-state brain has important scientific importance for understanding the working mechanism of the brain and has prospective clinical applications in the prevention and treatment of brain diseases, including AD.

Currently, dynamic functional connectivity (dFC) based on sliding window correlation (SWC) and co-activation patterns (CAP) are two popular methods for AD dynamics analysis. The former was based on dynamically intercepting signals through windows of specific length and then performing functional connectivity analysis within each dynamic window. In recent years, a number of studies have been devoted to the extraction of high-level features from the dFC to achieve effective filtering of invalid information in the dFC and extraction of dynamic change features associated with the disease, contributing to exploring abnormal brain function networks and improving the classification accuracy of AD (Sendi et al., 2021; Gao et al., 2022; Matsui and Yamashita, 2022; Qiao et al., 2022; Ghanbari et al., 2023; Penalba-Sánchez et al., 2023). The principle of CAP was to extract co-activation patterns in certain specific peak points of the BOLD signal time series using a clustering algorithm. By analyzing the spatio-temporal features of these patterns to reveal the underlying mechanisms of abnormal brain function in AD patients, providing some potential biomarkers for the diagnosis and treatment of AD (Ma et al., 2020; Adhikari et al., 2021). The methods and conclusions of recent studies on the dynamic brain function network analysis of AD are shown in Table 1.

The regularities presented by activity patterns in the resting brain and the underlying mechanisms are also well suited for research using statistical-physical and nonequilibrium dynamics approaches (Huang et al., 2020). One of the commonly used methods is energy landscape analysis, a data-driven approach based on statistical mechanics (Watanabe et al., 2014; Ezaki et al., 2017; Gu et al., 2018; Kang et al., 2019). This method is similar to CAP that focuses on the nonequilibrium process of switching between resting-state active modes in the brain, but the energy landscape analysis better describes this process by constructing an energy topography of the state space in the brain system based on the statistical distribution, whose structure represents the stability and interrelationship of the system states and reflects the dynamic characteristics of the system in more detail.

In the present study, we extracted a time series based on representative ROIs in brain regions of the triple networks and used the energy landscape approach to analyze the dynamic characteristics of AD patients in the resting state. Some common dynamic indicators were used to characterize the resting triple-network dynamic system in the subjects and correlate it with the clinical index to further

TABLE 1 Dynamic brain function network analysis method for AD.

Target	Authors	Method	Conclusions
AD/NC	Gao et al. (2022)	dFC	Extraction of potential advanced features enhanced the classification and diagnosis of brain diseases.
AD/MCI/NC	Ghanbari et al. (2023)	dFC	Redundancy could provide a basis for neuroprotective mechanisms of cognitive ageing and act as an early biomarker of AD.
vmAD/NC	Sendi et al. (2021)	dFNC	From NC to AD, the connectivity strength changed and the temporal properties of the FNC also became dysregulated.
AD/ASD	Qiao et al. (2022)	dFC	Inter-component dFC could be used as a biomarker for the diagnosis of AD et al. and provide a basis for brain connectomics.
AD/MCI/NC	Ma et al. (2020)	CAP	The DMN and visual network of AD are impaired, and transition and CAP entropies can be used as new biomarkers.
AD/NC	Adhikari et al. (2021)	CAPs	Resting-state co-activation patterns could be a biomarker for the diagnosis and prediction of AD.

explore the dynamic characteristics of the three resting networks and the hidden neural mechanisms of AD in patients, providing some theoretical inspiration for the prevention, diagnosis and treatment of diseases. Finally, the random walk method was used to simulate the dynamic changes in activity patterns in the triple network as a method to verify the effectiveness of the energy landscape analysis method.

2. Materials and methods

2.1. Subjects

The fMRI data from all subjects investigated in this study were obtained from the Alzheimer's Disease Neuroimaging Initiative (ADNI) database and were acquired using a Philips 3.0 T MRI instrument.[1] The downloaded data from each subject included 3 T structural fMRI data and behavioral data. This study included two groups of subjects selected based on the following criteria: (1) 33 patients with confirmed AD and MMSE scores = 6–26 points who were able to complete the entire data collection process and maintain a stable resting state during the entire time and (2) 39 normal healthy elderly people with MMSE scores = 26–30 points, without depression or other types of dementia, and no history of receiving medication for psychiatric diseases.

Resting-state fMRI data were obtained from scans acquired with a 3.0 T Philips instrument. The acquisition parameters were as follows: (1) parameters of the fMRI scan were EPI fast imaging sequence, flip angle = 80°, matrix = 64 × 64 × 6,720, slice thickness = 3.3 mm, TR = 3,000 ms, TE = 30 ms, and pixel spacing = 3.3 × 3.3 × 3.3 mm^3. (2) Scan parameters of the 3D-weighted T1 structural images were an acquisition plan = sagittal, flip angle=9°, and matrix = 256 × 256 × 170.

2.2. Data preprocessing

We preprocessed the resting-state fMRI data using the FSL toolkit and the AFNI toolkit. The preprocessing steps are described below. (1) The first four time points were deleted to ensure that all data were derived from a stable magnetic field. (2) Head movements were corrected. (3) Gaussian spatial smoothing was performed with a half-peak width of 6 mm. (4) Bandpass filtering was performed at 0.01–0.1 Hz. (5) Linear registration FLIRTt with the MNI152 standard spatial template was conducted. (6) White matter and cerebrospinal fluid signals were removed.

2.3. Triple-network ROI time series extraction

The ROI template used in this study was obtained from the Neurofunctional Imaging of Mental Disorders Laboratory at Stanford University.[2] We used this ROI template to extract time series of representative brain regions within the three networks. We selected representative ROIs from the three networks to extract their time series. The coordinates of the selected ROI corresponding to the Brodmann area (BA) and the MNI standard space are shown in Tables 2–5.

TABLE 2 Demographic and clinical scale information of subjects.

	AD (n=33)	NC (n=39)	p-value
Gender(female/male)	14/19	16/23	0.90
Age(mean ± SE)	73.35 ± 1.30	74.44 ± 1.07	0.51
MMSE(mean ± SE)	22.97 ± 0.42	28.87 ± 0.20	< 0.001
CDR(mean ± SE)	0.76 ± 0.08	0.00 ± 0.00	< 0.001

2.4. Energy landscape analysis method

The energy landscape approach aims to study the interactions among local brain regions from a statistical-physical perspective. The definition of energy can be used to describe the state of a brain system composed of different brain regions. This state model is essentially determined by the empirical distribution of fMRI data in different brain regions. Based on the model defined by the energy function, the energy landscape of the brain system in the state space can be obtained. The structure of the energy landscape reflects the stability and interactions of the states of the brain system. Furthermore, the energy landscape can also reflect a series of dynamic characteristics of the system.

We fit the subjects' fMRI data to the pairwise maximum entropy model (MEM) using the criteria described below (Ezaki et al., 2018). Due to the large amount of data required for this method, we collected the fMRI signals from the same group of subjects and then performed pairwise MEM fitting. As each network contains a certain number of ROIs, we labeled each ROI as $i\ (i = 1,2.....)$ and denoted the binarized activity of the fMRI sequence at moment t as $\sigma_i^t\ (1 \le t \le T)$, with +1 and -1 representing the activation and deactivation states, respectively. We set a threshold value for each ROI of each subject, and we considered the ROI in an active state when it exceeded this threshold value. The threshold is the average signal value of the ROI for the subject over the whole time course, and thus the ROI of each subject is active approximately 50% of the time moments. The pattern of activity at moment t is represented by the N_{ROI} -dimensional binary vector $\left[\sigma_1^t,\sigma_2^t,....,\sigma_{N_{ROI}}^t\right]$, and there exist $2^{N_{ROI}}$ possible patterns of ROI activity, which are enumerated as $V_1 = [-1,-1,...,-1].....V_{2^{N_{ROI}}} = [1,1,...,1]$.

For each ROI, we aggregated the data from the same set of subjects according to the time scale and calculated the occurrence frequency of each activity pattern $V_k\left(k = 1,...,2^{N_{ROI}}\right)$, denoted as $P(V_k)$. In the paired maximum entropy model, the frequencies conform to the Boltzmann distribution as follows:

$$P(V_k) = e^{-E(V_k)} / \sum_{i=1}^{2^{N_{ROI}}} e^{-E(V_i)} \quad (1)$$

where $E(V_k)$ represents the energy of the active mode V_k, which we calculate using the following equation:

1 https://adni.loni.usc.edu/

2 http://findlab.stanford.edu/research

TABLE 3 Brain coordinates in the DMN.

Number	ROI	Brain area	BA	MNI space		
				x	y	z
1	dDMN_1_ROI	Left Medial Frontal Gyrus	10	0	49	12
2	dDMN_2_ROI	Left Angular Gyrus	39	−48	−73	32
3	dDMN_3_ROI	Right Media Frontal Gyrus	8	18	38	51
4	dDMN_4_ROI	Precuneus	31	0	−57	30
5	dDMN_5_ROI	Cingulate Gyrus	24	0	−17	35
6	dDMN_6_ROI	Right Angular Gyrus	39	48	−66	29
7	dDMN_7_ROI	Thalamus	/	−6	−6	3
8	dDMN_8_ROI	Left Parahippocampal Gyrus	35	−24	−37	−9
9	dDMN_9_ROI	Right Parahippocampal Gyrus	35	24	−21	−23

TABLE 4 Brain coordinates in the CEN.

Number	ROI	Brain area	BA	MNI space		
				x	*y*	*z*
1	LCEN_1	Left Precentral Gyrus	9	−35	21	3
2	LCEN_2	Left Middle Frontal Gyrus	10	−44	46	1
3	LCEN_3	Left Inferior Parietal Lobule	40	−44	−65	4
4	LCEN_4	Left Middle Temporal Gyrus	21	−65	−38	12
5	RCEN_1	Right Precentral Gyrus	9	32	26	4
6	RCEN_2	Right Middle Frontal Gyrus	10	35	62	7
7	RCEN_3	Right Inferior Parietal Lobule	40	46	−54	49
8	RCEN_4	Right Middle Frontal Gyrus	8	3	36	44

$$E(V_k) = -\sum_{i=1}^{N} h_i \sigma_i - \frac{1}{2}\sum_{i=1}^{N}\sum_{\substack{j=1 \\ j\neq i}}^{N} J_{ij}\sigma_i\sigma_j \quad (2)$$

The fitting parameters h_i and J_{ij} denote the tendency of the ith ROI to be active when it is isolated and the strength of the interaction between the ith ROI and the jth ROI, respectively. Based on this definition, a smaller energy value corresponds to a greater frequency of occurrence of a pattern of activity on the time scale.

We obtain h_i and J_{ij} $(i,j = 1,2,\ldots,N_{ROI})$ by initially calculating the mean and two-by-two correlations for each state in the fMRI data from the subjects. The formula used for the calculation is as follows (where $\langle\ \rangle$ denotes the average value):

$$\langle\sigma_i\rangle = \left(\frac{1}{T}\right)\sum_{t=1}^{T}\sigma_i^t \quad (3)$$

$$\langle\sigma_i\sigma_j\rangle = \left(\frac{1}{T}\right)\sum_{t=1}^{T}\sigma_i^t\sigma_j^t \quad (4)$$

For a particular h_i and $J_{ij}(i,j = 1,2,\ldots,N_{ROI})$, the mean and correlation expected from the model in equation (1) are as follows:

$$\langle\sigma_i\rangle_m = \sum_{k=1}^{2^{N_{ROI}}}\sigma_i(V_k)P(V_k)$$

$$\langle\sigma_i\sigma_j\rangle_m = \sum_{k=1}^{2^{N_{ROI}}}\sigma_i(V_k)\sigma_j(V_k)P(V_k)$$

Notably, only the information on the average activity in each brain region and the coactivity between two brain regions in the fMRI data were used in the calculation. Other information was not considered in the model, such as information on the coactivity patterns between multiple brain regions. We must calculate the relative entropy of the model distribution of the brain system states and their empirical distribution, which is the K-L divergence (Kullback–Leibler divergence). The model distribution is defined as the Boltzmann distribution, and the empirical distribution is the actual probability distribution of each state in the fMRI data. The difference between the two can be measured using the following K-L divergence D_2:

$$D_2 = \sum_{k=1}^{2^{N_{ROI}}} P(V_k)\cdot\log_2\left(P(V_k)/P_{model}(V_k)\right) \quad (5)$$

We iteratively adjust the values of h_i and J_{ij} according to $h_i^{new} = h_i^{old} + \alpha\left(\langle\sigma_i\rangle - \langle\sigma_i\rangle_m\right)$ and $J_{ij}^{new} = J_{ij}^{old} + \alpha\left(\langle\sigma_i\sigma_j\rangle - \langle\sigma_i\sigma_j\rangle_m\right)$, where α is the iteration step, until they gradually approach the values $\langle\sigma_i\rangle_m$ and $\langle\sigma_i\sigma_j\rangle_m$ given in eqs. (3, 4) of the model.

The principle of this iteration is based on the gradient descent method, which minimizes the given K-L scatter, improves the accuracy of the model fit by iteratively training the two parameters h and j continuously, and finally obtains an optimized model. The energy landscape of the system is constructed based on this optimized model. The dynamics of different states of the brain system can be characterized by the local minimum, basin, dis-connectivity graph and energy barrier in the energy landscape.

In the energy landscape, among the 2^n state vectors constructed, the two states in which only one element differs are considered adjacent states, such that each state has n neighboring states. When the energy value of a state is less than all n neighboring states, the state is defined as a local minimal state. It is also possible to construct disconnected diagrams to represent the main features of each state, including information such as the energy of local minimal states and the energy barrier of switching between neighboring states. The disconnected graph is a tree-like branching graph structure, where different branches represent different local minima, and the branch heights between neighboring local minima represent the energy barriers between them. The disconnected diagram is a more concise and intuitive representation of the relationship between the substable states of the system compared to the energy landscape. The detailed steps used to construct it are as follows:

(1) First, the energy landscape is constructed based on the fitted optimization model and visualized to some extent in the superlattice diagram. Each state has a corresponding energy location and is connected to neighboring states, constituting multiple energy basins.
(2) Second, the energy maximum corresponding to all current states is set as the energy threshold, which is denoted as Eth.
(3) Then, the states and corresponding edges in the superlattice diagram with energies larger than the threshold Eth are removed.
(4) Finally, all local minimal states in the superlattice diagram are checked to confirm that they have at least one path to achieve an interconnection.
(5) Steps (3) and (4) are repeated and the threshold Eth is set to the maximum energy value in the remaining states, repeating this process until all local minimal states are disconnected from each other.
(6) The energy threshold Eth corresponding to the first disconnection of each two local minimal states is recorded, and this value is the energy barrier between these two states, which is the height of the potential barrier between them in the disconnection diagram. As a result, the disconnected graph of local minimal states is obtained.

The energy landscape analysis method is a calculation method that can directly interpret multivariate time series. The analysis consists of the following four main steps: (1) binarization of the BOLD signal; (2) estimation of the maximum entropy model (Boltzmann distribution); (3) construction of the disconnected map and the local minimal state (basin) of energy; and (4) calculation of the dynamic index for the energy landscape. This method was originally designed to analyze fMRI data, but in principle, it is also applicable to other types of data. Based on experience, the energy landscape analysis method has a better performance when the number of variables is approximately 6 to 15. For a model with more variables, the calculation cost becomes significant, and the interpretation of the results becomes difficult. The energy landscape analysis process is shown in Figure 1.

3. Results

3.1. Construction of the triple-network energy landscape in the resting-state brain

Based on the structure of the energy landscape described above, we subsequently conducted studies on the dynamic characteristics of the triple networks in the resting-state brains of AD patients and NC subjects.

First, we constructed the corresponding energy landscape with fMRI data from two groups of subjects in the triple networks. The structure of the energy landscape in the triple networks from NC subjects and AD patients is shown in Figure 2. Nine ROIs were selected for the DMN, for a total of 2^9 activation states. The diagram in Figure 2A1 shows the activity patterns corresponding to the 8 local minimal states in AD patients, where black represents the inactivated state and white the activated state. The figure shows strong complementarity between the brain area states of these 8 activation patterns. For example, in pattern 1, all 9 brain areas are inactive, while in pattern 8, all 9 brain areas are activated; in pattern 2, only the left and right angular gyrus and precuneus are activated, while the remaining brain areas are inactive, which is completely opposite and complementary to pattern 7. Figure 2A2 shows the nonconnected graph of the local minimal state of AD patients, which visualizes the basic characteristics of each activity pattern, and the branches of the tree represent the hierarchical structure of each activity pattern in the energy landscape. Each branch corresponds to a local minimal state, and the difference in height between each two states is the energy barrier, which measures the amount of energy required to jump between these two states. The larger the energy barrier, the less easy it is to jump between states and the lower the frequency of occurrence. Conversely, if the jump between neighboring states is easier, the frequency is higher on the time scale. As shown in Figure 2A2, pattern 4 and pattern 8, pattern 1 and pattern 5 are neighboring patterns, and their energy is relatively low, while the energy of the remaining four states is relatively high. Based on this structural feature of the energy landscape and the similarity between the two groups of subjects, we grouped the two lower energy pairs of local minimal states into two major brain states, denoted by major state 1 and major state 2, and the other higher energy local minimal states were uniformly defined as secondary brain states, which were denoted as minor states. These three states correspond to different colors in the nonconnected graph. The subsequent representation of the triple-network dynamics is based on these three states (major state 1, major state 2 and minor state) (Table 5).

Figure 2A3 shows five activation patterns corresponding to the local minimal state in the DMN energy landscape of NC subjects, where pattern 2 is characterized by activation in the left and right angular gyrus, left and right medial frontal gyrus, cingulate gyrus and precuneus, which are complementary to pattern 4. In pattern 3, only the left and right para-hippocampal gyrus, left and right angular gyrus and precuneus brain regions are activated, while the remaining brain regions are inactive and have no complementary activation patterns.

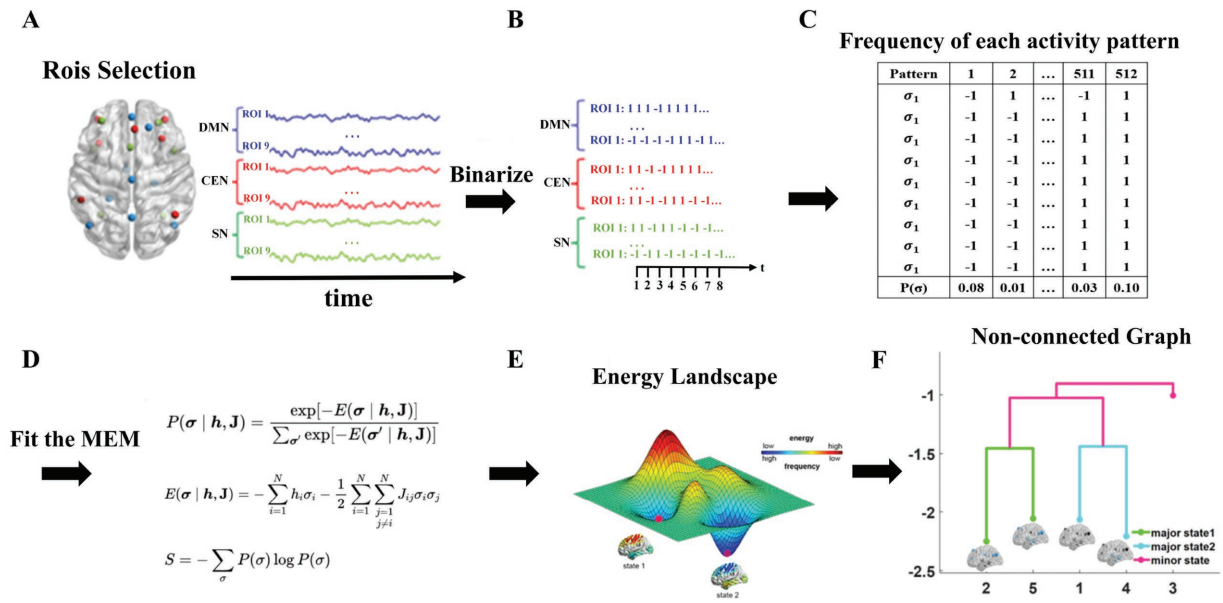

FIGURE 1
The process of energy landscape analysis. **(A)** extraction of ROI time series, **(B)** binarization of data, **(C)** calculation the frequency of appearance in each activity pattern, **(D)** fitting MEM **(E)** construction of energy landscape **(F)** construction of non-connected graph.

Compared with the results from the AD group, the NC group has 3 fewer brain activity patterns. Figure 2A4 shows the nonconnected graph of the energy landscape of the DMN in NC subjects with a structure similar to AD, pattern 2. Pattern 5, pattern 1 and pattern 4 are adjacent to each other, the energy required to jump between two states is smaller, and the energy of these four patterns is significantly lower than pattern 3. We inferred that these four patterns potentially represent the major activity patterns of the DMN in the resting state of NC subjects.

Figure 2B1 shows the activity patterns corresponding to the 8 local minimal states in AD patients, which are represented by the combination of 8 ROI activation states. Similar to the DMN, a strong complementary relationship exists between these 8 activation patterns corresponding to the states of brain regions. For example, in pattern 1, all 8 brain regions are inactive, which is complementary to pattern 8, where all 8 brain regions are activated; in pattern 3, only the left and right middle frontal gyrus and the left and right inferior parietal lobule are active, which is complementary to the activation status of pattern 6. Figure 2B2 shows the nonconnected graph of the local minimal state in AD patients, where pattern 7 and pattern 8, as well as pattern 1 and pattern 2 are adjacent to each other, and the energy of these four patterns is relatively low compared to other patterns. Figure 2B3 shows six activation patterns corresponding to the local minimal states in the CEN energy landscape of NC subjects. Similar to the results from AD patients, the activation patterns are complementary, such as the lack of activation in all brain regions in pattern 1 that is complementary to activation in pattern 6; in pattern 2, only the right precentral gyrus, right middle frontal gyrus and right inferior parietal lobule are activated, which is complementary to the status of pattern 4. However, compared with subjects with AD, pattern 3 and pattern 5 in NC subjects have no complementary patterns, and two patterns of brain activity are missing. The nonconnected graph in the CEN of NC subjects is shown in Figure 2B4. Similarly, patterns 5 and 6 and patterns 1 and 3 are neighboring, the energy required to jump between states with close branches is smaller, and two additional states with higher energy are observed. Overall, the structure of the CEN energy landscape for the AD and NC groups is similar to their DMN results.

Figure 2C1 shows 8 local minimal states corresponding to activation patterns in AD patients, which are represented by the combination of eight ROI activation states. All activation patterns in the figure are complementary. For example, in pattern 2, the left and right middle frontal gyrus and left cingulate gyrus are activated, while the remaining brain regions are not activated, which is complementary to the states of pattern 7. In pattern 3, only the left and right insula are activated, which is completely opposite to the state of pattern 6. Figure 2C2 shows the nonconnected graph of the local minimal states of AD patients, where pattern 1 and pattern 5, as well as pattern 4 and pattern 8, are adjacent to each other, and the energy of these four patterns is relatively low compared to the other patterns. Figure 2C3 represents the 8 brain area activation patterns in the SN energy landscape of NC, which are completely consistent with the activation patterns of AD patients. The nonconnected graphs of the SN in NC subjects are shown in Figure 2C4, with pattern 1 and pattern 5, as well as pattern 4 and pattern 8 located adjacent to each other, and the energy of these two groups of patterns is significantly lower than the other four states. We infer that these four patterns potentially represent the major activity patterns in the resting-state SN of NC subjects. Overall, unlike the DMN and CEN, the results of the energy landscape analysis of the SN network in the AD and NC groups were less different.

3.2. Dynamic characterization of the triple-network activity patterns in the brain

Based on the accurately fitted energy landscape model mentioned above, some frequently occurring brain major states are sufficiently

10.3389/fnins.2023.1171549

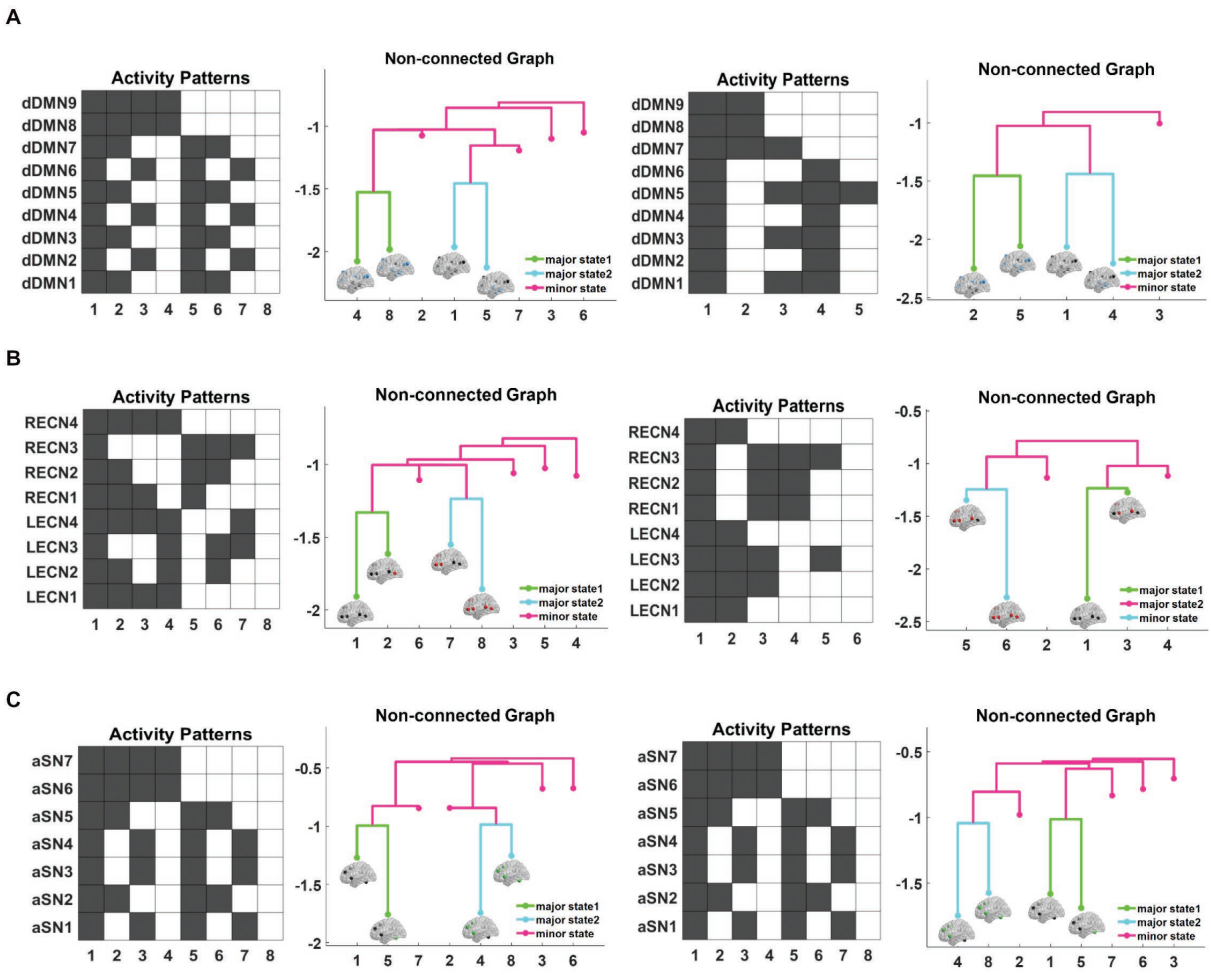

FIGURE 2
The structure of the energy landscape is shown for DMN from AD patients and NC subjects **(A1–A4)**, CEN **(B1–B4)**, and SN **(C1–C4)**. Comparing the three networks reveals that the differences between AD and NC are the least in SN and the greatest in DMN.

TABLE 5 Brain coordinates in the SN.

Number	ROI	Brain area	BA	MNI space		
				x	*y*	*z*
1	aSN1	Left Middle Frontal Gyrus	10	−32	45	26
2	aSN2	Left Insula	13	−41	15	−2
3	aSN3	Left Cingulate Gyrus	32	−2	17	45
4	aSN4	Right Middle Frontal Gyrus	10	28	43	26
5	aSN5	Right Insula	13	44	13	1
6	aSN6	Left Cerebellum	/	−33	−54	−42
7	aSN7	Right Cerebellum	/	33	−55	−43

representative of the resting-state brain activity pattern. The energy landscape analysis revealed the hierarchical relationships between the 2^n states by calculating the energy values for all possible brain activity patterns and systematically searching for brain activity patterns with the lowest local energy values that play a dominant role and are more easily observed compared to others. This value is essentially a statistical indicator of the probability that each activity pattern occurs on a time scale. Patterns of activity with lower energy values tend to occur more frequently, and these patterns are considered relatively more stable.

The results of the study showed that the energy landscape of the triple networks of subjects in the AD and NC groups had a similar structure that was dominated by the activity patterns with complementary relationships. Moreover, both had two sets of

neighboring and low-energy activity patterns. Meanwhile, the remaining patterns were relatively high in energy. This suggests that the other local minimal states were less stable than these four patterns, which all had similar activation patterns in the triple networks. For instance, patterns 1/4/5/8 in the DMN of AD patients was similar to patterns 1/2/4/5 in the ROI activation pattern of NC subjects.

Based on the classification of the triple-network brain activity states described above, we selected some common dynamic indicators to quantitatively represent the dynamic characteristics of the three networks in the subjects, which include the appearance frequency, transition frequency and duration.

First, we calculated the frequency of occurrence of each state in the fMRI time series and used it to quantify the dominance of different states. The comparison of the frequency of each state in the DMN between the AD and NC groups is shown in Figure 3A. Within a single group of subjects, the frequencies of major state 1 and major state 2 were much higher than that of the minor state. The proportion of the frequency of brain states in the DMN of AD patients was similar to that of NC subjects, and both showed a significantly higher proportion of major states than minor states. This finding is consistent with the results of the energy landscape analysis, where states with low energy appear more frequently in time, are more stable, and dominate the pattern of brain activity. In addition, for major state 1, the frequency of occurrence was 42.1% in AD patients and 47.6% in NC subjects, representing a significantly lower percentage in AD patients than in NC subjects ($p < 10^{-8}$). Similarly, the frequency of major state 2 was 43.5% in AD patients and 50.5% in NC subjects, which was significantly lower in AD patients than in NC subjects ($p < 10^{-12}$). However, the frequency of the minor state in the AD group was 14.4%, while the frequency in the NC group was 1.8%, representing a significantly higher frequency in the AD group than in the NC group ($p < 10^{-25}$).

Figure 3C shows the comparison of the frequency of each state in the CEN between the AD and NC groups. Within a single group of subjects, the proportions of the frequencies of major state 1 and major state 2 were significantly higher than that of the minor state. The proportions of the frequencies of CEN brain states in AD patients was similar to that in NCs, both showing a significantly higher proportion of major states than minor states. Similarly, for major state 1, the frequency of occurrence was 40.2% in AD patients and 44.9% in NC subjects, and was significantly lower in AD patients than in NC subjects ($p < 10^{-4}$). The frequency of major state 2 was 38.8% in AD patients compared with 43.1% in NC subjects, and was significantly lower in AD patients than in NC subjects ($p < 10^{-3}$). In addition, the frequency of the minor state was 21.1% in the AD group compared with 11.9% in the NC group, representing a significantly higher frequency in the AD group than in the NC group ($p < 10^{-6}$). The results of this analysis were generally similar to those obtained for the DMN network.

Figure 3E shows the frequency results for each state in the SN between the AD and NC groups. Within a single group of subjects, the frequency proportions of major state 1 and major state 2 were significantly higher than those of the minor state. For different groups of subjects, a significant difference was not observed between groups in the frequency of major state 1, which was different from the results obtained for the first two networks ($p = 0.9026$). In addition, the frequency of major state 2 was significantly lower in patients with AD than in NC subjects ($p < 10^{-6}$), and the frequency of major state 2 was 37.5% in patients with AD and 42.9% in NC subjects. In contrast, the frequency of minor states was significantly higher in AD patients than in NCs ($p < 10^{-3}$), as the frequency of minor states was 22.2% in AD patients and 16.8% in NC subjects.

The aforementioned results indicate that the frequency of major brain states in AD patients is significantly lower than that in NC subjects, while the frequency of minor states is significantly higher than that in NC subjects. We further analyzed the dynamics of brain activity states by calculating and visualizing the transition frequency matrices between different brain activity states in the triple networks of the AD and NC groups. The transition frequency matrix of the DMN is shown in Figure 4C, and it depicts that the activity pattern transitions in both the AD and NC groups are mainly concentrated between the two major states. The difference is that the transition frequency between the minor state and the major state is higher in patients with AD, while it is approximately 0 in NC subjects.

The transition frequency matrix between different brain states of the CEN is shown in Figure 4D, and it indicates that although the activity state transitions in both the AD and NC groups were mainly concentrated between the two major states, the concentration trend was more obvious in NC subjects. Meanwhile, the transition frequency between the minor state and major states was significantly higher in AD patients.

The transition frequency matrix between different brain states of the SN network is shown in Figure 4E. Compared with the first two networks, the transition frequency between the minor state and major states was significantly increased for both groups. However, the active state transitions of NC subjects were still mainly concentrated between the two major states, while patients with AD had similar transition frequencies between the minor state and major states compared to the two major states.

In summary, the results showed that the minor state was less frequent in both AD patients and NC subjects, and the transition frequency from the minor state was also low. Therefore, we classified the transitions of brain activity states into the following two types: direct transitions between major states only and indirect transitions between the two major states through the minor state. For simplicity, we refer to the minor state as the intermediate state between the major states, which mainly appears in the jump transition between major states. The two types of state transitions are defined in Figure 4B.

Based on this definition, we further calculated the frequency of direct transitions between major states and the frequency of indirect transitions between major states through minor states and compared the statistical analysis of AD patients with NC subjects. The comparison of the transition frequencies between major states in the DMN for both groups is shown in Figure 5A. The direct transition frequencies were higher than the indirect transition frequencies in both the AD and NC groups. However, the direct transition frequency between major states was significantly lower in AD patients than in NC subjects ($p < 10^{-8}$), being 19.9% in AD patients and 27.6% in NC subjects. In contrast, the indirect transition frequency for major states was significantly higher in subjects with AD than in NC subjects ($p < 10^{-21}$), being 6.8% in the AD group compared to 0.9% in the NC group.

The comparison of the transition frequencies between major states in the CEN for both groups is shown in Figure 5C. The direct transition frequency of major states in the CEN was 17.4% in AD patients and 21.9% in NC subjects, which was significantly lower in

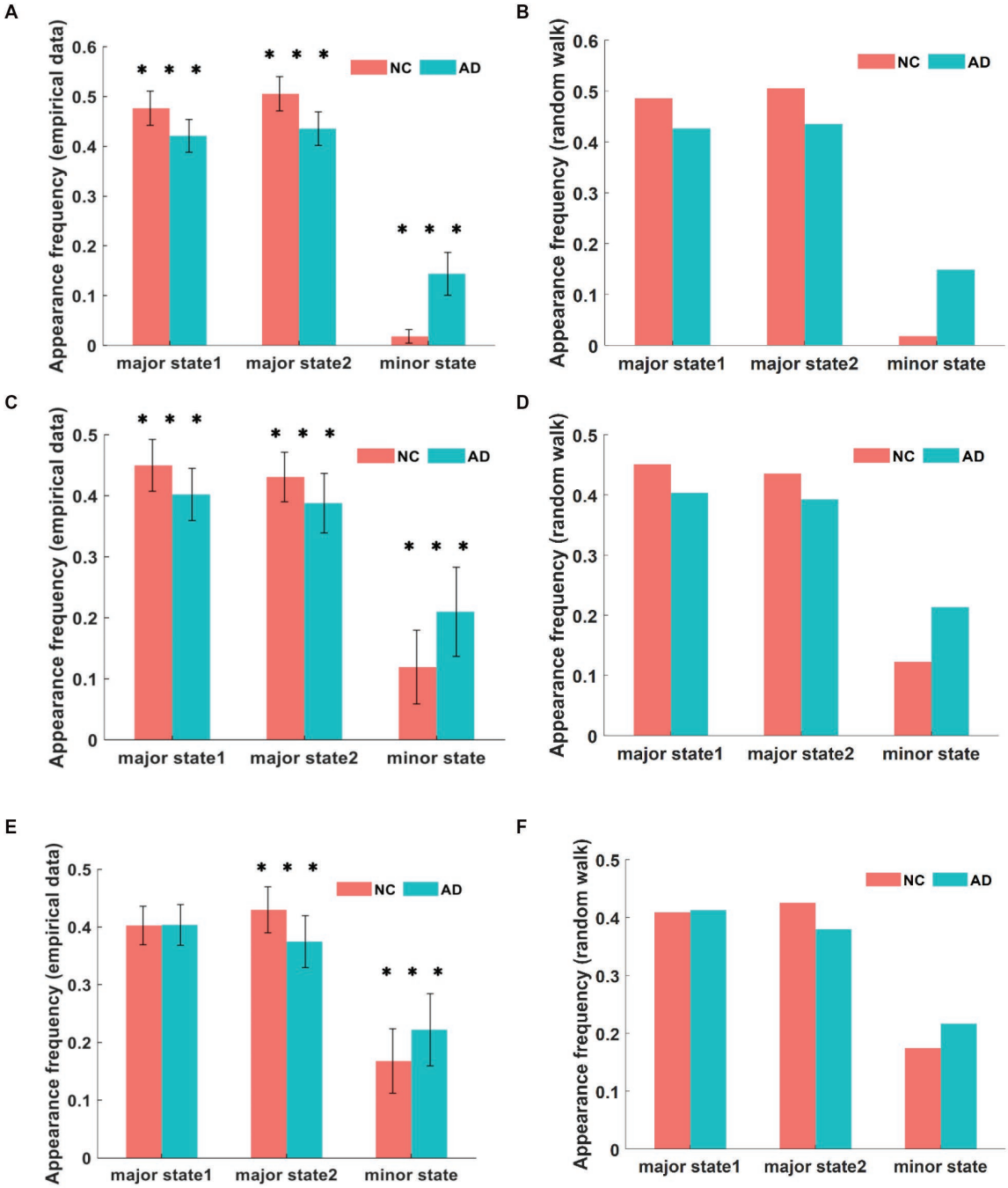

FIGURE 3
The frequency of different brain states in DMN between AD and NC in empirical data is compared in **(A)**. In simulation, the frequency of appearance for each state in DMN is shown in **(B)**. The frequency of appearance of each state in CEN is presented in **(C,D)** for empirical data and simulation, respectively. Similarly, the frequency of appearance of each state in SN is shown in **(E,F)** for empirical data and simulation. Although no significant difference is observed between the two types of data, there are significant differences between AD and NC, and these differences have varying degrees in the three networks. ***$p < 0.001$ in t-test.

AD patients than in NC subjects ($p < 10^{-3}$). Conversely, the frequency of indirect transitions between major states was 7.5% in patients with AD compared to 4.4% in NC subjects, and the value of the AD group was significantly higher than that for the NC group ($p < 10^{-5}$).

The comparison of the transition frequencies between major states in the SN for both groups is shown in Figure 5E. The direct transition frequency of the SN was 15.9% in AD patients and 18.5% in NC subjects, indicating a significantly lower value for AD patients than for NC subjects ($p = 0.0048$). In contrast, the indirect transition frequency of the major state was 8.5% in the AD group compared to 7.2% in the NC group, where the value of the AD group was higher than that of the NC group ($p = 0.025$).

The state transition frequency difference in the three networks was similar in both groups, with lower direct transition frequencies and

10.3389/fnins.2023.1171549

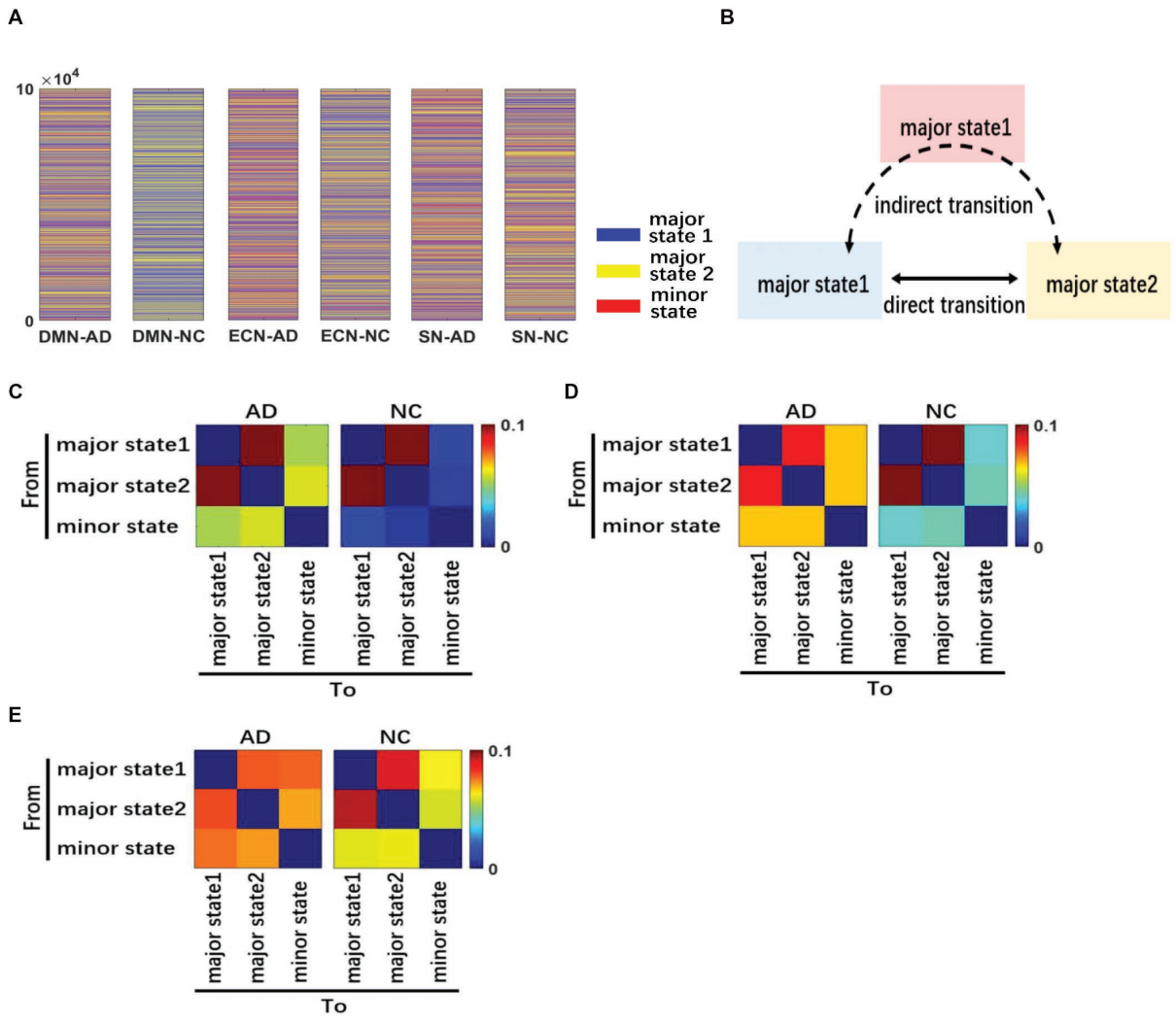

FIGURE 4
Dynamics of brain activity patterns. We performed a 10^5 random-walk numerical simulation to characterize the dynamics in brain states for each network of AD and NC **(A)**. A schematic diagram showing different types of transitions between brain activity states is presented. We divide the transition pattern of major states into direct and indirect forms **(B)**. The transition frequency matrix between different brain states of DMN **(C)**. The transition frequency matrix in CEN **(D)**. The transition frequency matrix in SN **(E)**. The three networks have different degrees of difference.

higher indirect transition frequencies in AD patients compared to NC subjects. However, within the AD group, the direct transition frequencies were significantly higher than the indirect transition frequencies. This abnormal state transition indicates that the brain activity states of AD patients tend to remain in minor states for a longer time than those of NC subjects. We confirmed this inference by subsequently calculating the duration of brain activity patterns in the three states, where this index was the average duration of each state over the time series, quantified as the mean length of repetition over time. The unit of duration is step of TR, shortened to s. The comparison of the mean duration in the DMN between both groups is shown in Figure 6A. The duration of both major states in the AD group was significantly smaller than that of the NC group, where the mean duration of major state 1 was 2.78 s in patients with AD and 3.23 s in NC subjects ($p = 0.0019$), and the mean duration of major state 2 was 2.76 s in patients with AD and 3.51 s in NC subjects ($p < 10^{-8}$). However, the duration of the minor state in AD patients was significantly longer than that in NC subjects, with a mean duration of 1.27 s in AD patients and 0.88 s in NC subjects ($p < 10^{-4}$). The comparison of the mean duration in the CEN between both groups is shown in Figure 6C. The duration of both major states in the AD group was significantly smaller than that in the NC group, where the average duration of major state 1 in patients with AD was 2.62 s and 3.03 s in NC subjects ($p = 0.0011$); the average duration of major state 2 in the AD group was 2.49 s and 2.83 s in the NC group ($p = 0.0017$). Unlike the results for the DMN, the duration of the minor state in the CEN of AD patients was not significantly different from that of NC subjects, with a mean duration of 1.51 s in AD patients and 1.42 s in NC subjects ($p = 0.18$). Figure 6E shows the comparison of the mean duration of states in the SN between both groups. The mean duration of major state 1 was 2.56 s in AD patients and 2.59 s in NC subjects, which were not significantly different ($p = 0.74$); the mean duration of major state 2 was 2.47 s in AD patients and 2.81 s in NC subjects, and was significantly smaller in the AD group than in the NC group ($p = 0.0024$). In addition, the duration of the

10.3389/fnins.2023.1171549

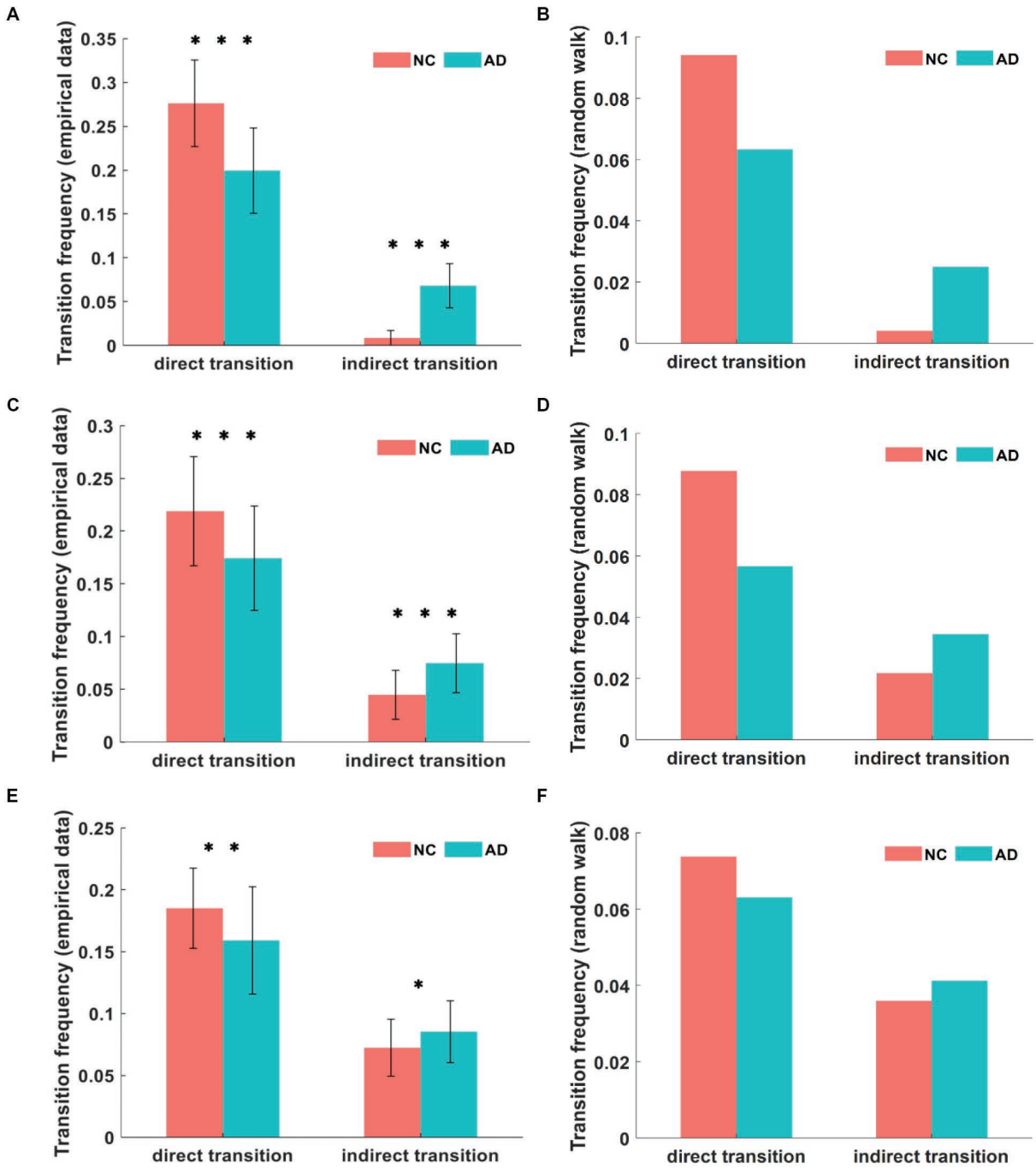

FIGURE 5
In the empirical data, the comparison of transition frequencies between major states in DMN **(A)**. In the simulation, the transition frequencies in DMN **(B)**. The transition frequencies between major states in CEN from empirical data and simulation **(C,D)**. The transition frequencies in SN from empirical data and simulation **(E,F)**. We can find that the empirical value is greater than the simulation value, and there are different degrees of variability in AD and NC among the three networks. *$p < 0.05$, **$p < 0.01$, ***$p < 0.001$ in t-test.

minor state in AD patients was longer than that in NC subjects ($p = 0.017$), and the average duration of the minor state was 1.47 s in AD patients and 1.35 s in NC subjects.

Compared to the NC group, brain activity in the AD group was characterized by a shorter duration in major states and a significantly longer duration in transition states, but the duration of major states was significantly longer than that of transition states within the AD group. Notably, the duration of each state in the triple networks differed to varying degrees, with the DMN differing most significantly, followed by the CEN and SN.

In conclusion, compared with the NC group, the AD group has a higher frequency and duration of minor states and a higher frequency of indirect transitions, which indirectly reflects the abnormal dynamic characteristics of brain activity states in individuals with AD.

10.3389/fnins.2023.1171549

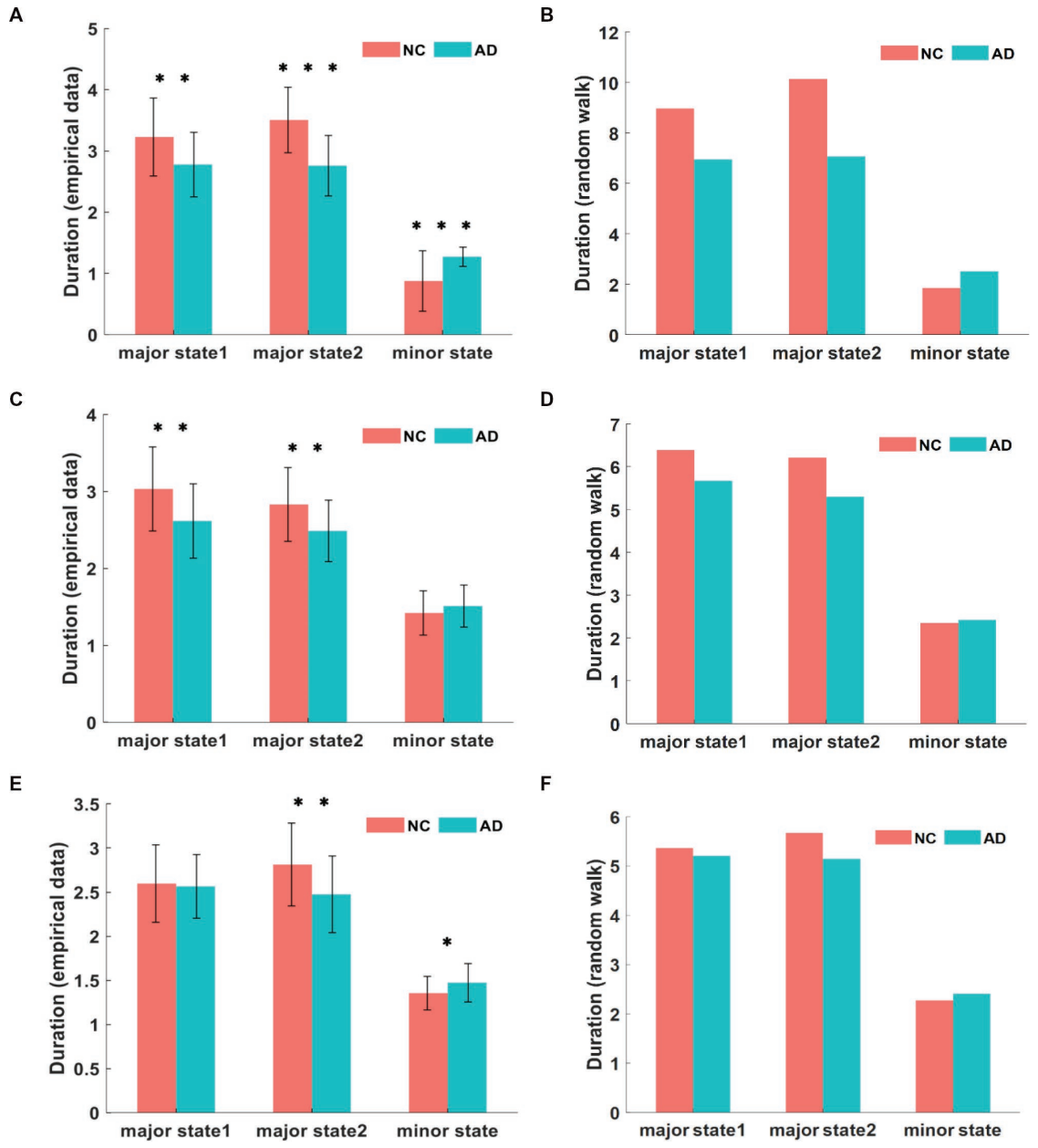

FIGURE 6
The comparison of empirical data on state duration in DMN **(A)**. The comparison of simulated data for state duration in DMN **(B)**. The state duration of each state in CEN from empirical data and simulation **(C,D)**. The state duration in SN from empirical data and simulation **(E,F)**. It can be found that the empirical value is smaller than the simulated value, and there are different degrees of variability in AD and NC among the three networks. *$p < 0.05$, **$p < 0.01$, ***$p < 0.001$ in t-test.

3.3. Random-walk simulation of the dynamics of the energy landscape

We performed 10^5 random walk data simulations to characterize the dynamic changes in the brain states of the AD and NC groups, as shown in Figure 4A. The variability of dynamic changes in brain states differed among the three networks, with the most significant difference noted in the DMN, followed by the CEN, and the least significant difference detected in the SN. Compared with patients with AD, the frequency of major states in the DMN of NC subjects was extremely high, but the frequency of minor states was low. In the CEN, the frequency of minor states in NC subjects is increased, but there was still a gap compared with AD patients. In the SN, the difference between the NC and AD groups was significantly reduced, and the frequency of each state was similar. The SN usually plays a moderating and transitional role between the DMN and CEN; thus, we hypothesized that the coordination relationship between the networks of dynamic brain systems in patients with AD might be less affected by the disease.

We characterized the dynamics of three core networks related to cognitive functions in AD and NC groups based on the energy landscape. Based on the results, the energy landscape structures of

the AD and NC groups are similar, the tree-like branching structures of the nonconnected graph have two sets of adjacent and relatively low energy local minimal states, and some similarity in the activation patterns of the three networks is observed between the two groups. Nevertheless, the results of the energy landscape analysis and the differences in dynamic characteristics of the AD and NC groups were significant. We analyzed three dynamic characteristics. The first characteristic is the appearance frequencies of different brain states, as shown in Figure 3B, Figure 5B and Figure 6B. In both the AD and NC groups, all three networks showed a significantly higher frequency of major states over time than minor states, while the frequency of major states in patients with AD was lower than that in NC subjects, which was also evident from the transition frequency matrix between the different brain activity states. Thus, the activity of minor states in patients with AD increased and the total number of appearances of major states decreased significantly in the same time period. The second feature is the frequency of different transition modes of the major state, as shown in Figure 3D, Figure 5D and Figure 6D. The direct transition frequencies between the major states in patients with AD are all lower than those of NC subjects. In contrast, their indirect transition frequencies are significantly higher than NC subjects. Therefore, the minor state of patients with AD, which functions as a transition state, affects the stability of the switching between the major states, and thus the direct switching between the major states is more easily interrupted by the appearance of the minor states. Finally, we analyzed the average durations of the three networks in the AD and NC groups, and the results in Figure 3F, Figure 5F and Figure 6F showed that the average durations of the two major states in patients with AD were less than those in NC subjects. Combining the results for these three characteristics, we propose that the major states in patients with AD showed instability phenomena, which might arise from the abnormal minor states. The total number of minor state appearances increased on the time scale, the AD group was more likely to jump from the major state to the minor state, and the duration of each minor state appearance increased. Based on these results, the brain regions associated with the minor state are more likely to be activated, and the activation level is increased and more persistent, disrupting the original steady state.

3.4. Study of the correlation between triple-network dynamic characteristics and clinical MMSE scores

We further explored whether the abnormal dynamic characteristics of the triple-network brain activity states in patients with AD are related to the disease by analyzing the dynamic indicators in combination with the subjects' clinical behavioral data, the scores of which range from 0–30 points, with lower scores representing a more severe intellectual impairment. In the figure, R represents the correlation coefficient, and P represents the level of significance of the correlation.

We first calculated the correlation between the appearance frequencies of each state in patients with AD and the MMSE scores. The results for the DMN are shown in Figure 7A. The frequency of appearance of both major states had a significant positive correlation with the MMSE score ($R = 0.484$, $p < 10^{-4}$; $R = 0.606$, $p < 10^{-7}$). In contrast, the frequency of the minor state was significantly negatively correlated with MMSE scores ($R = -0.724$, $p < 10^{-12}$). The correlation between the frequency of each state in the CEN of patients with AD and the MMSE score is shown in Figure 7B. The frequencies of both major states were positively correlated with the MMSE score ($R = 0.475$, $p < 10^{-4}$; $R = 0.335$, $p = 0.004$). In contrast, the frequency of the appearance of the minor state was significantly negatively correlated with the MMSE score ($R = -0.494$, $p < 10^{-4}$). The correlation between the frequency of each state in the SN of AD patients and MMSE scores is shown in Figure 7C. No correlation was observed between the frequency of major state 1 and the MMSE score ($R = 0.042$, $p = 0.724$), but a significant positive correlation was observed between the frequency of major state 2 and the MMSE score ($R = 0.528$, $p < 10^{-5}$). In contrast, the frequency of the minor state was negatively correlated with the MMSE score ($R = -0.389$, $p = 0.001$).

Second, we calculated the correlation between the transition frequency of patients with AD and the MMSE score. The result for the DMN is shown in Figure 8A. The direct transition frequency was significantly positively correlated with the MMSE score ($R = 0.548$, $p < 10^{-6}$). In contrast, a significant negative correlation was detected between the indirect transition frequency and MMSE score ($R = -0.736$, $p < 10^{-12}$). The correlation between the frequency of transitions in the CEN and the MMSE score is shown in Figure 8B. The frequency of the direct transition in patients with AD was positively correlated with the MMSE score ($R = 0.336$, $p = 0.004$). In contrast, the indirect transition frequency had a negative correlation with the MMSE score ($R = -0.421$, $p < 10^{-3}$). The correlation analysis between the frequency of transitions in the SN and the MMSE score is shown in Figure 8C. The frequency of the direct transition in patients with AD was positively correlated with the MMSE score ($R = 0.416$, $p < 10^{-3}$). The indirect transition frequency, on the other hand, had a negative correlation with the MMSE score ($R = -0.329$, $p = 0.005$). The correlations between each transition frequency and the MMSE score were similar for the three networks.

Finally, we analyzed the correlation between the mean duration of states in patients with AD and the MMSE score, and the results for the DMN are shown in Figure 9A. The correlation between the mean duration of major state 1 and the MMSE score was not significant ($R = 0.194$, $p = 0.103$), but the mean duration of major state 2 displayed a significant positive correlation with the MMSE score ($R = 0.459$, $p < 10^{-4}$). In contrast, the mean duration of the minor state was significantly negatively correlated with the MMSE score ($R = -0.363$, $p = 0.002$). Notably, due to the low frequency of the minor state in patients with AD, some outliers in their mean duration (duration close to 0) are present, which may have affected the results of the correlation analysis. The correlation analysis between the duration in the CEN of patients with AD and the MMSE score is shown in Figure 9B. Unlike the previous results, the mean durations of both major states in the CEN were positively correlated with the MMSE score ($R = 0.352$, $p = 0.002$; $R = 0.302$, $p = 0.01$). A weaker negative correlation was observed between the duration of the minor state and MMSE score ($R = -0.168$, $p = 0.158$). The correlation analysis between the mean duration in the SN of patients with AD and the MMSE score is shown in Figure 9C. The mean duration of major state 1 in patients with AD was not correlated with the MMSE score ($R = -0.055$, $p = 0.644$), whereas the mean duration of major state 2 was weakly positively correlated with the MMSE score ($R = 0.257$, $p = 0.029$).

10.3389/fnins.2023.1171549

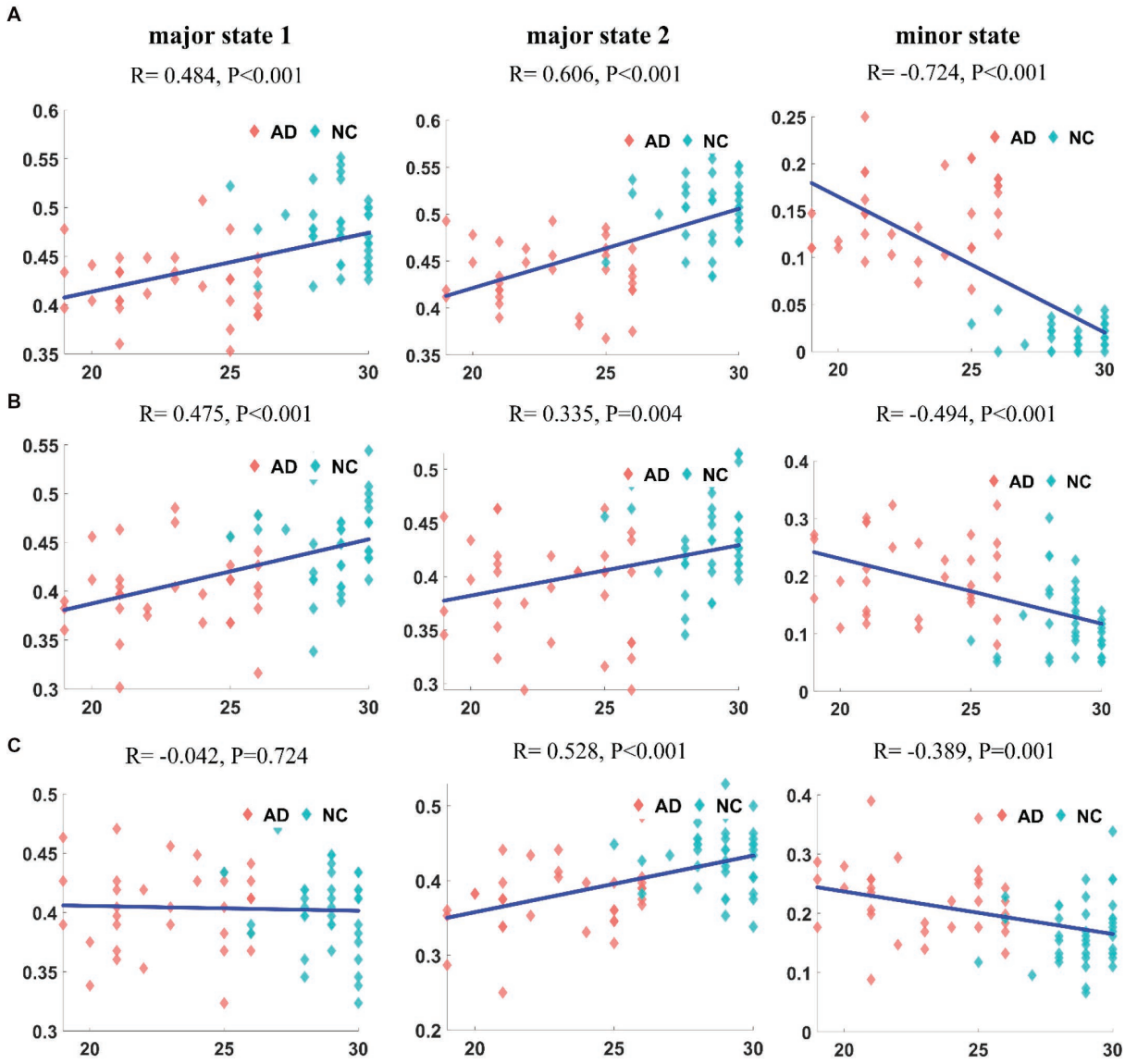

FIGURE 7
The correlation between the frequency of each state and MMSE in DMN **(A1–A3)**. The correlation between the frequency of each state and MMSE in CEN **(B1–B3)**. The correlation between the frequency of each state and MMSE in SN **(C1–C3)**. It can be found that the frequency of appearance and MMSE are correlated, and the correlation is most significant in DMN.

In addition, a weaker negative correlation was observed between the duration of the minor state and the MMSE score ($R = -0.259$, $p = 0.028$).

4. Discussion

4.1. Time-varying characteristics of the triple-network dynamics in the resting brain

In the present study, we explored the differences in dynamic characteristics of three networks in the resting brain between the AD and NC groups by conducting an energy landscape analysis. In all three networks, the brain activity patterns of patients with AD lacked a more stable major state compared to NC subjects, while the minor state was more active. This property may cause frequent switching in resting-state brain activity patterns between different substates, increasing the frequency of transitions between major and minor brain states, and the occurrence of minor states is significantly higher. Patients with AD experience difficulty in focusing on the major state for a long time and lose stability of the three networks.

According to previous studies of the normal ageing process of the brain, its internal balance system actively inhibits the effects of various genetic and environmental factors, whereas the balance system fails in patients with neurodegenerative diseases such as AD. The instability of spontaneous neuronal activity in cortical and hippocampal circuits is a typical feature of AD (Palop et al., 2007; Frere and Slutsky, 2018). Researchers observed a strong correlation between the formation of amyloid plaques, the appearance of overactive neurons and the impairment of learning abilities in animals. By performing functional studies of individual cortical neurons in a mouse model of AD, researchers found that the presence of overactive neurons near

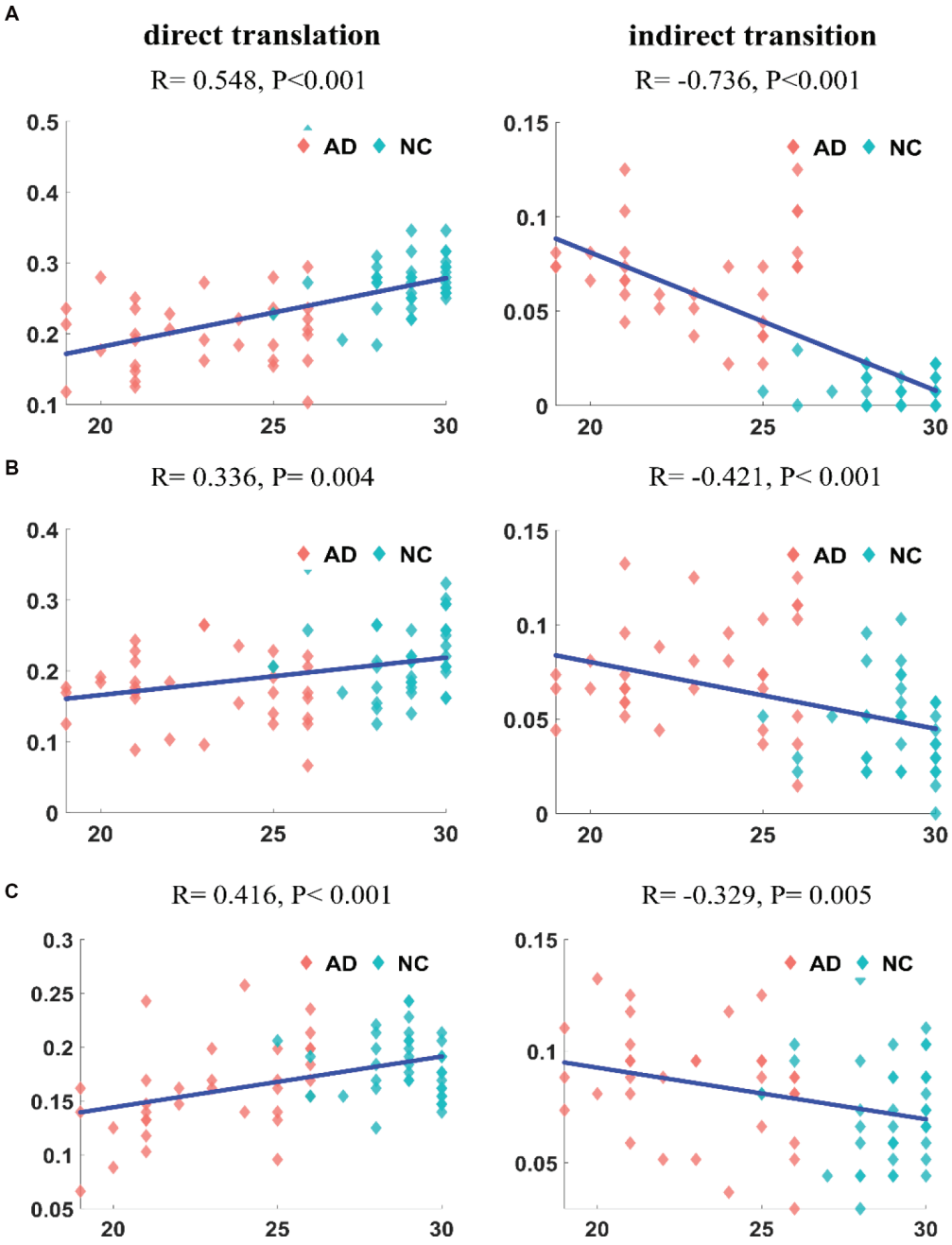

FIGURE 8
The correlation of transition frequencies between major states and MMSE in DMN **(A1,A2)**. The correlation of transition frequencies between major states and MMSE in CEN **(B1,B2)**. The correlation of transition frequencies between major states and MMSE in SN **(C1,C2)**. It can be found that the frequencies of different transition methods are significantly correlated with MMSE, and the degree of correlation is different for the three networks.

amyloid plaques accounted for 50% of neurons, which was 16 times more than that in normal mice. This phenomenon causes serious dysfunction of the neural network of AD mice (Busche et al., 2008). Impaired synaptic function and decreased neural plasticity are the early symptoms of AD and are closely related to the decline in cognitive ability. Based on a study using transcranial magnetic stimulation, cortical inhibition is weakened in AD patients, and the cortical excitability is significantly higher than that of elderly individuals with normal cognition. Lower cognitive performance is significantly associated with higher cortical excitability and lower inhibition (Spires-Jones and Knafo, 2012; Chou et al., 2022). These results are consistent with the findings from our study that the stability of major states in the network associated with cognitive function is disrupted in patients with AD compared with normal subjects, and the patient's brain is unable to easily suppress this active abnormal activity. In recent years, Ma et al. have used co-activation pattern analysis to study the AD brain and found that the increase in transition and CAP entropies and the diversity of CAP transition probabilities suggest variable information flow and higher system uncertainty Ma et al. (2020). Our study has also revealed that the triple-networks of AD patients exhibit decreased main state occurrence, increased minor state occurrence, and increased system instability, which is consistent

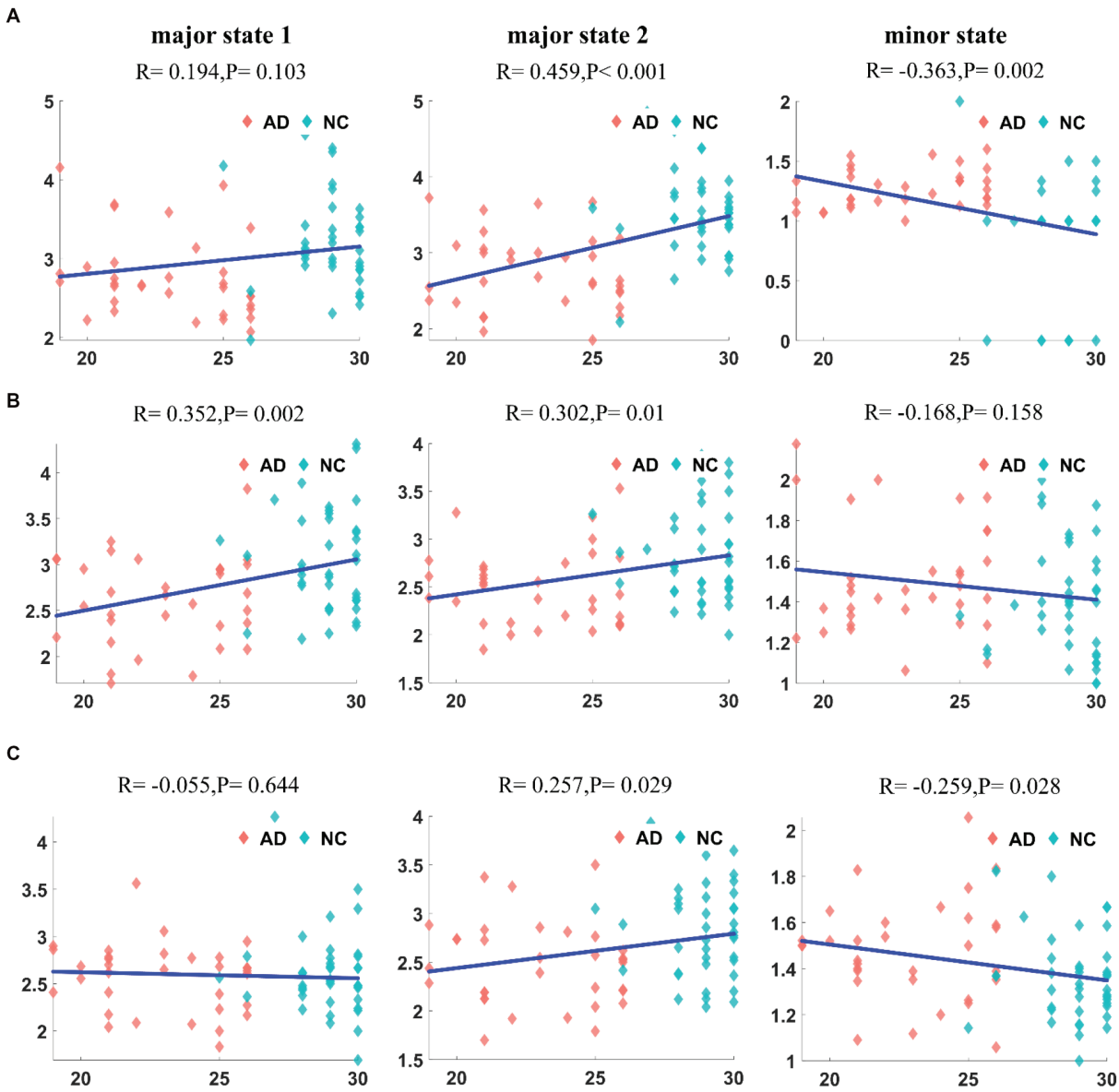

FIGURE 9
The correlation between the duration of each state and MMSE in DMN **(A1–A3)**. The correlation between the duration of each state and MMSE in CEN **(B1–B3)**. The correlation between the duration of each state and MMSE in SN **(C1–C3)**. It can be found that there is a significant correlation between duration and MMSE, but the degree of correlation is not significant in SN.

with the previous study. Sendi et al. observed during normal brain development toward very mild AD that there were significant interruptions in all states, and that connectivity of multiple networks, such as the subcortical, auditory, and visual networks, decreased (Sendi et al., 2021). Recombination patterns were also found in connections within and between multiple networks. Similarly, our results show changes in the energy landscape of different states in AD patients when compared to those of NC individuals. This suggests a network reorganization may be occurring in AD patients. Ghanbari et al. employed a sliding window method to estimate the dynamic functional connectivity (dFC) of each network, from which they extracted the Mean of Redundancy (MOR) and Fluctuation of Redundancy (FOR) features. Statistical analysis based on these features revealed that redundancy significantly increased in AD patients compared to NC individuals (Ghanbari et al., 2023). Our study also found that the stability of the main state decreased, while the indirect switching increased in AD patients, which may account for the increase in redundant dynamic characteristics.

Therefore, we considered that all three core networks associated with cognitive function are affected by AD-related disorders. Previous studies have observed varying degrees of damage to the three networks in AD patients, where the number of functional connections in the module is significantly reduced and closely related to cognitive impairment.

The DMN consists mainly of the posterior cingulate cortex (PCC), precuneus (PCu), and inferior parietal lobe (IPL) and is mainly associated with some higher cognitive functions of the brain, such as situational memory, visuospatial processing, and consciousness

(Ciftci, 2011; Mohan et al., 2016). The DMN in the normal brain is characterized by a symmetrical, well-organized pattern (Raichle et al., 2001). However, in the mild AD group, the symmetry or functional connectivity between interhemispheric homogeneous regions decreases in some disease-related functional networks. Patients with AD perform normally when using intrahemispheric processing but poorly when interhemispheric communication is needed. This loss of symmetry may reflect a state of cognitive decline and imbalance in the functional networks of the patient's brain (Lee et al., 2009; Chen et al., 2013). For example, the functional connectivity of the precuneus, posterior cingulate and medial frontal cortex in the DMN of patients with AD is reduced, and the correlation between nodes in the DMN is reduced (Palesi et al., 2016). The CEN is the functional brain network associated with executive tasks, mainly comprising the dorsolateral prefrontal cortex (DLPFC) and the posterior parietal cortex (PPC), covering multiple medial-frontal regions, including the anterior and paracallosal cingulate, which are presumed to help process information related to working memory, decision-making and retention, and operational target detection (Ramezanzadeh et al., 2014; Wang et al., 2015). Compared to NC subjects, patients with AD exhibit enhanced functional connectivity in the suprafrontal gyrus (SFGmed.L) and middle frontal gyrus (MFG.L) regions of the CEN network, while the anterior cingulate cortex (ACG.R) region of the CEN shows reduced functional connectivity. These changes may contribute to impaired executive function (Jilka et al., 2014). The SN is similar to a "dynamic switch" network that plays a regulatory and transitional role, mainly comprising the ventral lateral prefrontal cortex (VLPFC) and the anterior cingulate cortex (ACC), and is proposed to play a key coordinating role between the CEN and the DMN (Ciftci, 2011; Brier et al., 2012). Functional connectivity within the SN is not significantly different between the NC and AD groups, but abnormal connectivity with the DMN and CEN occurs in AD patients (Wang et al., 2015).

However, among the three networks, the dynamic characteristics of the DMN and CEN were significantly different between the two groups compared with the SN. For example, the intermediate transition states of the DMN and CEN in the AD group are greater than those in the NC group, whereas the energy landscape constructed by the SN had high similarity, corresponding to the same pattern of brain area activation. In addition, group differences in the frequency and duration of major state 1 were not found in the SN, and the differences in the probability of transitions between the major states were not as significant as in the other two networks. Our results indicated that the SN may be less affected by the disease, while the DMN and CEN are more severely damaged than the SN in the early stage of AD.

In clinical practice, AD usually begins with a situational memory impairment followed by a slow progression to wider impairments in daily activities such as attention, executive functioning, language, and visuospatial functioning, eventually leading to loss of independent daily living abilities (Dai et al., 2015). As mentioned above, the DMN plays a key role in cognitive processes, particularly in situational memory processing. Therefore, the DMN plays a central role in brain activity and connects other participating networks, indicating that AD pathology may spread from the DMN to nearby networks, including those involved in visual space and executive function, as well as other peripheral networks (Fair et al., 2008; Liu et al., 2018). Significant degeneration of functional connectivity has been observed within the DMN network in AD patients, with the bilateral angular gyrus (AG) identified as one of the typical areas. Additionally, both clusters of the right middle frontal gyrus and the superior frontal gyrus in the CEN related to the control of executive functions showed a significant decrease in functional connectivity (Sridharan et al., 2008). In contrast, no significant differences in the functional connectivity of internal networks were observed in the SN of both the AD and NC groups (Zhu et al., 2016). Compared with age-matched controls, individuals with early-onset AD showed lower functional connectivity in all networks, such as auditory, sensorimotor, and default mode networks, whereas patients with late-onset AD showed lower functional connectivity only in the DMN. Patients with early-onset AD have more extensive disorganization of brain function than those with late-onset AD (Hodges, 2006; Adriaanse et al., 2014). These results support the hypothesis that the DMN is more severely impaired than the CEN and that the SN is less affected by the disease in AD patients.

4.2. Comparison of the dynamic characteristics based on random walk data simulations

We conducted 10^5random walk data simulations to characterize the dynamic changes in resting brain activity in the three networks of AD patients and NC subjects as an approach to verify our results. We analyzed the dynamic characteristics of the simulation data and compared them with the empirical data to verify the effectiveness and rationality of the energy landscape model. Through comparison, we found that the statistical results of the dynamic characteristics of the simulated data and empirical data were consistent. Based on the findings described above, we further confirmed that the SN is less affected by the disease. We verified that the energy landscape achieves a better description of the nonequilibrium process of switching between resting-state activity patterns in the brain, from which the stability and interactions of the states can be determined and the dynamics characteristics can be described in more detail. The method is also suitable for analyzing specific networks and ROI brain regions.

4.3. The relationship between the dynamic changes in the three networks and a cognitive index

We tested the correlation between the dynamic features that were significantly different in AD patients and the clinical index. The frequency of occurrence, frequency of state transitions and duration of the major states in the three networks of these subjects were correlated with the MMSE scores. The characteristics of major states were generally positively correlated with MMSE scores; the higher the score, the more stable the major states were. Meanwhile, the characteristics of minor states were negatively correlated with MMSE scores; the lower the score, the more active the minor states were. The degree of correlation differed among the three networks, with the DMN exhibiting the highest correlation with MMSE scores, followed by the CEN, and the weakest correlation was observed with the SN. Therefore, we suggest that the abnormalities in the dynamic characteristics of the three networks of patients with AD are related to their cognitive impairment, with the DMN and CEN identified as

more strongly associated with cognitive impairment and the SN showing a weaker correlation.

Our research provides empirical evidence that AD patients are characterized by abnormally nonequilibrium large-scale brain network dynamics. Although previous neuroimaging studies have reported neural synchronization disorders in patients with AD and identified a unique variety of structural and functional whole-brain architectures, most studies have not directly studied brain dynamics (Uhlhaas and Singer, 2006). In contrast, we illustrate the time-varying characteristics of dynamic brain activity patterns in three core brain networks associated with cognitive function and directly report the link between abnormalities in nonequilibrium brain dynamics in patients with AD and their clinical cognitive performance. Given the results of previous studies, our current study may be considered as providing additional empirical support, emphasizing the importance of studying brain dynamics to obtain a biological understanding of various developmental and psychiatric disorders and provide a deeper understanding of the intrinsic neural mechanism and system dynamics characteristics of the AD brain in the resting state.

5. Limitations and future work

We have studied and revealed the dynamic characteristics of functional network activity patterns in the resting brains of AD patients from the perspective of nonequilibrium dynamics. The data used in this study are derived from subjects included in a single database, and the number of samples used in this study is limited, including only 33 AD patients and 39 healthy subjects. In the future, other data sources and a larger sample size must be considered, as well as the inclusion of patients with mild cognitive impairment as an intermediate control group, which will help to improve the reliability of the research methods and results. Additionally, the analysis performed in this study only used one clinical behavioral data point, the MMSE score of the subjects, and thus the study lacked comprehensiveness. Thus, we need to include more clinical behavioral data as indicators for the correlational analysis to increase the persuasiveness of the findings and conclusions. Currently, various artificial intelligence (AI) techniques and advanced signal processing methods have been used for accurate diagnosis of mental illnesses such as AD, Schizophrenia (SZ), and ASD (Khodatars et al., 2021; Sadeghi et al., 2022; Illakiya and Karthik, 2023). Combining dynamic indicators with deep learning can significantly reduce network training costs, which has become one of the hotspots in current research on mental illness diagnosis. We will continue to develop function magnetic resonance data analysis methods based on non-equilibrium dynamics in the future, and combine them with deep learning to strive for breakthroughs in the diagnosis of multiple neurological diseases such as AD and ASD.

6. Conclusion

The main focus of this paper was to perform an energy landscape analysis of three networks in the brains of patients with AD and NC subjects, to further characterize dynamics-related features based on the constructed energy landscape, and to observe the correlation between a series of dynamic characteristics and the clinical cognitive function of the subjects. In the Introduction section, we introduced the triple-network model and related background information, followed by the Methods, which described the extraction of the ROI time series and the most important method of the energy landscape analysis. Our study was divided into four parts. First, we compared the structure of the triple-network energy landscape between the two groups and then further explored the resting-state brain dynamic characteristics of the AD and NC groups. We confirmed our inference that AD brain activity patterns are in an abnormal nonequilibrium state, and the dynamics of patients with AD tend to be unstable, with an unusually high flexibility in switching between states. Then, we correlated the subjects' dynamic features with clinical data and found that the atypical balance of large-scale brain systems in patients with AD is associated with abnormally active brain dynamics, which may explain the general cognitive impairment of patients. Finally, we simulated the dynamic changes in activity patterns using a random walk model and verified that the energy landscape analysis method can reveal the kinetic features in the model. The results of this paper are helpful for further understanding the intrinsic dynamic characteristics and pathological mechanism of the resting-state brain in AD patients.

Data availability statement

The original contributions presented in the study are included in the article/supplementary material, further inquiries can be directed to the corresponding author.

Author contributions

YL, CS, NY, and Z-GH designed the project. SA, TZ, SZ, CL, JJ, and YM analyzed the data. YL, SA, NY, and Z-GH interpreted the results and wrote the manuscript. All authors participated in the revision of the manuscript, read and approved the submitted version. All authors provide approval for publication of the content and agree to be accountable for all aspects of the work in ensuring that questions related to the accuracy or integrity of any part of the work are appropriately investigated and resolved.

Funding

The work was supported by the National Key R&D Program of China (nos. 2022ZD0208500 and 2021ZD0201300), Natural Science Basic Research Plan in Shaanxi Province of China (No. 2023-JC-YB-071), Scientific Research Program Funded by Shaanxi Provincial Education Department (No. 22JP053), NNSF of China (no. 11975178), the Open Project of State Key Laboratory of Cognitive Neuroscience and Learning (no. CNLYB1802), K. C. Wong Education Foundation.

Conflict of interest

The authors declare that the research was conducted in the absence of any commercial or financial relationships that could be construed as a potential conflict of interest.

Publisher's note

References

Adhikari, M. H., Belloy, M. E., Van der Linden, A., Keliris, G. A., and Verhoye, M. (2021). Resting-state co-activation patterns as promising candidates for prediction of Alzheimer's disease in aged mice. *Front. Neural Circu.* 14:612529. doi: 10.3389/fncir.2020.612529

Adriaanse, S. M., Binnewijzend, M. A., Ossenkoppele, R., Tijms, B. M., van der Flier, W. M., Koene, T., et al. (2014). Widespread disruption of functional brain organization in early-onset Alzheimer's disease. *PLoS One* 9:e102995. doi: 10.1371/journal.pone.0102995

Balthazar, M. L. F., de Campos, B. M., Franco, A. R., Damasceno, B. P., and Cendes, F. (2014). Whole cortical and default mode network mean functional connectivity as potential biomarkers for mild Alzheimer's disease. *Psychiatry Res. Neuroimaging* 221, 37–42. doi: 10.1016/j.pscychresns.2013.10.010

Brier, M. R., Thomas, J. B., Snyder, A. Z., Benzinger, T. L., Zhang, D., Raichle, M. E., et al. (2012). Loss of intranetwork and internetwork resting state functional connections with Alzheimer's disease progression. *J. Neurosci.* 32, 8890–8899. doi: 10.1523/JNEUROSCI.5698-11.2012

Buckner, R. L., Andrews-Hanna, J. R., and Schacter, D. L. (2008). The brain's default network: anatomy, function, and relevance to disease. *Ann. N. Y. Acad. Sci.* 1124, 1–38. doi: 10.1196/annals.1440.011

Busche, M. A., Eichhoff, G., Gabelsberger, H., Abramowski, D., Wiederhold, K. H., Haass, C., et al. (2008). Clusters of hyperactive neurons near amyloid plaques in a mouse model of Alzheimer's disease. *Science* 321, 1686–1689. doi: 10.1126/science.1162844

Chen, G., Zhang, H. Y., Xie, C., Chen, G., Zhang, Z. J., Teng, G. J., et al. (2013). Modular reorganization of brain resting state networks and its independent validation in Alzheimer's disease patients. *Front. Hum. Neurosci.* 7:456. doi: 10.3389/fnhum.2013.00456

Chou, Y. H., Sundmana, M., That, V. T., Greena, J., and Trapani, C. (2022). Cortical excitability and plasticity in Alzheimer's disease and mild cognitive impairment: a systematic review and meta-analysis of transcranial magnetic stimulation studies. *Ageing Res. Rev.* 79:101660. doi: 10.1016/j.arr.2022.101660

Ciftci, K. O. (2011). Minimum spanning tree reflects the alterations of the default mode network during Alzheimer's disease. *Ann. Biomed. Eng.* 39, 1493–1504. doi: 10.1007/s10439-011-0258-9

Cummings, J. L., Tong, G., and Ballard, C. (2019). Treatment combinations for Alzheimer's disease: current and future pharmacotherapy options. *J. Alzheimers Dis.* 67, 779–794. doi: 10.3233/JAD-180766

Dai, Z., Yan, C., Li, K., Wang, Z., Wang, J., Cao, M., et al. (2015). Identifying and mapping connectivity patterns of brain network hubs in Alzheimer's disease. *Cereb. Cortex* 25, 3723–3742. doi: 10.1093/cercor/bhu246

Damoiseaux, J. S., Rombouts, S. A. R. B., Barkhof, F., Scheltens, P., Stam, C. J., Smith, S. M., et al. (2006). Consistent resting-state networks across healthy subjects. *Proc. Natl. Acad. Sci. U. S. A.* 103, 13848–13853. doi: 10.1073/pnas.0601417103

Delbeuck, X., Van der Linden, M., and Collette, F. (2003). Alzheimer'disease as a disconnection syndrome? *Neuropsychol. Rev.* 13, 79–92. doi: 10.1023/A:1023832305702

Ezaki, T., Sakaki, M., Watanabe, T., and Masuda, N. (2018). A ge-related changes in the ease of dynamical transitions in human brain activity. *Hum. Brain Mapp.* 39, 2673–2688. doi: 10.1002/hbm.24033

Ezaki, T., Watanabe, T., Ohzeki, M., and Masuda, N. (2017). Energy landscape analysis of neuroimaging data. *Philos. Trans. R. Soc. A Math. Phys. Eng. Sci.* 375:20160287. doi: 10.1098/rsta.2016.0287

Fair, D. A., Cohen, A. L., Dosenbach, N. U., Church, J. A., Miezin, F. M., Barch, D. M., et al. (2008). The maturing architecture of the brain's default network. *Proc. Natl. Acad. Sci. U. S. A.* 105, 4028–4032. doi: 10.1073/pnas.0800376105

Frere, S., and Slutsky, I. (2018). Alzheimer's disease: from firing instability to homeostasis network collapse. *Neuron* 97, 32–58. doi: 10.1016/j.neuron.2017.11.028

Gao, L., Hu, Z., Li, R., Lu, X., Li, Z., Zhang, X., et al. (2022). Multi-perspective feature extraction and fusion based on deep latent space for diagnosis of Alzheimer's diseases. *Brain Sci.* 12:1348. doi: 10.3390/brainsci12101348

Ghanbari, M., Li, G., Hsu, L. M., and Yap, P. T. (2023). Accumulation of network redundancy marks the early stage of Alzheimer's disease. *Hum. Brain Mapp.* doi: 10.1002/hbm.26257

Greicius, M. D., Krasnow, B., Reiss, A. L., and Menon, V. (2003). Functional connectivity in the resting brain: a network analysis of the default mode hypothesis. *Proc. Natl. Acad. Sci.* 100, 253–258. doi: 10.1073/pnas.0135058100

Gu, S., Cieslak, M., Baird, B., Muldoon, S. F., Grafton, S. T., Pasqualetti, F., et al. (2018). The energy landscape of neurophysiological activity implicit in brain network structure. *Sci. Rep.* 8:2507. doi: 10.1038/s41598-018-20123-8

Hodges, J. R. (2006). Alzheimer's centennial legacy: origins, landmarks and the current status of knowledge concerning cognitive aspects. *Brain* 129, 2811–2822. doi: 10.1093/brain/awl275

Huang, W. M., Cao, L. C., Chen, Q. J., Chun-Wang, S. U., You-Jun, L. I., and Huang, Z. G. (2020). Modelling and analysis of brain functional network. *Scientia Sinica Physica, Mechanica & Astronomica* 50:010506. doi: 10.1360/SSPMA2019-0149

Illakiya, T., and Karthik, R. (2023). Automatic detection of Alzheimer's disease using deep learning models and neuro-imaging: current trends and future perspectives. *Neuroinformatics* 21, 339–364. doi: 10.1007/s12021-023-09625-7

Jilka, S. R., Scott, G., Ham, T., Pickering, A., Bonnelle, V., Braga, R. M., et al. (2014). Damage to the salience network and interactions with the default mode network. *J. Neurosci.* 34, 10798–10807. doi: 10.1523/JNEUROSCI.0518-14.2014

Kang, J., Pae, C., and Park, H. J. (2019). Graph-theoretical analysis for energy landscape reveals the organization of state transitions in the resting-state human cerebral cortex. *PLoS One* 14:e0222161. doi: 10.1371/journal.pone.0222161

Khodatars, M., Shoeibi, A., Sadeghi, D., Ghaasemi, N., Jafari, M., Moridian, P., et al. (2021). Deep learning for neuroimaging-based diagnosis and rehabilitation of autism spectrum disorder: a review. *Comput. Biol. Med.* 139:104949. doi: 10.1016/j.compbiomed.2021.104949

Lee, D. Y., Fletcher, E., Martinez, O., Ortega, M., Zozulya, N., Kim, J., et al. (2009). Regional pattern of white matter microstructural changes in normal aging, MCI, and AD. *Neurology* 73, 1722–1728. doi: 10.1212/WNL.0b013e3181c33afb

Lei, P., Ayton, S., and Bush, A. I. (2021). The essential elements of Alzheimer's disease. *J. Biol. Chem.* 296:100105. doi: 10.1074/jbc.REV120.008207

Lerman, C., Gu, H., Loughead, J., Ruparel, K., Yang, Y., and Stein, E. A. (2014). Large-scale brain network coupling predicts acute nicotine abstinence effects on craving and cognitive function. *JAMA Psychiat.* 71, 523–530. doi: 10.1001/jamapsychiatry.2013.4091

Liao, H., Cai, S., Shen, Q., Fan, J., Wang, T., Zi, Y., et al. (2021). Networks are associated with depression in patients with Parkinson's disease: a resting-state imaging study. *Front. Neurosci.* 14:573538. doi: 10.3389/fnins.2020.573538

Liu, X., Chen, X., Zheng, W., Xia, M., Han, Y., Song, H., et al. (2018). Altered functional connectivity of insular subregions in Alzheimer's disease. *Front. Aging Neurosci.* 10:107. doi: 10.3389/fnagi.2018.00107

Ma, X., Zhuo, Z., Wei, L., Ma, Z., Li, Z., Li, H., et al. (2020). Altered temporal organization of brief spontaneous brain activities in patients with Alzheimer's disease. *Neuroscience* 425, 1–11. doi: 10.1016/j.neuroscience.2019.11.025

Matsui, T., and Yamashita, K. I. (2022). Static and dynamic functional connectivity alterations in Alzheimer's disease and neuropsychiatric diseases. *Brain Connect.* doi: 10.1089/brain.2022.0044

Menon, V. (2011). Large-scale brain networks and psychopathology: a unifying triple network model. *Trends Cogn. Sci.* 15, 483–506. doi: 10.1016/j.tics.2011.08.003

Mohan, A., Roberto, A. J., Mohan, A., Lorenzo, A., Jones, K., Carney, M. J., et al. (2016). The significance of the default mode network (DMN) in neurological and neuropsychiatric disorders: a review. *Yale J. Biol. Med.* 89, 49–57.

Palesi, F., Castellazzi, G., Casiraghi, L., Sinforiani, E., Vitali, P., Gandini Wheeler-Kingshott, C. A., et al. (2016). Exploring patterns of alteration in Alzheimer's disease brain networks: a combined structural and functional connectomics analysis. *Front. Neurosci.* 10:380. doi: 10.3389/fnins.2016.00380

Palop, J. J., Chin, J., Roberson, E. D., Wang, J., Thwin, M. T., Bien-Ly, N., et al. (2007). Aberrant excitatory neuronal activity and compensatory remodeling of inhibitory hippocampal circuits in mouse models of Alzheimer's disease. *Neuron* 55, 697–711. doi: 10.1016/j.neuron.2007.07.025

Penalba-Sánchez, L., Oliveira-Silva, P., Sumich, A. L., and Cifre, I. (2023). Increased functional connectivity patterns in mild Alzheimer's disease: a rsfMRI study. *Front. Aging Neurosci.* 14:1037347. doi: 10.3389/fnagi.2022.1037347

Qiao, J., Wang, R., Liu, H., Xu, G., and Wang, Z. (2022). Brain disorder prediction with dynamic multivariate spatio-temporal features: application to Alzheimer's disease and autism spectrum disorder. *Front. Aging Neurosci.* 14:912895. doi: 10.3389/fnagi.2022.912895

Raichle, M. E., MacLeod, A. M., Snyder, A. Z., Powers, W. J., Gusnard, D. A., and Shulman, G. L. (2001). A default mode of brain function. *Proc. Natl. Acad. Sci. U. S. A.* 98, 676–682. doi: 10.1073/pnas.98.2.676

Ramezanzadeh, B., Arman, S. Y., Mehdipour, M., and Markhali, B. P. (2014). Analysis of electrochemical noise (CEN) data in time and frequency domain for comparison corrosion inhibition of some azole compounds on cu in 1.0 M H2SO4 solution. *Appl. Surf. Sci.* 289, 129–140. doi: 10.1016/j.apsusc.2013.10.119

Sadeghi, D., Shoeibi, A., Ghassemi, N., Moridian, P., Khadem, A., Alizadehsani, R., et al. (2022). An overview of artificial intelligence techniques for diagnosis of schizophrenia based on magnetic resonance imaging modalities: methods, challenges, and future works. *Comput. Biol. Med.* 146:105554. doi: 10.1016/j.compbiomed.2022.105554

Sendi, M. S., Zendehrouh, E., Miller, R. L., Fu, Z., Du, Y., Liu, J., et al. (2021). Alzheimer's disease projection from normal to mild dementia reflected in functional network connectivity: a longitudinal study. *Front. Neural Circu.* 14:593263. doi: 10.3389/fncir.2020.593263

Spires-Jones, T., and Knafo, S. (2012). Spines, plasticity, and cognition in Alzheimer's model mice. *Neural Plast.* 2012:319836. doi: 10.1155/2012/319836

Sridharan, D., Levitin, D. J., and Menon, V. (2008). A critical role for the right fronto-insular cortex in switching between central-executive and default-mode networks. *Proc. Natl. Acad. Sci. U. S. A.* 105, 12569–12574. doi: 10.1073/pnas.0800005105

Uhlhaas, P. J., and Singer, W. (2006). Neural synchrony in brain disorders: relevance for cognitive dysfunctions and pathophysiology. *Neuron* 52, 155–168. doi: 10.1016/j.neuron.2006.09.020

Vemuri, P., Jones, D. T., and Jack, C. R. (2012). Resting state functional MRI in Alzheimer's disease. *Alzheimers Res. Ther.* 4, 1–9. doi: 10.1186/alzrt100

Wang, Z., Xia, M., Dai, Z., Liang, X., Song, H., He, Y., et al. (2015). Differentially disrupted functional connectivity of the subregions of the inferior parietal lobule in Alzheimer's disease. *Brain Struct. Funct.* 220, 745–762. doi: 10.1007/s00429-013-0681-9

Wang, P., Zhou, B., Yao, H., Zhan, Y., Zhang, Z., Cui, Y., et al. (2015). Aberrant intra- and inter-network connectivity architectures in Alzheimer's disease and mild cognitive impairment. *Sci. Rep.* 5, 1–12. doi: 10.1038/srep14824

Watanabe, T., Masuda, N., Megumi, F., Kanai, R., and Rees, G. (2014). Energy landscape and dynamics of brain activity during human bistable perception. *Nat. Commun.* 5:4765. doi: 10.1038/ncomms5765

Yang, J., Gohel, S., and Vachha, B. (2020). Current methods and new directions in resting state fMRI. *Clin. Imaging* 65, 47–53. doi: 10.1016/j.clinimag.2020.04.004

Yao, N., Su, C. W., Li, Y. J., Wang, J., and Huang, Z. G. (2020). Dynamics of the default mode network in human brain. *Acta Physica Sinica -Chinese Edition* 69:080203. doi: 10.7498/aps.69.20200170

Zhu, H., Zhou, P., Alcauter, S., Chen, Y., Cao, H., Tian, M., et al. (2016). Changes of intranetwork and internetwork functional connectivity in Alzheimer's disease and mild cognitive impairment. *J. Neural Eng.* 13:046008. doi: 10.1088/1741-2560/13/4/046008

frontiers | Frontiers in Neuroscience

TYPE Original Research
PUBLISHED 24 May 2023
DOI 10.3389/fnins.2023.1207149

OPEN ACCESS

EDITED BY
Jiajia Li,
Xi'an University of Architecture and Technology, China

REVIEWED BY
Song Tong,
Tsinghua University, China
Hyo Jong Lee,
Jeonbuk National University, Republic of Korea

*CORRESPONDENCE
Hua Bai
✉ baihua@tiangong.edu.cn
Quanfeng Ma
✉ zhang20220614@163.com

RECEIVED 17 April 2023
ACCEPTED 09 May 2023
PUBLISHED 24 May 2023

CITATION
Zhang Z, Zhang X, Yang Y, Liu J, Zheng C, Bai H and Ma Q (2023) Accurate segmentation algorithm of acoustic neuroma in the cerebellopontine angle based on ACP-TransUNet.
Front. Neurosci. 17:1207149.
doi: 10.3389/fnins.2023.1207149

Accurate segmentation algorithm of acoustic neuroma in the cerebellopontine angle based on ACP-TransUNet

Zhuo Zhang[1], Xiaochen Zhang[2], Yong Yang[3], Jieyu Liu[1], Chenzi Zheng[4], Hua Bai[1]*and Quanfeng Ma[2]*

[1]Tianjin Key Laboratory of Optoelectronic Detection Technology and Systems, School of Electronic and Information Engineering, Tiangong University, Tianjin, China, [2]Tianjin Cerebral Vascular and Neural Degenerative Disease Key Laboratory, Tianjin Huanhu Hospital, Tianjin, China, [3]School of Computer Science and Technology, Tiangong University, Tianjin, China, [4]College of Foreign Languages, Nankai University, Tianjin, China

Acoustic neuroma is one of the most common tumors in the cerebellopontine angle area. Patients with acoustic neuroma have clinical manifestations of the cerebellopontine angle occupying syndrome, such as tinnitus, hearing impairment and even hearing loss. Acoustic neuromas often grow in the internal auditory canal. Neurosurgeons need to observe the lesion contour with the help of MRI images, which not only takes a lot of time, but also is easily affected by subjective factors. Therefore, the automatic and accurate segmentation of acoustic neuroma in cerebellopontine angle on MRI is of great significance for surgical treatment and expected rehabilitation. In this paper, an automatic segmentation method based on Transformer is proposed, using TransUNet as the core model. As some acoustic neuromas are irregular in shape and grow into the internal auditory canal, larger receptive fields are thus needed to synthesize the features. Therefore, we added Atrous Spatial Pyramid Pooling to CNN, which can obtain a larger receptive field without losing too much resolution. Since acoustic neuromas often occur in the cerebellopontine angle area with relatively fixed position, we combined channel attention with pixel attention in the up-sampling stage so as to make our model automatically learn different weights by adding the attention mechanism. In addition, we collected 300 MRI sequence nuclear resonance images of patients with acoustic neuromas in Tianjin Huanhu hospital for training and verification. The ablation experimental results show that the proposed method is reasonable and effective. The comparative experimental results show that the Dice and Hausdorff 95 metrics of the proposed method reach 95.74% and 1.9476mm respectively, indicating that it is not only superior to the classical models such as UNet, PANet, PSPNet, UNet++, and DeepLabv3, but also show better performance than the newly-proposed SOTA (state-of-the-art) models such as CCNet, MANet, BiseNetv2, Swin-Unet, MedT, TransUNet, and UCTransNet.

KEYWORDS

deep learning, acoustic neuroma, image segmentation, transformer, UNet

1. Introduction

Acoustic neuroma is one of the most common tumors in the cerebellopontine angle area, accounting for about 85% of the tumors in this region. Although these tumors are typically non-life-threatening, postoperative morbidity can be associated with injury to the facial nerve, cochlear nerve, cerebrospinal fluid leaks, and other wound complications. Permanent facial paralysis can occur in 3 to 5% of cases, and up to 22% of patients may experience cerebrospinal fluid leaks (North et al., 2022). Fortunately, the surgical mortality rate is low, with less than 1% of cases resulting in death (McClelland et al., 2011). The main manifestation of acoustic neuroma is the thickening of the auditory nerve. Due to the limitation of bone canal, the tumor gradually grows to the cerebellopontine angle area with less resistance (Ling et al., 2016). The tumor originates from the vestibular part of the VIII pair of cranial nerves. The early lesions are small and often grow in the internal auditory canal. Neurosurgeons need to use Magnetic Resonance Imaging (MRI), which not only takes a lot of time, but also is susceptible to subjective factors. Therefore, it is of great significance to realize the automatic and accurate segmentation of acoustic neuroma. MRI has the characteristics of no bony artifacts, multi-directional and multi angle imaging, clear anatomical structure and high-level resolution for tissues. It can clearly show the size, shape, edge contour, peritumoral edema and adjacent structural changes of tumor, providing information for the preoperative diagnosis of tumor. It has become a preferred method for the examination of space occupying lesions in cerebellopontine angle (Xiaoxia et al., 2014).

At present, in the medical field, manual segmentation is mainly used in brain tumor segmentation. Manual segmentation is to manually outline the tumor area in all tumor MRI image slices. Although manual segmentation is accurate, it is time-consuming, laborious and subjective, which is not conducive to the timely diagnosis and treatment of patients. Therefore, scholars have been exploring automatic segmentation methods. In the early stage, people mainly focused on traditional segmentation methods, such as threshold segmentation (Xiaobo et al., 2019), watershed segmentation (Yongzhuo and Shuguang, 2018), region segmentation (Qiulin and Xin, 2018). There are also more complex segmentation methods based on statistical shape model [6] and graph cut (Corso et al., 2008). Despite the high speed of these segmentation methods, its result depends on the parameters specified by the user and the preprocessing of MRI images (Lingmei et al., 2020), which greatly limits its generalization ability.

With the rapid development of artificial intelligence in recent years, deep learning methods have been successfully applied to the field of medical images. Deep learning models solve the problems of poor accuracy and strong dependence on data in traditional automatic segmentation methods, such as threshold segmentation, region segmentation, and clustering segmentation, and have made great progress in medical image segmentation. AlexNet (Krizhevsky et al., 2017), VGG (Simonyan and Zisserman, 2014), GoogLeNet (Szegedy et al., 2014), ResNet (He et al., 2016), DenseNet (Huang et al., 2016), and other deep and wide network structures have been proposed one after another to learn deeper data features. UNet (Ronneberger et al., 2015) is a network structure proposed by Ronneberger et al. in 2015, which was originally applied in the field of biomedical cell segmentation. In 2019, Mumtaz et al. used a new method based on 3D fully convolutional neural networks (FCNNs; Shelhamer et al., 2016) and a 3D level set segmentation algorithm to classify and segment colon and rectal cancer. Their accuracy was 0.9378, which was 0.0755 lower than the previous accuracy of 0.8623 (Soomro et al., 2018). Cuixia et al. (2019) discussed and compared various classification models for breast tumors using deep learning in 2019 and proposed a novel method that combines deep learning features. Deep learning is also widely applied in brain tumor segmentation. Thillaikkarasi and Saravanan (2019) proposed a brain tumor segmentation algorithm using a support vector machine to extract features and CNN segmentation in 2019, resulting in an accuracy of 84%. Dong et al. (2017) used UNet to segment MRI images of brain tumors and achieved good results by splicing feature vectors of the expansion path and contraction path through skip connections. Lingmei et al. (2020) improved the UNet structure in 2020 and applied it to the segmentation of glioma magnetic resonance images. Specifically, they used an attention module on the contraction path of UNet to distribute weight to convolution layers of different sizes, promoting the utilization of spatial and contextual information. Replacing the original convolution layer with the residual compact module can extract more features and promote network convergence. In 2021, Russo et al. (2020) applied a spherical transformation preprocessing input training model, which was better than the Descartes input training model in predicting glioma tumor core segmentation and enhancing tumor category. The two models were combined to further improve prediction accuracy.

Undoubtedly, CNN represents a very promising method for image processing. However, its convolution operation has limitations, especially for samples with large texture differences, resulting in weak performance. In recent years, scholars have proposed several solutions to address this issue. For instance, Chen et al. (2014) introduced the Atrous Spatial Pyramid Pooling (ASPP) module in DeepLabv3+ (Chen et al., 2018a) after several generations of improvements (Chen et al., 2017, 2018b). The addition of ASPP into CNN enables atrous convolution to expand the vision field of the filter without increasing computational demand. Therefore, ASPP can obtain feature information of different scales without using a pooling layer, overcoming the limitations of local information loss caused by grid effect and the lack of correlation between long-distance information when using a single atrous convolution. Moreover, some studies suggest building a self-attention mechanism based on CNN features (Wang et al., 2017) as an effective means to solve the limitations of convolution operations. This method has also garnered much attention in the field of artificial intelligence. For instance, Tian et al. (2020) used channel attention in ADNet to accurately extract useful information hidden in the complex background. Huang et al. (2020) proposed the Criss-cross attention module in CCNet to capture contextual information of the complete image. Fan et al. (2020) introduced the self-attention mechanism in 2020 and proposed Multi-scale Attention Net (MA-Net).

Furthermore, Transformer has emerged as an alternative architecture designed for sequence-to-sequence prediction, and its success has been widely demonstrated in various fields such as machine translation and natural language processing (NLP; Vaswani et al., 2017; Devlin et al., 2018). In various image recognition tasks, Transformer has proven to reach or even exceed the state-of-the-art (Zheng et al., 2020; Dosovitskiy et al., 2021). For example, Chen et al. (2021) combined Transformer as a powerful encoder for medical image segmentation tasks with UNet in 2021, proposing TransUNet

as a powerful alternative for medical image segmentation. Yang et al. added an attention mechanism to TransUNet (Yang and Mehrkanoon, 2022), showing that the combination of attention mechanism and TransUNet can optimize the segmentation effect. Subsequently, Valanarasu et al. proposed the MedT (Valanarasu et al., 2021) containing Local–Global (Logo) training strategy based on Transformer, which further improved the model's performance. Cao H et al. fused high-resolution features from different scales of the encoder by skip connections, and Swin-Unet (Cao et al., 2021) was proposed to mitigate the loss of spatial information due to the pooling operation.

It is worth noting that acoustic neuromas have different shapes and may grow into the inner auditory canal, which is challenging for accurate feature extraction. We believe that the combination of ASPP, attention mechanism and Transformer can solve this challenge well. Therefore, we propose a novel model called ACP-TransUNet for accurate segmentation of acoustic neuromas, with TransUNet as the core framework. Specifically, the ASPP module is added to increase the receptive field, enabling more accurate and noticeable extraction of tumor features during the segmentation process. We also incorporate the CPAT module, which combines channel attention (Jie et al., 2019) and pixel attention (Zhao et al., 2020) to better explore channel and pixel features of acoustic neuromas while recovering the original input image size. The use of feature multiplication between attentions enhances the ability of feature representation and improves the feature propagation strategy, resulting in higher performance under the same computational load (Zhao et al., 2020; e.g., RCAN, Zhang et al., 2018; CARN, Ahn et al., 2018). By arranging the channel attention and pixel attention sequentially, we aim to improve the feature extraction capability of ACP-TransUNet.

Our main contributions are as follows:

1. Our proposed ACP TransUNet combines Transformer and CNN to capture the global and local features of the segmentation target.
2. In the down-sampling process, the ASPP module is added after the convolutional neural network to gain contextual information at multiple scales and resolutions.
3. In the up-sampling process, channel attention and pixel attention are used to improve model performance and accuracy by weighting important features.

2. Related works

2.1. TransUNet

UNet has become the most commonly used method to accurately segment lesions in medical segmentation tasks, and Transformer has also become a structural system that replaces the self-attention mechanism. TransUNet combines Transformer with UNet as a powerful alternative for medical image segmentation, possessing the advantages of both. To compensate for the loss of feature resolution due to Transformers, TransUNet adopted a hybrid CNN-Transformer architecture to exploit the detailed high-resolution spatial information of CNN features and the global context encoded by Transformers. Inspired by U-Shape, the attention features encoded by Transformers are combined with different high-resolution CNN features during upsampling to achieve precise localization. This design enables the model to preserve the advantages of Transformer and also facilitates the segmentation of medical images. On the one hand, Transformer encodes the tokenized image patches of the convolutional neural network (CNN) feature map as an input sequence for feature extraction; on the other hand, the decoder up-sampling the encoded features, and then combines them with the feature map in CNN to achieve accurate positioning (Chen et al., 2021). Currently, TransUNet and its variants have achieved great success in image segmentation. Nurçin used TransUNet for the segmentation step of the red blood cells to improve the segmentation quality of overlapping cells (Nurçin, 2022). MS-TransUNet++ (Wang et al., 2022) employed a multi-scale and flexible feature fusion scheme between different levels of encoders and decoders to achieve competitive performance in prostate MR and liver CT image segmentation. Liu et al. proposed an efficient model called TransUNet+ (Liu et al., 2022) through a redesigned skip connection, which has achieved promising results in medical image segmentation. Wang et al. proposed UCTransNet (Wang et al., 2021), which used the CTrans block to replace the skip connection in U-Net and obtained a higher segmentation effect. DS-TransUNet (Lin et al., 2022) applied swin transformer block (Liu et al., 2021) to encoder and decoder. This may be the first attempt to combine the advantages of layered Swin Transformer into both encoder and decoder of standard U-shaped architecture with the aim of improving the segmentation quality of different medical images. In TransAttUnet (Chen et al., 2021), multilevel guided attention and multiscale skip connection were co-developed to effectively improve the functionality and flexibility of the traditional U-shaped architecture. Zhao et al. proposed an automatic deep learning pipeline nn-TransUNet (Zhao et al., 2022) for cardiac MRI segmentation by combining the experimental planning of nn-UNet and the network architecture of TransUNet. EG-TransUNet (Pan et al., 2023) used progressive enhancement module, channel spatial attention, and semantic guidance attention to be able to capture object variability on different biomedical datasets. In summary, the architecture of TransUNet combines the advantages of Transformer and CNN, which is not only good for local information extraction, but also can explore long-range modeling.

2.2. Channel attention

Channel attention was first proposed in SE-Net and achieved excellent performance. In CBAM (Woo et al., 2018), channel attention has been improved significantly. Specifically, channel attention compresses the feature of spatial dimension, i.e., each two-dimensional feature map becomes a real number, which is equivalent to the pooling operation with global receptive field. The number of feature channels remains unchanged, and the module structure is shown in Figure 1. Channel attention aggregates spatial information of feature maps based on global average pooling $\mathrm{AvgPool}(\mathrm{F})$ and maximum pooling $\mathrm{MaxPool}(\mathrm{F})$ operations, generating two different spatial context descriptors: $\mathrm{F}^{\mathrm{c}}_{\mathrm{avg}}$ and $\mathrm{F}^{\mathrm{c}}_{\mathrm{max}}$, representing average pool features and maximum pool features, respectively. After adding the two feature maps of the multilayer

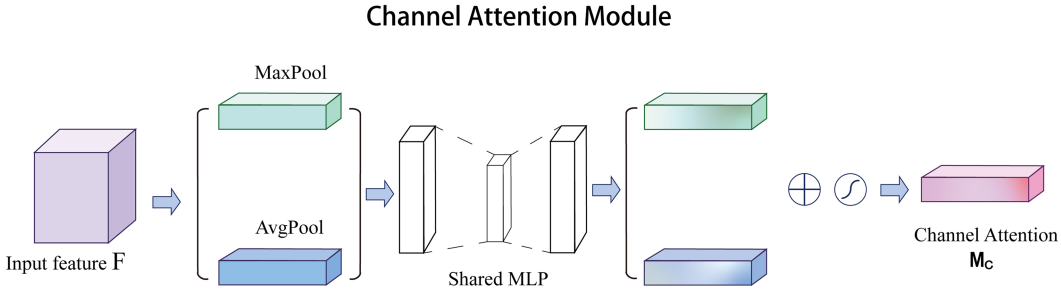

FIGURE 1
Overview of the channel attention structure.

perceptron (MLP), the Sigmoid function is used to generate channel feature map, as follows in Eq. (1):

$$M_C(F) = \sigma(MLP(AvgPool(F)) + MLP(MaxPool(F))) = \sigma(W_1(W_0(F^c_{avg})) + W_1(F^c_{max})) \quad (1)$$

where A represents the Sigmoid function, W_0 and W_1 represent the two convolution operations, respectively, and F^c_{avg} and F^c_{max} represent the average pooling and max pooling, respectively. Sigmoid function can map the result to 0–1 with the amplitude unchanged, so we can get the weight of each feature point of the input channel feature layer.

In recent years, channel attention has been widely used to solve medical challenges. Yuan et al. improved the accuracy of automatic vessel segmentation in fundus images by embedding an adaptive channel attention module to automatically rank the importance of each feature channel (Yuan et al., 2021). Du et al. applied channel attention to the automatic segmentation of early gastric cancer (EGC) to extract subtle discriminative features of EGC lesions by capturing the interdependence between channel features (Du et al., 2023). In addition, channel attention paired with other excellent attention mechanisms can also improve the quality of super-resolution reconstruction of medical images. Song et al. and Zhu et al. obtained high-quality reconstructed images for glioma MRI images and lung cancer CT images, respectively (Zhu et al., 2022; Song et al., 2023). Therefore, channel attention has great potential in the field of medical image processing.

2.3. Pixel attention

The channel attention aims to obtain a $1D\,(C\times1\times1)$ vector of attentional features. In contrast, pixel attention (Zhao et al., 2020) is able to generate $3D\,(C\times H\times W)$ matrices as attention features. Note that C is the number of channels, and H and W are the height and width of the features, respectively. Specifically, pixel attention generates attention coefficients for all pixels of the feature map. As shown in Figure 2, pixel attention uses only 1×1 convolutional layers and Sigmoid functions to obtain the attention map, and then multiplies the attention map with the input features, as follows in Eq. (2):

$$M_P(F') = \sigma\left(f^{1\times1}_{PA}(F')\right) \quad (2)$$

where A represents the Sigmoid function and $f^{1\times1}_{PA}$ represents a convolution operation with the filter size of 1×1.

Pixel attention not only reduces the number of parameters, but also eliminates unnecessary pooling operations that can lead to image smoothing (Tang et al., 2021). Relying on this advantage, pixel attention is widely used in the field of medical images for segmentation (Roy et al., 2022) and super-resolution reconstruction tasks (Rajeshwari and Shyamala, 2023).

3. Methods

3.1. Overview

In this section, we describe our ACP-TransUNet with more details. The ACP-TransUNet model proposed in this paper is based on the TransUNet (Chen et al., 2021) model, and is improved and extended on the basis of the latter, as shown in Figure 3.

Given an input image with resolution $H\times W$ and C number of channels, the segmentation map is obtained by down-sampling and up-sampling. The down-sampling process consists of five parts, which are CNN, ASPP, Image Sequentialization, Patch Embedding, and Transformer Layer. The input image is first extracted by CNN layer to get the feature map. After that, the ASPP module is used to increase the receptive field to obtain a feature map with different scales. Then, Hidden Feature and Linear Projection reshape the feature map into N flattened 2D patches for Image Sequentialization, with each patch of size $P\times P$, $N=\frac{H'W'}{P^2}$, H' and W' being the length and width of each feature map. In order to encode the spatial information of the patches, we add positional embedding to the patch embedding to preserve the positional information, as follows in Eq. (3):

$$Z_0 = \left[x^1_pE;\ x^2_pE;\ \ldots;\ x^N_pE\right] + E_p \quad (3)$$

where $E\in\mathbb{R}^{(P^2.C)\times D}$ represents the patch embedding projection, x_p represents the vectorized patch, and $E_P\in\mathbb{R}^{N\times D}$ represents the position embedding.

The Transformer (Vaswani et al., 2017) layer is added at the end of the down-sampling to obtain the global features, which consists of

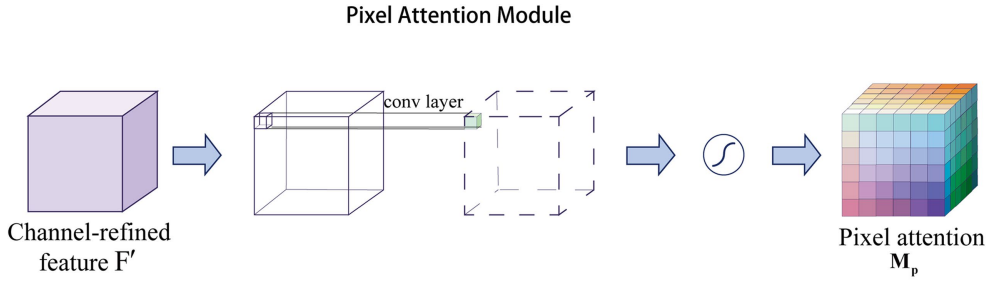

FIGURE 2
Overview of pixel attention structure.

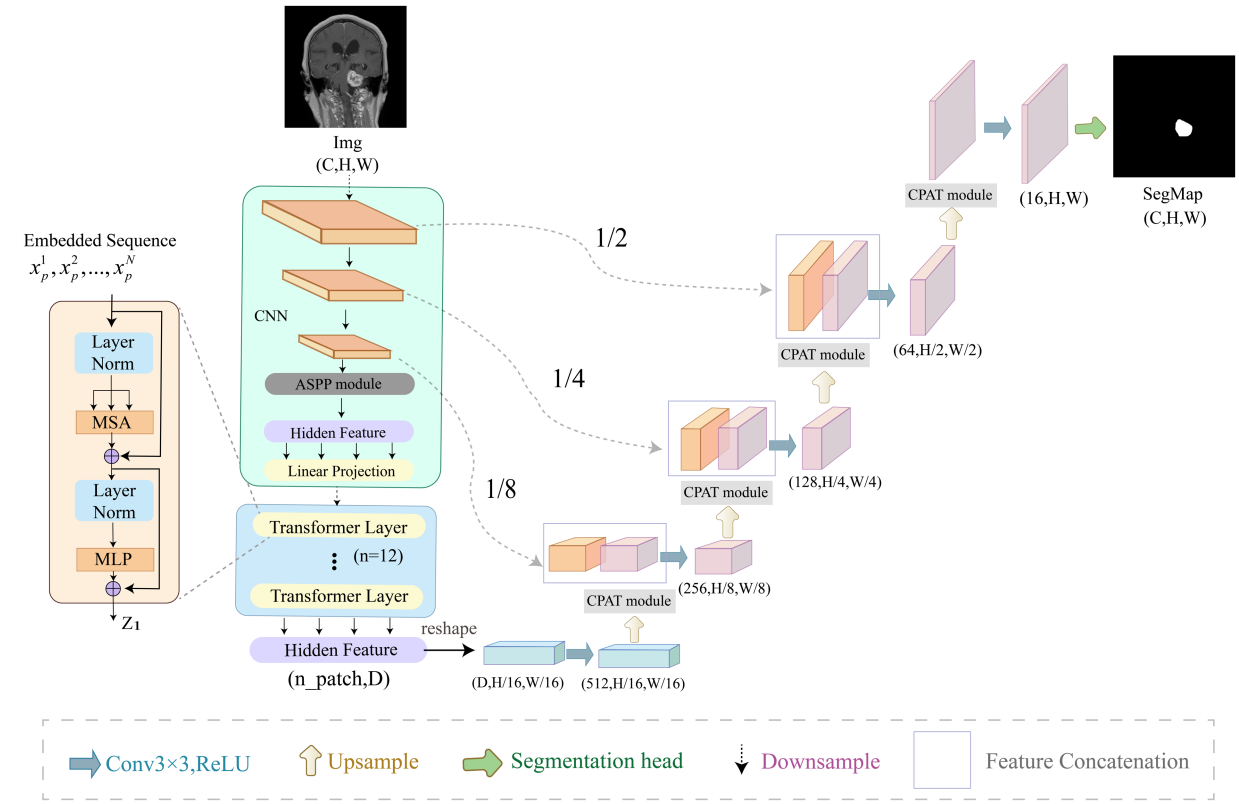

FIGURE 3
Overview of ACP-TransUNet. The input is an acoustic neuroma MRI image, and the output is the corresponding prediction map generated by ACP-TransUNet.

Multi-head Attention (MSA) and Multi-layer Perceptron (MLP) as shown in Eqs. (4) and (5):

$$Z_n' = \mathrm{MSA}\left(\mathrm{LN}\left(z_{n-1}\right)\right) + z_{n-1} \tag{4}$$

$$Z_n = \mathrm{MLP}\left(\mathrm{LN}\left(z_n'\right)\right) + z_n' \tag{5}$$

where $\mathrm{LN}(\cdot)$ denotes the layer normalization operator and z_n is the encoded image representation.

In the up-sampling process, we added CPAT modules in each layer to weight the important features in recovering the image size to improve the performance and accuracy of the model.

3.2. ASPP module

Acoustic neuromas vary in shape. Some are irregular in shape and grow into the inner auditory canal, while some have clear boundary. Therefore, we need a larger receptive field to extract the feature of acoustic neuromas. The ordinary convolution structure cannot fully extract features, so in this paper we choose to use ASPP module to strengthen the ability of the model to segment objects at

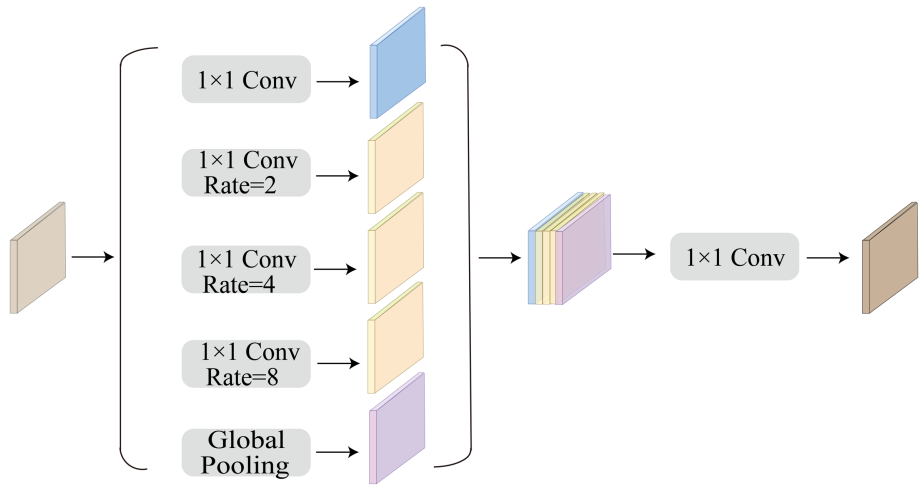

FIGURE 4
Overview of ASPP Module.

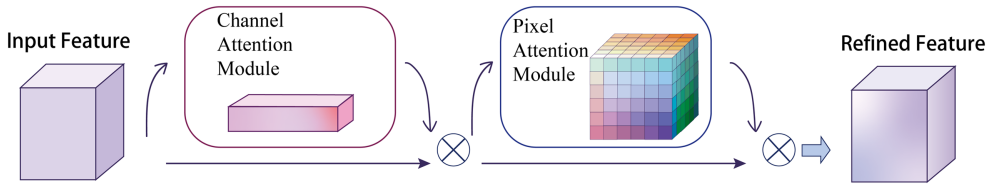

FIGURE 5
Overview of CPAT structure. This module has two submodules: channels and pixels, where ⊗ denotes element-wise multiplication. The intermediate feature map is adaptively refined through our module (CPAT).

different scales. As shown in Figure 4, in this paper, ASPP module is equipped in the last layer of CNN, with dilation rate set to 2, 4, 8. The rate of atrous convolution is based on the ordinary convolution, and the interval between adjacent weights is $\text{rate}-1$. The rate of ordinary convolution is defaulted to 1, so the actual size of atrous convolution is $k+(k-1)(\text{rate}-1)$, in which k is the size of the original convolution kernel. ASPP overcomes the shortcomings of local information loss and lack of correlation in remote information caused by grid effect when using single atrous convolution, making it possible to obtain different scale feature information without using pooling layer.

3.3. CPAT module

Given an intermediate feature map $F \in \mathbb{R}^{C\times H\times W}$ as input, CPAT module sequentially infers a 1D channel attention map $M_c \in \mathbb{R}^{C\times 1\times 1}$ and a 3D pixel attention map $M_P \in \mathbb{R}^{C\times H\times W}$ as illustrated in Figure 5. For the arrangement of attention modules, we found through experiments that the result is better when using two sequential attentions than using one attention, which will be discussed in the ablation experiments, as shown in Eqs. (6) and (7):

$$F' = M_c(F)\otimes F \tag{6}$$

$$F'' = M_P(F')\otimes F' \tag{7}$$

where F' denotes the feature map obtained by channel attention, F'' denotes the feature map obtained by pixel attention, and ⊗ denotes element multiplication.

4. Experimental results

In this section, we introduce the details of the experimental data and results. In order to verify whether ACP-TransUNet can effectively and accurately segment acoustic neuromas, we first performed comparative experiments and ablation experiments on all test sets (including coronal view, sagittal view, and transverse view). To test the accuracy of the model's segmentation effect in a single view, we also conducted

multi-view evaluation, performing a comparison experiment and ablation experiment on the three views separately. The results are discussed in detail below. Among them, ACP-TransUNet achieves 95.74% Dice Similarity Coefficient on the test set, and Hausdorff 95 reaches 1.9476 mm, which are superior than other models.

4.1. Dataset

We selected MRI images of sagittal view, coronal view and transverse view of patients with cerebellopontine angle (CPA) acoustic neuroma diagnosed by experts in Tianjin Huanhu Hospital from January 2019 to January 2022, with all the patients signing informed consent. The scanning equipment we used was Siemens Skyra 3.0 T MRI scanner, which could collect magnetic resonance images of multiple sequences. However, compared with other sequences, T1WI-SE could better distinguish the lesion and its surrounding adjacent tissues. Therefore, this paper adopts contrast - enhanced fast low-angle shot 2-dimensional sequence (T1_fl2d) with Gd-GDPA. Scanning parameters are as follows: slice thickness is 5 mm; slice interval, 1.5 mm; echo time (TE), 2.46 ms; repetition time (TR), 220 ms. After screening, a total of 300 magnetic resonance images of acoustic neuromas were selected in this paper, in which the ratio of training set, verification set and test set is 8: 1: 1 and each part has no cross.

4.2. Preprocessing

To avoid the deviation of the experimental results caused by the inconsistent data format, the training, verification and test MRI images in this paper are all set to the same format. Because the dataset is small, to improve the generalization ability of the model, the images are subjected to data augmentation processing such as inversion and flipping. In order to save training resources, the images are set to 512×512 pixels. The gray value visualization of the MRI image is shown in Figure 6.

4.3. Experimental setup

In the experiment, the framework we used was Pytorch, and batchsize was set to 4. All networks trained 100 epochs on Nvidia Tesla V100 GPU. Specifically, we used a pre-training model (R50 + ViT-B_16) that was trained on the ImageNet21k dataset. The pre-training model can be found at the following link: https://console.cloud.google.com/storage/vit_models/. In addition, we use the Adam optimizer (Kingma and Ba, 2014) to optimize, the initial learning rate is 10^{-4}, and use the StepLR mechanism to set the learning rate attenuation according to epoch. The StepLR mechanism is a way to adjust the learning rate during training in machine learning. It reduces the learning rate by a certain factor after a fixed number of epochs or iterations. We set the "step_size" parameter to 7 and the "gamma" parameter to 0.1, which means that the learning rate was reduced by a factor of 0.1 every 7 epochs. By gradually reducing the learning rate, we aimed to improve the convergence of the model and prevent overfitting.

4.4. Evaluation metrics

In order to objectively evaluate the results of different models, this paper uses the Dice Similarity Coefficient (Mehta, 2015; Liu et al., 2020) and Hausdorff 95 (Huttenlocher et al., 1993; Beauchemin et al., 1998) as representative segmentation performance indicators, which measure the similarity and maximum mismatch between the segmentation result and the labeling result, respectively. These metrics are widely used in medical image segmentation studies and have been shown to be effective in evaluating segmentation performance.

4.5. Comparative experiment

To verify the validity of the proposed model, we compared several classical networks such as PANet (Liu et al., 2018), PSPNet (Zhao et al., 2016), UNet++ (Zhou et al., 2018), and DeeplabV3 (Chen et al., 2018a), as well as some emerging networks such as CCNet (Huang et al., 2020), MANet (Fan et al., 2020), BiseNetv2 (Yu et al., 2021), Swin-Unet (Cao et al., 2021), MedT (Valanarasu et al., 2021), TransUNet (Chen et al., 2021), and UCTransNet (Wang et al., 2021), which have shown great performance on segmentation tasks in recent years. Table 1 summarizes the comparison results between our scheme and these representative networks. For each model, we visualized the segmentation effect in the coronal (cor), sagittal (sag), and transverse (tra) views, and the results are shown in Figure 7.

The results show that ACP-TransUNet achieved the best performance on the test set, with a Dice value of 95.74% and a Hausdorff 95 value of 1.9476 mm. Compared with the original UNet network proposed by Ronneberger et al. (2015), ACP-TransUNet achieved improvements of 1.09% and 2.5506 mm in Dice and Hausdorff 95, respectively.

In the comparative experiments, our scheme achieved optimal Dice and Hausdorff 95 values, outperforming other network models. Specifically, our scheme improved Dice by 2.63% (PSPNet), 2.28% (DeepLabv3), 1.08% (UNet++), 1.86% (PANet), 10.42% (CCNet), 0.79% (MANet), 5.88% (BiseNetv2), 4.28% (Swin-Unet), 2.48% (MedT), 0.72% (TransUNet), and 0.68% (UCTransNet), respectively. Hausdorff 95 was increased by 1.2669 mm (PSPNet), 2.4962 mm (DeepLabv3), 1.8268 mm (UNet++), 2.3923 mm (PANet), 3.3072 mm (CCNet), 1.8007 mm (MANet), 3.7427 mm (BiseNetv2), 4.3982 mm (Swin-Unet), 2.8318 mm (MedT), 2.0561 mm (TransUNet), and 2.127 mm (UCTransNet), respectively. The corresponding segmentation effect in Figure 7 demonstrates the superior performance of ACP-TransUNet.

In comparison experiments, for some regular acoustic neuromas, such as the tumor shown in the sagittal view, it can be seen that the selected networks can achieve basic segmentation of the tumor except for BiseNetv2 and MedT. However, comparing the internal filling and boundary of the segmentation map, only ACP-TransUNet is closest to Ground Truth; for the part that shows irregular shape and grows into the internal auditory canal, as shown in the coronal view, PSPNet, PANet, CCNet, BiseNetv2 and MedT cannot well segment some tumors growing in the internal auditory canal. Although UNet++ and MANet could segment the tumors in the internal auditory tract, the segmentation results were inferior to the rest of the networks. DeepLabv3, UNet and TransUNet performed comparably

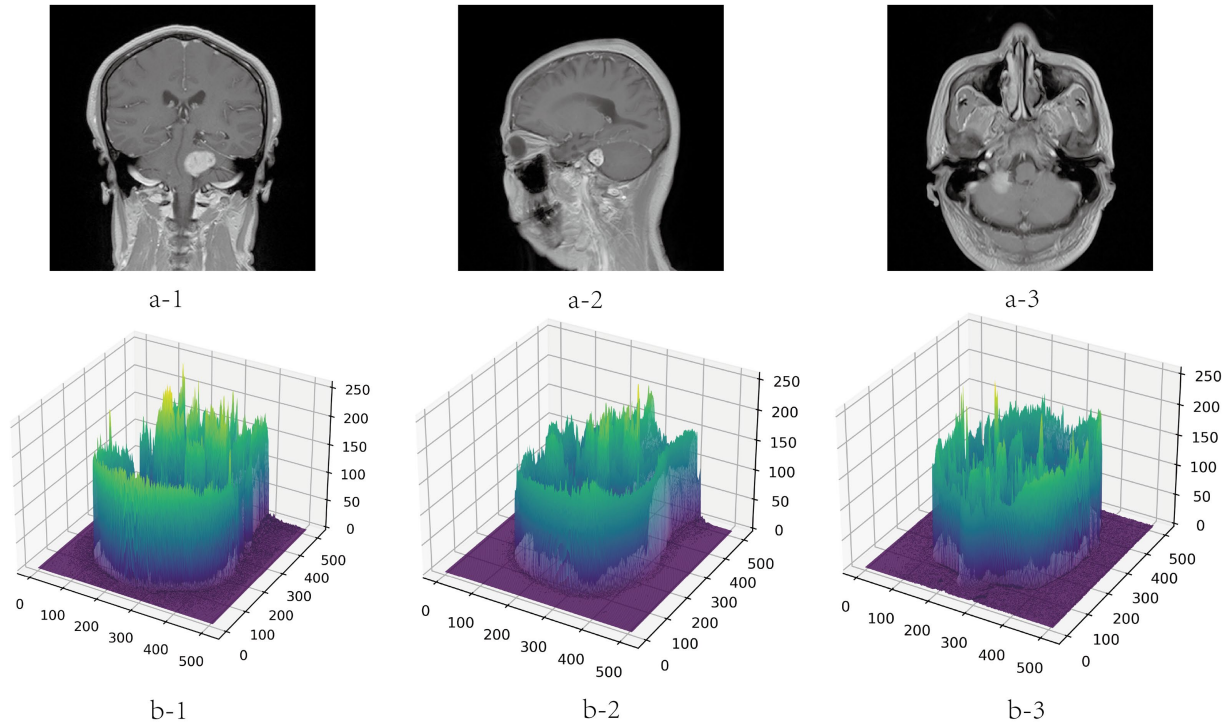

FIGURE 6
Gray visualization of MRI images in three directions. a-1, a-2, and a-3 represent coronal, sagittal and transverse MRI images, respectively. b-1, b-2, and b-3 are three-dimensional gray-scale visualization images of nuclear magnetic resonance, which represent the corresponding directions. The x-axis and y-axis represent the length and width of the image respectively, and the value range is [0, 512]. The z-axis represents the gray value distribution of the image, and the value range is [0, 255].

TABLE 1 Results of comparative experiment.

Model	Dice (%)	Hausdorff 95 (mm)
UNet (2015)	94.65	4.4982
PSPNet (2016)	93.11	3.2145
DeepLabv3 (2017)	93.46	4.4438
UNet++ (2018)	94.66	3.7744
PANet (2018)	93.88	4.3399
CCNet (2020)	85.32	5.2548
MANet (2020)	94.95	3.7483
BiseNetv2 (2021)	89.86	5.6903
Swin-Unet (2021)	91.46	6.3458
MedT (2021)	93.26	4.7794
TransUNet (2021)	95.02	4.0037
UCTransNet (2022)	95.06	4.0746
Ours	**95.74**	**1.9476**

Bold font is the best data for each column.

to ACP-TransUNet for segmenting the tumors in the internal auditory tract, but UCTransNet and ACP-TransUNet outperformed the rest of the models in terms of edge detail. However, in the transverse (tra), only TransUNet and ACP-TransUNet can well segment the acoustic neuroma. We noticed that the models containing Transformer structures (such as MedT, Swin-Unet, TransNet, and UCTransNet) were deficient in processing edge details, which may be explained by the limited Transformer localization ability caused by insufficient low-level details. After adding the CPAT module and ASPP module, the segmentation map edge contours have been greatly improved.

4.6. Multi-view evaluation

To further verify the effectiveness of the model, we conduct comparative experiments and ablation experiments on the segmentation effects of the coronal, sagittal and transverse views in the test set, respectively. The results of the multi-view evaluation in the comparative experiments are shown in Table 2.

It can be seen that although the Hausdorff 95 is not as good as MANet in the transverse view, our model is generally better than other models through the evaluation of dice and Hausdorff 95 values. Dice values of the coronal view, sagittal view and transverse view reached 94.88, 95.45 and 96.45% respectively; and the Hausdorff 95 values reached 2.541 mm, 1.4056 mm and 1.902 mm, respectively.

4.7. Ablation experiment

To demonstrate the efficacy of the incorporation module, we performed two groups of ablation experiments based on the principle of "fixing two items and changing one item."

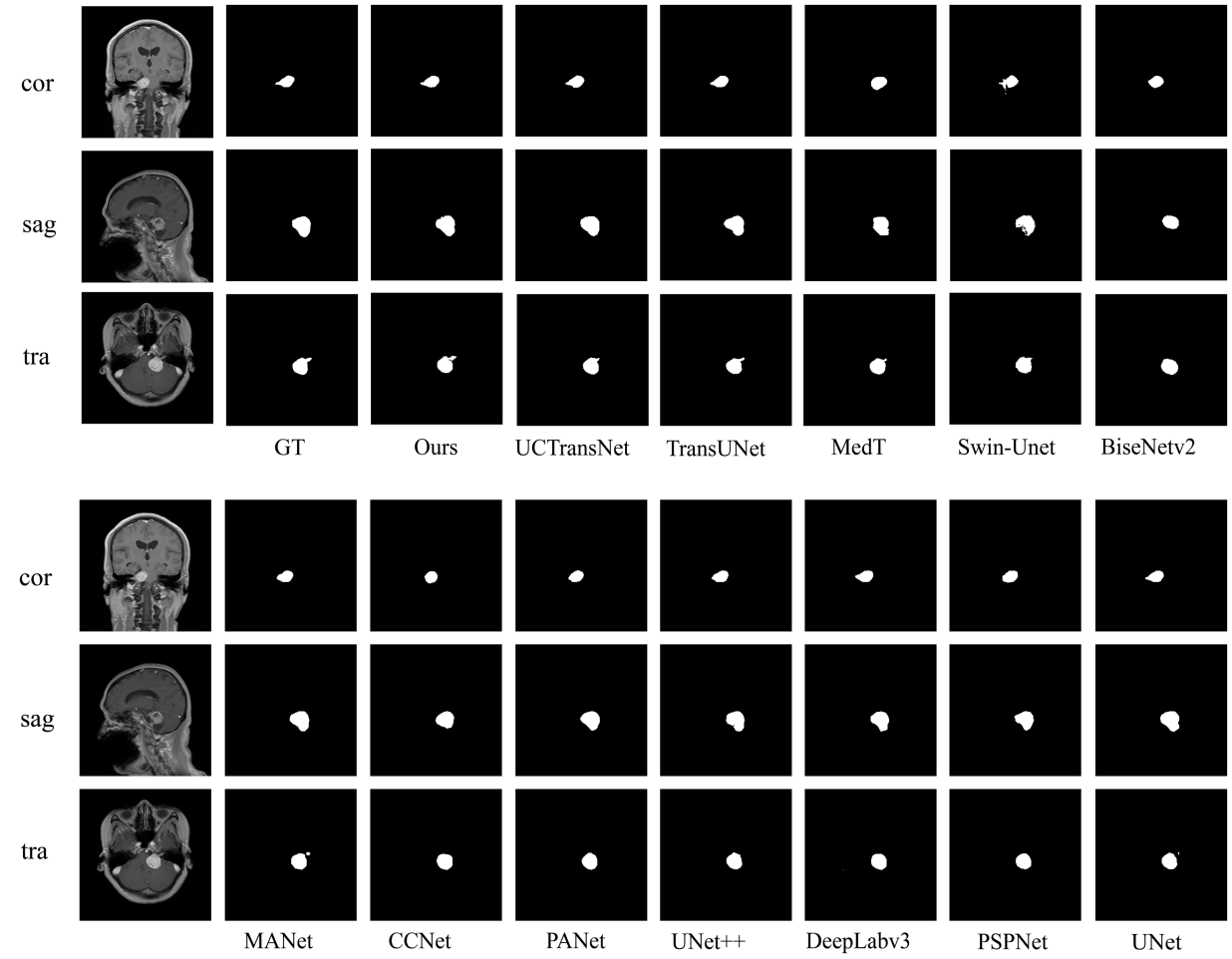

FIGURE 7
Examples of predictions for each network on acoustic neuromas in comparative experiments.

4.7.1. Ablation experiment of attention module

We examine four different experimental configurations to verify the efficacy of adding attention modules, i.e., TransUNet with ASPP (TransUNet+ASPP) as the baseline, and further with channel attention (TransUNet+ASPP+C), pixel attention (TransUNet+ASPP+P), and CPAT module (TransUNet+ASPP+CPAT). Tables 3, 4 show the segmentation results for the overall and multiple views, respectively.

From Tables 3, 4, we have some observations as follows.

1. When we added channel attention to "TransUNet+ASPP," not only the Dice and Hausdorff 95 of "TransUNet+ASPP+C" in Table 3 improved by 0.05% and 0.5062 mm, respectively, but also the experimental results of multiple views in Table 4 were better than those of "TransUNet+ASPP", which proves the effectiveness of adding channel attention.
2. When we added pixel attention to "TransUNet+ASPP," the Dice and Hausdorff 95 of "TransUNet+ASPP+P" in Table 3 were 95.52% and 2.4821 mm, respectively, and the experimental results in Table 4 were also improved significantly, thereby proving that the addition of pixel attention is effective.
3. The results of "TransUNet+ASPP+CPAT" in Tables 3, 4 are significantly better than those of "TransUNet+ASPP+C" and "TransUNet+ASPP+P," demonstrating that the sequential connection of channel attention and pixel attention is better than using either attention module.

4.7.2. Ablation experiment of ASPP module

To demonstrate the efficacy of the ASPP module, two different experimental configurations were studied, i.e., TransUNet with CPAT (TransUNet +CPAT) as a baseline and further addition of the ASPP module (TransUNet +CPAT+ASPP). Tables 5, 6 show the segmentation results for the overall and multiple views, respectively. As can be seen from Table 5, the addition of the ASPP module improves the "TransUNet+CPAT+ASPP" Dice and Hausdorff 95 by 0.2% and 1.5166 mm, respectively. In addition, according to Table 6, Hausdorff 95 with "TransUNet +CPAT+ASPP" is excellent in other views, although it is lower than "TransUNet +CPAT" in the transverse view. The above results prove the efficiency of ASPP module.

TABLE 2 Comparative experiment from multiple perspectives.

Model	Dice (%)			Hausdorff 95 (mm)		
	cor	sag	tra	cor	sag	tra
UNet (2015)	94.16	94.76	94.94	7.6671	1.6476	3.8948
PSPNet (2016)	92.3	92.11	94.13	3.454	2.6466	3.4861
DeepLabv3 (2017)	92.43	93.62	94.11	7.23	1.8961	3.9505
UNet++ (2018)	93.12	94.94	95.6	7.0516	1.4254	2.6112
PANet (2018)	93.14	94.03	94.33	7.4731	1.5437	3.7234
CCNet (2020)	90.9	90.15	93.76	8.0307	2.7355	4.7462
MANet (2020)	93.83	94.52	95.91	6.8507	2.4254	**1.8365**
BiseNetv2 (2021)	89.84	84.93	92.07	8.3099	4.3865	4.2442
Swin-Unet (2021)	88.9	89.93	93.8	10.3311	4.7801	3.7695
MedT (2021)	91.52	92.32	94.89	8.2466	3.1183	2.8071
TransUNet (2021)	94.31	94.34	95.81	6.7094	2.3035	2.8282
UCTransNet (2022)	94.4	94.01	95.99	7.5424	2.6062	1.9285
Ours	**94.88**	**95.45**	**96.45**	**2.541**	**1.4056**	1.902

Bold font is the best data for each column, and the coronal, sagittal, and transverse views are represented by cor, sag, and tra, respectively.

TABLE 3 Results of ablation experiments with attentional module.

Model	Dice (%)	Hausdorff 95 (mm)
TransUNet+ASPP	95.18	4.2574
TransUNet+ASPP+C	95.23	3.7512
TransUNet+ASPP+P	95.52	2.4821
TransUNet+ASPP+CPAT	**95.74**	**1.9476**

Bold font is the best data for each column.

5. Discussion

At present, the results of Dice and Hausdorff distance of our model in acoustic neuroma segmentation have reached our expectations. Given the fact that acoustic neuromas vary in shape--some with irregular shape and growing into the inner auditory canal, while some with clear boundary, we need a larger receptive field to extract the feature of acoustic neuromas. As ordinary convolution structure cannot fully extract features, we added the ASPP module. Furthermore, since acoustic neuromas often occur in the cerebellopontine angle area with relatively fixed position, we intended to make our model automatically learn the weights at different scales by adding the attention mechanism. Therefore, we added the channel attention and pixel attention in the up-sampling, so that the channel information and pixel information are combined to better explore the channel characteristics and pixel characteristics while restoring the original input image size. In the comparison experiments, we can see that most of the networks with the added Transformer structure achieve good results in segmentation of acoustic neuromas, for example, the Dice value of these networks is almost equal to that of ACP-TransUNet. However, Hausdorff 95 cannot be comparable to ACP-TransUNet. which is due to Transformer's inadequacy to capture low-level details and its limited positioning ability. Given that, we combined ASPP and attention mechanism to make up for this deficiency. In the ablation experiment, it is observed that the segmentation performance of the model becomes better and better with the addition of ASPP and CPAT modules, proving the effectiveness of our choice to add the modules.

However, there are still problems existing in the current work. For example, in the multi-view evaluation, we did not achieve desirable segmentation results in the transverse view. The Hausdorff 95 value of our model in the transverse view is 1.902 mm. That figure is inferior to the MANet, which reached 1.8365 mm in the comparison experimental. The reasons we believe are of two aspects. First, it could be explained by the relatively low importance of channel weight in the down-sampling of acoustic neuromas in the transverse view direction. But the addition of pixel attention could make all the pixels of the feature map generate attention coefficient, which makes up for the disadvantage of using channel attention alone. Second, although the addition of ASPP module would increase the receptive field, making each convolution output contain a large range of information, the information of smaller tumors in the transverse view could be lost. Given that, in our future work, we will gradually increase the dataset and study the performance changes when increasing or decreasing the single direction module. In addition, our current research task is to achieve accurate segmentation of acoustic neuromas. We hope that the application of ACP-TransUNet will not be limited to acoustic neuromas, so its effectiveness in segmenting other medical images will also be the focus of our future experimental research.

In our research work, the improvement of the accuracy of acoustic neuroma segmentation means that we need to abandon some indicators in some aspects. We have considered trade-offs in these issues. First, the addition of ASPP module, attention mechanism and deeper transformer layer means longer training time and larger model parameters. We believe that the medical segmentation task is different from other segmentation tasks that pursue timeliness (such as face segmentation). Between lightweight and precision, we prefer the latter. Second, since Transformer lacks the inductive bias of convolution, it requires more sample size than CNN. Transformer needs to learn this kind of information from a large amount of data. Considering the precious resources and insufficient data support of current medical images, instead of choosing to train from scratch, we resort to pre-trained models to achieve the same or even better performance than CNN. In the future, we will conduct research for Transformer on small-scale datasets.

6. Conclusion

In this paper, we proposed a novel model named ACP-TransUNet based on the improved TransUNet structure, with all the data on the basis of MRI images. Through deep learning, we realized the automatic

TABLE 4 Results of ablation experiments with attentional module from multiple perspectives.

Model	Dice (%)			Hausdorff 95 (mm)		
	cor	sag	tra	cor	sag	tra
TransUNet+ASPP	94.18	94.85	95.75	6.2425	1.9845	3.8742
TransUNet+ASPP+C	94.24	94.98	95.91	5.9475	1.4863	2.8431
TransUNet+ASPP+P	94.66	95.05	96.34	5.7424	1.8574	1.9527
TransUNet+ASPP+CPAT	**94.88**	**95.45**	**96.45**	**2.541**	**1.4056**	**1.902**

Bold font is the best data for each column, and the coronal, sagittal, and transverse views are represented by cor, sag, and tra, respectively.

TABLE 5 Results of ablation experiments with ASPP module.

Model	Dice (%)	Hausdorff 95 (mm)
TransUNet +CPAT	95.54	3.4642
TransUNet +CPAT+ASPP	**95.74**	**1.9476**

Bold font is the best data for each column.

TABLE 6 Results of ablation experiments with ASPP module from multiple perspectives.

Model	Dice (%)			Hausdorff 95 (mm)		
	cor	sag	tra	cor	sag	tra
TransUNet +CPAT	94.68	95.34	96.23	7.0574	1.4682	**1.8472**
TransUNet +CPAT+ASPP	**94.88**	**95.45**	**96.45**	**2.541**	**1.4056**	1.902

Bold font is the best data for each column, and the coronal, sagittal, and transverse views are represented by cor, sag, and tra, respectively.

and accurate segmentation of acoustic neuromas in the cerebellopontine angle region. Dice and Hausdorff 95 reached 95.74% and 1.9476 mm respectively, and the dividing boundary was closer to the gold standard. The overall effect of segmentation was significantly improved, which was valuable for clinical application and auxiliary physician diagnosis. With decreased intervention of human factors, we greatly improved the diagnostic efficiency and reliability. In addition, the ASPP module was introduced into ACP-TransUNet, which not only increases the receptive field and obtains multi-scale and multi-resolution background information, but also makes the features contained in the sequence of the imported Transformer more accurate and significant. The CPAT module with sequential channel attention and pixel attention is added to the upsampling process so that channel information and pixel information are combined to improve model performance and accuracy by weighting important features. The experimental results show that our model can effectively segment acoustic neuroma. Compared with other methods, the proposed method has different degrees of performance improvement in the segmentation of acoustic neuroma.

Data availability statement

The original contributions presented in the study are included in the article/supplementary material, further inquiries can be directed to the corresponding author.

Ethics statement

Ethical review and approval was not required for the study on human participants in accordance with the local legislation and institutional requirements. The patients/participants provided their written informed consent to participate in this study.

Author contributions

ZZ and HB: conceptualization. HB: methodology, formal analysis, supervision, and funding acquisition. ZZ: software, data, writing original draft preparation, and visualization. ZZ, HB, and QM: validation. JL and XZ: investigation. YY: resources. HB, QM, and CZ: writing review and editing. QM: project administration. All authors contributed to the article and approved the submitted version.

Funding

This work was supported in part by National Natural Science Foundation of China (61201106) and Tianjin Research Innovation Project for Postgraduate Students (2022SKY126).

Conflict of interest

The authors declare that the research was conducted in the absence of any commercial or financial relationships that could be construed as a potential conflict of interest.

Publisher's note

References

Ahn, N, Kang, B, and Sohn, KA (2018). Fast, accurate, and lightweight super-resolution with cascading residual network.

Beauchemin, M., Thomson, K. P., and Edwards, G. (1998). On the Hausdorff distance used for the evaluation of segmentation results. *Can. J. Remote. Sens.* 24, 3–8. doi: 10.1080/07038992.1998.10874685

Cao, H, Wang, Y, Chen, J, Jiang, D, Zhang, X, Tian, Q, and Wang, M (2021). Swin-Unet: Unet-like pure transformer for medical image segmentation.

Chen, B, Liu, Y, Zhang, Z, Lu, G, and Zhang, D (2021). TransAttUnet: Multi-level attention-guided U-net with transformer for medical image segmentation. arXiv.

Chen, J, Lu, Y, Yu, Q, Luo, X, and Zhou, Y (2021). TransUNet: Transformers make strong encoders for medical image segmentation. arXiv [Preprint].

Chen, LC, Papandreou, G, Kokkinos, I, Murphy, K, and Yuille, AL (2014). Semantic image segmentation with deep convolutional nets and fully connected CRFs. Computer science: 357–361.

Chen, L. C., Papandreou, G., Kokkinos, I., Murphy, K., and Yuille, A. L. (2018b). DeepLab: semantic image segmentation with deep convolutional nets, Atrous convolution, and fully connected CRFs. *IEEE Trans. Pattern Anal. Mach. Intell.* 40, 834–848. doi: 10.1109/TPAMI.2017.2699184

Chen, LC, Papandreou, G, Schroff, F, and Adam, H (2017). Rethinking Atrous convolution for semantic image segmentation.

Chen, LC, Zhu, Y, Papandreou, G, Schroff, F, and Adam, H, (2018a). Encoder-decoder with Atrous separable convolution for semantic image segmentation, European Conference on Computer Vision.

Corso, J. J., Sharon, E., Dube, S., El-Saden, S., Sinha, U., and Yuille, A. (2008). Efficient multilevel brain tumor segmentation with integrated Bayesian model classification. *IEEE Trans. Med. Imaging* 27, 629–640. doi: 10.1109/TMI.2007.912817

Cuixia, L., Mingqiang, L., Zhaoying, B., Wenbing, L., Dong, Z., and Jianhua, M. (2019). Establishment of a deep feature-based classification model for distinguishing benign and malignant breast tumors on full-filed digital mammography. *J. South Med. Univ* 39, 88–92. doi: 10.12122/j.issn.1673-4254.2019.01.14

Devlin, J, Chang, MW, Lee, K, and Toutanova, K (2018). BERT: pre-training of deep bidirectional transformers for language understanding.

Dong, H., Yang, G., Liu, F., Mo, Y., and Guo, Y. (2017). *Automatic brain tumor detection and segmentation using U-net based fully convolutional networks, annual conference on medical image understanding and analysis*. Edinburgh, UK: Springer, 506–517.

Dosovitskiy, A, Beyer, L, Kolesnikov, A, Weissenborn, D, Zhai, X, Unterthiner, T, Dehghani, M, Minderer, M, et al., (2021). "An image is worth 16x16 words: Transformers for image recognition at scale." in *International Conference on Learning Representations*.

Du, W., Rao, N., Yong, J., Adjei, P. E., Hu, X., Wang, X., et al. (2023). Early gastric cancer segmentation in gastroscopic images using a co-spatial attention and channel attention based triple-branch ResUnet. *Comput. Methods Prog. Biomed.* 231:107397. doi: 10.1016/j.cmpb.2023.107397

Fan, T., Wang, G., Li, Y., and Wang, H. (2020). MA-net: a multi-scale attention network for liver and tumor segmentation. *IEEE Access* 8, 179656–179665. doi: 10.1109/ACCESS.2020.3025372

He, K., Zhang, X., Ren, S., and Sun, J. (2016). *Deep residual learning for image recognition*. Las Vegas, NV, USA: IEEE.

Huang, G., Liu, Z., Laurens, V., and Weinberger, K. Q. (2016). *Densely connected convolutional networks*. Honolulu, HI, USA: IEEE Computer Society.

Huang, Z, Wang, X, Wei, Y, Huang, L, and Huang, TS (2020). CCNet: Criss-cross attention for semantic segmentation. IEEE transactions on pattern analysis and machine intelligence PP:1.

Huttenlocher, D. P, Klanderman, G. A, and Rucklidge, W. J (1993), Comparing images using the Hausdorff distance. *Pattern analysis and machine intelligence, IEEE transactions* on, 15, 850, 863, doi: 10.1109/34.232073.

Jie, Shen, Samuel, Albanie, Gang, Sun, and Enhua, (2019). Squeeze-and-excitation networks. IEEE transactions on pattern analysis and machine intelligence.

Kingma, D, and Ba, J (2014). Adam: A Method for Stochastic Optimization. Computer Science.

Krizhevsky, A., Sutskever, I., and Hinton, G. E. (2017). ImageNet classification with deep convolutional neural networks. *Commun. ACM* 60, 84–90. doi: 10.1145/3065386

Lin, A., Chen, B., Xu, J., Zhang, Z., Lu, G., and Zhang, D. (2022). Ds-TransUNet: dual swin transformer u-net for medical image segmentation. *IEEE Trans. Instrum. Meas.* 71, 1–15. doi: 10.1109/TIM.2022.3178991

Ling, C., Chao, Z., Mengling, T., Chen, Y., and Qingxiang, L. (2016). Effect analysis of MRI in differential diagnosis of cerebellopontine angle meningioma and acoustic neuroma. *Contemp. Med. Symp.* 14, 134–136. doi: CNKI:SUN:QYWA.0.2016-22-093

Lingmei, A., Tiandong, L., Fuyuan, L., and Kangzhen, S. (2020). Magnetic resonance brain tumor image segmentation based on attention U-net. *Laser Optoelectronics Progress* 57, 141030–141286. doi: 10.3788/LOP57.141030

Liu, Z, Chen, L, Tong, L, Zhou, F, Jiang, Z, Zhang, Q, Shan, C, Wang, Y, et al. (2020). Deep learning based brain tumor segmentation: A survey.

Liu, S, Qi, L, Qin, H, Shi, J, and Jia, J (2018). Path aggregation network for instance segmentation. 2018 IEEE/CVF Conference on Computer Vision and Pattern Recognition (CVPR).

Liu, Y., Wang, H., Chen, Z., Huangliang, K., and Zhang, H. (2022). TransUNet+: redesigning the skip connection to enhance features in medical image segmentation. *Knowl.-Based Syst.* 256:109859. doi: 10.1016/j.knosys.2022.109859

Liu, Z., Lin, Y., Cao, Y., Hu, H., Wei, Y., Zhang, Z., et al. (2021). "Swin transformer: hierarchical vision transformer using shifted windows." in *IEEE/CVF International Conference on Computer Vision (ICCV)*. pp. 9992–10002.

McClelland, S., Guo, H., and Okuyemi, K. S. (2011). Morbidity and mortality following acoustic neuroma excision in the United States: analysis of racial disparities during a decade in the radiosurgery era. *Neuro-Oncology* 13, 1252–1259. doi: 10.1093/neuonc/nor118

Mehta, R (2015). Introducing dice, Jaccard, and other label overlap measures to ITK.

North, M., Weishaar, J., Nuru, M., Anderson, D., and Leonetti, J. P. (2022). Assessing surgical approaches for acoustic neuroma resection: do patients perceive a difference in quality-of-life outcomes? *Otol. Neurotol.* 43, 1245–1251. doi: 10.1097/MAO.0000000000003720

Nurçin, F. V. (2022). Improved segmentation of overlapping red blood cells on malaria blood smear images with TransUNet architecture. *Int. J. Imaging Syst. Technol.* 32, 1673–1680. doi: 10.1002/ima.22739

Pan, S. M., Liu, X., Xie, N. D., and Chong, Y. W. (2023). EG-TransUNet: a transformer-based U-net with enhanced and guided models for biomedical image segmentation. *BMC Bioinform.* 24:85. doi: 10.1186/s12859-023-05196-1

Qiulin, J., and Xin, W. (2018). Brain tumor image segmentation based on region growing algorithm. *J. Changchun Univ. Technol.* 39, 490–493. doi: CNKI:SUN:JLGX.0.2018-05-013

Rajeshwari, P, and Shyamala, K. (2023). "Pixel attention based deep neural network for chest CT image super resolution." in *Advanced Network Technologies and Intelligent Computing: Second International Conference (ANTIC)*. pp. 393–407.

Ronneberger, O, Fischer, P, and Brox, T (2015). U-net: Convolutional networks for biomedical image segmentation. ArXiv abs/1505.04597.

Roy, K., Banik, D., Bhattacharjee, D., Krejcar, O., and Kollmann, C. (2022). LwMLA-NET: a lightweight multi-level attention-based network for segmentation of COVID-19 lungs abnormalities from CT images. *IEEE Trans. Instrum. Meas.* 71, 1–13. doi: 10.1109/TIM.2022.3161690

Russo, C, Liu, S, and Di Ieva, A (2020). Spherical coordinates transformation pre-processing in deep convolution neural networks for brain tumor segmentation in MRI. arXiv preprint arXiv:200807090.

Shelhamer, E, Long, J, and Darrell, T (2016). Fully convolutional networks for semantic segmentation.

Simonyan, K, and Zisserman, A (2014). Very deep convolutional networks for large-scale image recognition. Computer Science.

Song, Z., Qiu, D., Zhao, X., Lin, D., and Hui, Y. (2023). Channel attention generative adversarial network for super-resolution of glioma magnetic resonance image. *Comput. Methods Prog. Biomed.* 229:107255. doi: 10.1016/j.cmpb.2022.107255

Soomro, MH, De Cola, G, Conforto, S, Schmid, M, Giunta, G, Guidi, E, Neri, E, Caruso, D, et al., (2018). "Automatic segmentation of colorectal cancer in 3D MRI by combining deep learning and 3D level-set algorithm-a preliminary study." in *2018 IEEE 4th Middle East Conference on Biomedical Engineering (MECBME), IEEE*. pp. 198–203.

Szegedy, C., Liu, W., Jia, Y., Sermanet, P., and Rabinovich, A. (2014). *Going deeper with convolutions*. Boston, MA, USA: IEEE Computer Society.

Tang, J., Zou, B., Li, C., Feng, S., and Peng, H. (2021). Plane-wave image reconstruction via generative adversarial network and attention mechanism. *IEEE Trans. Instrum. Meas.* 70, 1–15. doi: 10.1109/TIM.2021.3087819

Thillaikkarasi, R., and Saravanan, S. (2019). An enhancement of deep learning algorithm for brain tumor segmentation using kernel based CNN with M-SVM. *J. Med. Syst.* 43, 1–7. doi: 10.1007/s10916-019-1223-7

Tian, C., Xu, Y., Li, Z., Zuo, W., and Liu, H. (2020). Attention-guided CNN for image denoising. *Neural Netw.* 124, 117–129. doi: 10.1016/j.neunet.2019.12.024

Valanarasu, JMJ, Oza, P, Hacihaliloglu, I, and Patel, VM, (2021). "Medical transformer: gated axial-attention for medical image segmentation." in *International Conference on Medical Image Computing and Computer-Assisted Intervention*.

Vaswani, A., Shazeer, N., Parmar, N., Uszkoreit, J., Jones, L., Gomez, A. N., et al. (2017). Attention is all you need. *Adv. Neural Inf. Proces. Syst.* 6000–6010. doi: 10.48550/arXiv.1706.03762

Wang, H, Cao, P, Wang, J, and Zaiane, OR (2021). UCTransNet: Rethinking the skip connections in U-net from a channel-wise perspective with transformer.

Wang, X, Girshick, R, Gupta, A, and He, K (2017). Non-local neural networks.

Wang, B., Wang, F., Dong, P., and Li, C. (2022). Multiscale transunet++: dense hybrid U-net with transformer for medical image segmentation. *SIViP* 16, 1607–1614. doi: 10.1007/s11760-021-02115-w

Woo, S, Park, J, Lee, JY, and Kweon, IS (2018). *CBAM: Convolutional block attention module*. Springer, Cham.

Xiaobo, L., Maosheng, X., and Xiaomei, X. (2019). Automatic segmentation for Glioblastoma Multiforme using multimodal MR images and multiple features. *J. Comp.Aided Design Comp. Graphics* 31, 421–430. doi: CNKI:SUN:JSJF.0.2019-03-008

Xiaoxia, P., Qian, M., Xia, T., Ziwei, L., and Daohai, X. (2014). MRI findings of lesions in the cerebellopontine angle. *J. Med. Imaging* 24, 12–15.

Yang, Y, and Mehrkanoon, S (2022). AA-TransUNet: Attention augmented TransUNet for Nowcasting tasks.

Yongzhuo, L., and Shuguang, D. (2018). Application of improved watershed algorithm in segmentation of brain tumor CT images. *Software Guide* 17, 157–159. doi: 10.11907/rjdk.172913

Yu, C., Gao, C., Wang, J., Yu, G., Shen, C., and Sang, N. (2021). BiSeNet V2: bilateral network with guided aggregation for real-time semantic segmentation. *Int. J. Comput. Vis.* 129, 3051–3068. doi: 10.1007/s11263-021-01515-2

Yuan, Y., Zhang, L., Wang, L., and Huang, H. (2021). Multi-level attention network for retinal vessel segmentation. *IEEE J. Biomed. Health Inform.* 26, 312–323. doi: 10.1109/JBHI.2021.3089201

Zhang, Y, Li, K, Li, K, Wang, L, Zhong, B, and Fu, Y (2018). Image super-resolution using very deep Residual Channel attention networks.

Zhao, H, Kong, X, He, J, Qiao, Y, and Dong, C (2020). Efficient image super-resolution using pixel attention.

Zhao, H., Shi, J., Qi, X., Wang, X., and Jia, J. (2016). *Pyramid scene parsing network*. Honolulu, HI, USA: IEEE Computer Society.

Zhao, L., Zhou, D. M., Jin, X., and Zhu, W. N. (2022). Nn-TransUNet: an automatic deep learning pipeline for heart MRI segmentation. *Life* 12:1570. doi: 10.3390/life12101570

Zheng, S, Lu, J, Zhao, H, Zhu, X, and Zhang, L (2020). Rethinking semantic segmentation from a sequence-to-sequence perspective with transformers.

Zhou, Z, Siddiquee, M, Tajbakhsh, N, and Liang, J (2018). UNet++: A nested U-net architecture for medical image segmentation.

Zhu, D., Sun, D., and Wang, D. (2022). Dual attention mechanism network for lung cancer images super-resolution. *Comput. Methods Prog. Biomed.* 226:107101. doi: 10.1016/j.cmpb.2022.107101

frontiers | Frontiers in Neuroscience

TYPE Original Research
PUBLISHED 16 August 2023
DOI 10.3389/fnins.2023.1155362

OPEN ACCESS

EDITED BY
Pan Lin,
Hunan Normal University, China

REVIEWED BY
Jianwei Shen,
North China University of Water Conservancy and Electric Power, China
Ergin Yilmaz,
Bulent Ecevit University, Türkiye

*CORRESPONDENCE
Yanmei Kang
✉ ymkang@xjtu.edu.cn

RECEIVED 31 January 2023
ACCEPTED 06 June 2023
PUBLISHED 16 August 2023

CITATION
Xu Z, Zhai Y and Kang Y (2023) Mutual information measure of visual perception based on noisy spiking neural networks. *Front. Neurosci.* 17:1155362. doi: 10.3389/fnins.2023.1155362

Mutual information measure of visual perception based on noisy spiking neural networks

Ziheng Xu, Yajie Zhai and Yanmei Kang*

School of Mathematics and Statistics, Xi'an Jiaotong University, Xi'an, China

Note that images of low-illumination are weak aperiodic signals, while mutual information can be used as an effective measure for the shared information between the input stimulus and the output response of nonlinear systems, thus it is possible to develop novel visual perception algorithm based on the principle of aperiodic stochastic resonance within the frame of information theory. To confirm this, we reveal this phenomenon using the integrate-and-fire neural networks of neurons with noisy binary random signal as input first. And then, we propose an improved visual perception algorithm with the image mutual information as assessment index. The numerical experiences show that the target image can be picked up with more easiness by the maximal mutual information than by the minimum of natural image quality evaluation (NIQE), which is one of the most frequently used indexes. Moreover, the advantage of choosing quantile as spike threshold has also been confirmed. The improvement of this research should provide large convenience for potential applications including video tracking in environments of low illumination.

KEYWORDS

low-illumination image, spiking neural network, aperiodic stochastic resonance, mutual information, quantile threshold

1. Introduction

Stochastic resonance, initially proposed by European physicists in explaining the climatic switches (Benzi et al., 1981), is an essentially cooperative effect through which an external weak signal can be maximally amplified at a suitable amount of noise. This phenomenon is hard to be reproduced in climatic research but can be confirmed by various artificially designed experiments including crayfish (Douglass et al., 1993), shark (Braun et al., 1994), rat (Collins et al., 1996), cricket (Levin and Miller, 1996), optical material (Dylov and Fleischer, 2010) and human (Winterer et al., 1999; Zeng et al., 2000). The experiments successfully revealed that noise can play a potential but positive role in neural information processing, and further encouraged extensive theoretical progress, such as noise enhanced weak signal detection (Kang et al., 2005; Sun et al., 2019; Kang et al., 2022), noise facilitated information coding (Du et al., 2010; Nakamura and Tateno, 2019; Guan et al., 2021) and noise enhanced chaos control (Lei et al., 2017). Nowadays how to utilize noise for developing novel brain-like algorithms, such as visual perception (Simonotto et al., 1997; Fu et al., 2020; Xu et al., 2022) and epileptic diagnosis preprocessing (Shi et al., 2023), has attracted more and more interest in the current age of artificial intelligence.

Exploring the neural mechanism and algorithm design of visual perception is a long-standing topic in the field of neuroscience (Shapley and Hawken, 2002; Chen and Gong, 2019; Dijkstra et al., 2019). The visual perception in a general sense refers to the process of organizing, identifying, and interpreting visual information in environmental awareness and understanding (Yang et al., 2021), while in a narrow sense it means the enhancement of image contrast (Rafael and Woods, 2002). There are scenarios where pictures of high contrast are hard to be captured in a dark or

low-illumination environment, such as in the cosmic exploration, in the battle front and in the deep-sea exploration. The traditional techniques (Land, 1997) for image enhancement are based on Retinex theory, where actual color sensations are assumed related to the intrinsic reflectance of objects. It is generally regarded that there are mainly two disadvantages of Single-Scale Retinex algorithm: one is that halo would be prone to occur in the transition field between strong light and shadow, and the other is that the image would be relatively dark after enhancement, so the Multi-scale Retinex algorithms (Rahman et al., 2004; Wang et al., 2021) have been proposed. Here, let us skip to assess the advantage or disadvantage of the improved variants, but choose to develop a different method based on different physical principles, namely stochastic resonance and spiking neuron models. In fact, the method proposed in this paper is an important development of our previous stochastic resonance-based spiking neural network methods in measure index, which is critical for identifying a target image.

How to effectively evaluate the perceptual quality of visual contents, such as image, is actually a long-standing issue. There are generally two categories of assessment indexes: the full-reference evaluation metric *via* the no-reference evaluation metric. The former category claims that the quality of the distorted image could be measured through comparing with a naturalistic reference image, including peak signal to noise ratio (Hore and Ziou, 2010) and structural similarity (Wang et al., 2004). The latter category covers perceptual quality metric (PQM) (Wang et al., 2002) and natural image quality evaluation (NIQE) (Mittal et al., 2013). As is known, PQM mainly concerns the blurring and blocking effect of a JPEG format image, while NIQE evaluates an image by calculating its distance from a fitted high-quality image. Nevertheless, when the both indices are applied to stochastic-resonance based visual perception algorithm design, it was found that the dependence of PQM on noise intensity tends to be too flat to pick out the best enhanced image (Fu et al., 2020), while the evolution of NIQE *via* noise intensity tends to have strong fluctuations due to the unpredictability in Gaussian distribution fitting and perturbation of external noise. It is these insufficiencies that motivate us to try a different measure from the viewpoint of information theory.

Our inspiration comes from the mutual information measure of aperiodic stochastic resonance (Collins et al., 1996; Levin and Miller, 1996; Patel and Kosko, 2008; Kang et al., 2021). Note that the external coherent input to stochastic resonant systems can be periodic or aperiodic, when it is aperiodic, the resonant phenomenon is specifically named as aperiodic stochastic resonance. In case of the aperiodic stochastic resonance, the quantifying indexes based on the mechanism of frequency matching, such as the signal-to-noise ratio and the spectral amplification factor, are no longer appropriate, and instead the input–output mutual information is a suitable choice for describing this matching mechanism of shape similarity. Following the investigation of aperiodic stochastic resonance (Kang et al., 2021), no matter how weak an external aperiodic signal is, it can always be maximally amplified by suitable amount of noise. Note that an image stimulus is such a typical aperiodic signal, thus the images of low contrast or illumination should always be optimally enhanced by an optimal dose of noise. This means there exists an optimal noise level at which the mutual information between the dark image and the target image can attain its maximum. As for whether the measure of mutual information is really a better choice for visual perception design, the comparison with NIQE should tell everything.

The paper is organized as follows. In Section 2 the phenomenon of aperiodic stochastic resonance in spiking neural networks consisting of integrate-and-fire neurons are exhibited within the information frame as preliminary. In Section 3 an improved visual perception algorithm is proposed based on the principle of aperiodic stochastic resonance. When applying the algorithm to both grayscale image and color image of low contrast, the reliability of the algorithm is verified. Different threshold strategies are also compared and the robustness of the mutual information measure is disclosed. Conclusions are finally drawn in Section 4.

2. Aperiodic stochastic resonance in an integrate-and-fire neural network

To enhance the plausibility of the subsequent visual perception algorithm, let us demonstrate here the principle of aperiodic stochastic resonance. Without loss of generality, let us continue to consider the spiking network consisting of the conductance-based fully connected integrate-and-fire neurons (Xu et al., 2022), as shown in Figure 1, with each neuron standing for one photoreceptor cell in the low illumination environment. The network is governed by the following Langevin equations

$$C_m \frac{dV_i(t)}{dt} = -g_l\left(V_i(t) - V_L\right) - I_{syn,i}(t) + I_{ext,i}(t),\ V_i(t) < V_{th},\ 1 \le i \le N \tag{1a}$$

$$I_{syn,i}(t) = g_s\left(V_i(t) - E_{syn}\right)\sum_{j=1}^{N} w_{ij} s_j(t) \tag{1b}$$

$$s_j(t) = \sum_{t_{j,k}} e^{\left(-\left(t - t_{j,k} - \tau_s\right)/\tau\right)} \delta\left(t - t_{j,k}\right) \tag{1c}$$

where $V_i(t)$ is the membrane potential of the ith neuron at time t, C_m is the membrane capacitance, g_l is a leaky conductance, V_L is a leaky

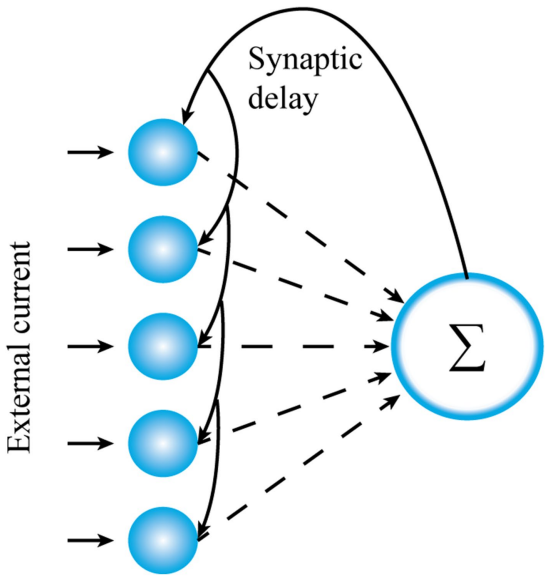

FIGURE 1
The network topology of the present study with each blue circle standing for one node neuron.

voltage, $I_{syn,i}(t)$ is the synaptic current at time t from other neurons in the network, and $I_{ext,i}(t)=S(t)+\sqrt{2D}\xi_i(t), 1\le i\le N$ denotes an external injected current. In the external current, $S(t)\in\{A,B\}$ is a binary signal representing an external visual stimuli, with $P(S(t)=A)=p$ and $P(S(t)=B)=1-p$ with $p\in(0,1)$, $\xi_i(t)$ is Gaussian white noise of noise intensity D and describing the external fluctuations satisfying $\langle\xi_i(t+s)\xi_j(t)\rangle=\delta_{ij}\delta(s)$ for $1\le i,j\le N$. Here, $\delta(\cdot)$ is Dirac function $\delta(\cdot)$ while δ_{ij} is Dirac notation such that $\delta_{ij}=1$ if $i=j$ and $\delta_{ij}=0$ otherwise. In Eq. (1b), g_s is the synaptic conductance, E_{syn} the synaptic reversal potential, w_{ij} the synaptic weight between neuron i and neuron j, τ is the synaptic constant, τ_s the synaptic delay, $t_{j,k}$ the kth spiking time of the neuron j, and $s_j(t)$ is the fractions of open synaptic channels of the jth neuron at time t. Once the membrane potential $V_i(t)$ reaches the threshold potential V_{th} from below, a spike is emitted and the membrane potential is immediately reset to the resting potential V_r and restarts a time-dependent evolution following Eq. (1a) after a short refractory period τ_{ref}. For the sake of simplicity, we set $\tau_{ref}=0$ by ignoring the influence of refractory period.

Note that the train of spikes is the main carrier for neural information, thus the output response of the ith neuron and the neural network can be, respectively, denoted as

$$y_i(t)=\sum_k\delta(t-t_{i,k}),\ y(t)=\frac{1}{N}\sum_{i,k}\delta(t-t_{i,k}) \tag{2}$$

We remark that the spike train $y_i(t)$ can be acquired by Euler-Maruyama scheme, namely

$$\begin{aligned}C_m\Delta V_i^{n+1}=&-\left(g_l\left(V_i^n-V_L\right)-I_{syn,i}(t_n)-I_{sig}(t_n)\right)\Delta t_n\\&+\sqrt{2D\Delta t_n}\,r_i^n,\ 1\le i\le N\end{aligned} \tag{3}$$

Here the superscript n denotes the nth iteration. $V_i^n=V_i(t_n)$, $I_{sig}(t_n)=S(t_n)$, $\Delta t_n=t_{n+1}-t_n$ is time step, $\Delta V_i^n=V_i(t_{n+1})-V_i(t_n)$ and $r_i^n\sim N(0,1)$ is a normal distributed pseudo random number. Note that Gaussian white noise is the formal derivative of Wiener process. Since the Wiener process is of independent increments, these mutually independent pseudo random numbers at each iteration are also statistically independent for different iterations.

Note that noise can play a beneficial role in improving neural information encoding through the mechanism of stochastic resonance (Rizzo, 1997). Particularly, the input–output mutual information is suitable for acting as a quantifying metric for aperiodic stochastic resonance (Kang et al., 2021). For the sake of completeness, let us explain how to calculate the input–output mutual information for the system (1). Let $I(X,Y)$ be the mutual information of discrete random variables X and Y with values in finite sets χ and γ, then

$$I(X,Y)=H(Y)-H(Y|X)=\sum_{x\in\chi}\sum_{y\in\gamma}p(x,y)\log\frac{p(x,y)}{p(x)p(y)} \tag{4}$$

where

$$H(Y)=-\sum_{y\in\gamma}p(y)\log\left(p(y)\right)$$

and

$$H(Y|X)=-\sum_{x\in\chi,y\in\gamma}p(x,y)\log\left(p_{Y|X}(y|x)\right)$$

are the entropy and the conditional entropy (Cover and Thomas, 2006; Yarrow et al., 2012), respectively. We follow the existing procedure (Kang et al., 2021) to calculate the mutual information $I(S(t),y(t))$ between the binary input $S(t)$ and the population firing output $y(t)$. As seen from Eq. (4), $I(S(t),y(t))$ is a mathematical expectation of the form

$$I(S(t),y(t))=E\left(\log\frac{p(s,y)}{p(s)p(y)}\right) \tag{5}$$

Thus, we can repeat 1,000 trials to get an arithmetic average for an improved accuracy based on the law of large number.

Note that the entropy $H(y(t))$ quantifies the average uncertainty of a random variable $y(t)$, while the conditional entropy $H(y(t)|S(t))$ measures the average uncertainty associated with $y(t)$ under the condition that the outcome of $S(t)$ are known, thus $I(S(t),y(t))$, as a measure of the shared information between the binary input and the population firing output, can be adopted as metric for the phenomenon of aperiodic stochastic resonance. When the input–output mutual information of the model (1) has a nonmonotonic dependence on noise intensity, it is usually said that the phenomenon of aperiodic stochastic resonance occurs (Collins et al., 1996). Particularly, when the input–output mutual information is maximized, the output signal should have a maximal resemblance in shape with the input signal.

We consider a realistic inhibitory synaptic weight $w_{ij}=-0.2$ (Rolls et al., 2008) for $1\le i,j\le N$ to observe aperiodic stochastic resonance for both a single neuron and the spiking network. Since the binary input is subthreshold (Figure 2A), there is no spike emission from the single neuron in the absence of noise (Figure 2B). When small amount of noise is injected, the single neuron is activated with the help of noise but the resultant output response is obviously different from the binary input signal in shape (Figure 2C). When the noise intensity is increased to a proper level where the input–output mutual information attains a peak value (Figure 2G), the resemblance between the output response and the input binary signal is greatly improved, as shown in Figure 2D. Note that the perception function of the brain is generally implemented at population level, while the effect of stochastic resonance can be enhanced by uncoupled array or coupled ensemble (Nakamura and Tateno, 2019; Sun et al., 2019). Thus, in order to simulate this synergetic effect of system size on the aperiodic stochastic resonance, we also show the shape similarity by raster plots for $N=5$ (Figure 2E) and $N=10$ (Figure 2F). From these pictures it is clear that the shape similarity significantly increases as the network size grows, thus a larger network should be necessary for the subsequent visual perception design. We emphasize that all the shape similarities are selected when the mutual information of Figures 2D–F reaches maximum. This demonstrates that the input–output mutual information as function of noise cannot unlimitedly increase, and therefore there exists an optimal noise intensity at which the weak input signal can be best detected. Additionally, from Figures 2G–I, it is clear that the aperiodic stochastic resonance has a strong dependence on the spike threshold: the lower the threshold, the prominent the resonant effect. This point has an important inspiration: a suitable

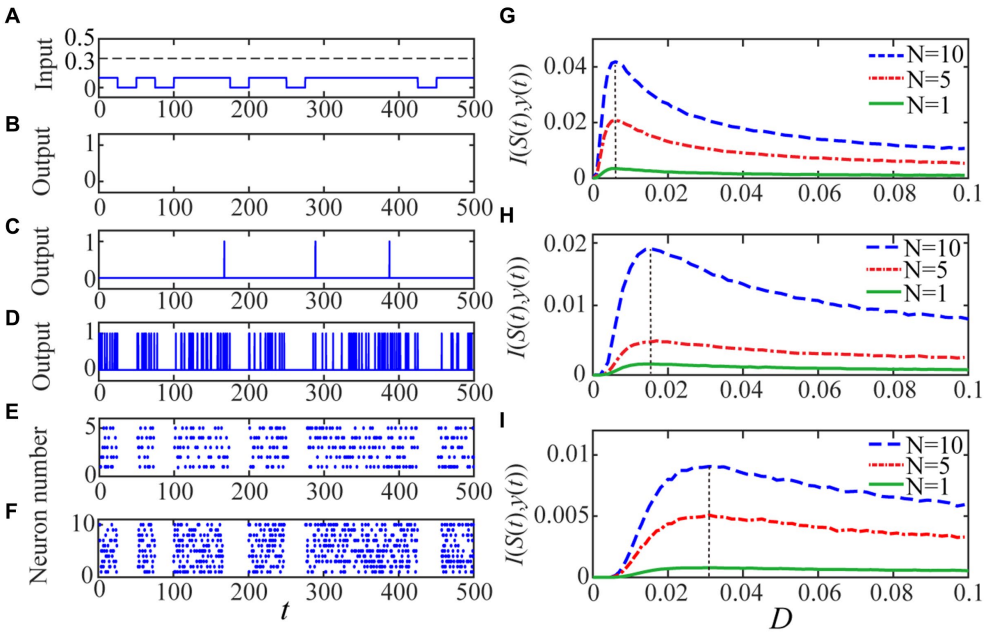

FIGURE 2
The quantized output and the input–output mutual information are displayed. The random binary signal is displayed in panel **(A)** with A =0.1, B =0 and p = 0.7. For given V_{th} = 0.2, as the panel **(B)** shows there is no 1 in the quantized output for the single neuron when the noise intensity is vanishing since the input signal is subthreshold. As the noise intensity is increased, the quantized output becomes more visible and clearly, there is more input–output similarly for a single neuron with panel **(D)** D = 0.006 than the other level **(C)** D = 0.001. The resemblance becomes evident when **(E)** N = 5 and **(F)** N = 10 for the optimal noise intensity, which is the same for different network size under the identical spike threshold. The mono-peak curves of mutual information I ($S(t)$,$y(t)$) via noise intensity with thresholds: **(G)** V_{th} = 0.2, **(H)** V_{th} = 0.3 and **(I)** V_{th} = 0.4 signify the occurrence of aperiodic stochastic resonance for different size' network. The other parameters are fixed as V_{re} = 0, gl = gs = 1, C_m = 1, E_{syn} = 0, τ_s = 1, τ_d = 0.5 and T = 500.

threshold should be chosen so that an optimally enhanced image can be acquired. In fact, the spike threshold in real neurons has certain circadian rhythm and self-adaptability, so it can be lower in a dimmer environment (Destexhe, 1998; Taillefumier and Magnasco, 2013).

As the last paragraph, let us emphasize that the shape similarity measured by the mutual information can be further improved by increasing the network size, as shown by Figures 2D–F, but the improvement should have limitation following the law of large number. In fact, According to the previous investigations, whether the quantifying index is the spectral amplification factor (Fu et al., 2020) or the signal to noise ratio (Xu et al., 2022), it cannot be improved infinitely; on the contrary, the limit level can be achieved with a network size $N \leq 50$ for the aperiodic binary $S(t)$. Noting the image signal is more complex than the binary input, we choose $N = 300$ in the subsequent algorithm implementation so that the benefit of network size can be maximally utilized. This should imply the following fact. Although there are over 100 million photoreception neurons for one normal person (Rieke and Baylor, 1998), not all of them participate in the perception task: the more complex the stimuli are, the more neurons are involved.

3. Visual perception algorithm and mutual information measure

Noise is not only ubiquitous in nervous systems but can play a positive role in neural information processing (Rizzo, 1997). As illustrated by the last section, noise can potentially assist human being in detecting weak aperiodic stimuli. Note that an image of low contrast is such a typical stimulus, thus some biologically plausible visual perception algorithms (Fu et al., 2020; Xu et al., 2022) have been proposed by combining the basic biophysical process behind visual perception, which includes three stages of encoding, decoding and integrating, with the principle of aperiodic stochastic resonance. Nevertheless, as mentioned in the introduction section, one of the most commonly used assessment indices, namely NIQE (Mittal et al., 2013; Xu et al., 2022), always gives rise to strong fluctuations as noise intensity increases. To overcome this insufficiency in the existing algorithms, we aim to present an improved algorithm within the frame of information theory.

3.1. Grayscale image enhancement

When light enters the eye, the photoreceptors in the retina transform the optical signal into an electrical signal through an inherent encoding process participated by rod cells. Note that there are two kinds of photoreceptors in the retina: rods and cones. The cones in charge of color are active to bright light while the rods in charge of profile are more sensitive to dim light. In the low-illumination environment, the rhodopsin in rod cells can decompose itself under the light stimulation so that the light signals can be transferred into electrical signals (Hartong et al., 2006). As a result, human can discern to certain extent the profile of hidden objects in dim surroundings. Thus, we use the spiking neural network (1) to simulate the rod cells and their feedback interaction (Xu et al., 2022), while the aperiodic binary input can be replaced by the weak image stimulus.

In the encoding state, let *Gray* be an M-dimensional grayscale matrix of a white-black image, with each pixel representing an illuminance value. Note that all the rods in the network are assumed to focus on the same image stimuli, thus the illuminance matrix can be received by every rod. Let $V_i^{m,n}(t)$ represents the time-dependent potential response of the ith rod cell when it receives the pixel $Gray(m,n)$ with $1 \le m,n \le M$, then the spiking neural network (1) can be rewritten into

$$C_m \frac{d}{dt} V_i^{m,n}(t) = -g_l\left(V_i^{m,n}(t) - V_L\right) + I_{syn,i}^{m,n}(t) + Gray(m,n) + \sqrt{2D}\xi_i^{m,n}(t) \tag{6a}$$

$$I_{syn,i}^{m,n}(t) = g_s\left(V_i^{m,n}(t) - E_{syn}\right)\sum_{j=1}^{N} w_{ij} s_j^{m,n}(t) \tag{6b}$$

$$s_j^{m,n}(t) = \sum_{t_{j,k}} \exp\left(-\left(t - t_{j,k}^{m,n} - \tau_l\right)/\tau\right)\delta\left(t - t_{j,k}^{m,n}\right) \tag{6c}$$

where $\xi_i^{m,n}(t)$ is Gaussian white noise satisfying $\xi_i^{m,n}(t+s)\xi_j^{m,n}(t) = \delta_{ij}\delta(s)$ for $i,j = 1,2,\ldots,N$. Once $V_i^{m,n}(t)$ reaches the spike threshold V_{th} from below, an action potential is generated by neuron i emits and then the membrane potential is immediately reset to the resting potential V_r, from where a new cycle of evolution restarts. In the encoding phase, $Index_i(m,n) \in \{0,1\}$, the (m, n) element of the spike matrix $Index_i$ is adopted to mark whether the ith neuron has generated spikes during given time span or not. That is, $Index_i(m,n) = 1$ if there is spike generation and $Index_i(m,n) = 0$ otherwise. Here, the time span T is taken as one millisecond to approximate the time cost by a gaze from a normal person and specifically, we emphasize that the grayscale image is taken as a continuous input during the whole time span. That is, every rod cell receives the same constant grayscale matrix. We emphasize that the encoding scheme follows from the previous algorithms (Fu et al., 2020; Xu et al., 2022), which also have certain association with image reconstruction algorithms (Roy et al., 2019; Li et al., 2022). Noting that there are N neurons in the network, there should be N such 0–1 counting matrices altogether. With these spike matrices available, ganglion cells in the last segment of the retina can then transmit the involving information to visual cortex for the next stage (Masland, 1996). For the sake of simplicity, we fix the neural network parameters $C_m = 1$, $g_l = g_s = 1$, $\tau_s = 1$, $\tau_d = 0.5$, $E_{syn} = 0$, $w_{ij} = -0.2$, $V_{re} = 0$, $T = 1$ and $N = 300$ but leave V_{th} and D tunable.

Note both the stage of decoding and the stage of integrating are implemented at the visual cortex. Since the binary spike trains are the main carrier of neural information (Strong et al., 1996), it is reasonable to assume that each encoded spike matrix should be decoded into a binary image. Then, the spike matrix $Index_i$ encoded by the ith neuron can be decoded as a gray image Pic_i of element

$$Pic_i(m,n) = \begin{cases} 0, Index_i(m,n) = 0 \\ 255, Index_i(m,n) = 1 \end{cases} \tag{7}$$

With all the decoded binary images available, an integrated grayscale image *Pic* can be obtained by an ensemble average, namely

$$Pic(m,n) = \frac{1}{N}\sum_{i=1}^{N} Pic_i(m,n) \tag{8}$$

Considering the visual perception process is carried on in noisy environment, every binary image Pic_i is actually a matrix-valued random variable. Thus, the treatment in Eq. (8) is somehow similar to the effect of large number law, which cancels out the influence of occasional factors by taking arithmetic average. In fact, this integration treatment has biophysical implication as well. As is known, a single visual cortex cell usually does not receive all the signals from photoreceptors but only a specifically dominated area (Lecun and Bengio, 1995). Thus, integrating over all the decoded binary images helps to assure that all the information of the visual content is processed.

The purpose of visual perception is to pick out the best enhanced image under the help of suitable amount of noise, but the noise intensity fixed in the above procedure is generally not optimal. Nevertheless, it is possible to capture an optimal value following the principle of aperiodic stochastic resonance. Let us measure the quality of the enhanced image by the input–output image mutual information, namely the mutual information between *Gray* and *Pic*. To this end, the pixels of *Gray* and *Pic* are divided into 255 bins of unit size: $[0, 1], \ldots, [254, 255]$; the frequency number of the pixels is counted in each bin and then the histograms for *Gray* and *Pic* are obtained; the joint histogram of *Gray* and *Pic* can be acquired in the same way. With these histograms to approximate the corresponding marginal distribution laws and the corresponding joint distribution law, the input–output image mutual information could be calculated by

$$I(Pic,Gray) = \sum_{Pic,Gray} P(Pic,Gray)\log\left(\frac{P(Pic,Gray)}{P(Pic)P(Gray)}\right) \tag{9}$$

Then, by examining the nonmonotonic dependence of the image mutual information *via* the noise intensity, one can attain the optimal noise intensity, at which the enhanced image is exactly the target image of our visual perception algorithm. Note that the external noise level of a neural network can be self-adjusted by synaptic weights (Feng et al., 2006), thus it is also biologically plausible to optimize the enhanced image by an optimal noise intensity.

Algorithm 1 summarizes the above procedure for visual perception, while Figures 3, 4 show the test results. For the test in Figure 3, we take 0.5 quantile as the spike threshold (Xu et al., 2022). The marginal histograms for the original picture (Figure 3A) and the target image (Figure 3B) are shown in Figures 3D,E, respectively. By comparing Figures 3D,E, it is clear that more pixels with relatively low grayscale value have been shifted to the area of relatively high grayscale value, which explains why the hidden objects such as flowers and visual charts can be revealed in the target image. Here, we emphasize that the nonmonotonic curve of the image mutual information *via* noise

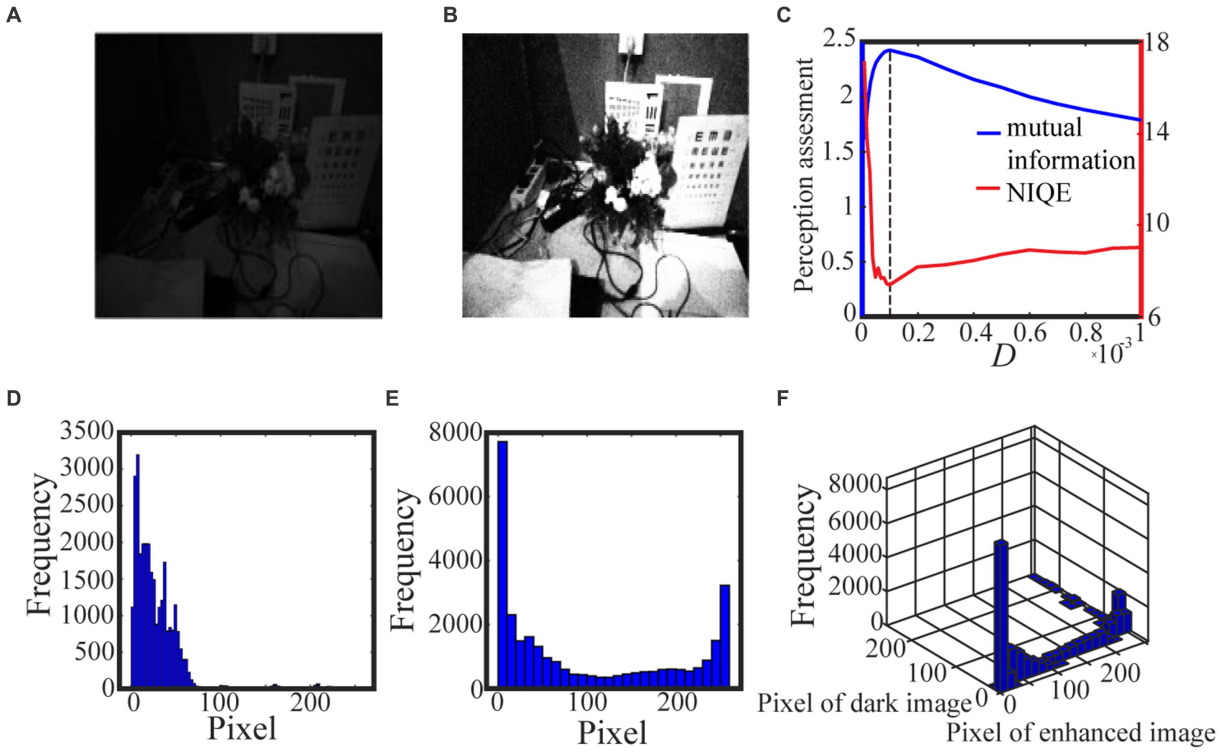

FIGURE 3
The low illuminance grayscale image in **(A)** is taken from the internet and the 0.5 quantile is adopted as the spike threshold. The marginal probability law of **(A)** is shown in **(D)** while the marginal probability law of the best enhanced image **(B)** selected by mutual information is shown in **(E)**. The joint probability law of **(A)** and **(B)** are shown in the two-dimensional histogram **(F)**. The quantifying indexes mutual information (blue solid line) and NIQE (red solid line) are plotted in **(C)** where the black dotted line denotes the optimal noise intensity.

intensity in Figure 3C signifies the occurrence of aperiodic stochastic resonance) and the target image in Figure 3B is picked out from the peak value of the mutual information curve. In fact, our numerical experience has confirmed that a bit derivation from the optimal noise intensity can cause degradation in the quality of the enhanced image. The performance of algorithm 1 can be further confirmed by a darker original image. As shown in Figure 4, the 0.6 quantile is taken as the spike threshold. Analogously, by comparing the marginal histograms of the dark image (Figure 4A) and the target image (Figure 4B), as shown in Figures 4D,E, it is clear to see that the low-value pixels have been increased. Therefore, the tower, trees, the building and the reflection of the tower become discernable in the target image, which corresponds to the peak value of the mutual information curve. Note that the distribution of the natural image features is close to the generalized Gaussian distribution (Moorthy and Bovik, 2010), thus the parameters of the generalized Gaussian distribution fitted with the image to be enhanced should have certain distance of the parameters fitted with natural images. The distance is the so called NIQE, defined by Mittal et al. (2013)

$$\mathrm{NIQE} = \sqrt{(\nu_1 - \nu_2)^T \left(\frac{\Sigma_1 + \Sigma_2}{2}\right)^{-1} (\nu_1 - \nu_2)} \qquad (10)$$

where ν_1 and Σ_1 are the mean vector and the covariance matrix fitted with the natural images, respectively, and ν_2, Σ_2 are the mean vector and the covariance matrix fitted with the images to be enhanced, respectively. It is clear that the smaller NIQE, the better the image quality. Therefore the minimum of NIQE corresponds to the best enhanced image. As seen from noise intensity denoted by the dash line in Figures 3C and 4C, although the optimal noise intensities obtained from the two metrics are almost the same, the mutual information curves are smoother than the NIQE curves. This suggests that the image mutual information is a more appropriate metric for assessing the grayscale image quality.

Algorithm 1 Image enhancement for grayscale images	
Step1:	Input the grayscale image *Gray* to the integrate and fire neuronal network under noise intensity D to get the matrix $Index_i, i = 1,\ldots,N$ which stores the spiking information.
Step2:	Transfer $Index_i, i = 1,\ldots,N$ to grayscale image $Pic_i, i = 1,\ldots,N$
Step3:	Calculate $Pic = \frac{1}{N}\sum_{i=1}^{N} Pic_i$, mutual information $I(Pic, Gray)$ and NIQE
Step4:	Change D and repeat Step1 to Step 3 until the best enhanced image is selected

3.2. Color image enhancement

The color image of low-illumination (contrast) has much difference from the grayscale images, since several color channels are usually involved in given color space. As is known, there are distinct color spaces, such as Red-Green-Blue (RGB) space, Hue-Saturation-Value (HSV) space and Y-cbcr color space (Smith, 1978; Rafael and Woods, 2002; Benjamin et al., 2016; Wu et al., 2021), among which the RGB space is suitable for computer Graphics, the Y-cbcr space is good at discrimination of luminance and chrominance, while the HSV space is in line with the human visual perception system. Based on this consideration, we can transfer the signal from the RGB space into the HSV space. Since the illumination of a color image is overwhelmingly dominated by its value matrix, it is enough to enhance the value information for color image perception.

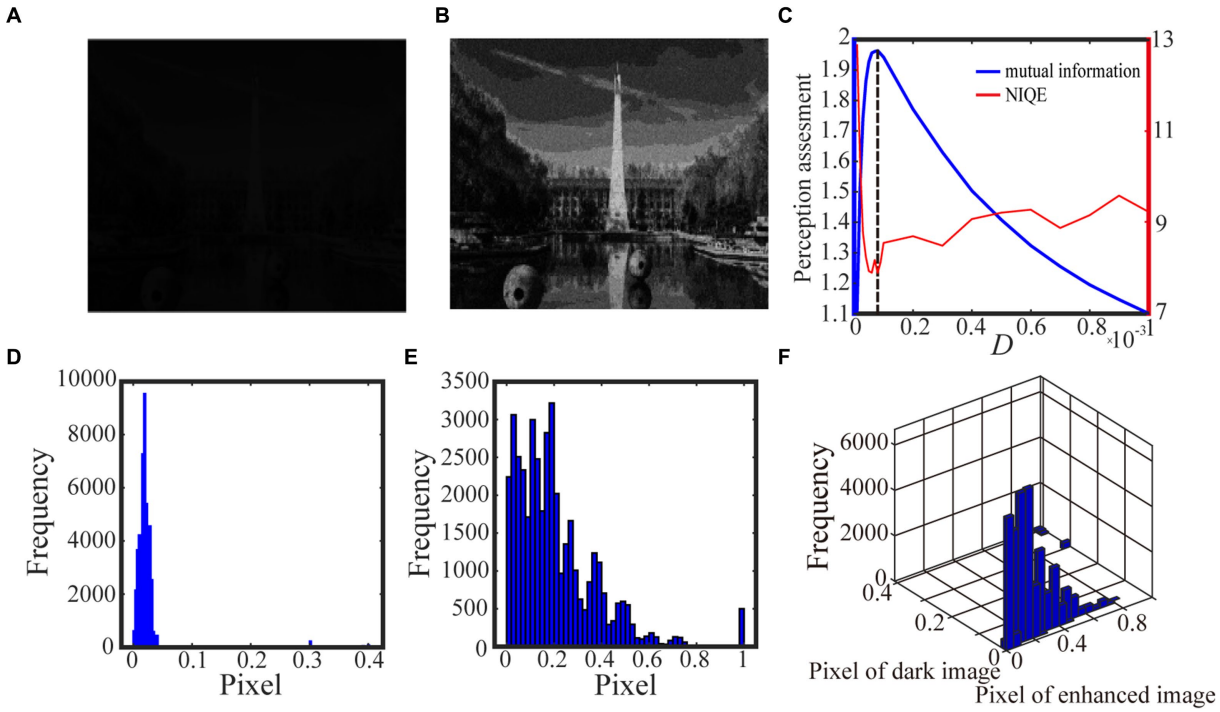

FIGURE 4
The darker grayscale picture in **(A)** is taken by us and the 0.6 quantile is taken as the spike threshold. The marginal probability law of **(A)** is shown in **(D)** while the marginal probability law of the best enhanced image **(B)** picked out by mutual information is shown in **(E)**. The joint probability law of **(A)** and **(B)** is shown in the two-dimensional histogram **(F)**. The perception assessments mutual information (blue solid line) and NIQE (red solid line) are plotted in **(C)** where the black dotted line denotes the optimal noise intensity.

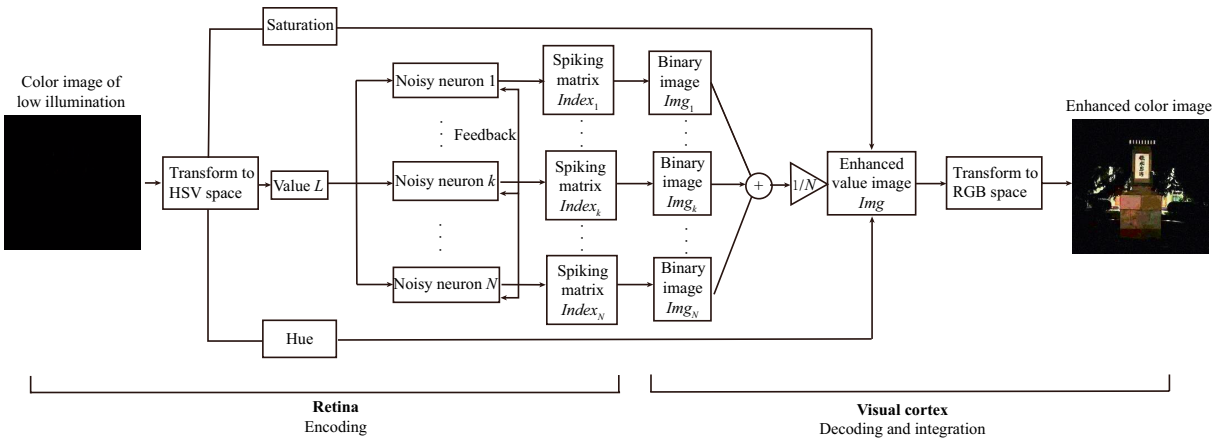

FIGURE 5
Schematic diagram of color image enhancement algorithm.

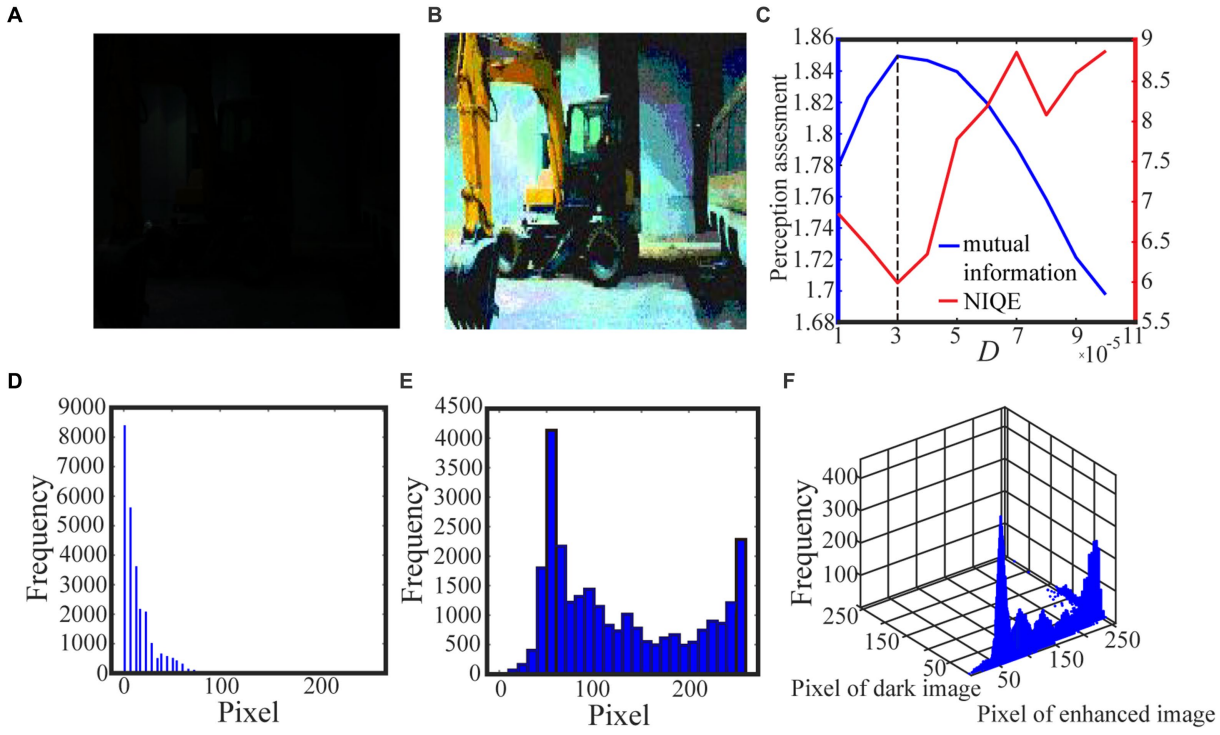

FIGURE 6
The dark color image in **(A)** is taken from the internet and the 0.6 quantile is used as the spike threshold. The marginal probability law of **(A)** is shown in **(D)** while the marginal probability law of best enhanced color image **(B)** selected by mutual information is shown in **(E)**. The joint probability law of **(A)** and **(B)** are shown in the two-dimensional histogram **(F)**. The quantifying indexes mutual information (blue solid line) and NIQE (red solid line) are plotted in **(C)** where the black dotted line denotes the optimal noise intensity corresponding to the maximal mutual information.

Let L be the value matrix. Following the general process of vision formation in low illuminance environment, we can adapt Algorithm 1 with the grayscale matrix *Gray* replaced by L so that the illumination information can be encoded by the rod cells on the retina. And then, the encoded spike matrices $Index_i$ for $i = 1,\ldots,N$ can be transmitted to visual cortex and finally integrated into a binary image *Img*. As the value information L is the input image and *Img* is the output image, we can measure the input–output similarity by the image mutual information defined by

$$I(Img,L) = \sum_{Img,\ L} P(Img,L)\log\left(\frac{P(Img,L)}{P(Img)P(L)}\right) \qquad (11)$$

Here $P(L)$ and $P(Img)$ are the marginal distribution laws for the original value matrix and the enhanced image which is noise intensity dependent, respectively, and $P(Img,L)$ denotes the joint distribution law. Again, these distribution laws can be approximated by their histograms, thus the input–output image mutual information is still easy to be obtained. Once the best enhanced value matrix is attained, an inverse transform from the HSV space into the RGB space can generate a best enhanced color image, which is the target image for color vision perception. The main procedure has been summarized in Algorithm 2. To enhance the intuitiveness, the flowchart of the algorithm is also displayed in Figure 5.

We exhibit two test results with low-contrast color images acquired from the internet and the real world in Figures 6 and 7, respectively. For the test in Figure 6, the 0.6 quantile is taken as the spike threshold. As shown from Figure 6C the nonmonotonic curve of the image mutual information via noise intensity again verifies the occurrence of aperiodic stochastic resonance) and the target image in Figure 6B is picked out from the peak value of the mutual information curve. By comparing the marginal histograms Figures 6D,E for the original picture Figure 6A and the target image Figure 6B, it is clear that more pixels with relatively low illumination value have been shifted to the area of relatively high illumination value, which again explains why the hidden objects such as a bus and an excavator become exposed in the target image. It is clear from Figure 7 that some details of the target image selected by the peak value of the mutual information curve become visible, such as the characters on the monument. Here, we emphasize that the image is indeed enhanced, although most of the pixels of the marginal histogram in Figure 7E are still relatively low. The reason behind this observation is that most of the pixel values are zero since no color and illuminance information can be available from this totally dark environment. Here we also would like to emphasize that the principle of stochastic resonance is powerful in enhancing weak signal, no matter how weak it is, but the weak signal must exist at first. Therefore, we claim that Figure 7B is already the best enhanced image and the corresponding noise intensity is optimal, as revealed by the perception indexes shown in Figure 7C. Finally, from Figures 6,7C we see again that the optimal noise intensities obtained from the two metrics are coincident and the mutual information curves are smoother than the NIQE curves. This again illustrates that the image mutual information is a more appropriate metric for assessing the quality of an enhanced color image.

Algorithm 2 Image enhancement for color images	
Step1:	Transform the image from RGB space to HSV space.
Step2:	Input the value matrix L to the integrate and fire neural network under noise intensity D to get the matrix $Index_i, i = 1,\ldots,N$ which stores the spiking information.
Step3:	Transfer $Index_i, i = 1,\ldots,N$ to grayscale image $Img_i, i = 1,\ldots,N$.
Step4:	Calculate $Img = \frac{1}{N}\sum_{i=1}^{N} Img_i$, mutual information $I(Img, L)$ and NIQE.
Step5:	Change D and repeat Step2 to Step 4 until the best enhanced value matrix is selected.
Step6:	Combine the best enhanced value matrix with hue matrix and saturation matrix and transform it from HSV space into the RGB space.

3.3. Effect of threshold strategy

As shown in Figure 2, the spike threshold has obvious influence on the aperiodic stochastic resonant effect. In fact, since the spike threshold always has important impact on neural activity and coding performance (Yu et al., 2005; Fu et al., 2020; Xu et al., 2022), it is also a critical parameter for the spiking neural network based visual perception. In the previous subsections, we choose some quantile of the relevant histogram of the original images as the spike threshold, and the results have showed that the metric of mutual information is more capable of picking out the best enhanced image. To strengthen this point, let us take a comparative perspective. To this end, let us attempt another threshold strategy (Reinhard et al., 2002), which takes a log-average luminance as threshold, namely

$$V_{th} = \exp\left(\frac{\sum_{m,n}\log(\delta + Gray)}{m * n}\right) \tag{12}$$

for grayscale images and

$$V_{th} = \exp\left(\frac{\sum_{m,n}\log(\delta + L)}{m * n}\right) \tag{13}$$

for color images. We remark that in Eqs. (12) and (13), a small positive number δ is introduced to avoid vanishing antilogarithm. In Figures 8, 9 we show the test results with the best quantile threshold and the log-average luminance threshold with different delta value.

For the grayscale image case, Figure 8 shows the variation of the target image and the assessment index under different spike thresholds. As seen from Figures 8A–C, the threshold change does not have much impact on the enhanced image, but it tends to be difficult for us to select the optimal noise intensity from the fluctuating curve

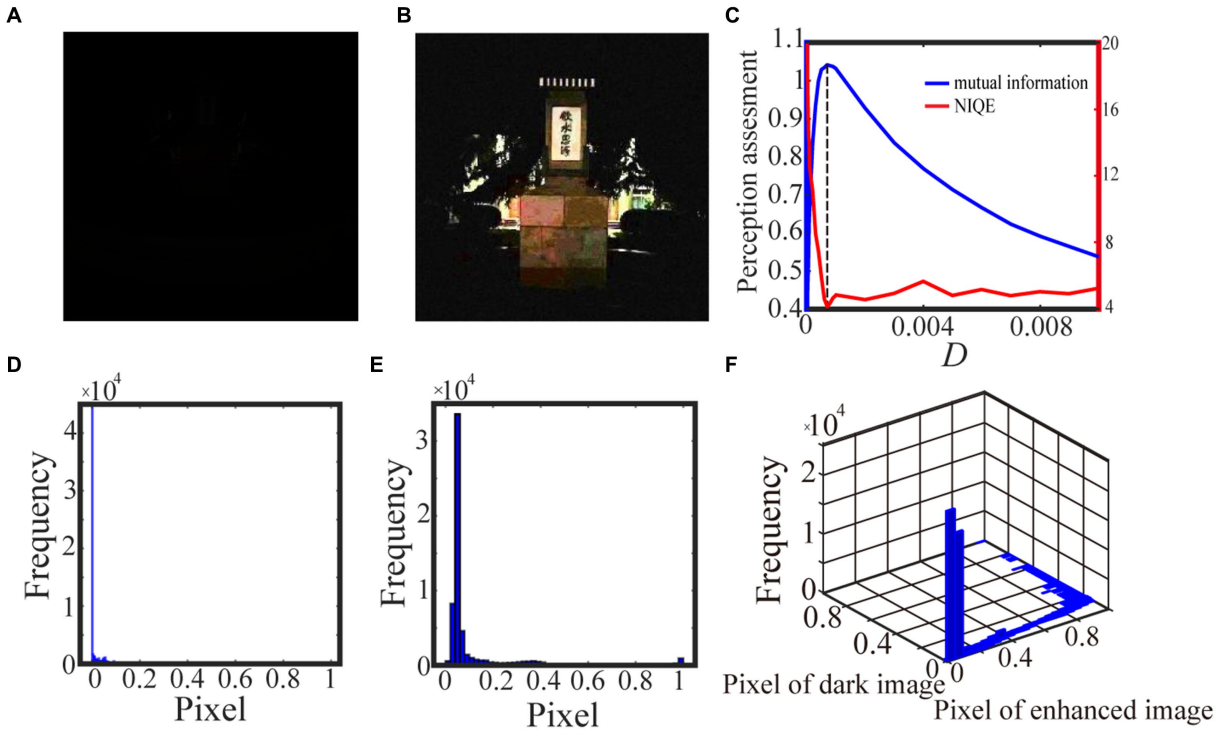

FIGURE 7
The low illuminance color image in **(A)** is taken by us and the 0.9 quintile is the spike threshold. The marginal probability law of **(A)** is shown in **(D)** while the marginal probability law of best enhanced color image **(B)** selected by mutual information is shown in **(E)**. The joint probability law of **(A)** and **(B)** are shown in the two-dimensional histogram **(F)**. The quantifying indexes mutual information (blue solid line) and NIQE (red solid line) are plotted in **(C)** where the black dotted line denotes the optimal noise intensity corresponding to the maximal mutual information.

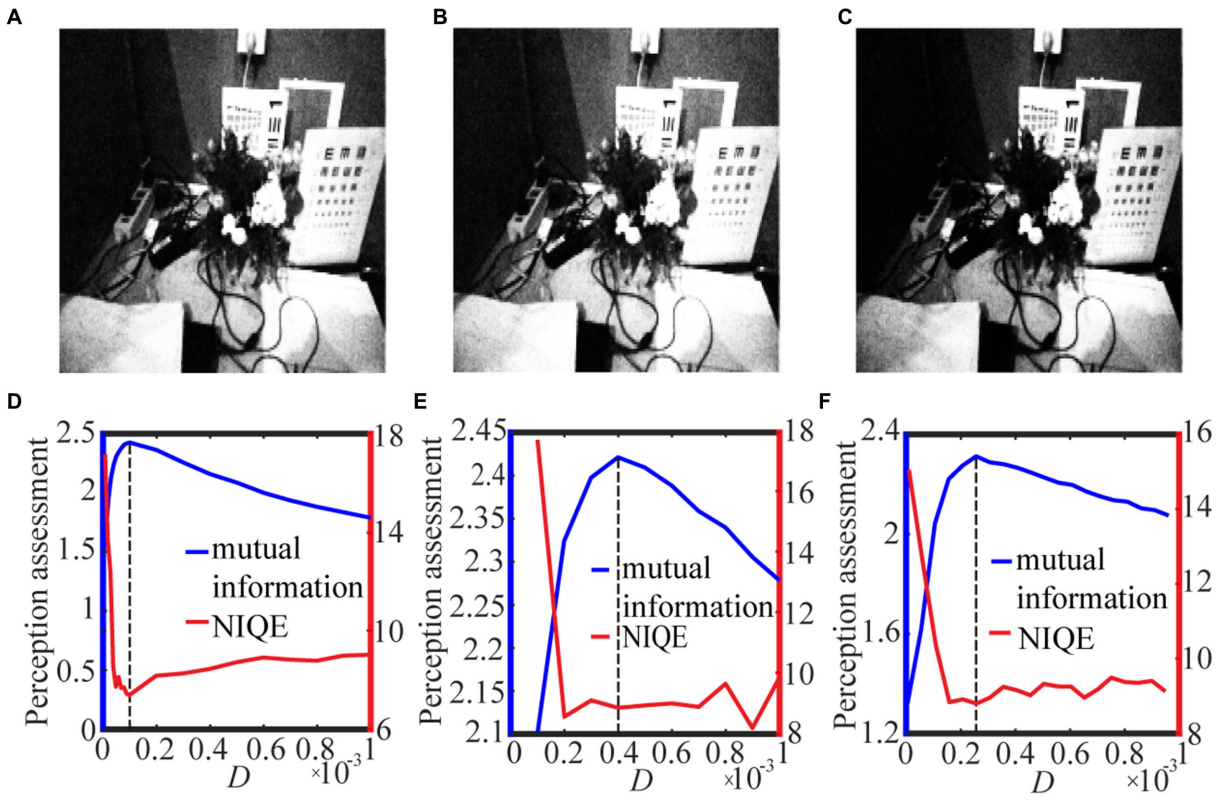

FIGURE 8
The best enhanced grayscale images selected by mutual information with spike thresholds **(A)** 0.5 quantile, **(B)** $\delta = 0.001$ and **(C)** $\delta = 0.01$ for Eq. (12). Their quantifying indexes which black dotted line denotes the optimal noise intensity corresponding to the maximal mutual information are plotted in panels **(D–F)**.

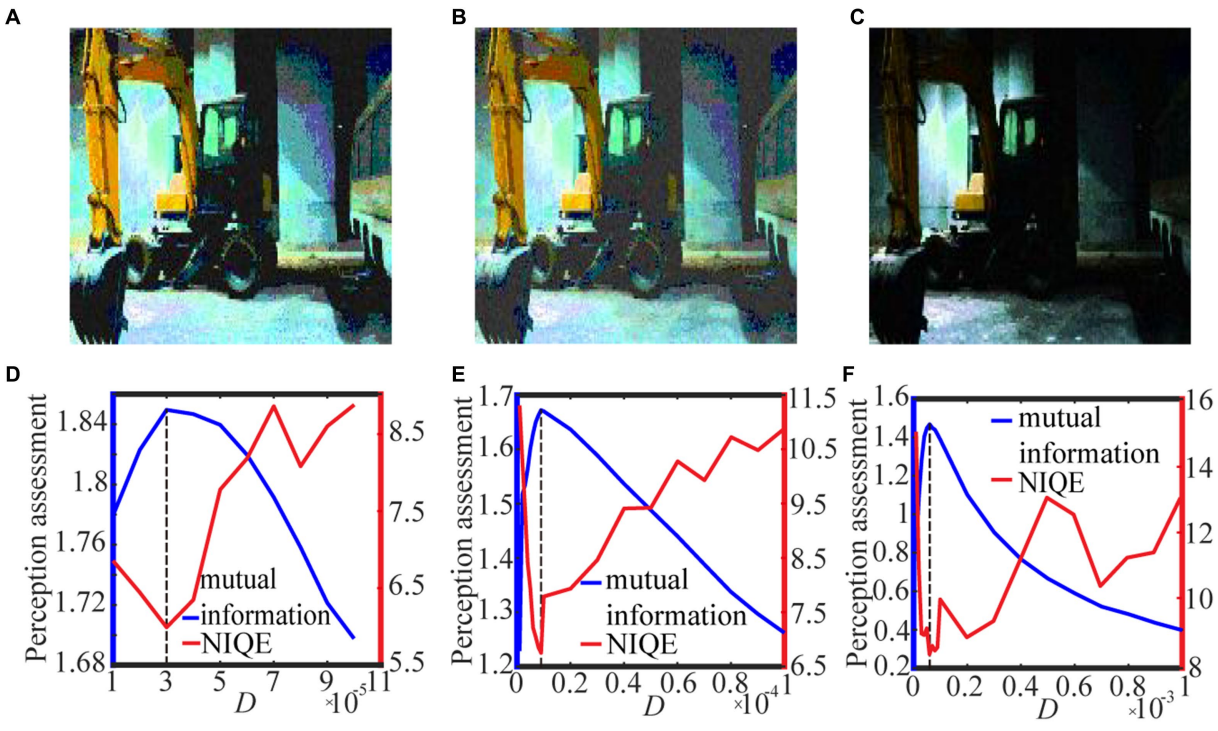

FIGURE 9
The best enhanced color images selected by mutual information with spike thresholds **(A)** 0.6 quantile, **(B)** $\delta = 0.001$ and **(C)** $\delta = 0.01$ for Eq. (13). Their quantifying indexes which black dotted line denotes the optimal noise intensity corresponding to the maximal mutual information are plotted in panels **(D–F)**.

of NIQE. By contrast, the curve of the image mutual information is smooth and sharp, as shown in Figures 8D–F, thus the mutual information metric is better for us to pick out the optimal noise intensity and then find the target image. Here, it is worthy to emphasize that the curve of the image mutual information is single-peaked, but the curve of NIQE has multiple local minimums. By checking the quality of the enhanced images at all the local optimal noise intensity, it is found that the enhanced image at the local optimal noise intensity, which is also the maximum point of the image mutual information, is the best enhanced image. This clearly demonstrates that the mutual information measure has advantage over the NIQE index in picking out the target image in the present visual perception research. That exactly manifests why we do this research. Additionally, it is observed that among the three strategies for the spike threshold, the mutual information curve corresponding to the one-half quantile has the most prominent peak, thus choosing a suitable quantile as the spike threshold (Xu et al., 2022) also has advantage over log-average luminance strategy (Reinhard et al., 2002).

For the color image case, Figure 9 shows the variation of the target image and the assessment index under different spike thresholds. It is clear that the optimal noise intensity with the image mutual formation is coincident with the optimal counterpart with the NIQE metric. This coincidence once again demonstrates both the metrics are effective for picking out the target image. Nevertheless, due to its smoothness, the image mutual information is more convenient than the NIQE metric, as suggested by the Figures. Additionally, it is evident that the target image (Figure 9C) is sensibly darker than the counterpart in Figures 9A,B, illustrating that the enhancement performance with the log-average threshold is sensitive to the choice of the small parameter. An inappropriate choice of the parameter delta in Eq. (13) can cause a bad enhancement. This of course is of inconvenience, and thus suggests that the quantile threshold strategy has merit from a viewpoint of antithesis.

4. Conclusion and discussion

We have revealed the phenomenon of aperiodic stochastic resonance in the conductance-based integrate-and-fire neuronal networks within the frame of information theory, and then we presented an improved spiking neural network based visual perception algorithm based on the principle of aperiodic stochastic resonance. In the improved algorithm, the image mutual information is adopted as a quantifying metric, since it can well measure the shared information between the input image stimulus and the enhanced target image. With the same trials in calculation, it was shown that the optimal noise intensity corresponding to the maximum of the mutual information coincides with one of the counterparts of the minimums of the NIQE index. More importantly, it was shown that the curve of the image mutual information *via* noise intensity is usually mono-peaked, sharper and smoother than that of the NIQE index *via* noise intensity. This illustrates that the applicability and advantage of the image mutual information over the frequently used index in visual perception. Additionally, with the numerical tests with the quantile of the image histogram as spike threshold scheme compared with those with the log-average luminance as spike threshold, it was further confirmed the mutual information index has more reliability than the NIQE index, since the results from the latter scheme are more sensitive to the increasing noise level. Nevertheless, note that the spike threshold is fixed during the entire implementation of the algorithm, so the quality of the best enhanced image might be further improved by an adaptive strategy, such as updating the threshold at each noise intensity by the quantile of the newly enhanced image. This is worthy to be explored in the near future. We also wish that the algorithm of this paper has application or inspiration in the relevant fields such as brain-machine interface, cosmic detection and target tracking in low-illumination environment.

Data availability statement

The original contributions presented in the study are included in the article/supplementary material, further inquiries can be directed to the corresponding author.

Author contributions

YK guided and sponsored the research. ZX did the simulation and algorithm design. YZ provided some data and attended the algorithm implementation. ZX and YK collaborated in writing and revising. All authors contributed to the article and approved the submitted version.

Funding

This work was financially supported by the National Natural Science Foundation under grant nos. 11772241 and 12172268.

Conflict of interest

The authors declare that the research was conducted in the absence of any commercial or financial relationships that could be construed as a potential conflict of interest.

Publisher's note

All claims expressed in this article are solely those of the authors and do not necessarily represent those of their affiliated organizations, or those of the publisher, the editors and the reviewers. Any product that may be evaluated in this article, or claim that may be made by its manufacturer, is not guaranteed or endorsed by the publisher.

References

Benjamin, S. G., Radhakrishnan, B., Nidhin, T. G., and Suresh, L. P. (2016). "Extraction of fire region from forest fire images using color rules and texture analysis" in *International conference on emerging technological trends (ICETT)* (Kollam, India), 1–7.

Benzi, R., Sutera, A., and Vupiani, A. (1981). The mechanism of stochastic resonance. *J. Phys. A* 14, 453–457.

Braun, H., Wissing, H., Schäfer, K., and Hirsch, M. (1994). Oscillation and noise determine signal transduction in shark multimodal sensory cells. *Nature* 367, 270–273. doi: 10.1038/367270a0

Chen, G., and Gong, P. (2019). Computing by modulating spontaneous cortical activity patterns as a mechanism of active visual processing. *Nat. Commun.* 10:4915. doi: 10.1038/s41467-019-12918-8

Collins, J. J., Imhoff, T. T., and Grigg, P. (1996). Noise-enhanced information transmission in rat SA1 cutaneous mechanoreceptors via aperiodic stochastic resonance. *J. Neurophysiol.* 76, 642–645. doi: 10.1152/jn.1996.76.1.642

Cover, T. M., and Thomas, J. A. (2006). *Elements of information theory* (*2nd*). Hoboken, NJ: Wiley-Interscience.

Destexhe, A. (1998). Spike-and-wave oscillations based on the properties of GABA(B) receptors. *J. Neurosci.* 18, 9099–9111. doi: 10.1523/JNEUROSCI.18-21-09099.1998

Dijkstra, N., Bosch, S., and van Gerven, M. (2019). Shared neural mechanisms of visual perception and imagery. *Trends Cog. Sci.* 23, 423–434. doi: 10.1016/j.tics.2019.02.004

Douglass, J., Wilkens, L., Pantazelou, E., and Moss, F. (1993). Noise enhancement of information transfer in crayfish mechanoreceptors by stochastic resonance. *Nature* 365, 337–340. doi: 10.1038/365337a0

Du, Y., Lu, Q., and Wang, R. (2010). Using interspike intervals to quantify noise effects on spike trains in temperature encoding neurons. *Cogn. Neurodyn.* 4, 199–206. doi: 10.1007/s11571-010-9112-2

Dylov, D. V., and Fleischer, J. W. (2010). Nonlinear self-filtering of noisy images via dynamical stochastic resonance. *Nat. Photonics* 4, 323–328. doi: 10.1038/nphoton.2010.31

Feng, J., Deng, Y., and Rossoni, E. (2006). Dynamics of moment neuronal networks. *Phys. Rev. E* 73:041906. doi: 10.1103/PhysRevE.73.041906

Fu, Y., Kang, Y., and Chen, G. (2020). Stochastic resonance based visual perception using spiking neural networks. *Front. Comput. Neurosci.* 14:24. doi: 10.3389/fncom.2020.00024

Guan, L., Gu, H., and Zhao, Z. (2021). Dynamics of subthreshold and suprathreshold resonance modulated by hyperpolarization-activated cation current in a bursting neuron. *Nonlinear Dyn.* 104, 577–601. doi: 10.1007/s11071-021-06230-8

Hartong, D. T., Berson, E. L., and Dryja, T. P. (2006). Retinitis pigmentosa. *Lancet* 368, 1795–1809. doi: 10.1016/S0140-6736(06)69740-7

Hore, A., and Ziou, D. (2010). Image quality metrics: PSNR vs. SSIM. 20th International Conference on Pattern Recognition, ICPR 2010, Istanbul, Turkey, 23-26 August 2010 2366–2369

Kang, Y., Fu, Y., and Chen, Y. (2022). Signal-to-noise gain of an adaptive neuron model with gamma renewal synaptic input. *Acta Mech. Sin.* 38:521347. doi: 10.1007/s10409-021-09029-6

Kang, Y. M., Liu, R. N., and Mao, X. R. (2021). Aperiodic stochastic resonance in neural information processing with Gaussian colored noise. *Cogn. Neurodyn.* 15, 517–532. doi: 10.1007/s11571-020-09632-3

Kang, Y., Xu, J., and Xie, Y. (2005). Signal-to-noise ratio gain of a noisy neuron that transmits subthreshold periodic spike trains. *Phys. Rev. E* 72:021902. doi: 10.1103/PhysRevE.72.021902

Land, E. H. (1997). The retinex theory of color vision. *Sci. Am.* 237:108.

Lecun, Y., and Bengio, Y. (1995). "Convolutional networks for images, speech, and time-series" in *The handbook of brain theory and neural networks*. ed. M. A. Arbib (Cambridge, MA: MIT Press)

Lei, Y., Zheng, F., and Shao, X. (2017). Chaos and chaos control of the Frenkel–Kontorova model with dichotomous noise. *Int. J. Bifurcation Chaos* 27:1750052. doi: 10.1142/S0218127417500523

Levin, J., and Miller, J. (1996). Broadband neural encoding in the cricket cereal sensory system enhanced by stochastic resonance. *Nature* 380, 165–168. doi: 10.1038/380165a0

Li, W., Joseph Raj, A. N., Tjahjadi, T., and Zhuang, Z. (2022). Fusion of ANNs as decoder of retinal spike trains for scene reconstruction. *Appl. Intell.* 52, 15164–15176. doi: 10.1007/s10489-022-03402-w

Masland, R. H. (1996). Processing and encoding of visual information in the retina. *Curr. Opin. Neurobiol.* 6, 467–474. doi: 10.1016/S0959-4388(96)80051-1

Mittal, A., Soundararajan, R., and Bovik, A. (2013). Making a 'Completely Blind' image quality analyzer. *IEEE Signal. Proc. Let.* 20, 209–212. doi: 10.1109/LSP.2012.2227726

Moorthy, A. K., and Bovik, A. C. (2010). Statistics of natural image distortions. *IEEE Int. Conf. Acoust. Speech Signal Process*, 962–965. doi: 10.1109/ICASSP.2010.5495298

Nakamura, O., and Tateno, K. (2019). Random pulse induced synchronization and resonance in uncoupled non-identical neuron models. *Cogn. Neurodyn.* 13, 303–312. doi: 10.1007/s11571-018-09518-5

Patel, A., and Kosko, B. (2008). Stochastic resonance in continuous and spiking neuron models with levy noise. *IEEE Trans. Neural Netw.* 19, 1993–2008. doi: 10.1109/TNN.2008.2005610

Rafael, C. G., and Woods, R. E. (2002). *Digital image processing. 3rd Edn.* New Jersey: Prentice Hall. 88–108

Rahman, Z., Jobson, D. J., and Woodell, G. A. (2004). Retinex Processing for Automatic Image Enhancement. *J. Electron. Imaging* 13, 100–110. doi: 10.1117/1.1636183

Reinhard, E., Stark, M., Shirley, P., and Ferwerda, J. (2002). Photographic tone reproduction for digital images. *ACM Trans. Graph.* 21, 267–276. doi: 10.1109/ICIP.2002.1038064

Rieke, F., and Baylor, D. A. (1998). Single-photon detection by rod cells of the retina. *Rev. Mod. Phys.* 70, 1027–1036. doi: 10.1103/RevModPhys.70.1027

Rizzo, A. M. (1997). Stochastic resonance: a new concept of neural coding. *Neuroscientist* 3, 211–214. doi: 10.1177/107385849700300408

Rolls, E., Loh, M., Deco, G., and Winterer, G. (2008). Computational models of schizophrenia and dopamine modulation in the prefrontal cortex. *Nat. Rev. Neurosci.* 9, 696–709. doi: 10.1038/nrn2462

Roy, D., Panda, P., and Roy, K. (2019). Synthesizing images from spatio-temporal representations using spike-based backpropagation. *Front. Neurosci.* 13:621. doi: 10.3389/fnins.2019.00621

Shapley, R., and Hawken, M. (2002). Neural mechanisms for color perception in the primary visual cortex. *Curr. Opin. Neurobiol.* 12, 426–432. doi: 10.1016/S0959-4388(02)00349-5

Shi, Z. Z., Liao, Z. Q., and Tabata, H. (2023). Enhancing performance of convolutional neural network-based epileptic electroencephalogram diagnosis by asymmetric stochastic resonance. *IEEE J. Biomed. Health Inform.* 1–12. doi: 10.1109/JBHI.2023.3282251

Simonotto, E., Riani, M., Seife, C., Roberts, M., Twitty, J., and Moss, F. (1997). Visual perception of stochastic resonance. *Phys. Rev. Lett.* 78, 1186–1189. doi: 10.1103/PhysRevLett.78.1186

Smith, R. A. (1978). Color gamut transform pairs. *SIGGRAPH Comput. Graph* 12, 12–19. doi: 10.1145/965139.807361

Strong, S. P., Koberle, R., De, R., and Bialek, W. (1996). Entropy and information in neural spike trains. *Phys. Rev. Lett.* 80, 197–200.

Sun, X., Liu, Z., and Perc, M. (2019). Effects of coupling strength and network topology on signal detection in small-world neuronal networks. *Nonlinear Dyn.* 96, 2145–2155. doi: 10.1007/s11071-019-04914-w

Taillefumier, T., and Magnasco, M. O. (2013). A phase transition in the first passage of a Brownian process through a fluctuating boundary with implications for neural coding. *Proc. Natl. Acad. Sci. U. S. A.* 110, 1438–1443. doi: 10.1073/pnas.1212479110

Wang, F., Zhang, B., Zhang, C., Yan, W., Zhao, Z., and Wang, M. (2021). Low-light Image Joint Enhancement Optimization Algorithm Based on Frame Accumulation and Multi-Scale Retinex. *Ad Hoc Networks* 113:10239 doi: 10.1016/j.adhoc.2020.102398

Wang, Z., Bovik, A. C., Sheikh, H. R., and Simoncelli, E. P. (2004). Image quality assessment: from error visibility to structural similarity. *IEEE Trans. Image Process.* 13, 600–612. doi: 10.1109/TIP.2003.819861

Wang, Z., Sheikh, H. R., and Bovik, A. C. (2002). No reference perceptual quality assessment of JPEG compressed images. *IEEE Int. Conf. Image Process.* 1, 477–480. doi: 10.1145/566570.566575

Winterer, G., Ziller, M., Dorn, H., Frick, K., Mulert, C., Dahhan, N., et al. (1999). Cortical activation, signal-to-noise ratio and stochastic resonance during information processing in man. *Clin. Neurophysiol.* 110, 1193–1203. doi: 10.1016/S1388-2457(99)00059-0

Wu, D., Zhang, C., Ji, L., Ran, R., Wu, H., and Xu, Y. (2021). Forest fire recognition based on feature extraction from multi-view images. *Trait. Signal* 38, 775–783. doi: 10.18280/ts.380324

Xu, Z., He, Y., and Kang, Y. (2022). Color image perception based on stochastic spiking neural network. *Acta Phys. Sin.* 71:070501 (in Chinese). doi: 10.7498/aps.71.20211982

Yang, J., Wang, C., Jiang, B., and Meng, Q. (2021). Visual perception enabled industry intelligence: state of the art, challenges and prospects. *IEEE Trans. Ind. Inform.* 17, 2204–2219. doi: 10.1109/TII.2020.2998818

Yarrow, S., Challis, E., and Series, P. (2012). Fisher and shannon information in finite neural populations. *Neural Comput.* 24, 1740–1780. doi: 10.1162/NECO_a_00292

Yu, Y. G., Potetz, B., and Lee, T. S. (2005). The role of spiking nonlinearity in contrast gain control and information transmission. *Vis. Res.* 45, 583–592. doi: 10.1016/j.visres.2004.09.024

Zeng, F., Fu, Q., and Morse, R. (2000). Human hearing enhanced by noise. *Brain Res.* 869, 251–255. doi: 10.1016/S0006-8993(00)02475-6

Frontiers in Neuroscience

Provides a holistic understanding of brain function from genes to behavior

Part of the most cited neuroscience journal series which explores the brain - from the new eras of causation and anatomical neurosciences to neuroeconomics and neuroenergetics.

Discover the latest Research Topics

See more →

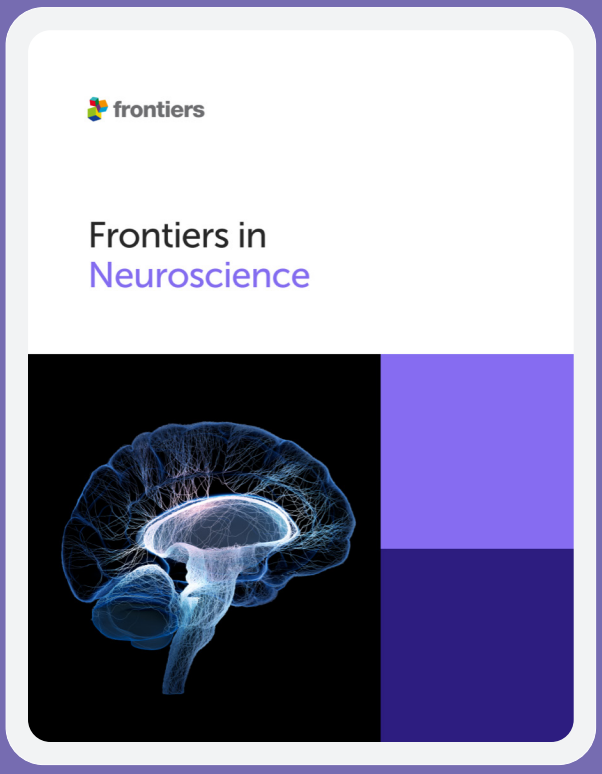

Frontiers

Avenue du Tribunal-Fédéral 34
1005 Lausanne, Switzerland
frontiersin.org

Contact us

+41 (0)21 510 17 00
frontiersin.org/about/contact